



HAL
open science

Réactivité des alliages de Mg dans l'eau - liquides ioniques hydrophiles

Dmitry Kurchavov

► **To cite this version:**

Dmitry Kurchavov. Réactivité des alliages de Mg dans l'eau - liquides ioniques hydrophiles. Chimie théorique et/ou physique. Université Paris sciences et lettres, 2022. Français. NNT : 2022UPSLC006 . tel-04027091

HAL Id: tel-04027091

<https://pastel.hal.science/tel-04027091>

Submitted on 13 Mar 2023

HAL is a multi-disciplinary open access archive for the deposit and dissemination of scientific research documents, whether they are published or not. The documents may come from teaching and research institutions in France or abroad, or from public or private research centers.

L'archive ouverte pluridisciplinaire **HAL**, est destinée au dépôt et à la diffusion de documents scientifiques de niveau recherche, publiés ou non, émanant des établissements d'enseignement et de recherche français ou étrangers, des laboratoires publics ou privés.



THÈSE DE DOCTORAT
DE L'UNIVERSITÉ PSL

Préparée à l'École Nationale Supérieure de Chimie de Paris

**Reactivity of Mg alloys
in water – hydrophilic ionic liquid**

Soutenu par

Dmitry Kurchavov

Le 07 Juin 2022

Ecole doctorale n° 388

**Chimie Physique et Chimie
Analytique de Paris-Centre**

Spécialité

Chimie physique

Composition du jury :

Frédéric KANOUI

Directeur de recherche CNRS,
Université de Paris

Président

Sviatlana LAMAKA

Directrice de recherche,
Helmholtz-Zentrum « Hereon »

Rapporteuse

Isabelle BILLARD

Directrice de Recherche CNRS,
INP Grenoble

Rapporteuse

Nick BIRBILIS

Full professor,
Australian National Univ.

Examineur

Virginie LAIR

Maître de conférences,
Chimie ParisTech

Examinatrice

Polina VOLOVITCH

Maître de conférences,
Chimie ParisTech

Directrice de thèse

Content

Content	3
Introduction	6
Context and objectives of the study	6
Methodological approach	9
Organization of the manuscript and summary of the main results	11
Part 1. State of the Art: Mg reactivity in aqueous and non-aqueous electrolytes.	12
Part 2. Methodological development.....	12
Part 3. Results.	12
Part 1. State of the art: Mg reactivity in aqueous and non-aqueous electrolytes.	25
Chapter 1: Reactivity of Mg in aqueous electrolytes	25
1.1. General information about Mg reactivity and Negative Difference Effect in aqueous electrolytes.....	25
1.2 Role of alloys composition for NDE	27
1.3. Role of surface films for NDE.....	30
Chapter 2: Water-Room Temperature Ionic Liquids (RTILs) mixtures as electrolytes to control Mg reactivity	41
2.1. General introduction to Room Temperature Ionic Liquids	41
2.2 Water-RTIL interactions.....	44
2.3. Mg reactivity in RTIL and water-RTIL mixtures.....	51
Part 2. Methodology.....	59
Chapter 3: RTIL design and experimental methods	59
3.1. Alloy compositions	59
3.2. RTIL design	60
3.1.1. Selection of RTIL compositions.....	60
3.2.2. Synthesis of RTILs, their identification and preparation of their mixtures with water	62
3.3. Characterization of RTILs and their mixtures with water.....	68
3.2.1. Electrochemical characterization.....	68
3.2.2. Chemical characterization of the electrolytes	72
3.3. Reactivity characterization at metal – electrolyte interfaces.....	74

3.4. Chemical characterization of solid surface and humid interface	77
Part 3. Results.....	81
Chapter 4: Mg-alloys in water – hydrophilic ionic liquid mixtures: is there a negative difference effect?.....	81
Chapter 5: Influence of PEG-containing cation on molecular state of water in water – acetate based ionic liquids mixtures	110
Chapter 6: Synergic effect of ionic liquid (IL) cation and anion inhibits negative difference effect on Mg in water - IL mixtures.....	153
Part 4. Conclusions and perspectives.....	187
Chapter 7: Results and perspectives	187
Bibliography.....	193
Appendix 1	209
Supplementary materials for the article “Mg-alloys in water – hydrophilic ionic liquid mixtures: is there a negative difference effect?”	209
Appendix 2	211
Supplementary materials for the article “Influence of PEG-containing cation on molecular state of water in water – acetate based ionic liquids mixtures”.....	211
Appendix 3	217
Supplementary materials for the article “Synergic effect of ionic liquid (IL) cation and anion inhibits negative difference effect on Mg in water - IL mixtures”	217
Résumé de la thèse	230
Contexte et objectifs de l'étude.....	230

Introduction

Context and objectives of the study

Mg and its alloys are considered as attractive materials for numerous applications in aerospace, automotive and biomedical industries due to their high strength to weight ratio, biocompatibility, high abundance and non-toxicity [1–5]. Electrochemically, Mg possesses relatively low standard oxidation/reduction potential ($E_0 = -2.37$ V vs. SHE) and high volumetric and gravimetric capacities (up to $3833 \text{ mAh}\cdot\text{cm}^{-3}$ and $2205 \text{ mAh}\cdot\text{g}^{-1}$ respectively) [6]. Thus, nowadays it is also considered as a perspective material for Mg-batteries with metallic anodes. However, many applications of Mg are limited by its high corrosion rate in aqueous electrolytes or even in the hybrid electrolytes containing water traces as well as by partly protective surface films and corrosion products leading to uncontrolled and strongly localized corrosion, which is also complicated by hydrogen gas formation and still not completely understood. The understanding and the control of Mg reactivity in different electrolytes is therefore necessary for both fundamental research and practical application of Mg alloys.

It is commonly accepted that in aqueous electrolytes the reactivity of Mg alloys is characterized by at least three processes: anodic Mg dissolution, cathodic water reduction and formation of corrosion products on the surface Mg [7,8]. Some interesting specific features of Mg alloys electrochemical behavior are its self-corrosion (increasing corrosion rate after anodic polarization) and so-called Negative Difference Effect (NDE) or anomalous hydrogen evolution (HE). The latter indicates that the rate of cathodic water reduction reaction accelerates under anodic polarization. It contradicts classical electrochemical kinetics models, typified by Butler-Volmer equation, whereas the rate of cathodic processes exponentially decreases with an increase of anodic potential [9]. Taking into account that Mg has the most negative electrochemical potential between all metallic engineering elements (Fe, Al and etc...), it can be easily anodically polarized in real applications,

making this phenomenon important not only from the fundamental point of view but also for practical applications. Anomalous HE can be also harmful for battery applications because it leads to a reduced Utilization Efficiency (UE) of metallic anode and abundant gas release able to the failure of the battery [10–12].

Mg corrosion in aqueous electrolytes has been extensively studied and numerous mechanisms have been proposed for Mg corrosion process and the NDE (Fig. 1) [13], even though there is no NDE mechanism which is commonly accepted by all the researchers.

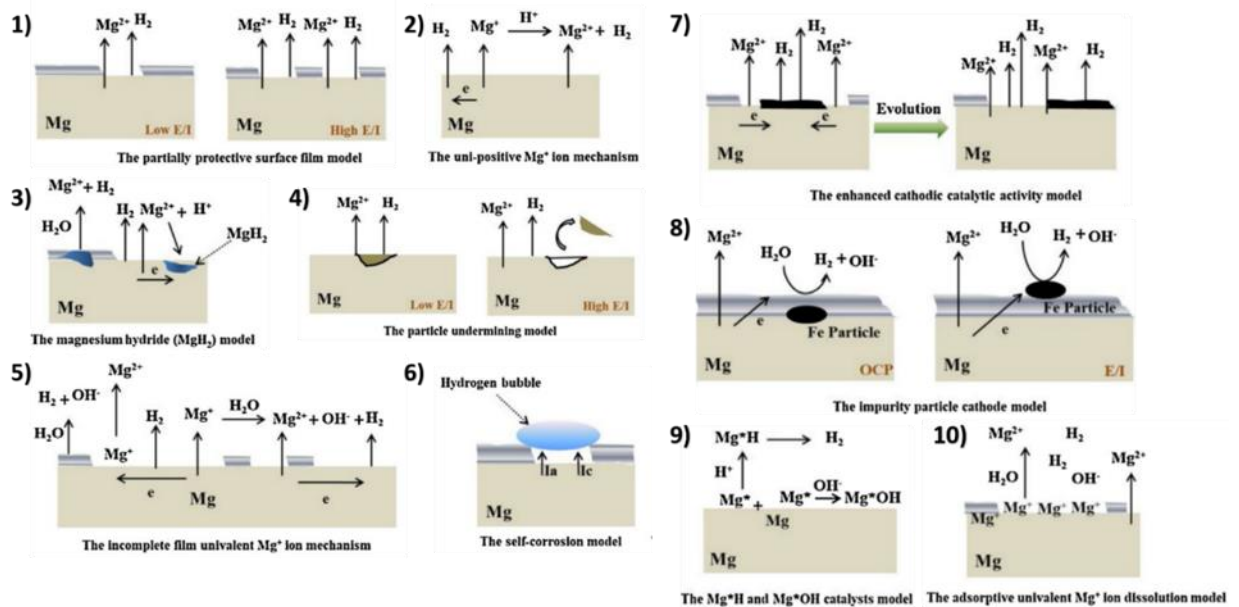


Fig. 1. Schematic illustration of various NDE or Mg dissolution models. Adopted from [13].

In contrast, the possibility of the NDE has never been discussed for non-aqueous electrolytes such as ionic liquids, which could contain water as an additive. Ionic liquids (ILs) are ionic compounds with melting point temperature below 100 °C. They usually consist of organic cations and organic or inorganic anions and their structure can contain function groups recognized as corrosion inhibitors for Mg, like carboxylate anions. ILs form a relatively new class of electrolytes attracting an enormous interest for energy applications because of their high conductivity, good

thermal stability, wide electrochemical potential window, low volatility and environmental friendliness [14–16].

The practical use of ILs is however limited by their limited stability in the presence of air and humidity, high viscosity and reduced transport properties. Formulation of hydrophilic ILs and dilution with water can help to overcome these difficulties [17]. Addition of water, however, narrows the electrochemical potential window (EPW) of the electrolyte. This effect could be potentially compensated and decreased by additional interactions between water and IL groups, *e.g.* hydrogen bonds formation which can be possible for example between water and acetic [18] and etheric [19] groups.

Despite the clear interest of the water – ILs mixtures, very little is known about the behavior of Mg alloys in such electrolytes and the role of the cations and anions of IL in the electrochemical processes. Considering Mg reactivity in water – IL mixtures, the question of the existence of the **NDE in these electrolytes is completely unexplored**. Taking into account these circumstances, the **first objective of this PhD is to preliminary discover Mg alloys reactivity in water-hydrophilic IL mixtures, to check the absence or the presence of the NDE and to compare the behavior of different Mg alloys in different ILs.**

For this aim an intermediate goal is to design new hydrophilic room temperature IL containing etheric groups and acetate anions and to understand the interactions between water and IL moieties, in particular the capacity of the cation to form intermolecular hydrogen bonds and its effect on the molecular state and reactivity of water.

Another intermediate objective is to explore the chemistry of the solid – liquid interface between Mg and hybrid electrolytes and the nature of the surface films existing in such systems.

Once the reactivity of Mg and interface chemistry are preliminary discovered and molecular state of water in hybrid electrolyte is determined, **the last objective**

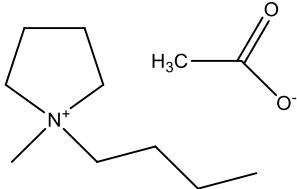
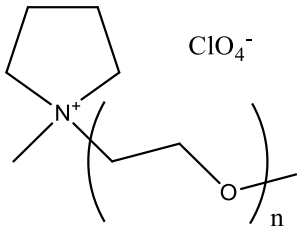
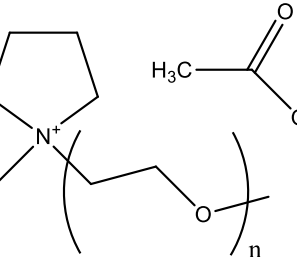
is to precise the role of the cation containing specific functional groups and to propose tentative mechanisms of Mg reactivity and of the NDE activation or inhibition in studied electrolytes.

The results of this work should contribute to fundamental understanding of Mg corrosion and the NDE phenomenon in H₂O-ILs electrolytes, in particular, of the effect of ILs cation, as well as of the molecular state of water in such electrolytes.

Methodological approach

Based on the literature review, acetate-based ionic liquids were selected because they revealed an excellent capacity to form intermolecular hydrogen bonds with water and are also expected to act as Mg corrosion inhibitors. For the IL cation design, polyetheric-substituted structure was proposed, because oxygen atoms of etheric groups are also expected to form hydrogen bonds with water. Moreover, dry polyethylene glycol (PEG) containing hydrophobic ionic liquids were reported to support Mg stripping. In order to separate the effects of acetic anion and PEG-substituted cation, additional ILs were designed in which either anion or cation were modified. The designed ILs are presented in **Table 1**. The synthesis route of these electrolytes was proposed, and the synthesis was realized. The composition of the ILs was verified by nuclear magnetic resonance (NMR) and mass spectroscopy. Specific conductivity of H₂O-ILs mixtures measurement by the electrochemical impedance spectroscopy (EIS) and the electrochemical window measurement were conducted in a especially designed small volume (200 µl) electrochemical cell.

Table 1. Systematical names, acronyms and graphical structures of designed ILs.

Ionic liquid; Their acronyms	Graphical formula
1-butyl-1-methylpyrrolidinium acetate, [BMPyr]OAc; ILA	
1-methoxy-polyethylenglycol-1-methylpyrrolidinium perchlorate, [mPEG _n MPyr]ClO ₄ ; ILEP	
1-methoxy-polyethylenglycol-1-methylpyrrolidinium acetate, [mPEG _n MPyr]OAc ILE	

*n – means variable numbers of etheric groups found by MALDI-TOF, $4 \leq n \leq 16$ with an average value $\langle n \rangle = 7$.

The reactivity of Mg alloys in designed water – IL mixtures was studied by electrochemical methods: potentiodynamic polarization and cycling potentiostatic polarization. A home-made electrochemical cell for electrochemical experiments was proposed, allowing to reduce the volume of the electrolyte (700 μ l), to separate HE on the working electrode from the H₂ evolved on the counter electrode and to survey the surface - solution interface transformation by Time Lapse Microscopy (TLM).

To investigate the chemical composition of the surface and the interface and detect Mg corrosion products Raman spectroscopy, Confocal Raman Microscopy (CRM), Attenuated Total Reflectance Fourier Transform Infrared Spectroscopy (ATR-FTIR) and Time-of-Flight Mass Spectroscopy (ToF-SIMS) were applied.

Additionally, molecular state of water and IL moieties in the mixtures was studied by Raman, ATR-FTIR spectroscopy and Molecular Dynamics Simulations. To verify the effect of leached by corrosion Mg^{2+} cations on the molecular state of the electrolyte, MD simulations of the mixtures H_2O -IL with and without addition of Mg ions were made.

Organization of the manuscript and summary of the main results

The manuscript is composed of 4 main parts.

After this introduction **Part 1 (State of the art) proposes a bibliographical review of the state of the art allowing to understand the context of the work and define open scientific questions which will be answered in the PhD.**

Part 2 (Methodological development) explains the choice of materials and methods and experimental strategy.

Part 3 (Results) proposes the answers on the questions asked in Part (1) on the basis of the experimental and theoretical results. This part is presented in the format of 3 scientific publications and is completed by several appendices after the end of the manuscript.

Finally, Part 4 formulates general Conclusions & Perspectives of the work.

The most important information presented in each part is briefly summarized below:

Part 1. State of the Art: Mg reactivity in aqueous and non-aqueous electrolytes.

This section is organized in 2 chapters. **Chapter 1, “Reactivity of Mg in aqueous electrolytes”**, includes a brief review of some basic principles describing aqueous reactivity of Mg alloys. The Negative Difference Effect (NDE) phenomenon is introduced. In particular, the role of surface films and of the electrolyte composition for it is underlined. **Chapter 2, “Water-Room-Temperature Ionic liquid (RTIL) mixtures as electrolytes for control of Mg-reactivity”**, introduces the basic knowledge about Room Temperature Ionic Liquids (RTILs or ILs), their interaction with water molecules and detailed literature review on the Mg reactivity in hydrophobic and hydrophilic ILs and their mixtures with water.

Part 2. Methodological development.

This part consists of only **Chapter 3**, which briefly describes the strategy of the IL design and synthesis roads, the design of the electrochemical experiments and electrochemical set up, as well as explains the selection of characterization technics and gives a basic theoretical information about the techniques chosen for the characterization of the solution.

Part 3. Results.

This part consists of three chapters presenting three scientific papers published or under evaluation. **Chapter 4, “Mg-alloys in water – hydrophilic ionic liquid mixtures: is there a negative difference effect?”** answers the question if the NDE is a universal effect in the presence of water or it can be suppressed in hybrid electrolytes. Electrochemical and Time Lapse Microscopy results are compared for two commercially available Mg alloys (commercially pure Mg and Al-containing alloy AZ61) in two proposed in this work acetate ILs containing 10 wt% of water. One IL contains cation with aliphatic tail ([BMPyr]⁺) and another RTIL with polyetheric tail ([mPEG_nMPyr]. NDE was observed for both alloys exposed in [BMPyr]OAc-H₂O electrolyte. However, in [mPEG_nMPyr]OAc-H₂O the NDE was

suppressed on CP Mg while hydrogen evolution was suppressed on AZ61, which correlated with the formation of a low adherent gel-like film (**Fig. 2**) which formed and healed under anodic polarization.

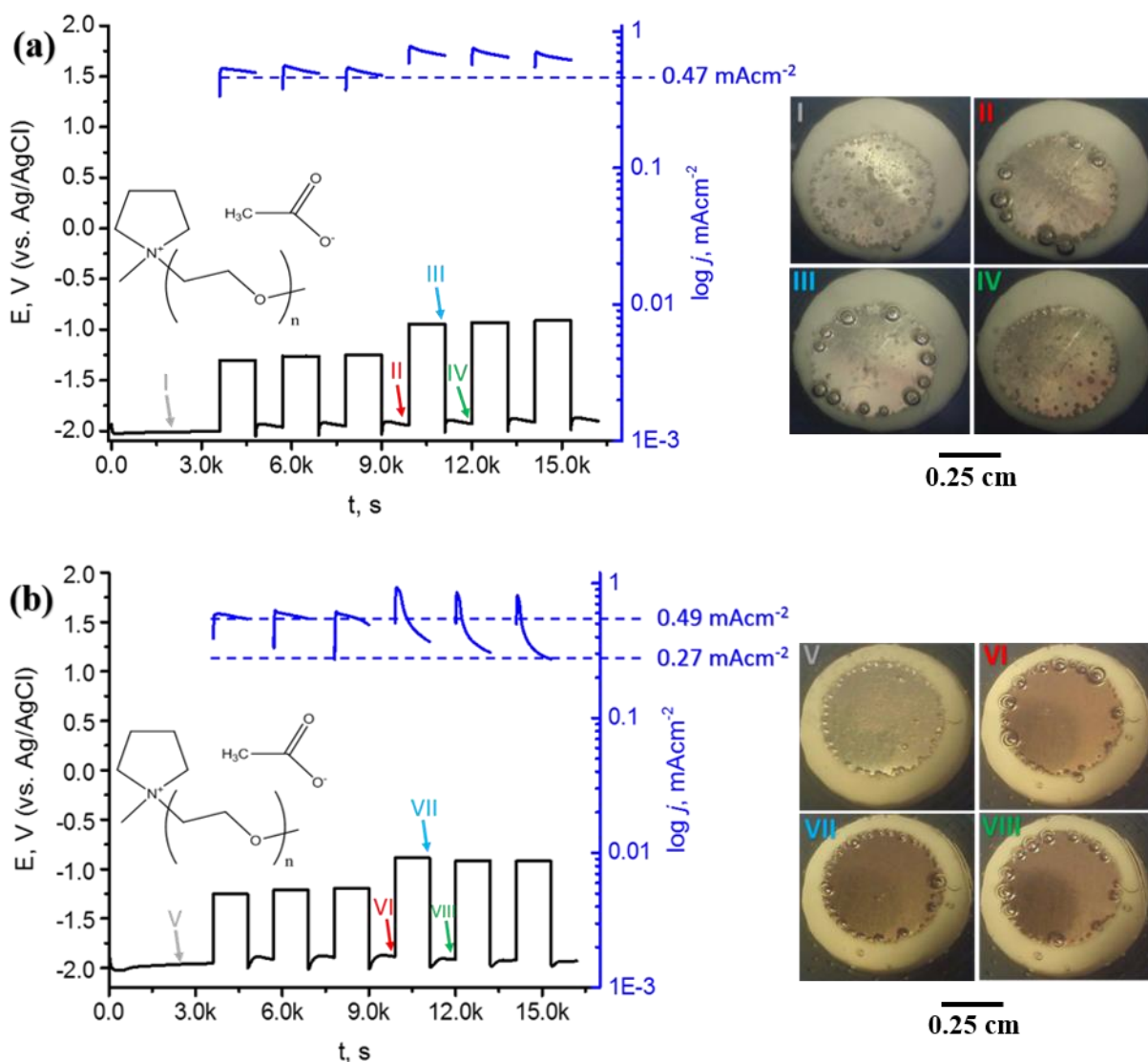


Fig. 2. Electrochemical response of (a) CP Mg and (b) AZ61 in [mPEG_nMPyr]OAc-H₂O mixture and typical TLM images of the surface taken during the experiments. The times at which the selected images were taken is indicated by arrows (I-VIII) on the potential evolution curve.

Raman microscopy and ATR-FTIR spectroscopy of the wet surfaces after electrochemical experiments in both electrolytes confirmed that chemically bound acetate is present on the surface after all the experiments. Homogeneously distributed Mg(OH)₂ film formed on CP Mg but no Mg(OH)₂ was detected on AZ61

independently of the used electrolyte. This indicates that in the water-IL mixtures the presence or not of the NDE can be correlated neither with the action of the acetate anions (which was expected to limit the NDE from the experience of aqueous corrosion) nor with the presence of corrosion products (which were expected to enhance the NDE following the experience of aqueous corrosion). The paper concludes that the role of the cation for the electrochemical reactivity of water in the hybride electrolyte and for the chemistry of the surface film needs to be better understood. These aspects are treated in the next chapters.

Chapter 5, “Influence of PEG-containing cation on molecular state of water in H₂O–acetate based ionic liquids mixtures”, illustrates in details molecular state of ions of ILs and water in their mixtures. The synthesis and identification of the water miscible acetate-based ionic liquids with hydrophobic aliphatic-substituted MPyr-cation and more hydrophilic polyetheric-substituted (mPEG_n-) tail in MPyr⁺ cation ([BMPyr]OAc and [mPEG_nMPyr]OAc respectively, see **Table 1** for graphical structures) is detailed. Their electrochemical properties such as electrochemical potential window (EPW) (**Fig. 3**) and specific ionic conductivity are shown.

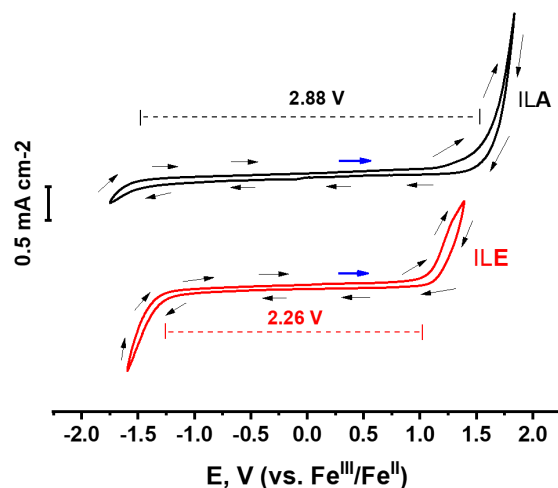


Fig. 3. Cyclic voltammograms recorded on glassy carbon disk electrode of “as synthesized” ILA and ILE, as indicated. Arrows indicate potential scanning direction starting from blue. Scan rate 50 mVs^{-1} . Electrochemical potential window is also shown by dash lines; the limits are determined at $0.1 \text{ mA}\cdot\text{cm}^{-2}$ current density cut off.

The evolution of conductivity and the molecular state of the electrolyte are studied as a function of water content in the electrolyte, which varied in a large concentration domain (from 2 to 99.8 wt. % of water).

The molecular interactions between water and IL ions in the electrolyte were monitored by Raman and ATR-FTIR spectroscopies for multiple compositions of water–IL mixtures. Based on vibration spectroscopy results some ideas about chemical environment of different functional groups and water molecules and about electrolyte structural organization are proposed. These assumptions are corroborated with Molecular Dynamic (MD) simulations done in collaboration with the *Institute of Chemistry for Life and Health Sciences, TCM team* at ChimieParisTech.

The results reveal that in the [BMPyr]OAc- H_2O electrolyte water molecules form hydrogen bonds (H-bonding) with acetate anions ($\text{HOH}\cdots\text{OAc}$) (identified by clear shifts in peaks positions in Raman and IR spectra, see example in **Fig. 4 a**). The probability of “free” water clusters formation is very low for water to IL ratios

up to $n(\text{H}_2\text{O}) / n(\text{ILA}) = 3$. Water molecules start to form water-clusters at $n(\text{H}_2\text{O}) / n(\text{ILA}) \geq 3$.

In contrast, in the $[\text{mPEG}_n\text{MPyr}]\text{OAc-H}_2\text{O}$, water molecules interact by H-bonding not only with acetate anions but also with the oxygens of etheric chain ($\text{HOH} \cdots \text{O}_{(\text{etheric})}$) (**Fig. 4 b**). Careful analysis of the infrared spectra in the region of O-H vibrations, reveals that the growth of water-clusters starts only at $n(\text{H}_2\text{O}) / n(\text{ILE}) \geq 7$. MD simulation confirmed that dilution of the aliphatically substituted ILA results in a continuous decrease of the probability of H-bonds between water and acetate and hence strongly increases the probability of the formation of water clusters in the IL with aliphatic tail. The effect is not the same for etherically substituted ILE. During dilution of the ILE the water molecules continue to be H-bonded with etheric groups, which significantly limit the probability of water cluster formation.

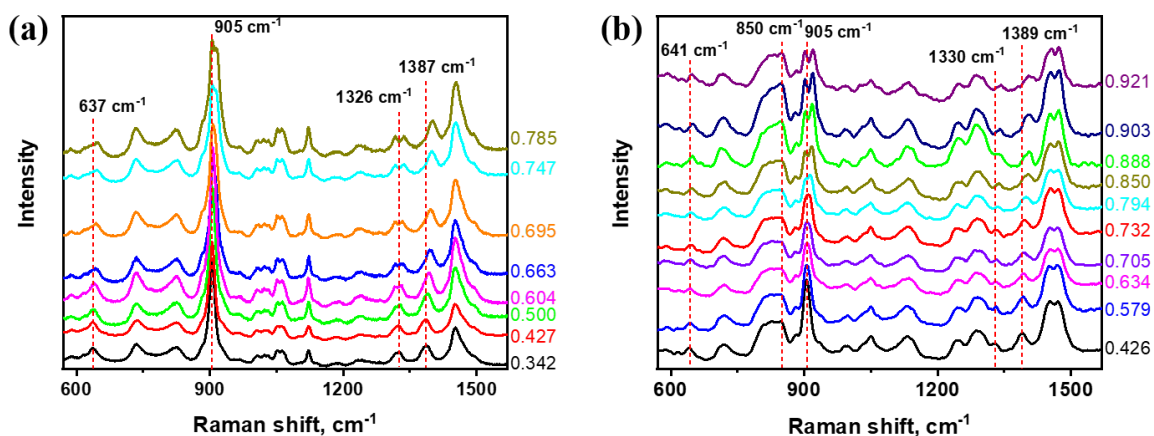


Fig. 4. Typical Raman spectra of water mixtures with ILA (a) and ILE (b) with different molar fractions of water (as indicated at right of each spectrum). On (a) all noted shifts are attributed to acetate groups vibrations. On (b) 850 cm^{-1} is attributed to C-O-C vibrations, the others – to acetate group. For detailed information see **Chapter 5**.

The modification of the molecular state of water with dilution of the electrolyte can be correlated with the evolution of specific ionic conductivity. The

formation of water-clusters tends to significantly increase ionic conductivity (**Fig. 5**). Once “free” water phase with water-water hydrogen bonds is formed, ionic conductivity very rapidly grows in both ILs. Transition from conductivity increase with water addition (behavior expected for slightly water diluted IL) to conductivity decrease with water addition (behavior typical for diluted aqueous solutions) occurs at molar water to IL ratios $n(\text{H}_2\text{O}) / n(\text{IL}) = 33$ for aliphatic substituted [BMPyr]OAc and at $n(\text{H}_2\text{O}) / n(\text{IL}) = 145$ for [mPEG_nMPyr]OAc.

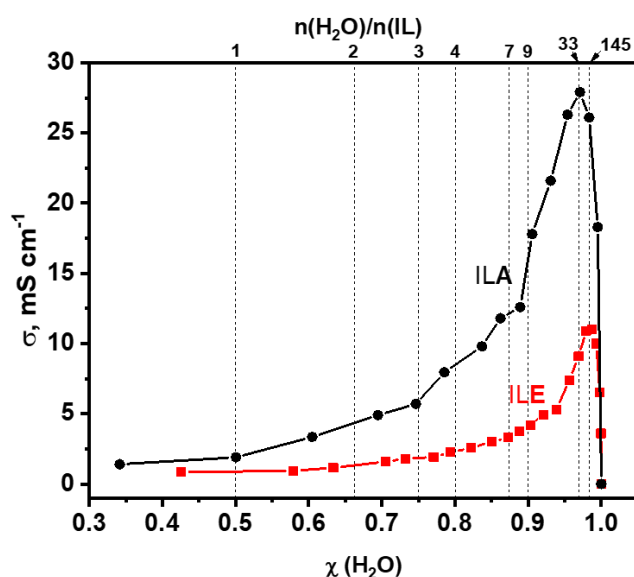


Fig. 5. Specific conductivity of water-ILA and water-ILE mixtures, σ , as a function of molar water content $\chi(\text{H}_2\text{O})$. Vertical lines show fractions for some selected molar ratios between water molecules and IL molecules $n(\text{H}_2\text{O}) / n(\text{IL})$ as indicated.

In Chapter 6, “Synergistic effect of ionic liquid (IL) cation and anion inhibits negative difference effect on Mg in water - IL mixtures”, the origins of the NDE inhibition in [mPEG_nMPyr]OAc-H₂O electrolyte and the role of both acetate anion and mPEG_n- substituted cation and their synergistic effect are demonstrated. The necessity of both, the anion and the cation, for the suppression of the NDE is demonstrated by additional experiments made in the additionally

designed electrolyte in which $[m\text{PEG}_n\text{MPyr}^+]$ cation is combined not with OAc^- but with ClO_4^- . If in $[m\text{PEG}_n\text{MPyr}]\text{OAc}-\text{H}_2\text{O}$ mixture the NDE was suppressed on CP Mg, and HE decreased on AZ61, in the $[m\text{PEG}_n\text{MPyr}]\text{ClO}_4-\text{H}_2\text{O}$ strong HE occurs and it is enhanced under anodic polarization (**Fig. 6**).

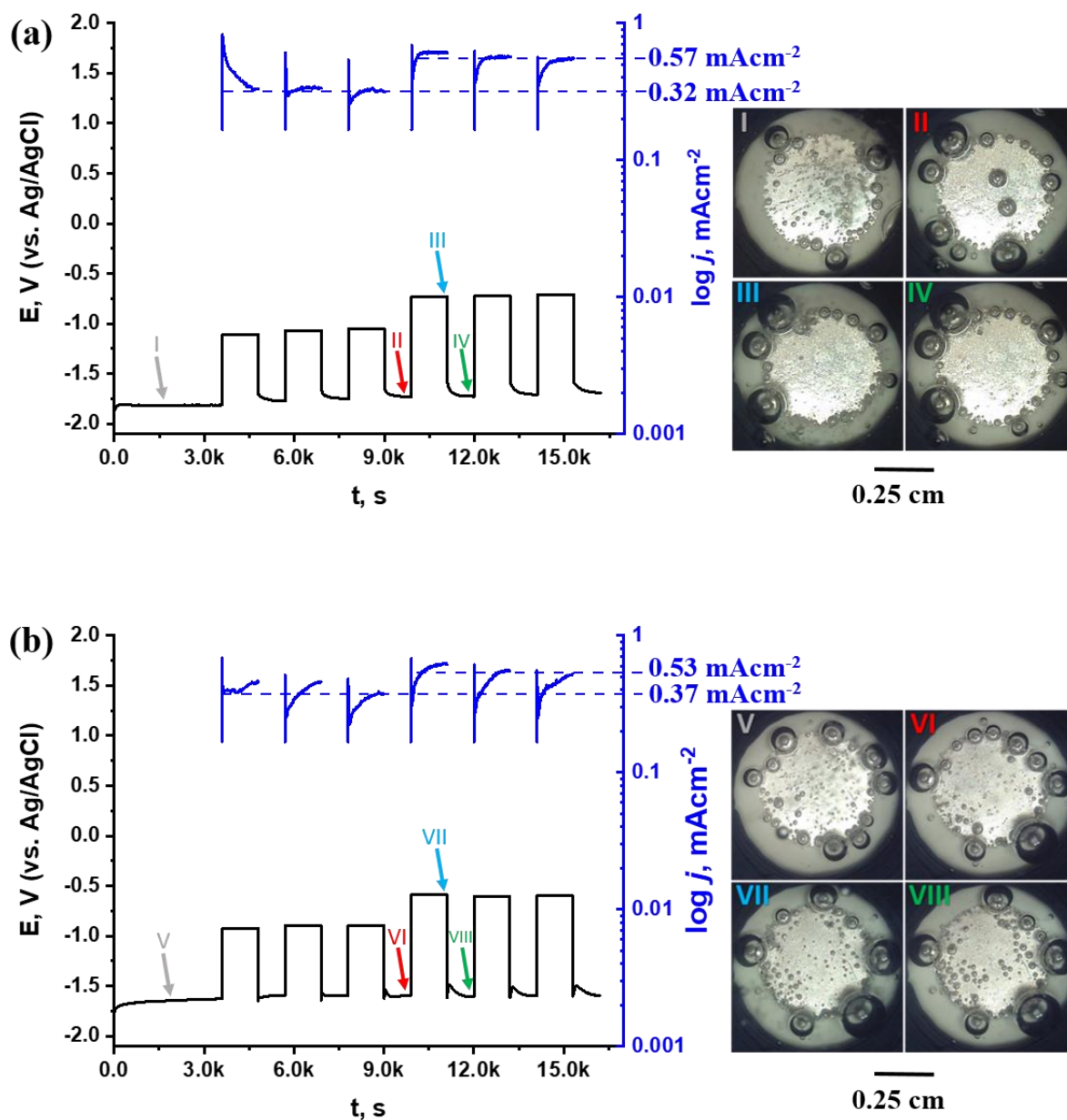


Fig. 6. Electrochemical response of (a) CP Mg and (b) AZ61 in $[m\text{PEG}_n\text{MPyr}]\text{ClO}_4-\text{H}_2\text{O}$ mixture and typical TLM images of the surface taken during the experiments. The time at which the selected images were taken is indicated by arrows (I-VIII) on the potential evolution curve.

Examination of the wet metallic surfaces by vibrational spectroscopies revealed the same tendency of $\text{Mg}(\text{OH})_2$ formation as in acetate-based ILs (the presence on CP Mg and its absence on AZ61) for all the electrolytes. For the samples reacted in $[\text{mPEG}_n\text{MPyr}]\text{ClO}_4\text{-H}_2\text{O}$ and $[\text{mPEG}_n\text{MPyr}]\text{OAc-H}_2\text{O}$ slight shifts of the Raman peaks positions in the region $\approx 790\text{-}830\text{ cm}^{-1}$ usually attributed to vibrations in etheric groups were also present. At the same time, the evolution of the Raman spectra around $\approx 1370\text{-}1381\text{ cm}^{-1}$ suggested probable decomposition of etheric groups of the electrolyte catalyzed by leached Mg^{2+} ions and formed OH^- ions, which was already reported in other PEG-containing systems [20]. One should conclude therefore that OAc^- anion in $[\text{mPEG}_n\text{MPyr}]\text{OAc-H}_2\text{O}$ can have an additional role, stabilizing the cation versus its electrochemical oxidation catalyzed by Mg^{2+} . This can be achieved by bonding Mg^{2+} in acetate complexes, which existence was confirmed by vibrational spectroscopy and ToF-SIMS.

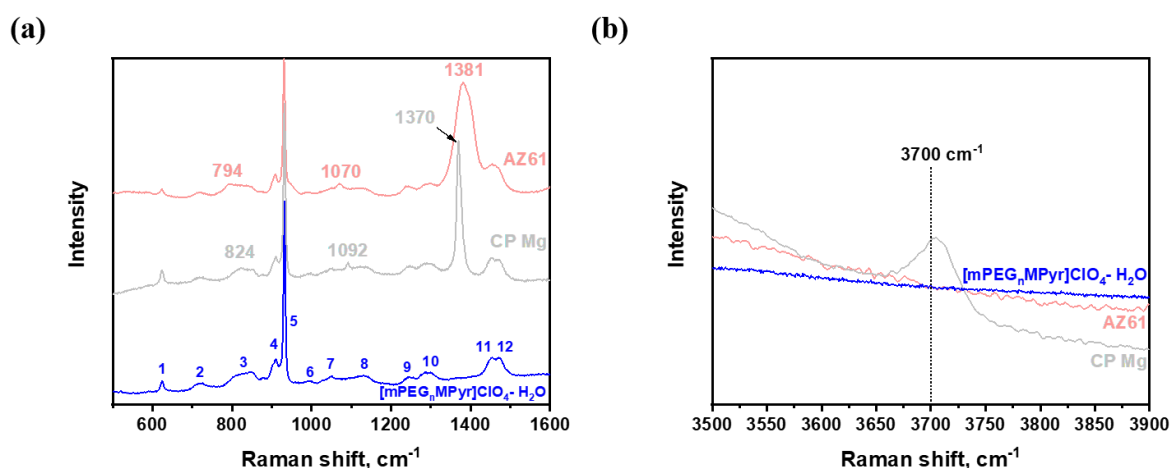


Fig. 7. Typical Raman spectra recorded on the surfaces of CP Mg and AZ61 (as indicated) after electrochemical experiment in $[\text{mPEG}_n\text{MPyr}]\text{ClO}_4\text{-H}_2\text{O}$ within $500\text{-}1600\text{ cm}^{-1}$ (a), $3500\text{-}3900\text{ cm}^{-1}$ (b). The spectrum of $[\text{mPEG}_n\text{MPyr}]\text{ClO}_4\text{-H}_2\text{O}$ mixture is shown for comparison.

Chemical depth profiles obtained by ToF-SIMS analysis allowed to detail the structure of the surface films and specifically of a pronounced condensed layer on the surface of AZ61 after the electrochemical experiment in $[\text{mPEG}_n\text{MPyr}]\text{OAc-H}_2\text{O}$ (**Fig. 8 b**) which probably prevents the NDE. The detailed

analysis by ToF-SIMS mass spectra of this film revealed that it predominantly consists of complexes with Al^{3+} and Mg^{2+} bounded with etheric groups and acetate anions. On the contrast, only oxide-hydroxide modification and adsorbed film but no condensed film was observed on CP Mg (**Fig. 8 a**).

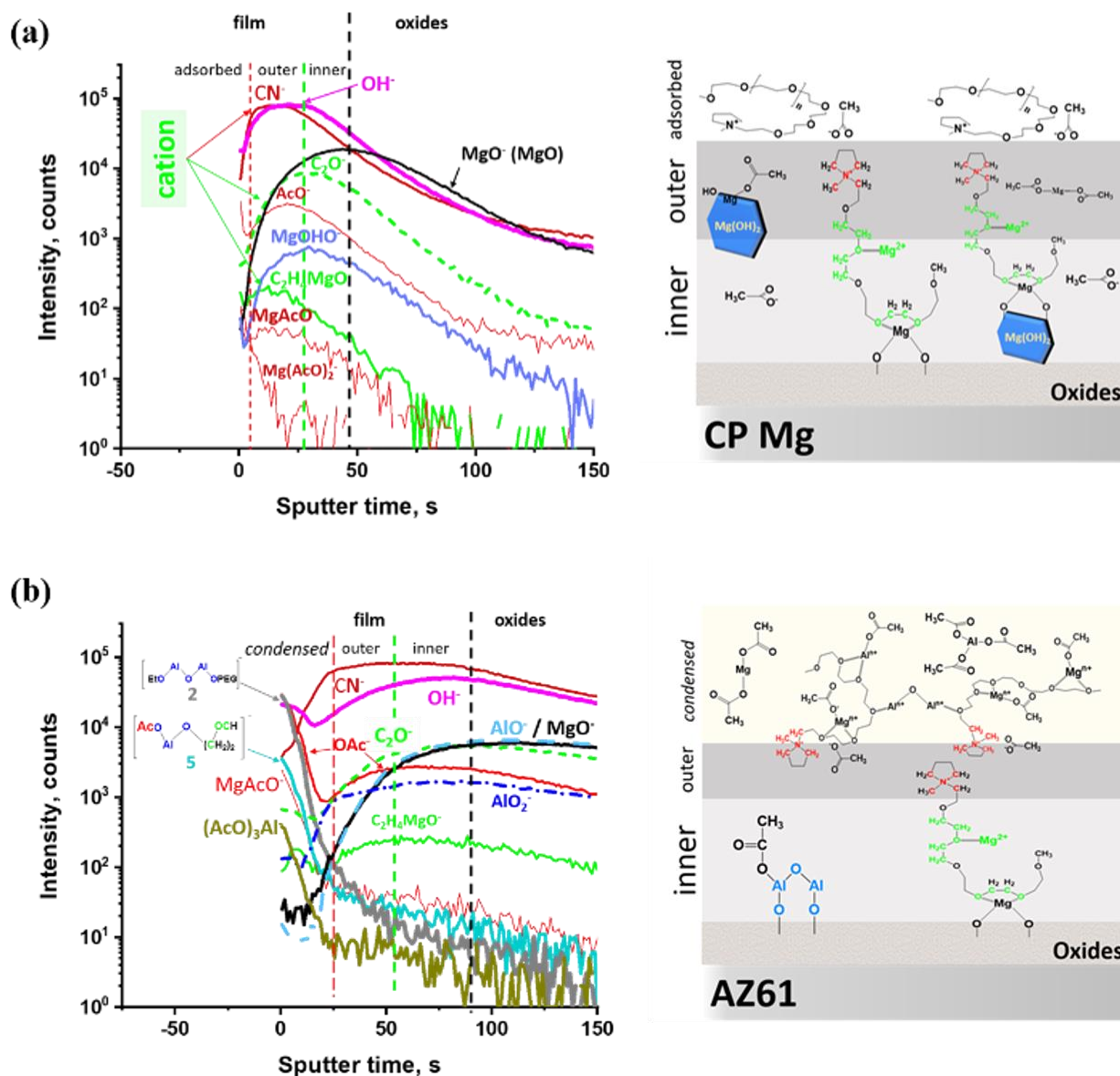


Fig. 8. Typical ToF-SIMS depth negative ions profile obtained after electrochemical experiments in $[\text{mPEG}_n\text{MPyr}]\text{OAc-H}_2\text{O}$ electrolyte on (a) CP Mg, (b) AZ61. Suggested layer organizations are also shown.

Detailed analysis of IR spectra in O-H vibrational region (3000-3700) (**Fig. 9**) recorded on wet surfaces of CP Mg and AZ61 after electrochemical experiments in $[\text{mPEG}_n\text{MPyr}]\text{OAc-H}_2\text{O}$ indicated that water molecules are still bonded with acetate anions and oxygens of etheric groups. At the same time, in

[BMPyr]OAc-H₂O and in [mPEG_nMPyr]ClO₄-H₂O water molecules seem to form interconnected water clusters (network water) which is illustrated by the increase of contribution of the low wavenumbers. Formation of water clusters in these electrolytes could explain the observed extensive water reactivity and HE on Mg electrode in them, while water bonding in [mPEG_nMPyr]OAc-H₂O can be considered as one of the reasons of reduced HE.

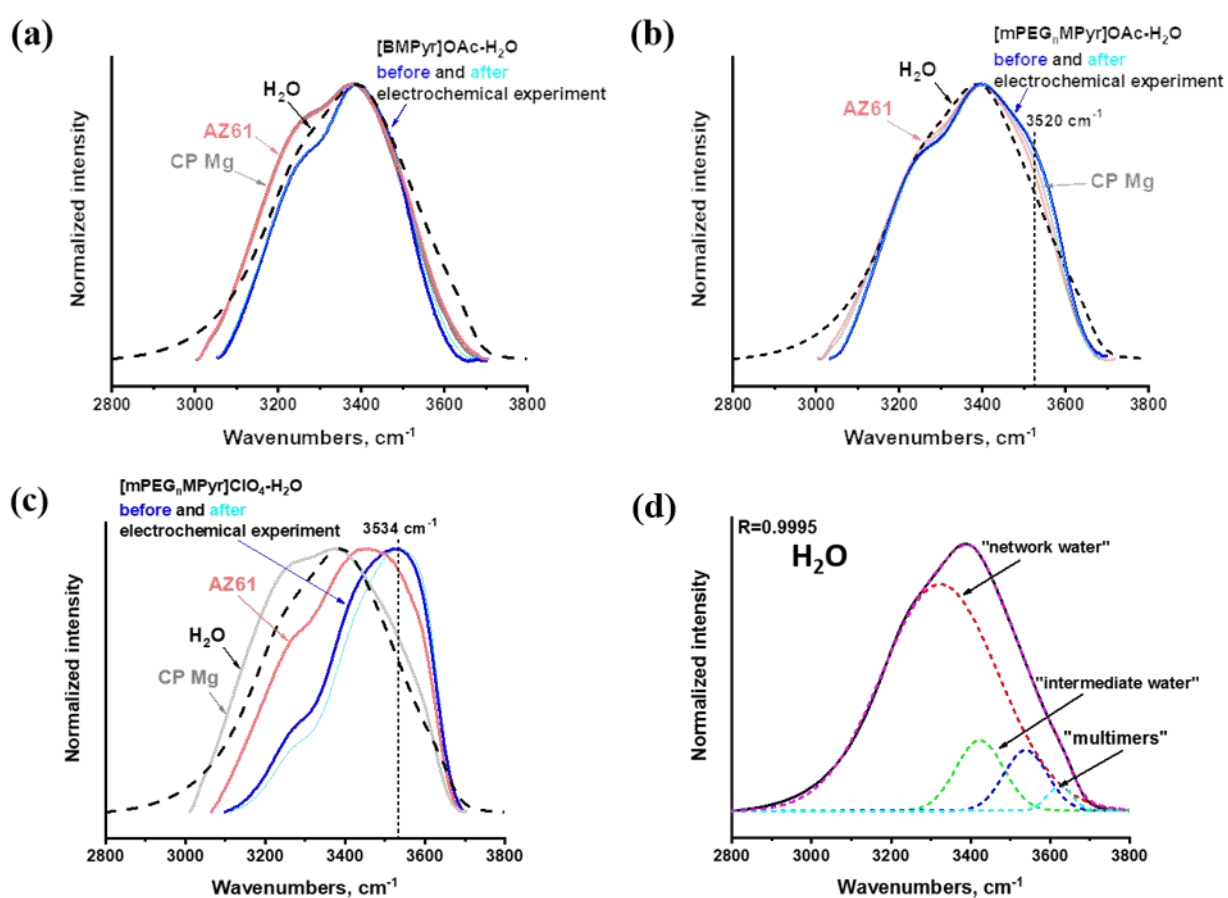


Fig. 9. Superposition of OH-vibration regions of ATR-FTIR spectra recorded on wet surfaces of CP Mg and AZ61 after the experiment in (a) - [BMPyr]OAc-H₂O; (b) - [mPEG_nMPyr]OAc-H₂O electrolyte; (c) – [mPEG_nMPyr]ClO₄-H₂O, as indicated; (d) – pure H₂O . The spectra of pure water and of the electrolyte before and after the experiment are shown for comparison.

Finally, MD simulations revealed that the presence of Mg-ions significantly decreases the probability of H-bonds between H₂O molecules and acetate

(**Fig. 10 a**). However, it seems that liberated water molecules form hydrogen bonds with oxygen of etheric groups in $[m\text{PEG}_n\text{MPyr}]\text{OAc}-\text{H}_2\text{O}$ mixtures thus limiting water reactivity and hence HE (**Fig. 10 b, c**).

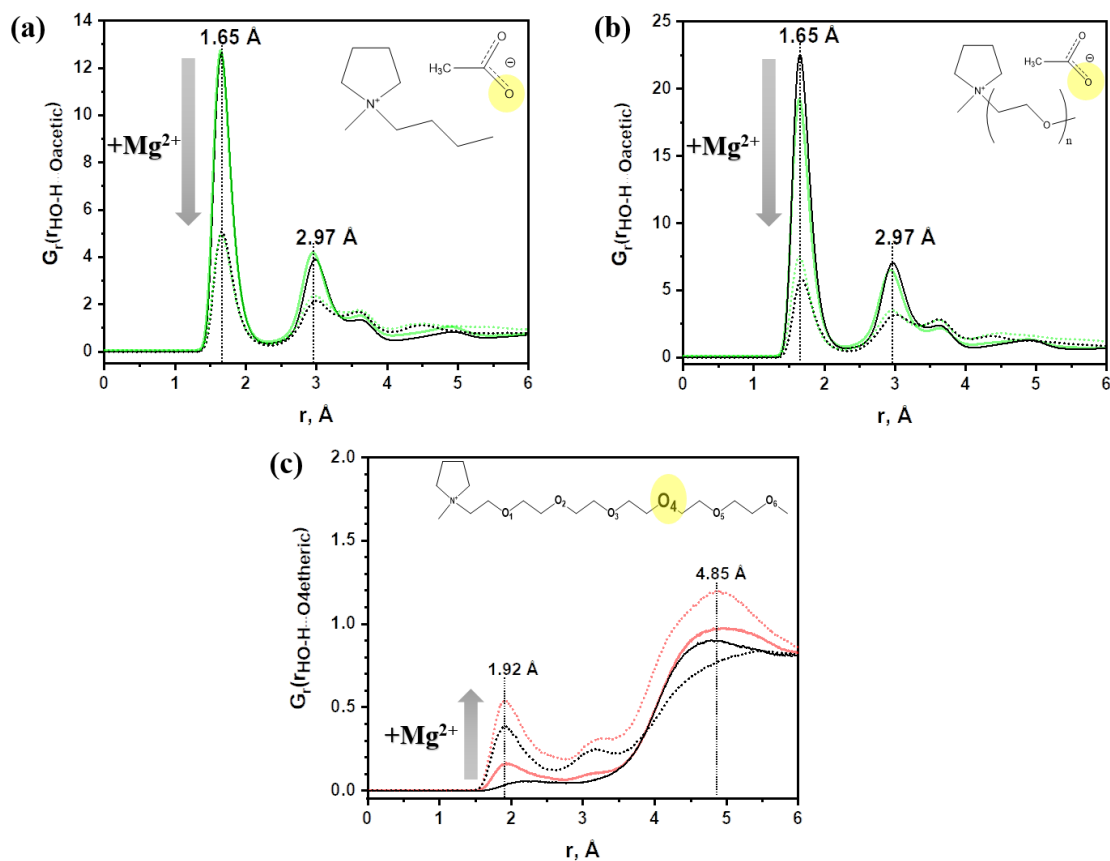


Fig. 10. Radial distribution function $G_r(r_{\text{HO-H}\cdots\text{Oacetate}})$ (**a, b**) and $G_r(r_{\text{HO-H}\cdots\text{O4etheric}})$ (**c**) of the distances, r , between acetate oxygen or etheric oxygen 4 (shown in the insets) and the closest water hydrogen, calculated for $[\text{BMPyr}]\text{OAc}-\text{H}_2\text{O}$ (**a**) and $[m\text{PEG}_n\text{MPyr}]\text{OAc}-\text{H}_2\text{O}$ (**b, c**) mixtures without (solid lines) and with (dot lines) Mg^{2+} ions in solution. Examples of the mixtures with molar ratios between water and IL $n(\text{H}_2\text{O}) / n(\text{IL}) = 1$ (black) and $n(\text{H}_2\text{O}) / n(\text{IL}) = 2$ (red) are presented.

Thus, schematic mechanisms of the NDE on CP Mg and AZ61 are suggested (**Fig. 11**). Two contributions to the NDE inhibition are proposed: (1) water bonding in the electrolyte and (2) formation of the surface film. Mechanisms of synergistic effect of acetate anions and poly-etheric substituted cation are proposed.

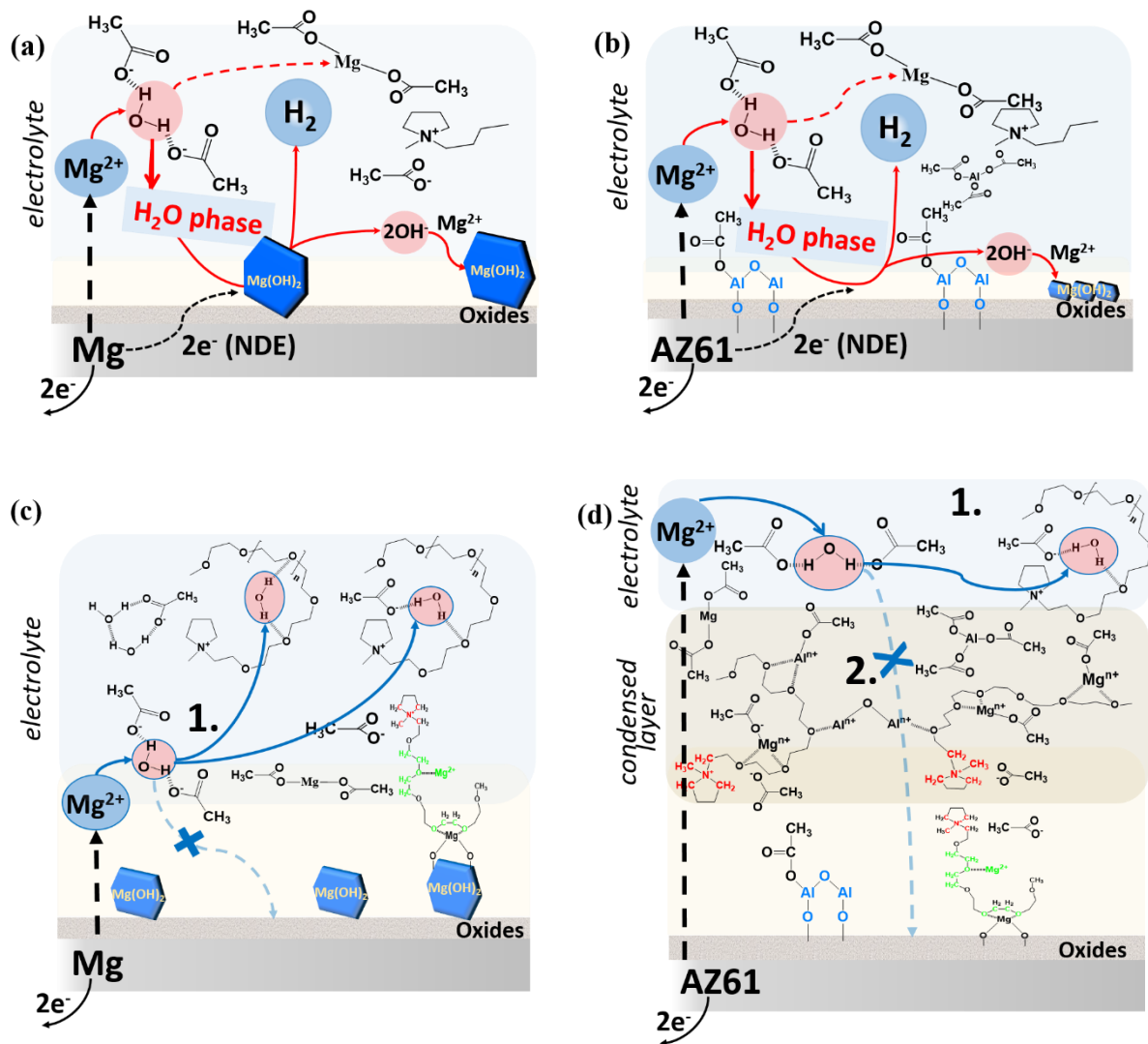


Fig. 11. Schematic mechanisms of NDE in $[BMPyr]OAc-H_2O$ (a, b) and NDE inhibition in $[mPEG_nMPyr]OAc-H_2O$ on CP Mg (a, c) and AZ61 (b, d).

Chapter 7, conclusions and perspectives, summarizes the main conclusions and findings of this work. The perspectives of possible further research directions and possible applications are discussed.

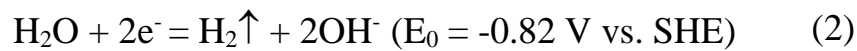
Part 1. State of the art: Mg reactivity in aqueous and non-aqueous electrolytes

Chapter 1:

Reactivity of Mg in aqueous electrolytes

1.1. General information about Mg reactivity and Negative Difference Effect in aqueous electrolytes

It is commonly accepted that Mg alloys reactivity in aqueous electrolytes is characterized by at least three processes: anodic Mg dissolution (reaction 1), cathodic water reduction (reaction 2) and formation of corrosion products on the surface Mg (reaction 3) [7,8]. More recently, some evidences of the contribution of naturally dissolved oxygen in cathodic reactivity have also been reported [21,22].



According to the classical electrochemical kinetics, typified by Butler-Volmer equation [9], the rate of cathodic reactions should exponentially decrease with increasing anodic polarization. However, Mg and its alloys exhibit the opposite behavior: cathodic hydrogen evolution (reaction 2) increases under anodic polarization. This phenomenon is commonly named as “Negative Difference Effect” (NDE) or “anomalous” Hydrogen Evolution (HE) and it was firstly reported in 1866 by Beetz [23]. It should be also noted that NDE is a historical term which defined as **a difference between the HE rate under open circuit conditions and the HE rate under anodic polarization.**

The anomalous HE under anodic polarization is accompanied by a significant mass loss of the electrode material which is higher than the mass loss calculated from Faraday's law of electrolysis for two electrons process. Certain amount of electrons, generated by Mg dissolution (reaction 1), does not flow through the potentiostat or an external electrical chain but is rather consumed by the cathodic water reduction reaction (2) occurring on the anode. Thus, oxidation rate of Mg cannot be quantitatively estimated using only electrochemical methods, supplemental technics should be employed.

Keeping in mind that Mg has the most negative standard oxidation - reduction potential among all other structural metals, it is supposed to be anodically polarized in the contact with other conducting materials in real applications (forming galvanic coupling). Thus, the understanding of the NDE mechanisms can be of interest from both scientific and technological point of view. Numerous models were proposed in order to explain this phenomenon in Mg corrosion, including:

- 1) partially protective surface film [24];
- 2) uni-positive Mg^+ ion [25,26];
- 3) Mg hydride (MgH_2) [27,28];
- 4) particle undermining [29];
- 5) incomplete film univalent Mg^+ ion [30];
- 6) self-corrosion [31];
- 7) enhanced cathodic catalytic activity [32];
- 8) the impurity particle cathode [8,32–34];
- 9) Mg^*H and Mg^*OH catalysts [35];
- 10) the adsorptive univalent Mg^+ ion dissolution [36].

These mechanisms are schematically presented in **Fig. 1.1**.

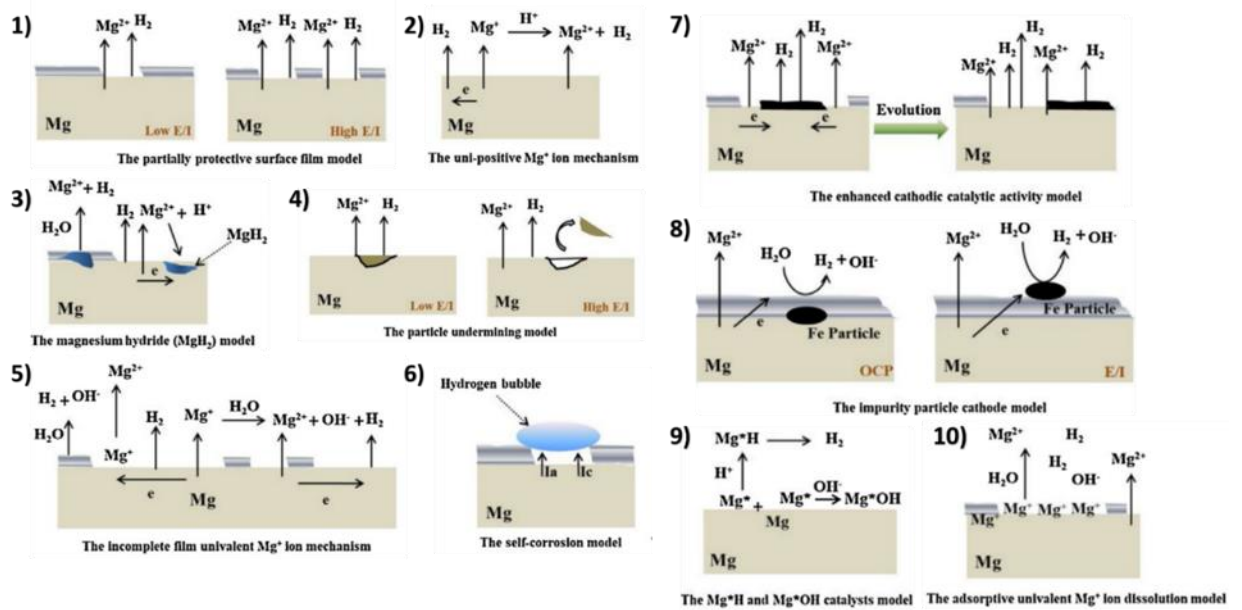


Fig. 1.1. Schematic illustration of various NDE or Mg dissolution models. Adapted from [13].

All of these models have their benefits and drawbacks, as discussed in the recent review of J. Huang, G. Song, A. Atrens and M. Dargusch [13]. Although there is no unanimously accepted universal theory describing the mechanism of the NDE, some specific factors are known to have major effects on the NDE and Mg-corrosion processes. Among them, the composition of the alloy, the presence and the distribution of the surface films and the chemical composition of the electrolyte are the most studied. These factors will be reviewed in the next sections.

1.2 Role of alloys composition for NDE

Alloying is widely used to improve corrosion resistance and mechanical properties of Mg alloys. To consider the influence of alloying on corrosion resistance and hydrogen evolution, their metallurgical state should be considered first. A large number of alloying elements have very low solubility in pure Mg, as it can be seen in **Fig. 1.2**. Another important point is that some minor solubility is followed complete insolubility and thus some elements can form intermetallic phases with Mg. This results in the formation of heterogeneities in the alloy matrix and appearance of zones with different electrochemical potentials when it is immersed in the electrolyte. Thus, more noble elements which are insoluble tend to form

heterogeneity and, hence, local galvanic couplings with Mg, leading to rapid corrosion.

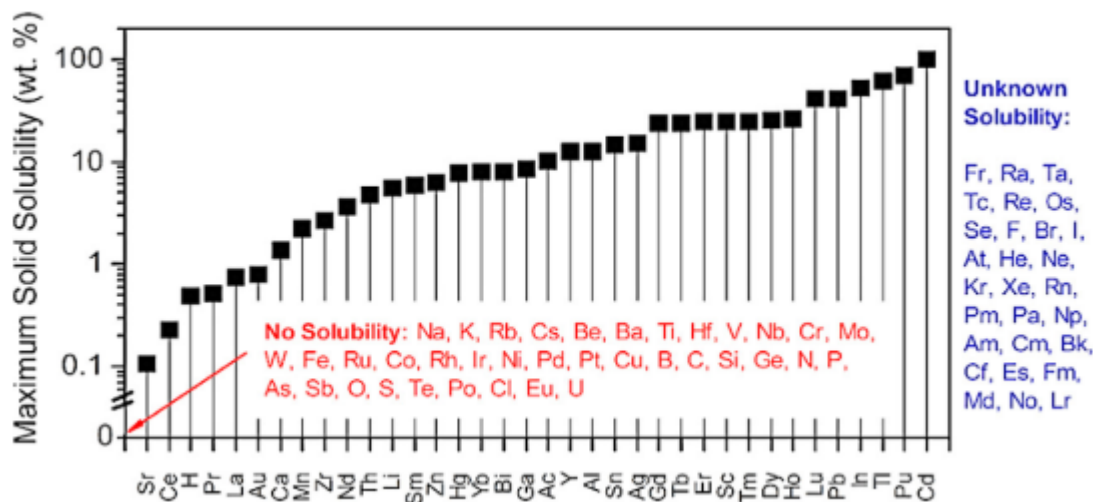


Fig. 1.2. Solubility of different alloying elements in Mg. Adopted from [37].

Considering noble alloying elements impurities, perhaps, the most known example of the effect of impurities on corrosion of Mg alloys is the effect of iron. The influence of Fe impurities in Mg alloy matrix is widely discussed in literature. It is considered as the most common impurity which can appear from the fabrication process. The importance of Fe-rich sites for hydrogen reduction reaction was demonstrated more than 50 years ago [38]. Thus, the model of more noble impurities responsible for hydrogen reduction reaction was developed by some research groups [39–44]. More recent studies revealed Fe enrichment in corrosion products (Mg oxide/hydroxide) [34,40,43]. It should be also added that simultaneous presence of Al and Mn in Mg alloys, the impurity of Fe can be significantly sequestered by the formation of intermetallic compound $Al_xMn_yFe_z$. That is also called as “Mn effect” [37].

Another important alloying element in widely used Mg alloys is Al. Al is present in the AZ (aluminum, zinc) series alloys such as AZ31 (Al-3 wt.%, Zn – 1 wt.%), AZ61 (Al-6 wt.%, Zn – 1 wt.%), AZ91 (Al-9 wt.%, Zn – 1 wt.%). The addition of Al generally ennoble the corrosion potential (E_{corr}). Compared to pure Mg, it is shifted up to +100 mV (or even more) in Cl^- containing solutions. Because

of low solubility of Al in Mg, the formation of intermetallic phases is typical for Mg-Al alloys. One of the most studied intermetallic phases is β -phase, $Mg_{17}Al_{12}$, which is known to serve as a local cathode due to its more noble electrochemical potential [45]. For example, in the work of Bacha *et al.* [46] the electrochemical potential of pure $Mg_{17}Al_{12}$ intermetallic was shown to be significantly higher ($\sim -1.2V$ vs. SCE) than the potential of pure Mg, confirming that it can act as a cathode in Mg-Al alloys. Experimental observations demonstrate however that the effect of cathodic β -phase is complex and not only the quantity but also the distribution play a primordial role in Mg alloys corrosion rate [37]. In the work of Fajardo *et al.* it was noted for AZ-families of Mg alloys (AZ31, AZ61 and AZ91) that higher Al content lower the rate of anomalous HE [47]. Authors refer to a model of anomalous HE, in which it occurs on anodic regions dominated by Mg dissolution, thus attributing the effect of higher Al content to the lower number of available sites of Mg oxidation. In the work of Serdechnova *et al.* [48] the selective dissolution from binary Mg-Al alloys (Mg from 0% to 99.999 wt%) have been studied. The authors reported that Al leaching contributed to the lowering of the interface pH and led to the formation of Mg-Al spinels in place of $Mg(OH)_2$, which significantly affected cathodic reactivity.

Alloying with more electrochemically active elements than Mg, such as Li [49–53] and Ca [54–56] is also extensively studied. These alloys are often reported as having low corrosion and HE rates. For example, in the work of Deng *et al.* [55], Mg-0.1Ca alloy was considered as an anode with high utilization efficiency in Mg-air batteries. Further studies revealed that Ca micro-alloying restricts cathodic water reduction and suppresses effect of impurities (like Fe and Si) [56].

The impact of alloying elements on the cathodic and anodic reactivity of crystalline Mg alloys is summarized in **Fig. 1.3**. More information about the effect of alloying can be found in recent reviews [37,45].

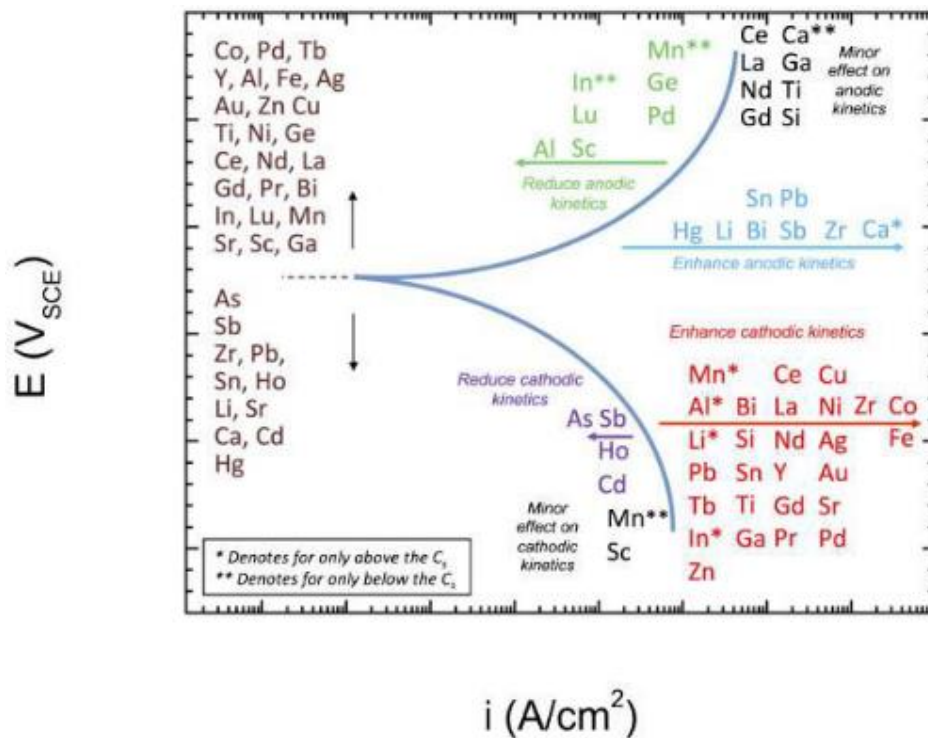


Fig. 1.3. Schematic representation of electrochemical impact of alloying elements.

Adopted from [37].

Although formation of intermetallic phases or inhomogeneous solubility of noble alloying elements strongly increases corrosion rate and HE of Mg alloys, these effects could be different in metallic glass, a relatively new class of amorphous alloys [57]. Although, their electrochemical behavior is similar to that of common alloys [58], recently, Cao *et al.* reported an amorphous alloy $Mg_{64}Zn_{36}$ which presented no hydrogen evolution during corrosion or anodic dissolution [59]. The authors attributed this feature to more positive electrochemical potential comparing to pure Mg which retard hydrogen reduction rate.

1.3. Role of surface films for NDE

It is well established that a freshly polished Mg piece reacts with atmospheric oxygen resulting in the formation of a MgO film with the thickness of a few nm [37]. Relatively high solubility of MgO ($K_{sp}(MgO) \approx 10^{-6}$ [37]) compared to $Mg(OH)_2$ ($K_{sp}(Mg(OH)_2) \approx 1.2 \cdot 10^{-11}$) leads to its transformation to $Mg(OH)_2$ in contact with

water via dissolution – precipitation mechanisms [60]. Thus, a typical surface film of Mg corrosion products consists of porous $\text{Mg}(\text{OH})_2$ followed by thin inner film of MgO (**Fig. 1.4**). However, it should be also noted that the layers can uptake species from the environment (atmosphere or electrolyte), so the presence of magnesium carbonates, chlorides etc. in the external film shown in **Fig. 1.4** is also possible.

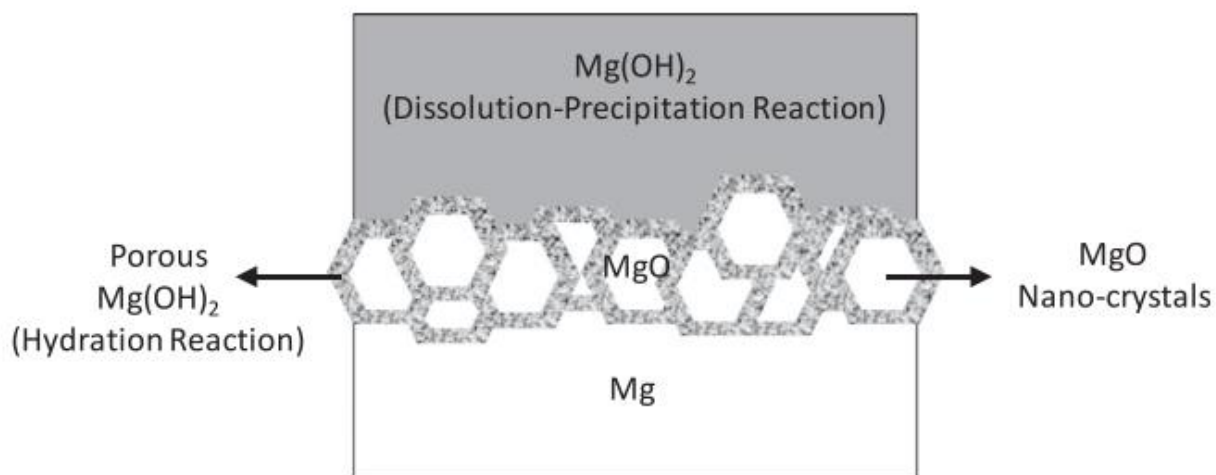


Fig. 1.4. Schematic of the diffuse bi-layer structure of the surface film formed on polished Mg after aging at E_{corr} for 48h in pure H_2O at room temperature. Adopted from [61].

Mg corrosion products attract a great attention because numerous works attribute to them a tendency to catalyze cathodic HE. Williams *et al.* [62] showed that strong hydrogen evolution occurs on dark circular regions, developing on Mg immersed in NaCl aqueous solution, using Scanning Vibrating Electrode Technique (SVET) the authors have demonstrated that the cathodically active site is the center of this circumference, while the periphery is anodically active (**Fig. 1.5**). Applied anodic polarization resulted in a faster propagation of the anodically active dark regions.

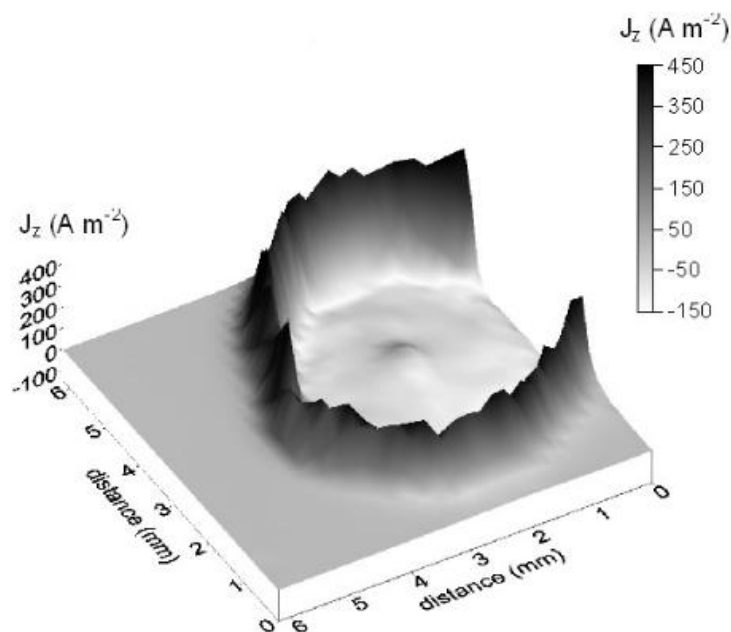


Fig. 1.5. SVET normal current density surface maps of commercial purity magnesium surface freely corroding in aerated 5% w/v NaCl (aq) at pH=6.5, obtained after 30 min of immersion. Adopted from [62].

Salleh *et al.* provided scanning electrochemical microscopy (SECM) on cathodically polarized pristine Mg covered and not covered by $\text{Mg}(\text{OH})_2$ [63]. The results demonstrated higher cathodic reactivity on the $\text{Mg}(\text{OH})_2$ covered side, confirming catalytic activity towards HER (**Fig. 1.6**). These observations were explained by the enhanced self-dissociation of water near $\text{Mg}(\text{OH})_2$. This hypothesis was also supported by DFT-based calculations [64].

Live imaging is largely used to observe the NDE, the works of the group of M. Curioni should be specially mentioned [65]. Authors performed live imaging of Mg surface immersed in NaCl aqueous electrolyte and studied size of H_2 bubbles in different zones of the surface (**Fig. 1.7**). Several types of bubbles were selected:

- 1) large and stable bubbles growing on certain location of uncorroded regions, mostly likely on cathodic intermetallics such as Fe;
- 2) hydrogen stream (fine bubbles) forming on the corrosion front;

3) medium size bubbles growing from specific locations behind the corrosion front which are also cathodically active.

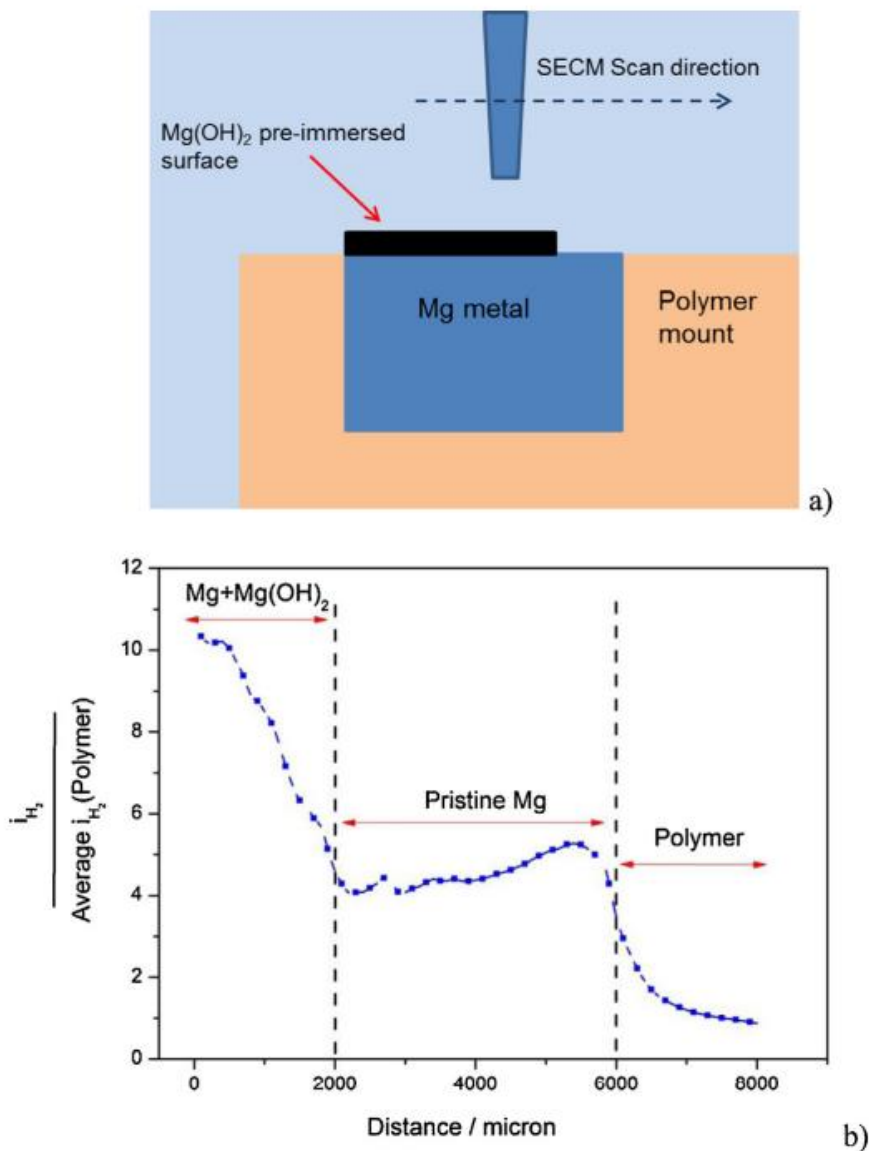


Fig. 1.6. a) schematic representation of the electrochemical cell, and conditions for SECM experiment. b) normalized hydrogen reduction currents measuring during a line scan from the Mg(OH)_2 coated Mg surface, through the pristine Mg surface, and to the polymer surface. Adopted from [63].

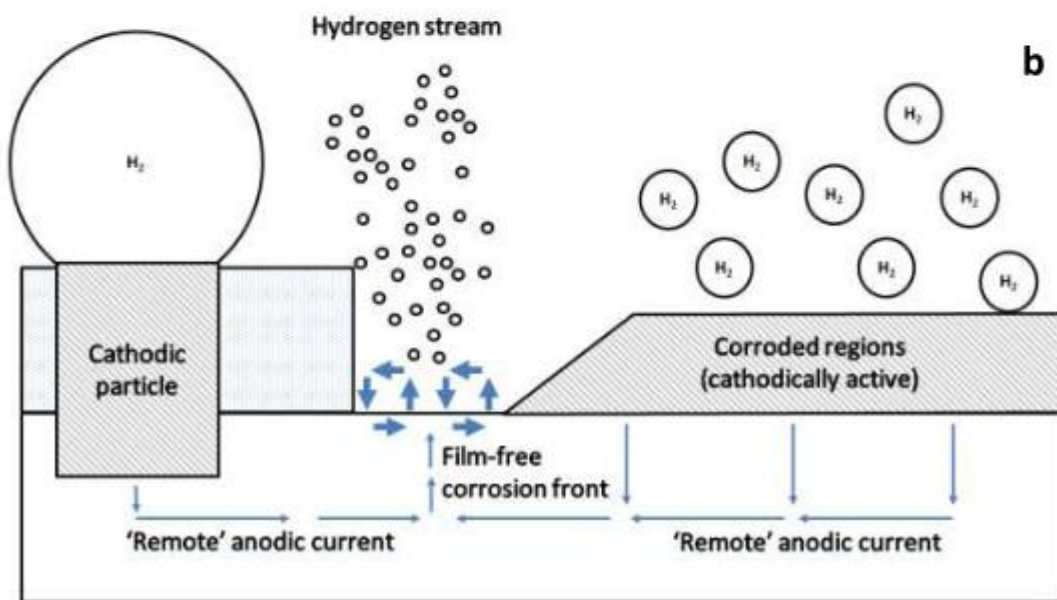
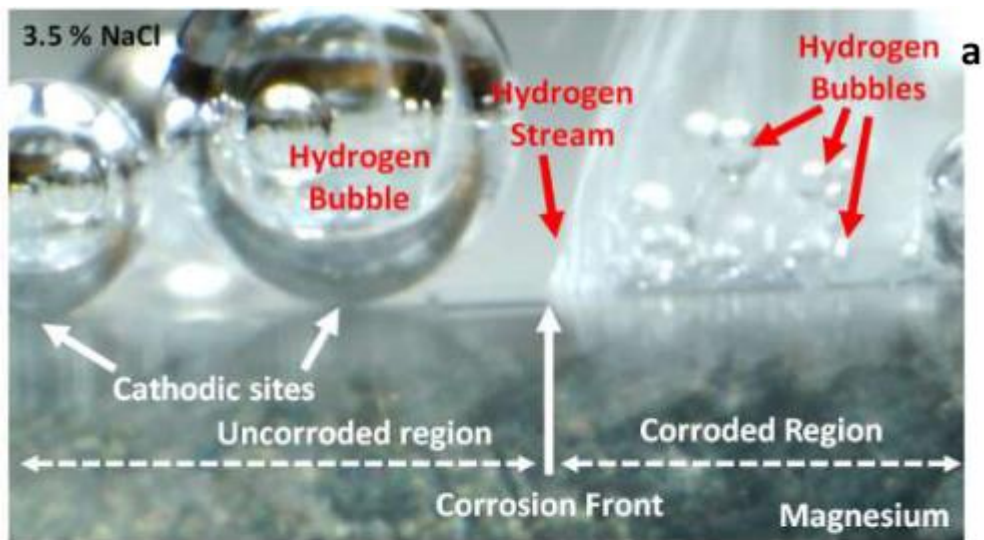


Fig. 1.7. a) Side view of magnesium corroding in 3.5% NaCl and b) schematic representation of the corrosion process, highlighting the locations generating ‘remote’ and ‘local’ anodic current. Adopted from [65].

Nevertheless, galvanic coupling between film-covered and film-free zones is possible if there are some defects in the film. If intact, $Mg(OH)_2/MgO$ can be considered as a partially protective film. Other surface films can be considered as protective for Mg corrosion. Ceramic-like plasma electrolytic oxidation (PEO) oxide coatings or layered double hydroxide (LDH) coatings [66], [67], organic coatings and electrochemical plating [68,69].

Mg(OH)₂/MgO films are usually detected in the most common electrolytes (NaCl, Na₂SO₄, etc...). Other films can be formed if some other species are present in the electrolyte. Fluorides, phosphates, chromates, molybdates and tungstates are inorganic precipitation-type corrosion inhibitors for Mg alloys. Mercier *et al.* reported selective inhibiting properties of sulfur blocking of the HE on iron impurities [39]. The authors proposed a mechanism of selective segregation of sulfur (from dissolved H₂S) on the cathodic sites of iron-impurities.

There is also a huge amount of organic inhibitors, like sodium salts of organic compounds containing carboxylic groups [70]. In the work of Lui *et al.* it has been shown that alkylcarboxylates form self-assembled monolayers on the surface on Mg protecting from corrosion processes [71-72]. The structure of the film was proposed as follows: the acidic groups are attached to the alloy substrate, long alkyl chains (often hydrophobic) make a barrier for water penetration to the metallic surface (**Fig. 1.8**). The efficiency of the inhibitors depends on the alloy composition, for example in a recent study of B. Vaghefinazari *et al.* [73] 2,5-pyridine carboxylate (2,5-PDC) have shown positive inhibition effect only on bare Mg alloys, while on the AZ21 alloy with PEO coating the effect was adverse. In some cases, common presence of two or more species in the solution can synergistic inhibition of sodium diethyldithiocarbamate and sodium acetate for AZ31B magnesium alloy in NaCl solution was also reported [74]. Lu *et al.* have reported sodium dodecyl sulfate (SDS) as an effective inhibitor for AZ91 Mg alloy [75]. The possible proposed mechanism is suppressed cathodic reaction (hydrogen reduction) by chemisorption of SDS on intermetallic sites, the anodic dissolution is retarded due to physisorption of SDS on Mg. Song *et al.* [76] also reported an inhibition effect of related SDBS (sodium dodecylbenzenesulfate) in ethylene glycol solutions proposing the mechanism of chemisorption of SO₃⁻ groups on the metallic surface and formation of a hydrophobic barrier of alkyl chain which limits the diffusion of reducible species.

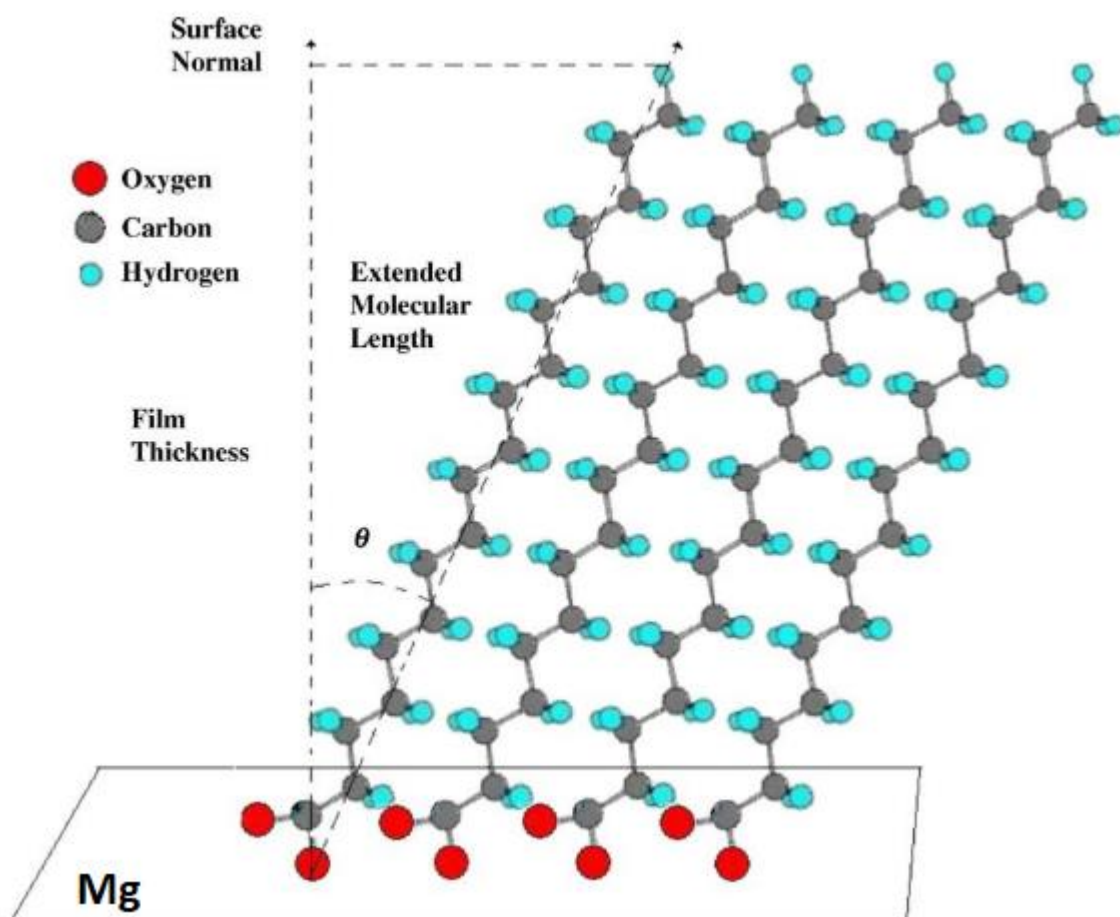


Fig. 1.8. Schematic structure of n-alkylcarboxylate monolayer on Mg alloy surface with C18 carboxylate as an example (the monodentate bonding was estimated assuming a C–O bond normal to the substrate surface). Adopted from [71].

1.4. Role of electrolyte composition for NDE

The NDE intensity is well known to depend on the electrolyte composition. For instance, in the work of Song, the anodic dissolution of Mg was compared in NaCl (aq.) and Na₂SO₄ (aq.) [77]. The presence of Cl⁻ accelerated dissolution of Mg and increased the NDE (**Fig.1.9**). Accelerated corrosion of Mg after anodic polarization in chloride containing aqueous solutions but not in sulphate containing solutions was also reported by Swiatowska *et al.* [78]. Richey *et al.* studied Mg reactivity in several electrolytes in application to Mg-O₂ batteries [79] and reported that the lowest evolved H₂ formed in NaNO₃ aqueous solution (**Fig. 1.10**). This was

attributed to the modification of the cathodic reaction because of the electrochemical reduction of nitrate anion which is in competition with hydrogen reduction reaction.

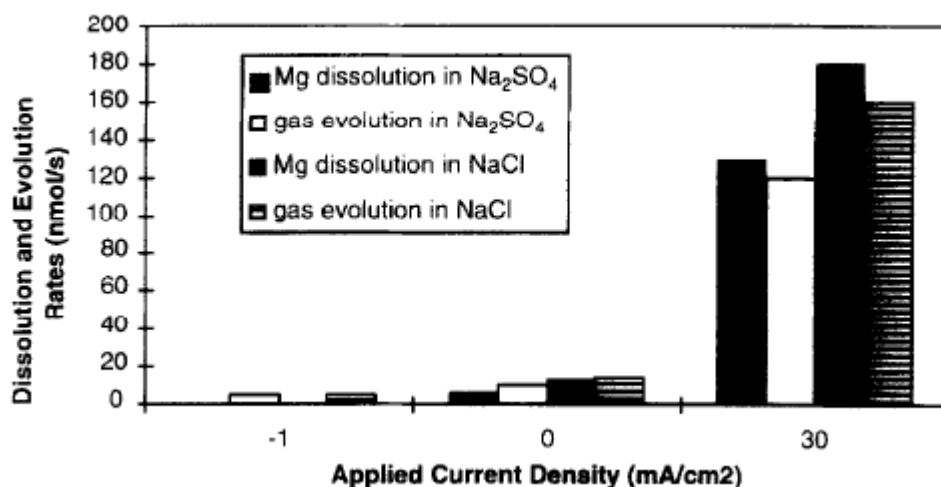


Fig. 1.9. Hydrogen evolution rates and anodic magnesium dissolution rates at different applied current densities in 1 N Na₂SO₄ and 1 N NaCl at pH 11. Adopted from [77].

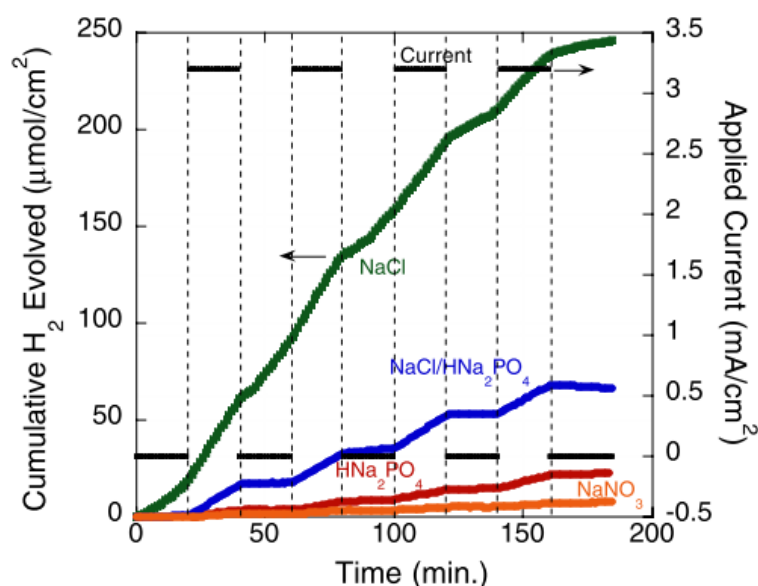


Fig. 1.10. H₂ evolution from a Mg working electrode (1.2 cm² surface area) in 0.5 M NaCl (green), 0.5 M NaCl / 0.05 M HNa₂PO₄ (blue), 0.5 M HNa₂PO₄ (red), and 0.5 NaNO₃ (orange) electrolytes. Four consecutive anodic chronopotentiometric scans (20 min at 3.2 mA/cm²) are shown in between holding the electrode at OCV for 20 minutes. Adopted from [79].

The theories explaining the harmful effect of the chloride ion on the Mg corrosion and anomalous hydrogen evolution are usually based on the disruption of the surface films. Considering that the stability of the surface film is strongly pH dependent, Mg corrosion processes strongly depend on the **local** pH near the surface, in particular, in the advanced corrosion state when the surface films are formed [80]. In contrast, in conditions in which the formation of the oxide-hydroxide film is not expected, the NDE was reported as absent. For example, in the work of Rosrucker *et al.* it has been shown that HER increases while pH decreases both at E_{oc} and during anodic polarization [81]. Under conditions whereas the surface pH was maintained by flowing buffered electrolyte, no appreciable NDE was observed. Enhanced catalytic HE activity occurred under galvanostatic anodic polarization with applied current $>+0.5$ mA/cm² in flowing unbuffered electrolyte, indicating a temporary modification of the surface film caused by changing in the surface pH during rapid dissolution Mg. Wang *et al.* compared the thickness of corrosion film formed on Mg during immersion in three solutions with adjusted pH of 3, 5.6 and 11 [82]. The results revealed that the thickest film was formed in acidic solution. This was attributed to the high local pH and relatively high oxygen consumption in the vicinity of Mg surface. The work of Lebouil *et al.* demonstrated that no NDE and no activation of corrosion after anodic polarization occur in buffered phosphate (pH=6.7) [83] thus supporting a mechanism involving the activation of the cathodic reaction related to the disruption of a protective surface film.

In summary, the control of Mg reactivity in aqueous media is the main fundamental problem to handle Mg alloys applications. Mg corrosion process is accompanied by abundant H₂ evolution which depends on the alloy and the electrolyte composition. Moreover, this gas formation accelerates under anodic polarization, which is also known as the Negative Difference Effect (NDE). Some mechanistic models have been proposed to explain it. Recent works demonstrated that the NDE is strongly enhanced by the presence of nonhomogeneities on the surface, such as noble elements inclusions or disruption of the oxide – hydroxide surface film. This knowledge allows to propose the strategies to reduce the

NDE controlling the surface composition. This can be achieved either by the formation of surface films of different nature or by stabilization or dissolution of the surface oxide-hydroxide film. Some organic additives have been shown to modify the surface film on Mg in aqueous solutions. However, the behavior of Mg and the NDE in non-aqueous electrolytes with addition of relatively small amounts of water are not well studied. These electrolytes can be, for example, mixtures of hydrophilic room temperature ionic liquids with water. Two main questions could be addressed concerning the reactivity of Mg in these electrolytes:

1) Does the NDE occur in the mixtures H₂O-IL and if yes – is it a universal effect?

2) What are the mechanisms of the effect or of its inhibition in such hybrid electrolytes?

The next chapter will briefly introduce ionic liquids (ILs), their interaction with water and behavior of Mg alloys, the effect of water on physico-chemical properties of ILs, in dry ILs and their mixtures with water.

Chapter 2:

Water-Room Temperature Ionic Liquids (RTILs) mixtures as electrolytes to control Mg reactivity

2.1. General introduction to Room Temperature Ionic Liquids

Room temperature ionic liquids (RTILs or ILs) are organic salts with melting points below 100 °C [84]. They entirely consist of ions, usually organic cation and organic or inorganic anion (**Fig. 2.1**).

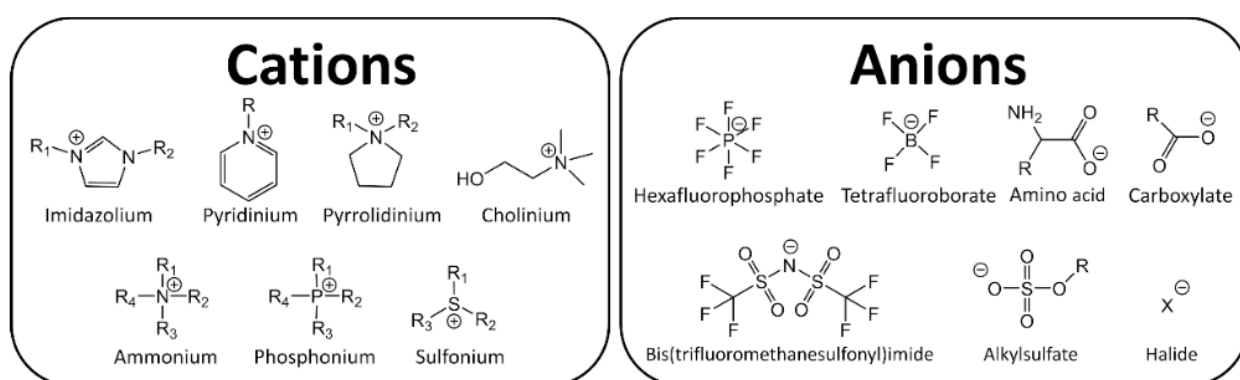
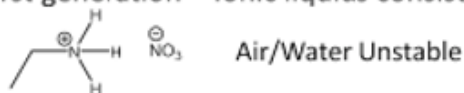


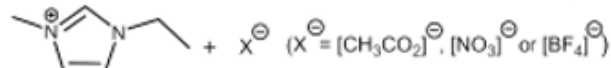
Fig. 2.1. Typical ions in ionic liquids. Adopted from [84].

The first reported in the literature IL is ethylammonium nitrate $[\text{EtNH}_3]\text{NO}_3$, discovered by Paul Walden's in 1914 [85]. It was characterized as a salt with melting point of 13-14 °C and high electrical conductivity. Some authors consider this discovery as the beginning of the First Generation of ILs [84]. These compounds are however highly unstable in contact with water and oxygen from air. Nowadays, there are at least three generations of ILs, which are characterized by improved chemical stability and some specific properties (**Fig. 2.2**).

1914 – First generation - Ionic liquids consist of bulky cations such as alkylammonium.



1992 - Second Generation - Air and water stable 1-ethyl-3-methylimidazolium based ILs.



~2000 - Third-generation - "Task-specific" ILs. Targeted biological properties combined with chosen physical chemical properties.

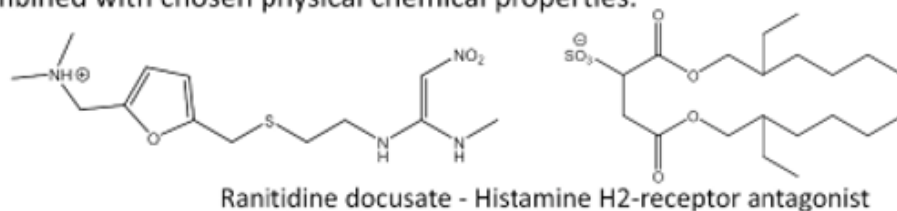


Fig. 2.2. Generations of ILs. Adopted from [84].

The Second Generation of ILs comes with the synthesis of air and water stable ILs by Wilkes and Zaworotko [86]. Their formulation was based on imidazolium cation and different anions such as acetate (CH_3COO^-), nitrate (NO_3^-) and tetrafluoroborate (BF_4^-). The Third generation was proposed in Visser's work [87], which realized an advanced design of functionalized ILs thanks to introduction of specific functional groups. The presence of specific functional groups offers some task-specific targeted properties, like for example a capacity to extract heavy metals such as Cd^{2+} and Hg^{2+} from aqueous solutions or ensure some biological compatibility.

As it can be expected from their chemical structures, the synthesis of ILs strongly depends on their design. Protic ILs can be obtained by mixing Brønsted acid and Brønsted base. Aprotic ILs are obtained through quaternization reaction followed by an anion exchange (**Fig. 2.3**).

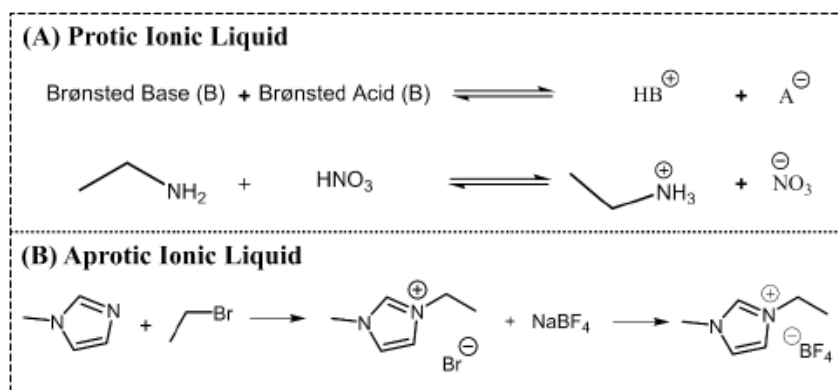


Fig. 2.3. Typical synthesis route of a protic (a) and aprotic (b) ILs. Adopted from [84].

Different combinations of cations and anions in RTILs result in unique tunable properties [88–94]. Due to these attracting properties, ILs gained scientific and industrial interest. One of the key employments of RTILs is as an electrolyte for energy storage systems [95,96] due to their improved electrochemical and thermal stability [16,89,97], relatively high conductivity [98], low volatility [99] and non-flammability [100]. Additionally, they can be used in organic synthesis [101], as catalysts [102], as electrolytes for deposition of metals and semiconductors [103,104] and in other applications. At the same time, it should be noted that ILs present some drawbacks which limit their practical use. Many ILs are not inert and can react with different chemical compounds which can be undesirable and can result in their destabilization, for example in contact with humid air [105]. Another significant disadvantage for their practical use, notably in electrochemical applications, is that they have relatively high viscosity (**Table 2.1**) [106] and reduced transport properties. The latter can be improved at some points, for example, by the dilution with conventional organic solvents or water.

Table 2.1. Selected properties of some alkyl-imidazolium-based ionic liquids. The viscosity of water is added for comparing. Adopted from [106].

Cation	Anion	Temperature (K)	Conductivity (κ), mS cm ⁻¹	Viscosity (ν), cP	Density (ρ), g cm ⁻³
[MMIM] ⁺	[(CF ₃ SO ₂) ₂ N] ⁻	293	8.4	44	1.559
[EMIM] ⁺	[BF ₄] ⁻	295	12		
[EMIM] ⁺	[BF ₄] ⁻	298	14	34	1.240
[EMIM] ⁺	[BF ₄] ⁻	298	14	32	1.279
[EMIM] ⁺	[BF ₄] ⁻	299	13	43	
[EMIM] ⁺	[BF ₄] ⁻	303	20		
[EMIM] ⁺	[PF ₆] ⁻	299	5.2		
[EMIM] ⁺	[CH ₃ CO ₂] ⁻	293	2.8	162	
[EMIM] ⁺	[CF ₃ CO ₂] ⁻	293	9.6	35	1.285
[EMIM] ⁺	[C ₃ F ₇ CO ₂] ⁻	293	2.7	105	1.450
[EMIM] ⁺	[CH ₃ SO ₃] ⁻	298	2.7	160	1.240
[EMIM] ⁺	[CF ₃ SO ₃] ⁻	293	8.6	45	1.390
[EMIM] ⁺	[CF ₃ SO ₃] ⁻	298	9.2	43	1.380
[EMIM] ⁺	[CF ₃ SO ₃] ⁻	303	8.2		
[EMIM] ⁺	[(CF ₃ SO ₂) ₂ N] ⁻	293	8.8	34	1.520
[EMIM] ⁺	[(CF ₃ SO ₂) ₂ N] ⁻	298	5.7	31	1.518
[EMIM] ⁺	[(CF ₃ SO ₂) ₂ N] ⁻	303	10		
[EMIM] ⁺	[(CF ₃ SO ₂) ₂ N] ⁻	298	9.2	34	1.510
[EMIM] ⁺	[(CF ₃ SO ₂) ₂ N] ⁻	299	8.4	28	
[EMIM] ⁺	[(C ₂ F ₅ SO ₂) ₂ N] ⁻	299	3.4	61	
[EMMIM] ⁺	[(CF ₃ SO ₂) ₂ N] ⁻	293	3.2	88	1.495
[EMM(5)IM] ⁺	[CF ₃ SO ₃] ⁻	293	6.4	51	1.334
[EMM(5)IM] ⁺	[(CF ₃ SO ₂) ₂ N] ⁻	293	6.6	37	1.470
[PMIM] ⁺	[PF ₆] ⁻	293			1.333
[PMMIM] ⁺	[BF ₄] ⁻	295	5.9		
[PMMIM] ⁺	[PF ₆] ⁻	308	0.5		
[PMMIM] ⁺	[(CF ₃ SO ₂) ₂ N] ⁻	299	3.0	60	

H₂O

1

2.2 Water-RTIL interactions

Water, coming from the moisture of atmosphere or synthesis procedure, is recognized as a common impurity in RTILs [107]. Generally, ILs can be separated in two big classes: 1) hydrophobic RTILs which pick up minimum of water and saturate at low water concentration; 2) hydrophilic (hygroscopic) RTILs which are infinitely miscible with water [108].

In some cases, high hygroscopicity can be considered as an advantage. For example, acetate-based RTILs were proposed as potential drying materials [109].

With addition of some amount of water specific physico-chemical properties can be tuned and improved. For example, viscosity reduces while specific conductivity increases with increasing water content (**Fig. 2.4 a, b**) [17,110–112]. **Interestingly, the maximum of conductivity almost in all hydrophilic ILs-water mixtures was observed at molar concentrations of water $\chi_{\text{water}} \approx 0.9$** [84].

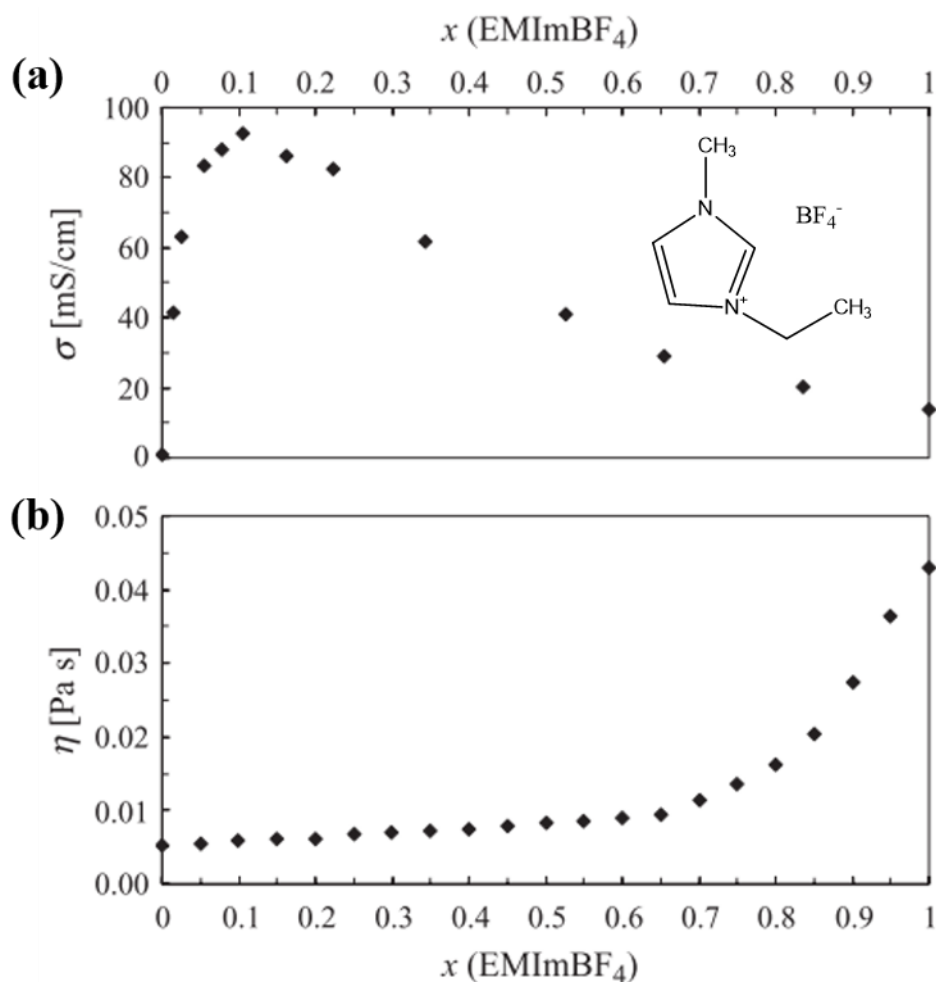


Fig. 2.4. Specific conductivity, σ , viscosity, η , for the mixture of EMImBF₄ with water as a function of its composition, expressed in the mole fraction units.

T=298 K. Adopted from [17].

However, addition of **water narrows the electrochemical window** of the electrolyte because of water splitting (**Fig. 2.5**) [113]. Some works however reported that water decomposition can be suppressed either by its low concentration or by strong interactions with the anions or even with cation of RTIL [114,115]. Therefore,

understanding interactions between water and ILs is important step to rationalize electrolyte decomposition for numerous applications.

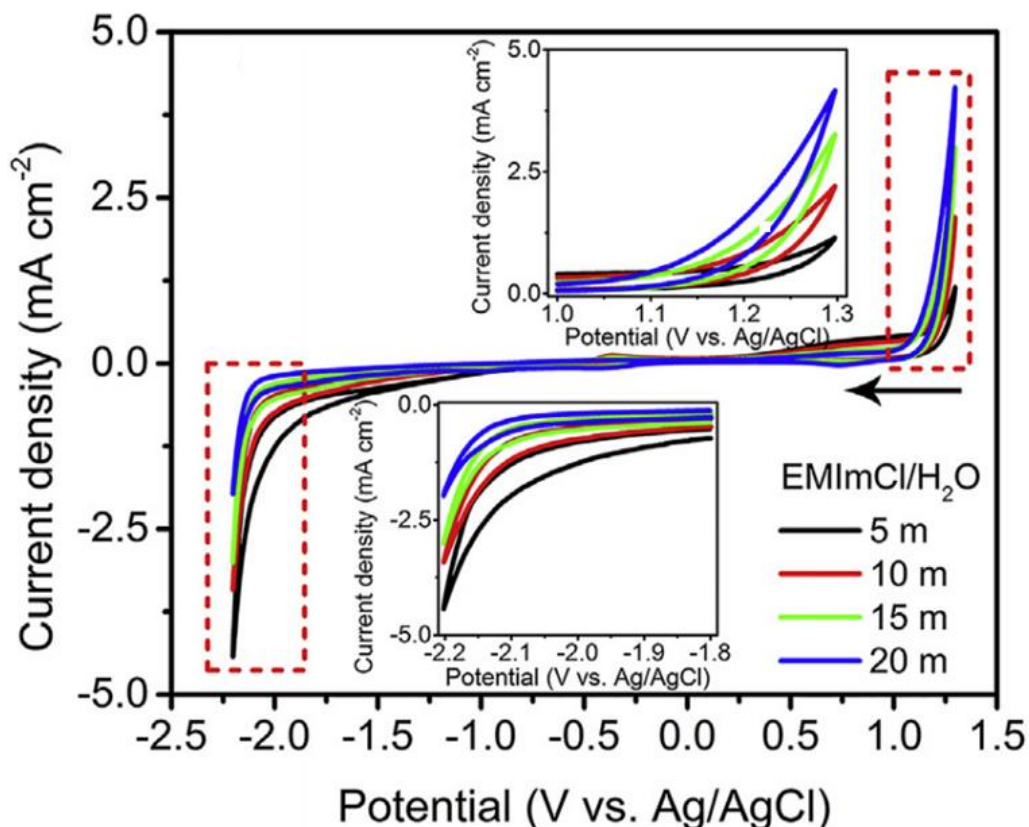


Fig. 2.5. Typical CV curves of N-ethyl-N'-methylimidazolium chloride/H₂O mixtures with different concentration of IL. 5 m in legend means 5 mmol of IL dissolved in 1 ml of water. Thus, blue curve recorded in the most concentrated solution, black is the most diluted. Adopted from [113].

According to the literature, **water molecules can form intermolecular hydrogen bonds predominately with anions of ILs** and these bonds can be even stronger than cation-anion interactions in RTILs [112,116–118]. H-bonds were reported for water with anions containing fluorine, such as BF₄⁻, SbF₆⁻, PF₆⁻ (F···H), but also through oxygen atoms in the anions such as NO₃⁻, ClO₄⁻ and etc. (O···H). Cammarata *et al.* [116] studied ILs with water absorbed from the air (low concentrations) using Attenuated Total Reflectance Infrared spectroscopy (ATR-IR). They reported that water molecules were not present in self-associated state but

formed H-bonded complexes: Anion \cdots HOH \cdots Anion. According to the results of this work, the strength of H-bonding between water molecules and anions increases in the order $[\text{PF}_6]^- < [\text{SbF}_6]^- < [\text{BF}_4]^- < [(\text{CF}_3\text{SO}_2)_2\text{N}]^- < [\text{ClO}_4]^- < [\text{CF}_3\text{SO}_3]^- < [\text{NO}_3]^- < [\text{CF}_3\text{CO}_2]^-$. Ludwig *et al.* have found that water exists in DD (double donor) and SD (single donor) structures (1 H₂O : 2 IL and 1 H₂O : 1 IL) [119], which was also confirmed for hydrophilic ionic liquids by Lendl [107]. Larrechi *et al.* [118], using near infrared spectroscopy (NIR-IR), reported that in certain hydrophilic imidazolium ionic liquids the amount of free water (which does not form hydrogen bonds with ILs moieties) depends on temperature, concentration of ILs and nature of anions. Gao *et al.* [120] investigated microstructure of the IL rich region in hydrophilic IL 1-butyl-3-methylimidazolium tetrafluoroborate ([BMIm]BF₄) with D₂O using Small-angle neutron scattering (SANS). According to this work, for the mixtures containing water molar fraction up to $\chi_w = 0.66$, corresponding to water to IL molar ratio 2:1 water molecules interact with anions and cations of IL by hydrogen bonds without any interruption of the microstructure of IL. Further addition of water ($\chi_w \approx 0.7$ and more) results in the formation of clusters, which size increases with D₂O fraction, forming a partition between water in the dissolved state and in a microphase separated state. **For molar water fractions χ_w above $\chi_w \approx 0.8$, a phase inversion occurs, forming IL aggregates in aqueous solution (Fig. 2.6).**

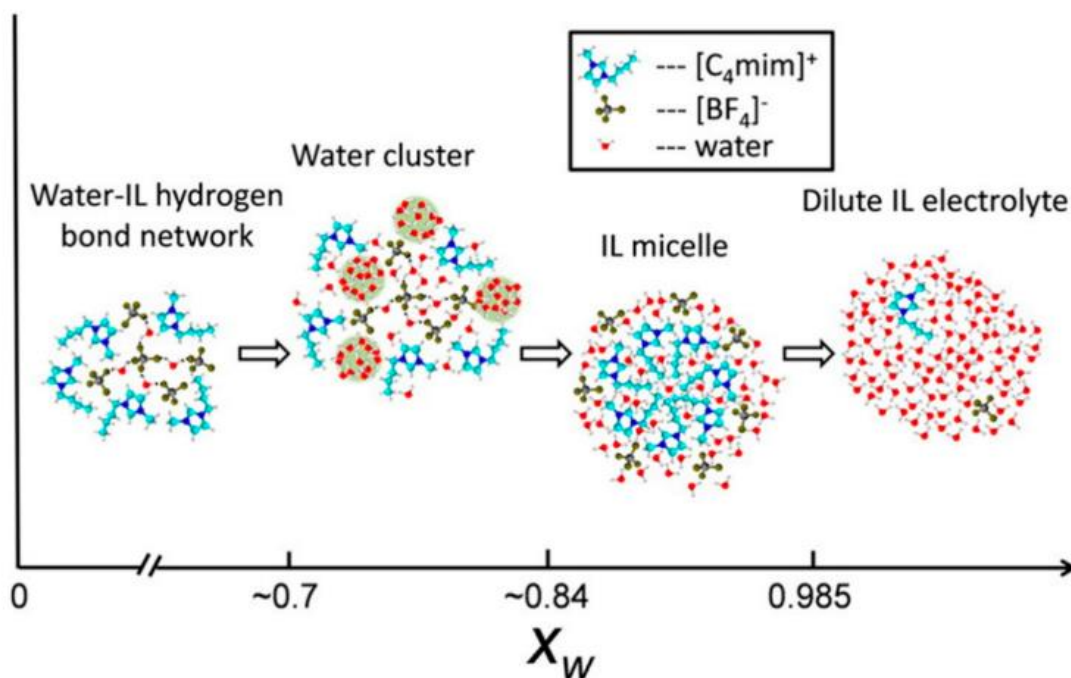


Fig. 2.6. Schematic illustration of structures in mixtures of [BMIm]BF₄ and D₂O determined by small-angle neutron scattering (SANS). Adopted from [120].

Using MD simulations, it was established that RTIL hydrophilicity is determined by the nature of ions and interactions between them [121–124]. Long substituted aliphatic tail in cations can contribute into water-ILs interactions. As such structure is nonpolar and hydrophobic, in diluted ILs aliphatic tail forms micelle-like structures (**Fig. 2.7**) [125]. Similar observations were made for IL with the same cation but with NO₃⁻ anion by Jiang *et al.* [122]. This work also reported that transport properties of the ILs improve with increasing water content.

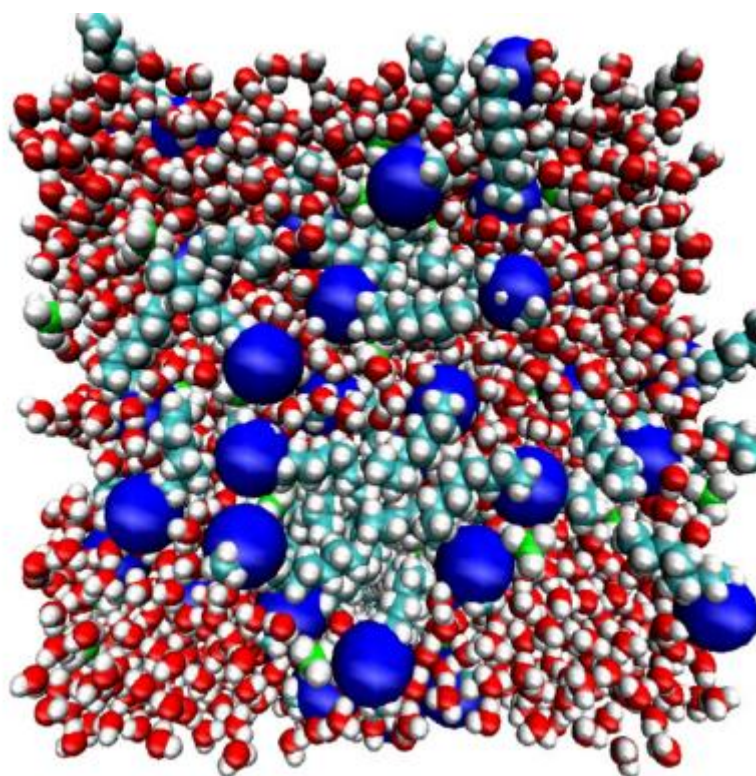


Fig. 2.7. Snapshot of 1-octyl-3-methyl-imidazolium-tetrafluoroborate (OMImBF₄)/water mixtures at water mole fraction ($\chi_w = 0.9615$), wherein micelle-like structures can be observed; the red spheres represent oxygen atoms and the green spheres are boron atoms. The white spheres are either fluorine atoms or hydrogen atoms (depending upon their respective attachment to boron or oxygen). The cyan spheres are carbon atoms and the large blue spheres are head groups. Head groups are termination CH₃ group in aliphatic tail. Adopted from [125].

In the work of Koishi [126], mixtures with water were simulated for four ILs based on 1-butyl-3-methylimidazolium (BMIm⁺) cation with two hydrophilic (NO₃⁻ and BF₄⁻) and two hydrophobic (PF₆⁻ and (CF₃SO₂)₂N⁻) anions. The results revealed that **nitrate and tetrafluoroborate anions are connected with water through hydrogen bonds forming anion-water-anion agglomerates and does not form water-clusters. But in PF₆⁻ and (CF₃SO₂)₂N⁻ ILs water is rather bonded with itself (Fig. 2.8).** These results are in agreement with the results experimentally obtained by Dominguez-Vidal *et al.* using far-infrared spectroscopy [127].

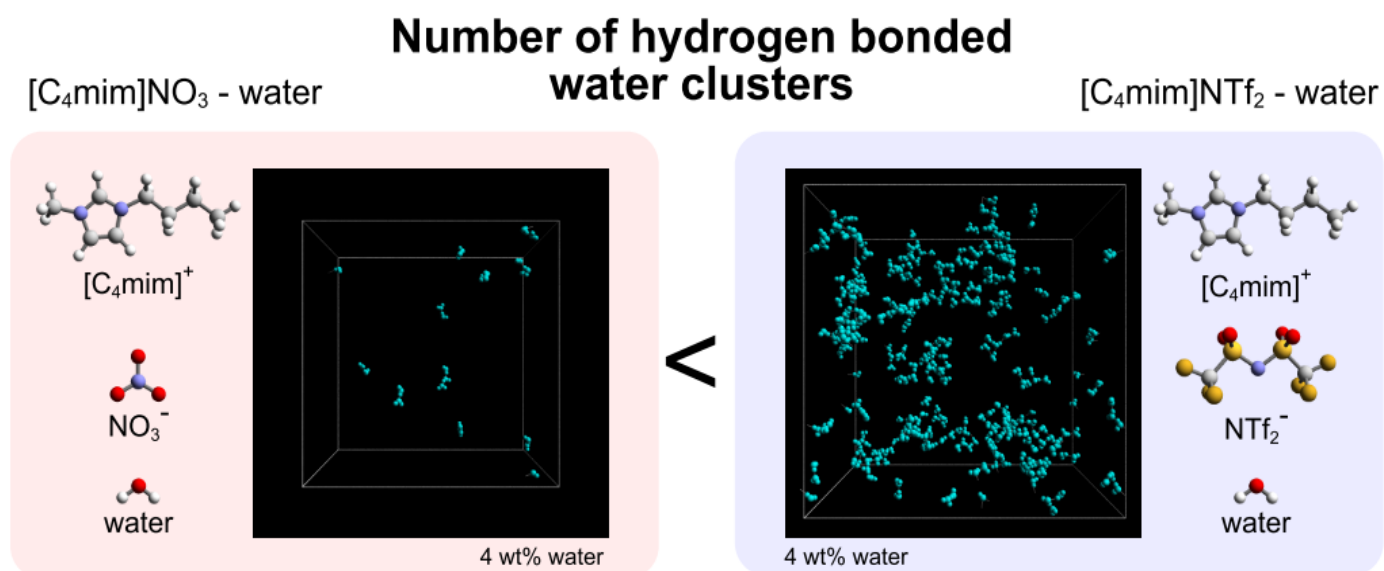


Fig. 2.8. Illustration of H-bonded water clusters in mixtures of [BMIm]NO₃ and [BMIm]NTf₂ with water. Adopted from [126].

The effect of cation on H-bonding between RTIL and water has also been theoretically studied. Paolone *et al.* [128] reported some evidence of hydrogen bonds formation between water and hydrophilic 1-butyl-1-methyl-pyrrolidinium cation. Brehm *et al.* [129,130] provided complex studies of mixtures of 1-ethyl-3-methylimidazolium acetate with water by *ab initio* MD. The authors demonstrated that **water molecules can interrupt hydrogen bonds formed between acetic anion and liable H atom in imidazolium-ring at C² atom**. The hydrogen bonds network connecting acetic anions and RTIL cations via water molecules was also observed. At moderate water content, acetic anions were coordinated to the same water molecule forming bridges (AcO⁻⋯HOH⋯⁻OAc) (**Fig. 2.9**).

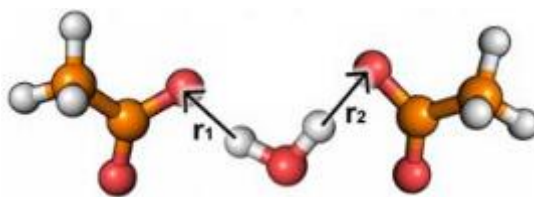


Fig. 2.9. Bridging behavior of water. Adopted from [130]

As previously emphasized in section 2.1 of this chapter, modification of some functional groups in the design of ILs can be used to access some targeted properties. Thus, the properties of any functional group should be considered. From the point of view of the interactions with water molecules etheric groups can be interesting. Fenn *et al.* [117] demonstrated that oxygen atoms of **etheric groups in poly-ethers can form intermolecular hydrogen bonds with water molecules (Fig. 2.10). However, to the best of our knowledge, interactions of water with etheric groups present in the cation or anion of ILs has not been studied yet.**

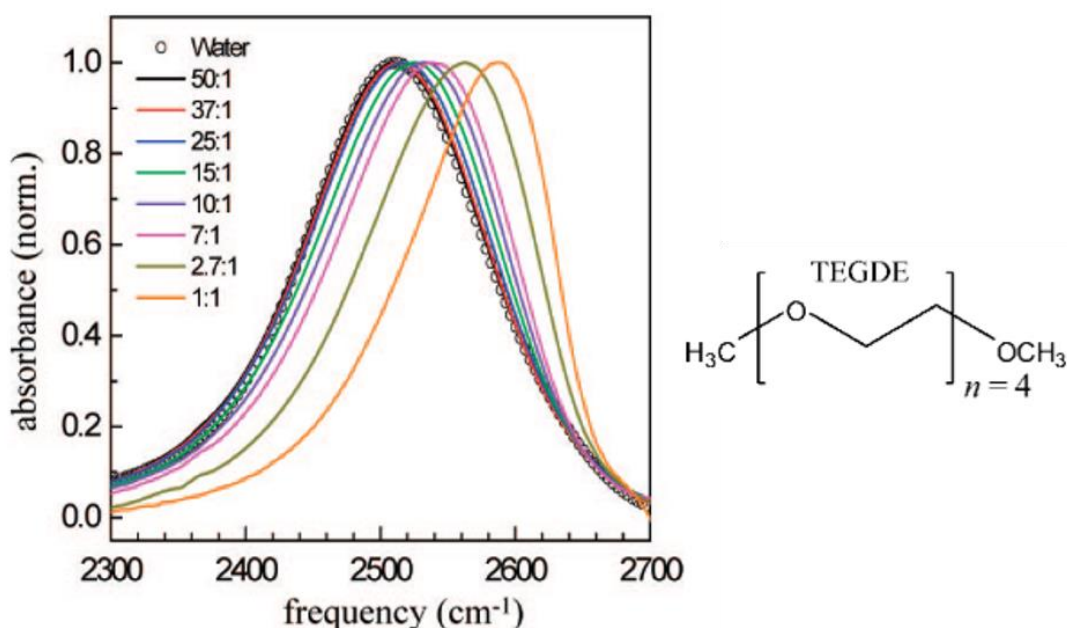


Fig. 2.10. FT-IR absorption spectra of the OD stretch of HOD in H₂O for eight water/TEGDE mixtures and water. An increasing blue shift can be seen as the water content decreases. Adopted from [19].

2.3. Mg reactivity in RTIL and water-RTIL mixtures

Reactivity of Mg alloys in RTILs and RTIL-rich water-RTIL mixtures is not well described in the literature. Only a few papers are dedicated to the investigation of the behavior of metallic Mg in ILs. Latham *et al.* found that anodizing AZ31 in phosphonium ILs resulted in formation of surface films, which were unstable in 0.01 M NaCl, but led to the anodic shift of the corrosion potential E_{corr} [131]. Authors attributed this effect to a combination of surface homogenization, and improved film

deposition and adhesion. The analysis of formed films revealed the presence of $\text{Mg}(\text{OH})_2$ and IL ion pairs. Similar effect was reported in the study of Forsyth *et al.* [132]. They immersed bare AZ31 Mg alloy in trihexyl-(tetradecyl)phosphonium bis(trifluoromethanesulfonyl)amide ($\text{P}_{6,6,6,14}\text{TFSA}$) for long time and then recorded potentiodynamic response in aqueous solution of 0.1 M NaCl (**Fig. 2.11**). The results revealed film formation on the surface which provides improved corrosion resistance to the alloy against humid environment as well as in the presence of chlorides. Similar result was obtained in trihexyl(tetradecyl)- phosphonium bis(2,4,4-trimethylpentyl)phosphinate ($\text{P}_{6,6,6,14}\text{M}_3\text{PPh}$) [133]. In the work of Caporali [96] *et al.* interactions between $[\text{BMIm}]\text{Tf}_2\text{N}$ IL and AZ91D Mg alloy were studied at different temperatures. The authors concluded that corrosion rate was relatively low at room temperature but became fast at 200 °C. Formation of oxides and fluorides on the surface was reported. The authors have also noted that the decomposition of the IL in the presence of AZ91D starts at much lower temperatures than the decomposition of the IL alone. **Thus, a catalytic effect of the metals on ILs decomposition can be suggested.**

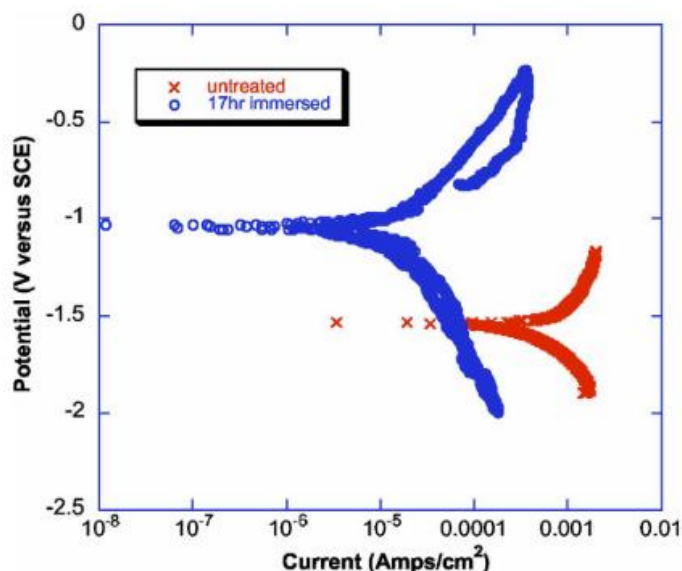


Fig. 2.11. Potentiodynamic scans on AZ31 alloys using a microcell setup with electrode diameter $\approx 80 \mu\text{m}$. Scans were performed in 0.1 M NaCl at 10 mV/s.

Adopted from [132].

Shkurankov *et al.* [134] investigated behavior of AZ91D alloy in 1-butyl-3-methylimidazolium trifluoromethylsulfonate ([BMIm]CF₃SO₃) with different concentrations of water. In dry IL AZ91D alloy was not reactive, however, reactivity increased with increasing water content (**Fig. 2.12**). Interestingly, **at low water concentrations hydrogen evolution was not observed on the surface, which is different from the behavior of AZ91D alloy in water-based electrolytes. Visible hydrogen evolution occurred only at water concentration of 75000 ppm (6.2 mol/L).** Corrosion rate was also significantly at lower water content than in aqueous solutions.

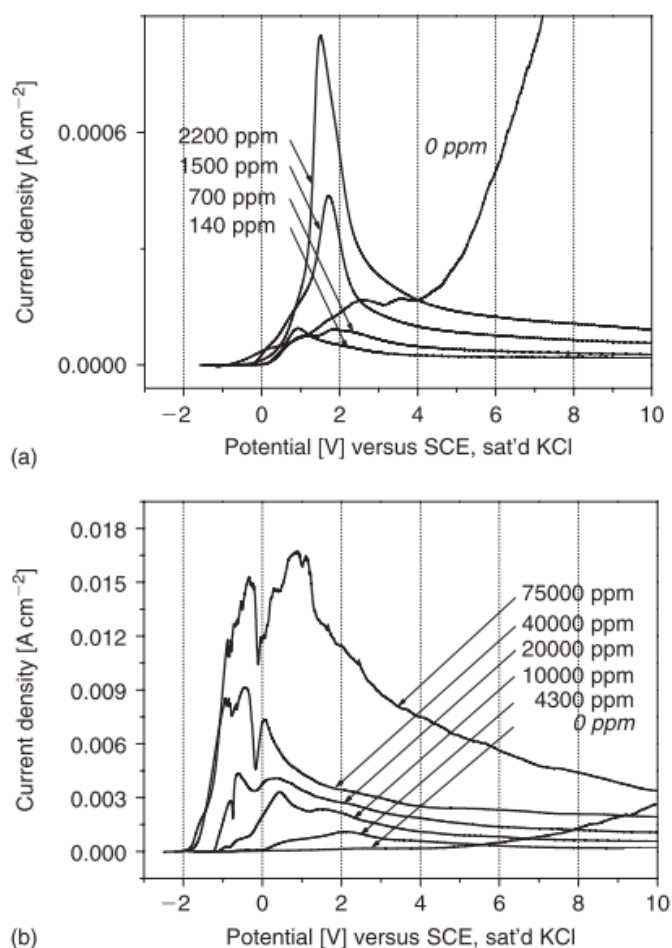


Fig. 2.12. Anodic polarization curves of poly- and microcrystalline magnesium in a mixture of [BMIm]CF₃SO₃ ionic liquid with different concentrations of H₂O: (a) 0–2200 ppm H₂O, (b) 4300 to 75000 ppm H₂O. Scan rate 10mVs⁻¹. Adopted from

[134]

Khoo *et al.* [135] reported the results of galvanostatic discharge of Mg electrode in trihexyl(tetradecyl)phosphonium chloride ($[P_{6,6,6,14}]Cl$) ionic liquid electrolyte containing 0, 2, 4 and 8 wt% H_2O (**Fig. 2.13**). After galvanostatic discharge, Mg samples were covered by a “gel-like” film (**Fig. 2.14**) which was characterized as passive at open circuit but conductive under anodic polarization. This film consisted of hydrated chloro-magnesium complexes with IL. **No hydrogen reduction reaction was observed in this work.**

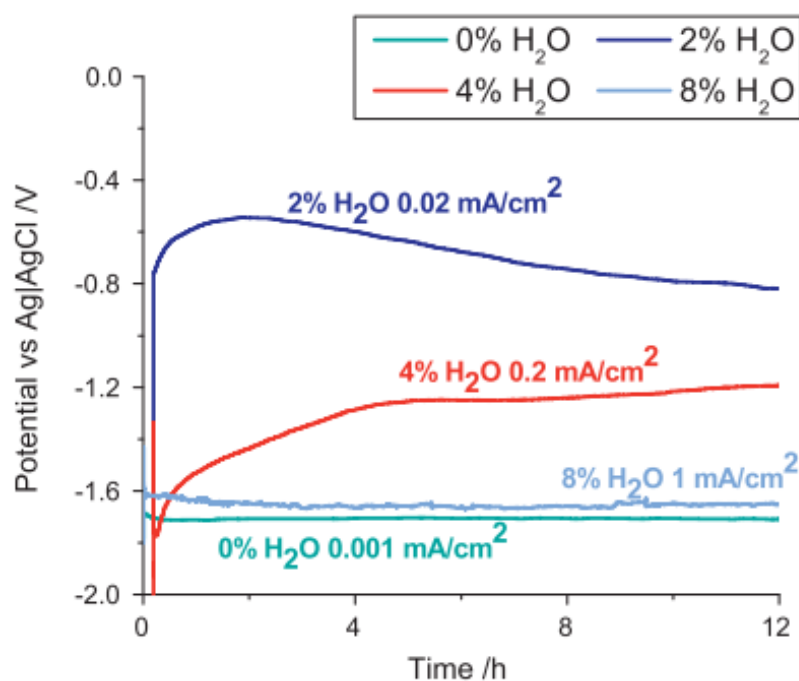


Fig. 2.13. Galvanostatic discharge curves of a Mg electrode in a $[P_{6,6,6,14}]Cl$ ionic liquid electrolyte containing 0, 2, 4 and 8 wt% H_2O . Higher rates of discharge are possible in electrolytes containing higher amounts of H_2O . Adopted from [135].

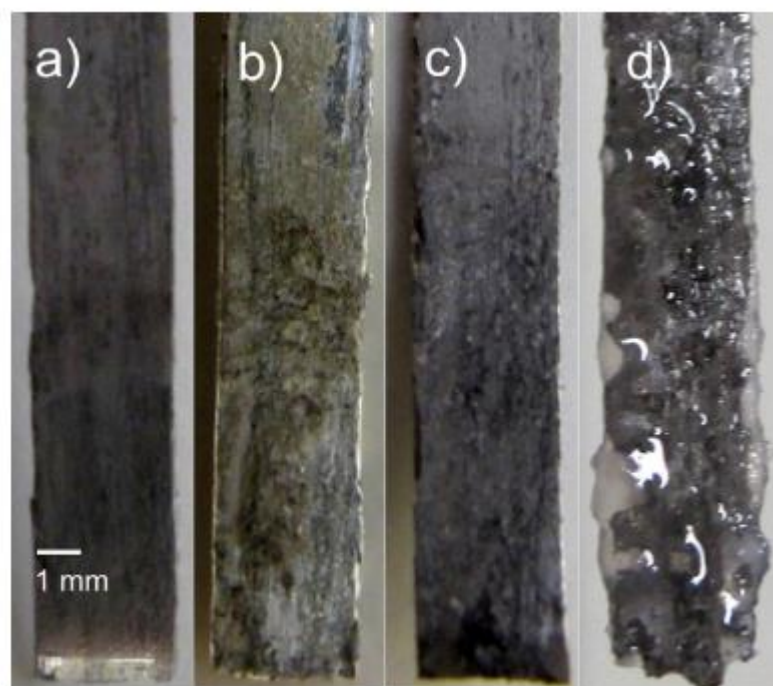


Fig. 2.14. Images of the magnesium surface (a) after OCP in 0 and (b) 8 wt% H₂O [P_{6,6,6,14}]Cl for 48 h. (c) After 24 h discharge in 8 wt% H₂O and (d) after 96 h discharge in 8 wt% H₂O [P_{6,6,6,14}]Cl. Adopted from [135].

Considering applications of ILs for Mg, an advanced progress has been made in the RTIL design for Mg battery application field. Enlarged electrochemical stability of **dry ILs** opens a possibility of reversible deposition of Mg. Especially, hydrophobic ILs with PEG (poly-ethylene-glycol) groups in their structure have been found as suitable electrolytes to support Mg stripping reaction (anodic dissolution) with low over potential and high coulombic efficiency (**Fig. 2.15**) [136–138]. This was attributed to complexation and stabilization of Mg-ions by PEG-groups. However, the ILs studied in these works systems are very sensitive to presence of water and oxygen [6]. **Modification of the RTIL design making it more compatible with humidity can be therefore an interesting direction for energy applications.**

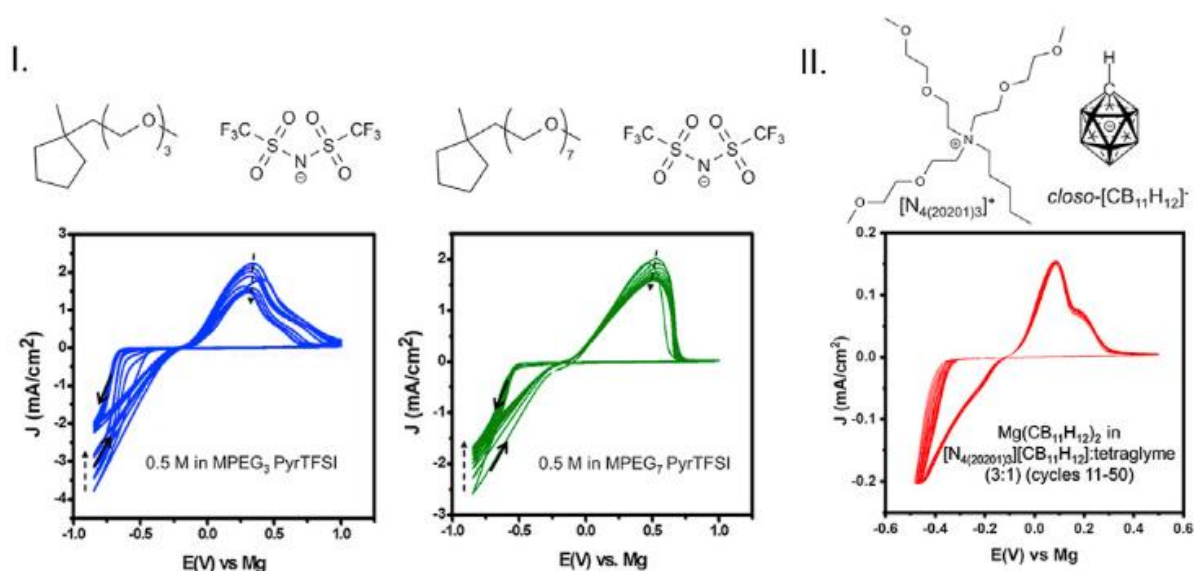


Fig. 2.15. Cyclic voltammetry curves in ionic liquids: (I) $\text{Mg}(\text{BH}_4)_2$ in two TFSI-based PEGylated ionic liquids (structure shown). (II) cyclic voltammetry curves of a saturated $\text{Mg}(\text{CB}_{11}\text{H}_{12})_2$ solution in a boron cluster-based ionic liquid (structure shown). Adopted from [6].

According to the existing knowledge, in hydrophilic ILs water molecules form intermolecular hydrogen bonds with IL, predominantly with the anions. In function of water content, water molecules can be isolated from each other and bound to IL moieties by H-bonds or can form water agglomerates or even percolating water clusters. In case of acetate containing RTILs, isolated water molecules can form H-bonded bridges between acetate anions or between acetate anion and cation. The presence of etheric groups in the cation structure can also impact the molecular state of water. H_2O state in hydrophilic ionic liquids with PEGylated cation has not been investigated yet.

Magnesium reactivity in water-RTIL mixtures is barely studied, no specific study has been devoted to the abnormal hydrogen evolution, but some works reported that hydrogen evolution is suppressed at low water contents. Formation of surface films in the presence of RTILs was also noted. Mg reactivity in hydrophilic RTILs with PEG-substituted cation is completely unexplored but can offer interesting possibilities because etheric groups can favor Mg stripping.

From the knowledge accumulated in aqueous corrosion of Mg, carboxylates can also offer a control of Mg reactivity and limit abnormal hydrogen evolution

Thus, the questions asked in the end of Chapter 1 are still unsolved and even have not been properly asked for the systems containing hydrophilic RTIL and water. Focusing on the role of the cation for the control of Mg reactivity in such mixtures and on the PEG-substituted cations, additional questions occur:

- 1) How water molecules interact with etheric groups in hydrophilic RTIL and how it influences stability and basic properties of the mixture?*
- 2) How water-RTIL interactions and formation of the surface films affect reactivity of Mg and its interactions with water in these mixtures?*

To sum up, the present PhD aims to answers to the following scientific questions

- 1) Does the NDE occur in the mixtures H₂O-hydrophilic IL and if yes – is it a universal effect? (Chapter 4)*
- 2) How does water interact with cation and anion in selected hydrophilic RTILs (with and without PEG-substitution in the cation) and how these interactions influence basic properties of the electrolyte (Chapter 5)*
- 3) What are the mechanisms of the NDE if it occurs and what are the mechanisms of the NDE inhibition in such hybrid electrolytes? (Chapter 6)*

The general strategy and experimental methodology, selected in order to answer on these questions is presented in Chapter 3

Part 2. Methodology

Chapter 3:

RTIL design and experimental methods

This chapter introduces the methodological approach used in the work. First, the materials selected for the study are presented and the design of the electrolytes is explained. Second, an overview of the experimental techniques used for in situ and ex situ characterization of the electrolytes and the whole system is given. The motivation led to the choice of specific technics and basic principles of the measurements are briefly explained. The design of specific experimental set up is also given.

3.1. Alloy compositions

The composition of the studied materials is shown in **Table 3.1**. Two different materials were chosen in order to take into account the effect of Al-alloying and to verify which tendencies of Mg reactivity in water-ionic liquids mixtures can be considered as common and which are specific to some alloys. Behavior of commercial purity (99.999 wt.%) Mg and of largely used AZ61 alloy (containing about 6 wt. % of Al and 1 wt. % of Zn) were compared. Commercial purity Al was used in order to clarify the possible role of Al impurities in AZ61 alloy. All the materials were used in the form of a foil. The foils with area of 1×1 cm were grinded by 800, 1200, 2400, 4000 SiC polishing paper grits using absolute ethanol as a lubricant, rinsed with ethanol and dried prior to the experiments.

Table 3.1. Metallic materials used in the work.

Sample name	Al ppm	Zn ppm	Mn ppm	Si ppm	Fe ppm	Ca ppm	Mg wt. %
CP Mg	70	<20	170	50	280	-	Balance
AZ61	62.000	7.400	2.300	40	40	1.3	Balance
CP Al	Balance	Cu- 0.3	-	0.8	0.3	-	1.2

3.2. RTIL design

3.1.1. Selection of RTIL compositions

In the literature (see **Chapter 2**) different designs of ionic liquids are presented. Since there are plenty of possible combinations of cations and anions, the choice of desired combinations leading to specific properties needs to be explained. Taking into account that the present work is focused on water-miscible ionic liquids and because water molecules participate in hydrogen evolution reaction (**reaction 2** in section **1.1**), the strategy of this work is to verify the role of the interactions between water and RTIL and so RTILs which can strongly interact with H₂O are of interest.

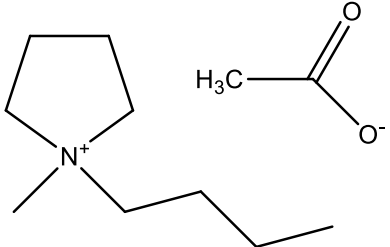
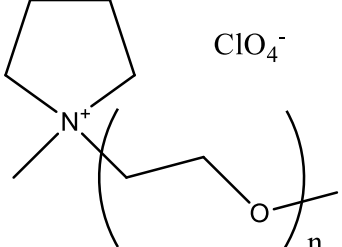
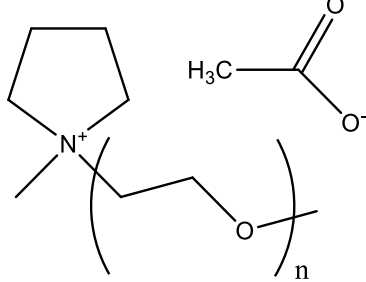
As it is shown in section **2.2**, acetic anions, which can be in the structure of ILs, form strong **intermolecular hydrogen bonds** with water. Moreover, some compounds with carboxylic groups display **inhibiting effect towards Mg corrosion**. Thus, **acetate ionic liquids can be considered as a perspective candidate**.

Etheric groups can in principle **form intermolecular hydrogen bonds** with water molecules (see section **2.2**), however, the interactions of water with etheric groups present in ILs are unknown. Taken into account the marked in section **2.3** improvement of Mg stripping process in hydrophobic anhydrous ILs by mPEGylated cations due to the **complex formation with Mg ions**, it seems promising to try to control Mg reactivity in hydrophilic ILs and their mixtures with water by **mPEG-substituted cations**. Methylpyrrolidinium based cations have been chosen in order to ensure good miscibility with water (see **section 2.2**).

The interactions of acetate anion and mPEG-substituted cation with Mg electrode and even with leached in the electrolyte Mg²⁺ ions in the hybrid electrolyte containing hydrophilic IL and water can however differ from the expected for both aqueous solutions and hydrophobic ionic liquids. These interactions need therefore be understood. Moreover, synergic effects could be also present. In order to

understand and separate the actions of mPEG-substituted cation and acetate anion in the RTIL composition for the reactivity of Mg alloys, three different ILs were proposed: one RTIL containing aliphatical-substituted cation (w/o etheric groups) and acetic anion (ILA), one containing mPEG-substituted cation and inorganic (perchlorate) anion (ILEP) and the targeted RTIL containing mPEG-substituted cation and acetate anion (ILE). The chemical structures, systematic names and used in the following text acronyms of the three studied ILs are presented in **Table 3.2**.

Table 3.2. Systematical names, acronyms and graphical structures of used ILs.

Ionic liquid; Their acronyms	Graphical formula
1-butyl-1-methylpyrrolidinium acetate, [BMPyr]OAc; ILA	
1-methoxy-polyethyleneglycol-1-methylpyrrolidinium perchlorate, [mPEG _n MPyr]ClO ₄ ; ILEP	
1-methoxy-polyethyleneglycol-1-methylpyrrolidinium acetate, [mPEG _n MPyr]OAc ILE	

*n – means variable numbers of etheric groups found by MALDI-TOF, $4 \leq n \leq 16$ with an average value $\langle n \rangle = 7$.

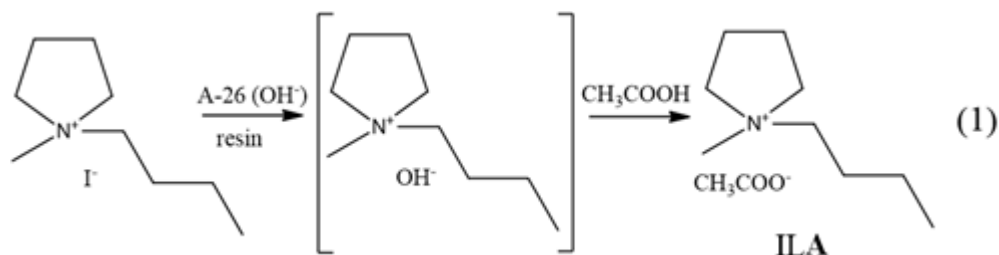
Variation of different cations (etheric and aliphatic) and anions (acetate and perchlorate) can provide the information about the role of each element of the IL's structure. Selection of perchlorate anion was motivated by its low donor number (DN) and expected formation of weak hydrogen bonds with H₂O [116,139]. The synthesis of the selected ILs is detailed in the next section.

3.2.2. Synthesis of RTILs, their identification and preparation of their mixtures with water

Materials used for synthesis. The following commercially available compounds were used for synthesis: Methoxy-terminated poly(ethylene glycol) (mPEG₇, CAS no. 9004-74-4, M.W. 350), 4-toluenesulfonyl chloride (TsCl, CAS no. 98-59-9, 99%), 4-dimethylaminopyridine (DMAP, CAS no. 1122-583, 99%), triethylamine (CAS no. 121-44-8, 99.5%), anhydrous potassium iodide (KI, CAS no. 7681-11-0, 99%), N-methylpyrrolidine (CAS no. 120-94-5, 97%), silver nitrate (AgNO₃ CAS no. 7761-88-8, ≥99%), ethyl acetate (CAS no. 141-78-6, ≥99.5%), toluene (CAS no. 108-88-3, 99.8%), 1-butyl-1-methyl-pyrrolidinium iodide (CAS no. 56511-17-2) supplied by Sigma-Aldrich. Acetone (CAS no. 67-64-1), chloroform (CAS no. 67-66-3), methanol (CAS no. 67-56-1), cyclohexane (CAS no. 110-82-7), acetic acid (CAS no. 64-19-7, ≥99.7%), perchloric acid (≥70% aqueous solution, CAS no. 7601-90-3) supplied by VWR. All chemicals were used as received.

Synthesis of 1-Butyl-1-methyl-pyrrolidinium acetate (ILA) is presented in **Scheme 3.1**. Four-step synthesis of 1-poly(ethylene-glycol)-1-methyl-pyrrolidinium acetate (ILE) is shown in **Scheme 3.2**.

Synthesis of ILA.



Scheme 3.1. Synthesis of [BMPyr]OAc (ILA).

Aqueous solution of 1-butyl-1-methyl-pyrrolidinium iodide (6 g, 0.022 mol) was passed dropwise through a chromatography column packed with Amberlyst A-26 hydroxide form (40 g). One equivalent amount of acetic acid was added to the resulting solution. Neutral pH was controlled with pH meter. The water was removed by evaporation under vacuum using rotary vapor at 60 °C. The iodide content of ionic liquid was determined by means of 0.1 M AgNO₃ aqueous solution (solubility of AgI is 3 · 10⁻⁷ g/100mL at 20 °C). Hence, the concentration of I⁻ in corresponding ionic liquids revealed to be inferior to this value.

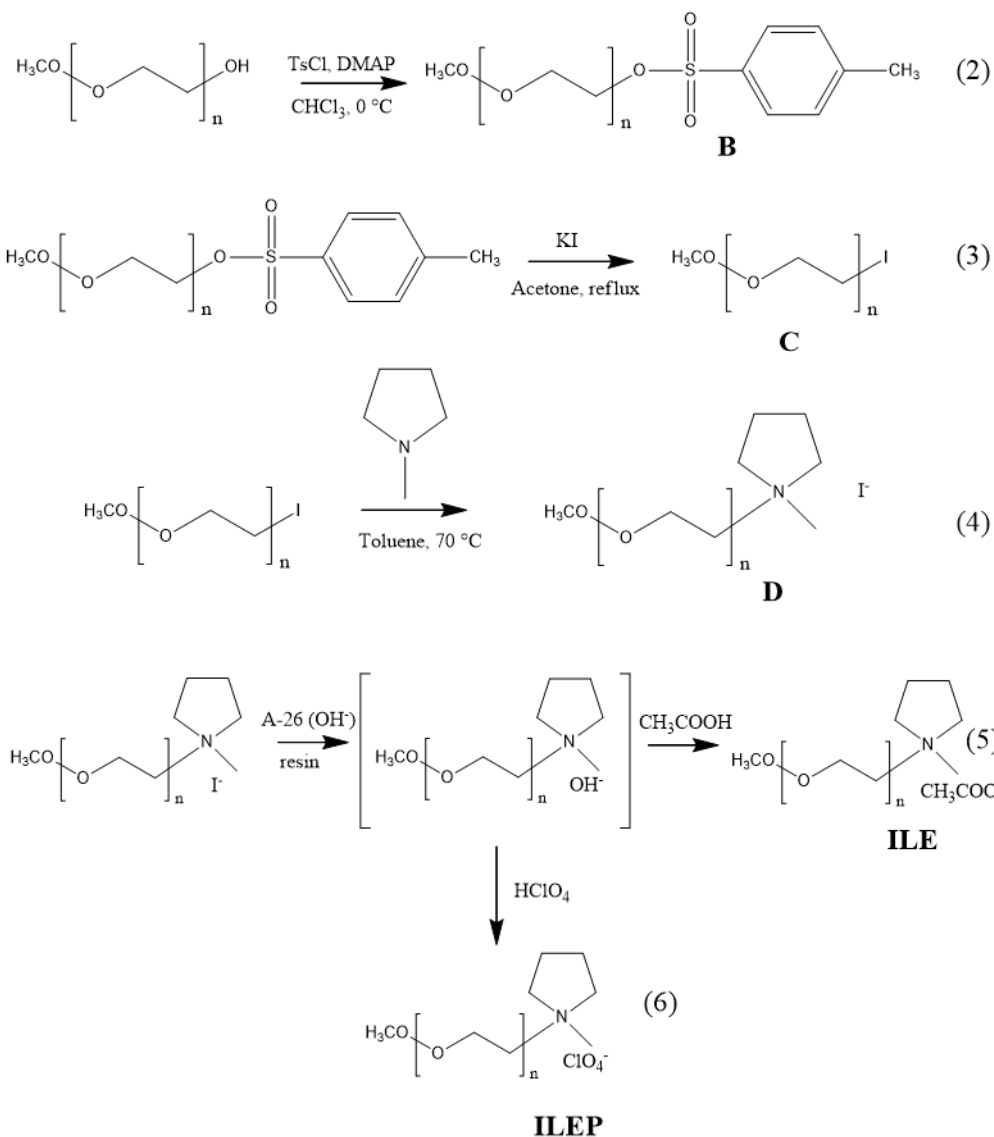
The structure of compound ILA, [BMPyr]OAc was confirmed by ¹H, ¹³C-Nuclear Magnetic Resonance (NMR) and high-resolution mass spectrometry (HRMS). The positive mass over charge ratios m/z detected in atmospheric pressure chemical ionization (APCI-Orbitrap) (+) were: m/z = 202.1807 (C₁₁H₂₄NO₂⁺), m/z = 142.1590 (C₉H₂₀N⁺). The detected NMR signals are listed below:

¹H NMR (400 MHz, CDCl₃) δ 3.73 – 3.51 (br m, 4H), 3.43 – 3.37 (br m, 2H), 3.13 (s, 3H), 2.22 – 2.11 (br m, 4H), 1.80 (s, 3H), 1.70 – 1.60 (br m, 2H), 1.40 – 1.27 (m, J = 36 Hz, 2H), 0.91 (t, J = 8 Hz, 3H)

¹³C NMR (101 MHz, CDCl₃) δ 176.6, 77.4, 63.9, 63.7, 48.1, 25.7, 25.4, 21.5, 19.7, 13.6

Water content in as synthesized ILA was 4.44 wt. % as determined by Karl Fischer (KF) coulometric titration (C20, Mettler Toledo).

Synthesis of ILE (scheme 2). General procedure was already published in the literature [140,141].



Scheme 3.2. Synthesis of [mPEG_nMPyr]OAc (ILE) and [mPEG_nMPyr]ClO₄ (ILEP).

The first step (reaction 2) was preparation of compound **B** by tosylation reaction. A solution of alcohol (15 g, 0.043 mol), trimethylamine (8.67 g, 0.086 mol) and 4-dimethylaminopyridine (0.3 g, 0.025 mol) in chloroform (100 mL) was cooled to 0°C (ice bath). Tosylchloride (12.26 g, 0.064 mol) diluted in chloroform (100 mL) was added dropwise and the solution was allowed to warm to room temperature under stirring for 12 hrs. Saturated NaHCO₃ (aq. 50 mL) was added, and the solution

was extracted, washed with H₂O (100 mL), dried over Na₂SO₄, and filtered. The solvent was removed under vacuum (rotary evaporator) at 55 °C, and the crude product was purified by flash chromatography starting with cyclohexane/ethyl acetate (80/20 by volume) in order to eliminate the excess of 4-toluenesulfonyl chloride followed by dichloromethane/MeOH (90/10 by volume) to recover the pure tosylated alcohol (compound **B**) as a colorless oil: 17.73 g (82 % yield). **Following to the procedure proposed by Ganapatibhotla [140], it is not needed to provide the purification of obtained product. However, our experience revealed that purification is necessary for further reactions.** The product was identified by ¹H, ¹³C-NMR and mass spectrometry. APCI (+) HRMS: major m/z = 495.2262 (C₂₂H₃₉O₁₀S⁺).

¹H NMR (400 MHz, CDCl₃) δ 7.79 – 7.75 (d, J = 8 Hz, 2H), 7.34 – 7.29 (d, J = 12, 2H), 4.16 – 4.10 (br m, 2H), 3.67 – 3.64 (br m, 2H), 3.63 – 3.57 (br m, 19H), 3.56 – 3.54 (br m, 4H), 3.53 – 3.50 (br m, 2H), 3.35 (s, 3H), 2.42 (s, 3H).

¹³C NMR (101 MHz, CDCl₃) δ 144.9, 133.1, 129.9, 128.0, 72.0, 70.8, 70.6, 69.3, 68.7, 59.1, 21.7

The next step was the synthesis of compound **C** by nucleophilic substitution (3). Tosylated alcohol (17.73 g, 0.035 mol) was diluted in dry acetone (100 mL) and placed in a round bottom flask equipped with a refrigerating apparatus. Potassium iodide (11.62 g, 0.07 mol) was added and the system was placed in dark (aluminum foil). The solution was refluxed for 24 hrs. **Following to the procedure proposed by Ganapatibhotla [140], NaI (sodium iodide) should be added, but according to our experience, KI is more reactive.** Resulting mixture was filtered through celite, diluted with H₂O (100 mL), and extracted twice with CH₂Cl₂. Organic layer was dried over Na₂SO₄, filtered, and the solvent was evaporated under vacuum to give the iodide compound (12.62 g, 75%) as a yellowish viscous oil (compound **C**) which was used without further purification. The later was identified by ¹H, ¹³C-NMR and mass spectrometry. APCI (+) HRMS: major m/z = 451.1189 (C₁₅H₃₂O₇I⁺).

^1H NMR (400 MHz, CDCl_3) δ 3.73 – 3.67 (br m, 2H), 3.64 – 3.56 (br m, 21H), 3.52 – 3.47 (br m, 2H), 3.32 (s, 3H), 3.23 – 3.18 (br m, 2H)

^{13}C NMR (101 MHz, CDCl_3) δ 71.9, 71.9, 70.6, 70.6, 70.2, 59.0, 3.0

Synthesis of compound **D** was made using quaternization reaction (reaction (4)). Iodide compound (12.62 g, 0,027 mol) and 1-methylpyrrolidine (2.52 g, 0,03 mol) were diluted in a round bottom flask and dissolved in toluene (100 mL). The mixture was stirred at 70 °C for 48 hours. Two separated liquid layers were observed. The resulting $\text{mPEG}_n\text{MPyrI}$ salt was separated from toluene phase and washed with toluene (3×20 ml) and diethyl ether (3×20 ml). The residual product was successfully identified by ^1H , ^{13}C -NMR and mass spectrometry as compound **D**. MALDI-TOF (matrix HCCA) (+) MS: major $m/z = 408.29$ ($\text{C}_{20}\text{H}_{42}\text{NO}_7^+$). MALDI-TOF (matrix DHB) (-) MS: $m/z = 126.90$ (I^-).

^1H NMR (400 MHz, CDCl_3) δ 3.99 – 3.85 (br m, 6H), 3.84 – 3.75 (br m, 2H), 3.69 – 3.63 (br m, 2H), 3.63 – 3.54 (br m, 19H), 3.53 – 3.47 (br m, 2H), 3.34 (s, 3H), 3.30 (s, 3H), 2.34 – 2.15 (br m, 4H)

^{13}C NMR (101 MHz, CDCl_3) δ 72.0, 70.6, 70.3, 65.8, 65.5, 63.3, 59.1, 49.4, 21.6

Finally, **ILE** was obtained by anion exchange via reaction (5). Anion exchange reaction was realized as mentioned above for $[\text{BMPyr}]\text{OAc}$. Aqueous solution of $\text{mPEG}_n\text{MPyrI}$ (6.17 g, 0,011 mol) was passed through a chromatography column packed with 40 g Amberlyst A-26 hydroxide (OH^- form) dropwise. Equimolar amount of acetic acid (0.65 g, 0,011 mol) or perchloric acid (1.57 g, 0,011 mol) was added to the resulting solution. Neutral pH was controlled with pH meter Mettler Toledo. The water was carefully removed under vacuum using rotary vapor at 60 °C during for few hours. Absence of residual iodide was controlled by AgNO_3 test. The product was identified as $[\text{mPEG}_n\text{MPyr}]\text{OAc}$ (compound **ILE**) and by ^1H , ^{13}C -NMR and mass spectrometry. APCI (+) HRMS: major $m/z = 468.3149$ ($\text{C}_{22}\text{H}_{45}\text{NO}_9^+$). Water content in as synthesized **ILE** was 2.73 wt. % as determined by Karl Fisher coulometric titration.

For **ILE**: ^1H NMR (400 MHz, CDCl_3) δ 3.97 – 3.87 (br, 4H), 3.86 – 3.76 (br m, 2H), 3.72 – 3.63 (br m, 2H), 3.61 – 3.50 (br m, 23H), 3.49 – 3.43 (br m, 2H), 3.32 – 3.26 (m, 3H), 3.20 (s, 3H), 2.25 – 2.05 (br m, 4H), 1.85 (s, 3H)

^{13}C NMR (101 MHz, CDCl_3) δ 177.2, 77.2, 70.5, 70.4, 70.2, 70.1, 65.6, 65.1, 63.0, 59.0, 48.3, 25.4, 21.4

For **ILEP**: ^1H NMR (400 MHz, CDCl_3) δ 3.99 - 3.90 (br. 2H), 3.78 – 3.57 (br m, 29H) 3.56 – 3.48 (br m, 2H), 3.40 – 3.32 (br m, 3H), 3.17 (s, 3H), 2.16 – 2.34 (br m, 4H)

^{13}C NMR (101 MHz, CDCl_3) δ 71.92, 70.5, 70.4, 70.3, 70.2, 65.6, 65.2, 63.4, 59.0, 48.9, 21.6

Mass analysis of the compounds **B**, **C** and **ILE** by MALDI-TOF mass-spectrometry was hindered due to the close mass of certain compounds. Firstly, mass analysis of initial alcohol (mPEG_nOH) revealed that it exists as an extended population of monomers n ($4 < n < 14$, where $n = -\text{CH}_2-\text{CH}_2-\text{O}-$), the difference of molecular masses is 44.0262 Da. Products **B** (mPEG_nOTs) and **C** ($\text{mPEG}_{n-1}\text{I}$) (scheme 2) differs by 0.0829 Da, hence, their distinguishing is difficult. Thus, we provided an analysis by high resolution mass spectrometry (HRMS) atmospheric pressure chemical ionization (APCI-Orbitrap) which allowed to more precisely identify products with high resolution masses and correctly observe anions in ionic liquids.

Water-RTILs mixtures in a very large range of water concentration were studied both in experimental work and by molecular dynamics (MD). For the experimental characterization the mixtures were prepared gravimetrically using freshly prepared Milli-Q water ($18.2 \text{ M}\Omega \cdot \text{cm}^{-1}$ at $25 \text{ }^\circ\text{C}$) and “as synthesized” ILs. The exact concentrations used in the work can be found in **Chapters 4, 5, 6**.

3.3. Characterization of RTILs and their mixtures with water

3.2.1. Electrochemical characterization

Conductivity measurements. To measure ionic conductivity of RTILs and their aqueous mixtures electrochemical impedance spectroscopy (EIS) method was selected. This method is one of the most applied to measure impedance (Z) in of ILs [106,138,140]. The advantages are that it requires the minimum amount of electrolyte, and it is easy to perform. This impedance arises from resistive (R) in and capacitive (C) contributions, and can be described by equation:

$$Z = \sqrt{\left(\frac{1}{\omega C}\right)^2 + R^2} \quad (3.1)$$

where ω is the frequency of the alternating current (AC) modulation [Hz]. As AC frequency increases the capacitive contribution to the impedance becomes vanishingly small and equation reduces to $Z = R$ [Ohm], the resistance of the IL in impedance cell. Under these conditions the conductivity, κ [$S \cdot cm^{-1}$], of the ionic liquid may be obtained from the measured resistance by equation (3.2)

$$\kappa = \frac{l}{AR} \quad (3.2)$$

where l [cm] is the distance between the two electrodes in the impedance cell and A [cm^2] is the area of the electrodes. The term l/A is often referred to as the cell constant and it is normally determined by measuring the impedance (resistivity) of the standard solution with determined conductivity (usually aqueous KCl).

All the experiments were performed using home-made dip-type conductivity cell having a cell constant of $3.78 \pm 0.05 \text{ cm}^{-1}$ with two parallel platinum electrodes (**Fig. 3.1**) at 10 mV amplitude vs. E_{oc} within the frequency range 100 kHz – 100 Hz. The cell constant was determined by measuring impedance of 0.01 M KCl aqueous solution ($\sigma = 1.408 \text{ mS/cm}$ at 25°C). All the measurements were conducted at least 5 times in Faradic cage and at the temperature $25 \pm 0.2 \text{ }^\circ\text{C}$. **Fig. 3.2** displays an

example of EIS spectra obtained in dip-type conductivity cell for ILA and ILE containing 4.44 and 2.73 wt. % of water respectively.



Fig. 3.1. Home-made dip-type conductivity cell.

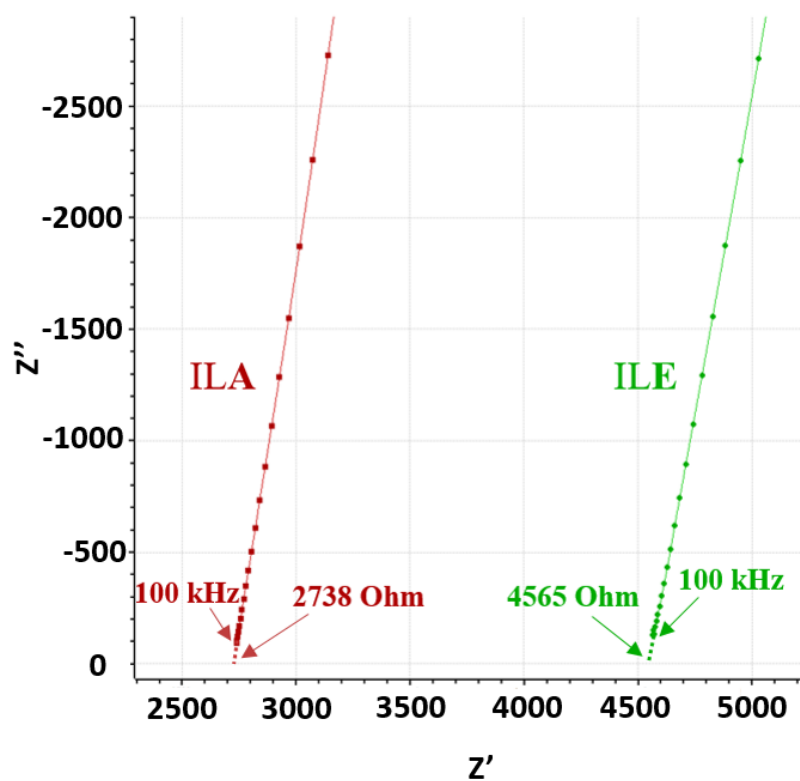


Fig. 3.2. EIS spectra obtained in dip-type cell of ILA and ILE containing 4.44 and 2.73 wt. % of water respectively. The resistivities are indicated.

Electrochemical potential window. The most common method used for the measurement of the electrochemical potential window of ILs is cyclic voltammetry. In a three-electrode cell, the potential of an inert working electrode (glassy carbon, Pt, W) is scanned out to successively greater positive (anodic) and negative (cathodic) potentials until current density rises rapidly due to the oxidation and reduction of the IL. The oxidative and reductive potential limits are assigned when the current density reaches, so called, cut-off limit (usually 1 mA/cm²). The electrochemical potential window is the difference between these anodic and cathodic potential limits.

The experiments were conducted in a home-made three-electrode system with the volume of ≈ 200 μ L of electrolyte (**Fig. 3.3**). Freshly polished glassy carbon disk ($S=0.0314$ cm²), Pt-wires and pseudo-AgCl/Ag electrode were used as working, counter and reference electrodes respectively. Pseudo-ref AgCl/Ag electrode was calibrated using 0.01 M K₃[Fe(CN)₆] solution of corresponding IL. IUPAC

recommends to use ferrocene as an internal standard to calibrate pseudo-reference electrodes. But in acetate-based ILs, ferrocene and its analogues were unstable and do not reveal reversible oxidation/reduction. Similar results were reported by Frenzel *et al.* [142], thus, $\text{K}_3[\text{Fe}(\text{CN})_6]$ has been selected. The potentials of oxidation/reduction pair of $\text{K}_3[\text{Fe}(\text{CN})_6]$ were determined as $V_{(\text{FeIII}/\text{FeII})} = -0.54 \text{ V}$ and $V_{(\text{FeIII}/\text{FeII})} = -0.395 \text{ V}$ in ILA and ILE respectively (**Fig. 3.4**).

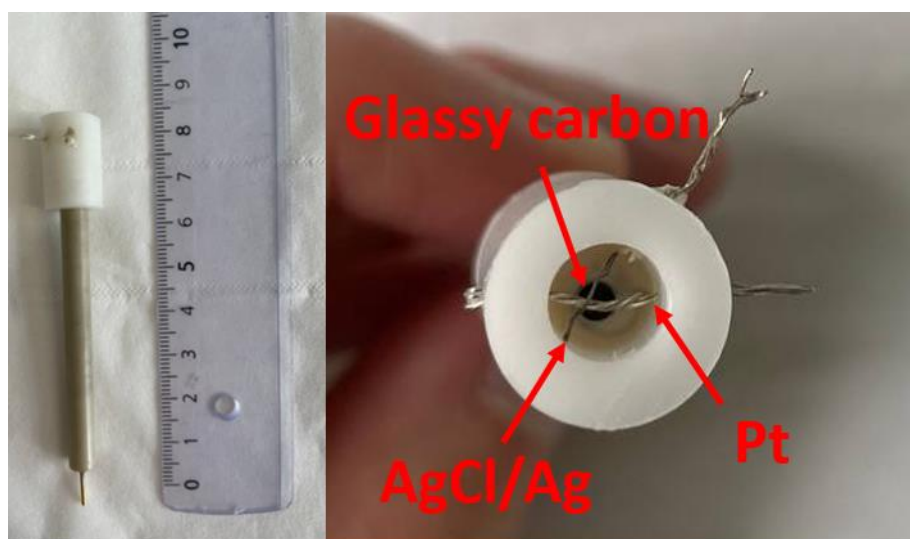


Fig. 3.3. Home-made electrochemical cell for EPW measurements.

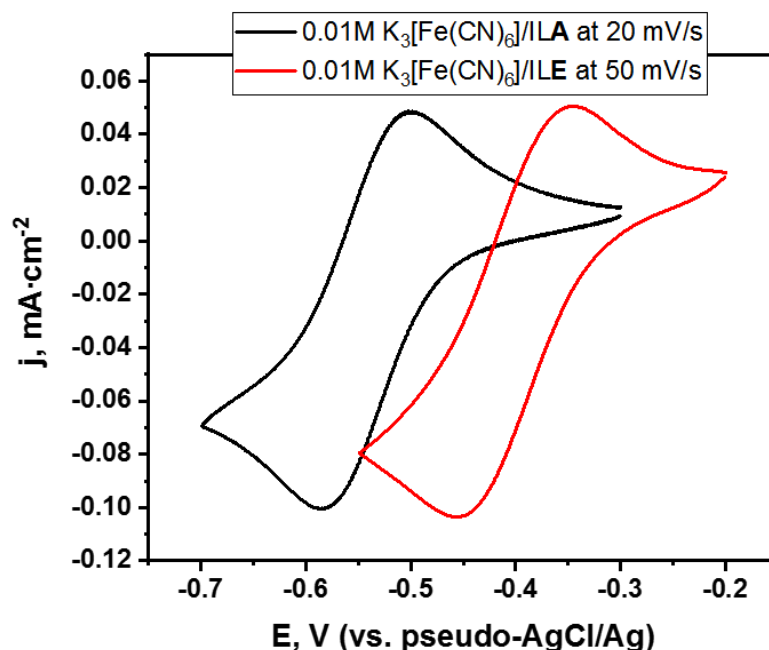


Fig. 3.4. Typical voltammograms recorded on glassy carbon electrode in 0.01M solution $K_3[Fe(CN)_6]$: in ILA at 20 mV/s – black curve; in ILE at 50 mV/s – red curve.

3.2.2. Chemical characterization of the electrolytes

In order to elucidate molecular state of each compound in water-IL mixtures, two complementary spectroscopic techniques, Raman and Attenuated Total Reflectance Infrared spectroscopy (ATR-IR), were used.

Raman spectroscopy is a non-contact, non-destructive, fast technique which provides the possibility to characterize liquids and solid materials as well as liquid – solid interfaces. It offers detailed information about chemical structure, phase and polymorphy, crystallinity and molecular interactions. It is based upon the interaction of light with the chemical bonds within a material. Excitation light puts the molecule into a **virtual energy state** for a short time before the photon is emitted. According to the theory, the emitted (or scattered) light can have the same frequency, $\nu_s = \nu_i$, and this is represented as elastic (Rayleigh scattering) contribution and does not provide any information. At the same, frequency of emitted photons can differ, $\nu_s \neq \nu_i$, it is represented as inelastic (Stokes and Anti-Stokes, Raman scattering) contribution in the scattered electric field. The latter occurs only if vibrations change

bond polarizability. Positions of Raman peaks depend on the atoms mass, bond length and the angles between atom-sharing bonds. Therefore, they are used as fingerprints for identification of particular substances. Raman spectroscopy is particularly sensible to homo-nuclear molecular bonds (C-C, C=C and etc...)

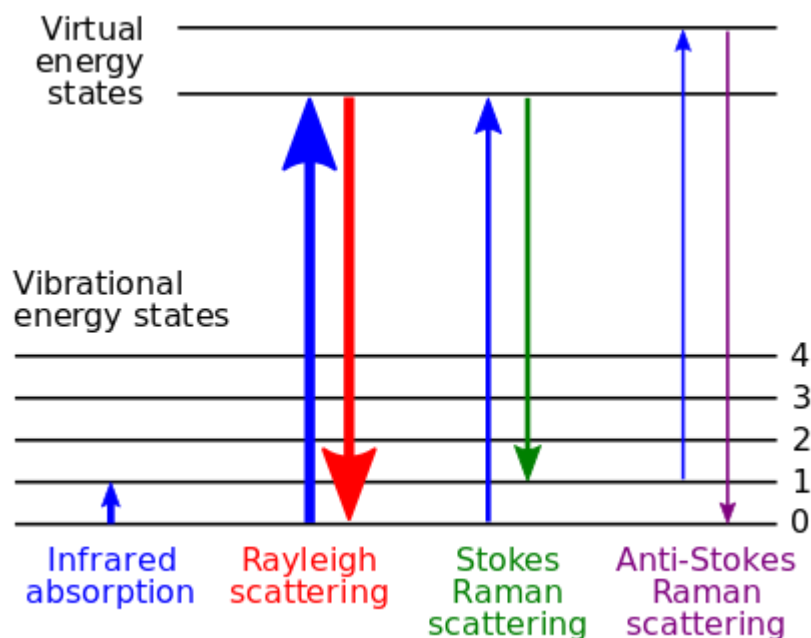


Fig. 3.5. Jablonski diagram of quantum energy transitions.

On the contrast to Raman, in Infrared Spectroscopy (IR) the **absorbed (or reflected or transmitted)** light is measured. The infrared radiation puts the molecule into a **real** excited energy state (**Fig. 3.5**). IR spectroscopy is particularly sensible to hetero-nuclear functional group vibrations and polar bonds, especially O-H stretching in water ($3000\text{-}3700\text{ cm}^{-1}$ wavelength shift).

Attenuated Total Reflection Fourier-Transform Infrared (ATR-FTIR) spectroscopy is a widely used versatile technique to study molecular state of water in organic solvents and RTILs. It does not require any sample preparation and allows to study liquid and solid materials. However, it requires special ATR cell. Further information can be found in [143].

To support the hypotheses about molecular interactions in the electrolyte, water-IL mixtures with different H₂O concentrations (from 0 to 99 at. % of water)

were simulated using Molecular Dynamics (MD). In addition, in order to elucidate the influence of Mg ions on molecular state of each particle (H_2O , IL and Mg^{2+}) the effect of addition of Mg-ions in the solution was also simulated for several selected mixtures. MD calculations were realized by an intern (Urmat Rustambek) in collaboration with TCM team of Institute of Chemistry for Life and Health Sciences at Chimie ParisTech (Dr. Alistar Ottochian). The details of the calculations are given in the corresponding papers (Chapters 5 and 6).

3.3. Reactivity characterization at metal – electrolyte interfaces

Electrochemical cell design. A three-electrodes home-made electrochemical cell was designed and printed by 3D-printer using inert PLA (polylactic acid) filament (Fig. 3.6).

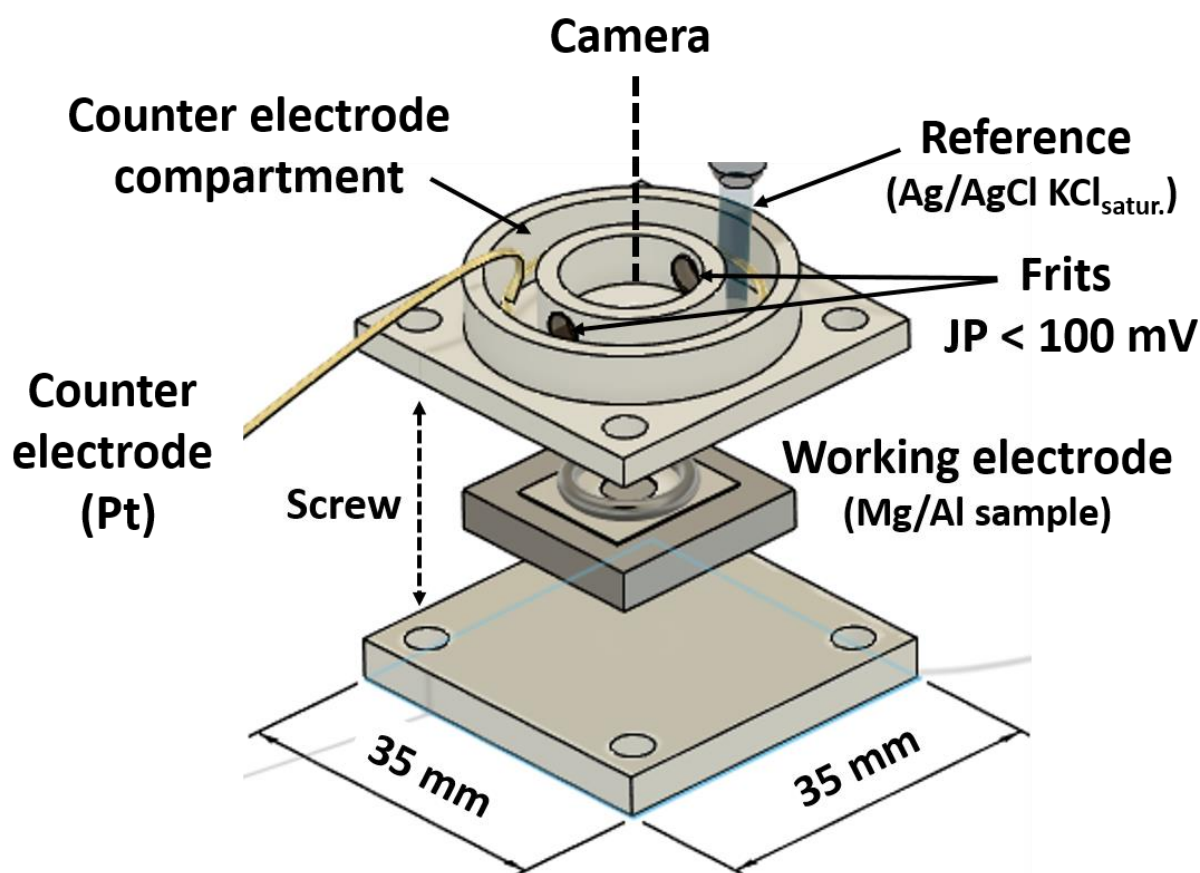


Fig. 3.6. Schematic representation of electrochemical cell.

The design of electrochemical cell has been developed in order to reduce the volume of used electrolyte and to be able to survey the working electrode area for *in situ* Time Lapse Microscopy (TLM).

The working electrode chamber was filled with 0.6 ml of water-ionic liquids solutions. Since ionic liquids contained 10 wt. % of water, we assumed that it permits to employ aqueous-based electrolyte (0.5 M magnesium acetate or perchlorate, $\text{Mg}(\text{OAc})_2$ or $\text{Mg}(\text{ClO}_4)_2$) in the counter electrode chamber. The counter electrode chamber communicated with the working electrode chamber via glass frits membrane. The separation was necessary to be able to observe the surface of the working electrode without perturbations due to the reaction products formed on the counter electrode, in particular to avoid the hydrogen gas bubbles not formed on the working electrode. Additionally, the reaction on the counter electrode can contribute in modification of the electrolyte if the WE and CE compartments are not separated. **Fig. 3.7** illustrates preliminary results obtained in electrochemical cell without spatial separation working and counter electrodes, hydrogen bubbles are formed on the counter electrode which anodically polarized Mg sample.

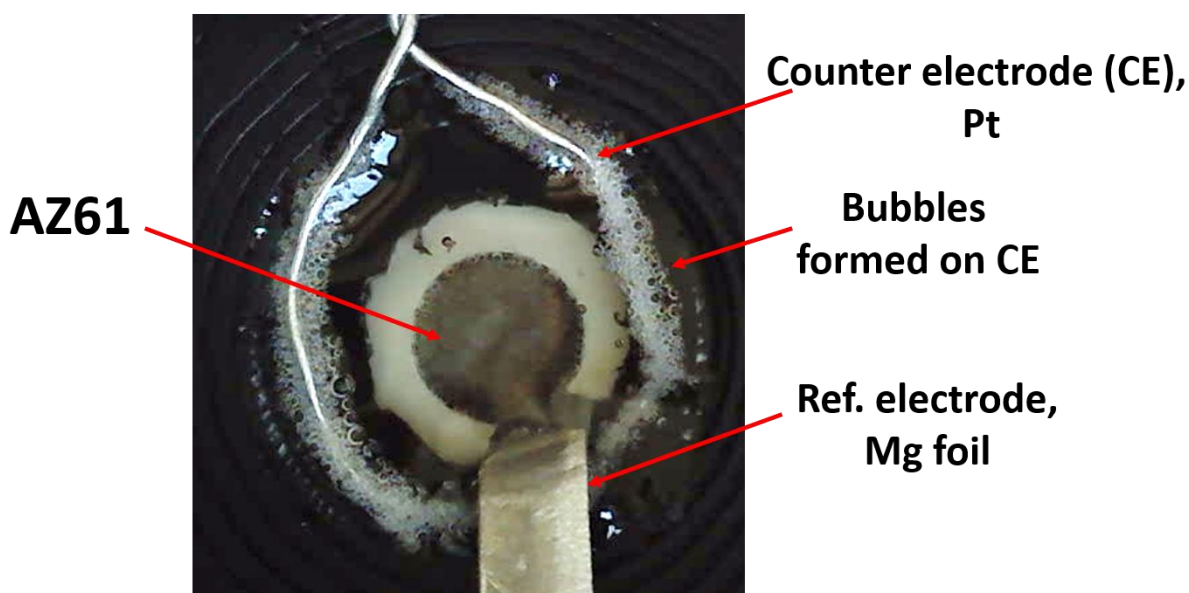


Fig. 3.7. Preliminary results obtained on AZ61.

The cell geometry, with the reference electrode into the counter electrode chamber, results in a junction potential between two phases (IL – water). Junction

potentials between the chambers, defined as the potential difference between two identical platinum wires, were 36 mV for [BMPyr]OAc-H₂O // 0.5M Mg(OAc)₂-H₂O, 49 mV for [mPEG_nMPyr]OAc-H₂O // 0.5M Mg(OAc)₂-H₂O and 86 mV for [mPEG_nMPyr]ClO₄-H₂O // 0.5M Mg(ClO₄)₂-H₂O junctions. Before each experiments electrochemical cell was immersed at least during the night in 0.5 M Mg(OAc)₂ (aq.) or 0.5 M Mg(ClO₄)₂ (aq.), depending on the used IL-H₂O electrolyte. Then the cell was rinsed, dried in the air stream and counter electrode chamber was refilled with a new solution.

Mg alloys were used as working electrode (exposed geometric area 0.196 cm² was delimited by PortHoles electrochemical sample mask), platinum rounded wire (S≈1.23 cm²) as a counter electrode and aqueous AgCl/Ag (in saturated KCl) reference electrode. Electrical contact with the working electrode was realized by a single sided copper tape.

All the electrochemical experiments were conducted using Gamry 3000 potentiostat at room temperature and under ambient atmosphere. Reactivity was studied at open circuit (OC) and under anodic polarization in potentiostatic and potentiodynamic conditions. Potentiodynamic anodic polarization curves were recorded after 30 minutes of OC potential (E_{oc}) measurement within the potential range from 0 to +1200 mV vs E_{oc} (scan rate of 1 mV/s). Additionally, cyclic potentiostatic polarizations were performed. The cycle started after stabilizing the E_{oc} within one hour. Cycles consisted of three polarizations at +700 mV vs E_{oc} , then 3 polarizations at +1 V vs E_{oc} . Each polarization lasted 20 minutes and was followed by 15 minutes of E_{oc} measurement. Two potentials + 700 mV and +1000 mV vs OCP were chosen in order to (1) ensure a sufficient polarization to evidence visually the enhancement or not of the hydrogen evolution under anodic polarization when compared to open circuit condition and (2) verify the effect of applied anodic potential and cycling on the current stability. At some point, it can be also assumed that anodic polarization simulates discharge electrochemical cell. The scheme of the polarization cycle is presented in **Chapters 4, 6**.

Time Lapse Microscopy (TLM) coupled to the electrochemical measurement.

Hydrogen collection is often applied for quantitative evaluation of cathodic hydrogen evolution during Mg corrosion. Such a measurement was however impossible in the present work because of very small volume of the reactor. The used in the literature systems for gas collection require comparatively big volume of the electrolyte, while we have exposed 0.19625 cm² of Mg in 700 µl of the electrolyte (from which water presents only 10 wt. %). This limitation comes from the fact that the studied ILs are not commercially available, they were proposed and synthesized specially for this work. So, the quantitative collection is difficult and the development of a specific cell and specific technics for the quantification in such limited volumes was out of the scope of the present work. Aiming to visualize hydrogen and surface evolution during E_{oc} measurement and during anodic polarization, *in situ* TLM was used. High definition (HD) USB microscope with 2 MP CMOS detector and a 4000 K white LED enlightenment was coupled with the electrochemical cell. Live images were taken every 30 seconds during the experiments. Some of these images captured during E_{oc} and anodic polarization were assembled into videos by specially written script on Python. Videos are available in the electronic and online versions of the articles presented in **Chapters 4 and 6**.

3.4. Chemical characterization of solid surface and humid interface

After the electrochemical experiments the surface state of the wet electrode was systematically examined by **Confocal Raman Microscopy (CRM)** and **ATR-FTIR** spectroscopy. Additionally, selected samples were characterized by Time-of-Flight Secondary Ions Mass spectroscopy (**ToF-SIMS**).

CRM and ATR-FTIR were used to analyze the surface chemistry and confirm the presence of corrosion products or adsorbed species on the **wet** metallic surface after electrochemical experiments. The presence of IL containing film was verified thanks to specific peaks typical for functional groups (detailed peaks attribution is presented in the results section and in **Appendices 1, 3**). Additionally, the presence and distribution of Mg(OH)₂ was also studied by Confocal Raman

Mapping because its formation was reported to correlate with an extensive hydrogen evolution reaction in aqueous solutions [144]. A_{1g} O-H stretch vibration (peak at 3652 cm^{-1}) was used for the $\text{Mg}(\text{OH})_2$ detection.

Raman spectroscopy and mapping were made with a Renishaw Confocal Raman Microscope InVia using red laser (HeNe, 633 nm, 17 mW power). Illumination and observation of the surface were performed through a microscope objective Leica of $\times 50$ magnification and numerical aperture (NA) of 0.75. The exposure time was 3 seconds, and 50 spectra were recorded at each point. The mapping was made in the spectral range of $3300\text{-}3900\text{ cm}^{-1}$. Typical area of one map was $7000\text{ }\mu\text{m}^2$ for CP Mg/[BMPyr]OAc- H_2O , $6000\text{ }\mu\text{m}^2$ for CP Mg/[mPEG_nMPyr]OAc- H_2O (with the step of $10\text{ }\mu\text{m}$); $7840\text{ }\mu\text{m}^2$ for AZ61/[BMPyr]OAc and AZ61/[mPEG_nMPyr]OAc (with step of $7\text{ }\mu\text{m}$). For mapping, the peak area at 3652 cm^{-1} was normalized on its maximum value, which was selected among all the results obtained on CP Mg surface immersed in [BMPyr]OAc solution.

ATR-FTIR spectra were recorded using a Thermo Scientific Nicolet 6700 FTIR spectrometer equipped with a mercury cadmium telluride detector cooled by liquid nitrogen at 77 K. The ATR accessory was a horizontal ZnSe crystal coated with diamond ($A = 2.54\text{ mm}^2$) with single reflection and an angle of incidence of 45° (Smart Miracle from PIKE). The droplets of ILs samples ($\sim 7\text{ }\mu\text{L}$) were placed on the crystal and spectra recording was started immediately. The Mg samples were pressed against the ATR crystal by dynamometric tool. The spectra were recorded with resolution of 2 cm^{-1} and were averaged from 64 scans. OMNIC software was used for the data collection and treatment.

ToF-SIMS was chosen as a powerful technic to analyze thin surface layers in order to obtain more precise information about formed corrosion products and adsorbed films at nanometric scale, which helps to precise the mechanism of corrosion and degradation of different metallic matrixes and the mechanisms of

inhibition by organic and inorganic molecules, especially for Mg-alloys [23,120,133,134]. This is an extremely sensitive technique (detection limits up to 1 ppm) which provides the information of masses of scattered (secondary) ions delaminated from the surface during its bombing, by their time of flight.

In this work, three different types of analysis were carried out: positive and negative ions mass spectra and negative ions depth profile. Negative and positive mass spectra (MS) were obtained by scanning a $500 \times 500 \mu\text{m}^2$ area using a 20 keV Bi^+ ion beam delivering 1.2 pA current. Negative ions depth profiles were conducted using the spectrometer in dual beam mode, meaning that Bi analyzing gun and Cs sputtering gun scan successively the surface. Thus, for generating the $300 \times 300 \mu\text{m}^2$ crater, the 2keV Cs^- ion beam delivering 100 nA was used. The analysis was realized by sputtering a $100 \times 100 \mu\text{m}^2$ area at the bottom of the crater using a 20keV Bi^+ ion beam delivering 1.2 pA current. The spectra were calibrated using, at least, 5 well identified peaks in the MS. In depth profiles, the intensities of all compounds are plotted versus sputtering time. Data treatment and post processing were carried out using the Ion-Spec software (version 6.9).

The measurements were provided using a ToF-SIMS V spectrometer (ION-TOF GmbH, Muenster, Germany). The operation pressure in the chamber was around 10^{-9} mbar (ultra-high vacuum, UHV). Ion mass spectra (MS) and depth profiles were recorded. A Bi^+ pulsed primary ions gun with a 45° angle to the surface was used for analysis. The surface sputtering was done using a Cs^+ gun, also oriented with a 45° angle to the surface. During analysis, atomic and molecular ions (secondary ions), characteristic of the surface composition, were emitted and analyzed. Their mass/charge (m/z) ration is measured by their time of flight to reach the detector.

To sum up, **Table 3.3** displays all physico-chemical methods used in this work.

Table 3.3. Summarized physico-chemical methods used in the work.

Experimental techniques	Studied phenomena / property
Electrolyte properties	
H-NMR, Mass spectrometry	Chemical composition of as synthesized RTIL
Cyclic voltammetry	Electrochemical potential window (EPW) of synthesized IL
Electrochemical impedance spectroscopy (EIS)	Conductivity of water-ILs solutions
Raman spectroscopy and Attenuated Total Reflectance spectroscopy (ATR-FTIR)	Molecular state of water and ILs in their mixtures
Molecular dynamic (MD) simulations (in collaboration)	Molecular state of water and ILs in their mixtures with and without addition of Mg ions
Reactivity of solid / liquid interface	
Potentiodynamic polarization and potentiostatic polarization cycles	Electrochemical reactivity of Mg alloys in RTIL-water mixtures
Time Lapse Microscopy (TLM)	Metallic surface evolution during the electrochemical experiments, hydrogen bubbles release from the surface under anodic polarization and during free corrosion (open circuit potential) conditions
Chemistry of solid / liquid interface and of reacted surface	
Confocal Raman Microscopy (CRM) and Attenuated Total Reflectance spectroscopy (ATR-FTIR)	Metallic surface state after electrochemical experiments
Time-of-Flight Secondary Ions Mass Spectroscopy (ToF-SIMS)	Composition of layers form on metallic surfaces

Part 3. Results

Chapter 4:

Mg-alloys in water – hydrophilic ionic liquid mixtures: is there a negative difference effect?

This chapter answers the questions “Does the NDE occur in the mixtures H₂O-IL? If yes – is it a universal effect?”

This chapter is prepared in the form of an article published in Corrosion Science.
<https://doi.org/10.1016/j.corsci.2022.110178>

Additional information (videos, see the text) can be downloaded from the online version. See the .gif files in the archive of Supplementary material.

D. Kurchavov^a, M. Haddad^b, V. Lair^a, P. Volovitch^{a*}

^a *Chimie ParisTech, PSL University, CNRS, Institut de Recherche de Chimie Paris (IRCP), F-75005 Paris, France*

^b *PSL University, Chimie ParisTech, CNRS UMR 8060, Institute of Chemistry for Life and Health Sciences, CSB2D team, 75005 Paris, France*

*Corresponding author.

E-mail addresses: polina.volovitch@chimieparistech.psl.eu (P. Volovitch)

Abstract

Commercial purity Mg and Mg-alloy AZ61 were exposed at open circuit potential and under anodic polarization in two ionic liquids containing 10 wt.% of water, formed by acetate anion and methylpyrrolidinium cation, substituted with either aliphatic (ILA) or etheric (ILE) chain. Hydrogen evolution strongly increased under anodic polarization (negative difference effect, NDE) in ILA, but not ILE. In both electrolytes Mg(OH)₂-film formed on Mg but not on AZ61. The NDE suppression correlated neither with the presence of carboxylate, nor with the absence of Mg(OH)₂, indicating strong differences between magnesium-water interaction in IL-water mixtures and in inorganic aqueous solutions.

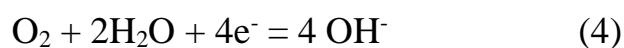
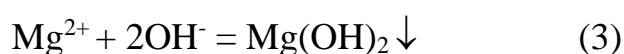
Keywords: A. Magnesium; A. Ionic liquid; B. polarization; B. Raman spectroscopy; C. negative difference effect

1. Introduction

Mg alloys are attractive materials for numerous applications in automotive, aerospace, biomedical and energy sectors because of low weight and high mechanical strength, bio compatibility, non-toxicity and high theoretical energy density [1–3]. Mg is highly reactive in the presence of electrolytes due to low standard oxidation/reduction potential ($E_0 = -2.37$ V vs. SHE) and different applications require good understanding and control of this reactivity.

In aqueous media under ambient conditions Mg dissolution proceeds through anodic dissolution (reaction 1), cathodic water reduction (reaction 2) and formation

of corrosion products on the surface (reaction 3) [7,8]. Some evidence of the contribution of naturally dissolved oxygen in cathodic reactivity have been also demonstrated (reaction 4) [21,22]. This may be critical to employ Mg-containing components in Mg-batteries due to decreasing of utilization efficiency (UE) by cathodic reactivity on the anode (reactions 2, 4) and passivation of the surface (reaction 3).



A particularity of Mg and its alloys is that, in many electrolytes, cathodic hydrogen evolution reaction (HER) increases under anodic polarization of the electrode (so called Negative Difference Effect, NDE) [147]. The NDE intensity depends on the nature of the electrolyte, in particular on the anions (see for instance [77,79]), the highest effect being reported in the presence of chloride. Carboxylic acid containing compounds are extensively studied as inhibitors for Mg corrosion and NDE in aqueous electrolytes [70–72,74]. The role of cations in the NDE has never been systematically considered because in aqueous corrosion research mainly sodium salts are used to form electrolytes. Numerous theories have been proposed to explain NDE in aqueous solutions including formation of unipositive species (Mg^+ , adsorbed MgOH^+ or MgH), magnesium hydride MgH_2 , local galvanic coupling between Mg matrix and either noble elements inclusions or corrosion products [25–27,34,40,62]. Each of these theories can be criticized or can find arguments in its favor. For example, simultaneous in situ quantification of external anodic current, dissolved magnesium and hydrogen formation have demonstrated that two electrons are liberated when dissolving one Mg atom in NaCl aqueous solutions [48,78,148], and that NDE is absent in neutrally buffered NaCl solutions in which the oxidized film is not formed [148,149]. These results can be seen as a support of the

mechanisms of NDE involving the activation of the cathodic reaction related to the disruption of a protective surface film. At the same time, electrochemical impedance spectroscopy results could be well fitted with introduction of unipositive species [36,150] which recently have been proposed as adsorbed MgOH or MgH species [35]. Although there is no unanimous opinion on the mechanisms of the NDE [13], the effect is well accepted and continuously studied in aqueous solutions. In contrast, the possibility of NDE has never been discussed for non-aqueous electrolytes such as ionic liquid, which could contain water as an additive.

Ionic liquids (ILs) are ionic compounds with melting temperature below 100 °C which usually contain organic cations and organic or inorganic anions. Room temperature ILs (with melting temperature below room temperature) form a relatively new class of electrolytes attracting an enormous interest for energy applications because of their high conductivity, good thermal stability, wide electrochemical potential window, low volatility and environmental friendliness [14–16]. Nowadays they are extensively studied as perspective electrolytes for Mg-based energy storage systems [136,138,151]. Moreover, these electrolytes can allow reversible deposition of Mg with high coulombic efficiency, as reported for some dry ILs containing etheric groups [136,137]. In these works, high efficiency was attributed to the complexation of Mg-ions through etheric oxygen in the substituted chain at tertiary nitrogen if at least three etheric groups were present. In the area of aqueous corrosion, it has been also shown that preliminary surface treatment of Mg alloy with some ILs can inhibit aqueous corrosion in chloride containing aqueous solutions [132]. Strongly passive layers formed on Mg surface by interaction with ionic liquids decrease self-corrosion but impede Mg ions release into the electrolytes. For example, in fluorine-containing ionic liquids, strongly passivating MgF₂ and MgO films on the surface inhibited reactivity [96,152]. The corrosion rate of polycrystalline magnesium and of AZ61D magnesium alloy in dry ILs was reported to be several orders of magnitude lower than in aqueous 3.5 wt.% NaCl

solution, however even small water addition to the electrolyte activated the surface, reducing corrosion potential and increasing corrosion rate [134].

Whatever the application of a IL is, the presence of traces of water can crucially decrease IL's stability and affect Mg reactivity. At the same time, conscious addition of a small quantity of water into ILs could be of interest for the application: it increases conductivity, reduces viscosity, density and melting point [113,153–156]. Although addition of water constricts electrochemical potential window of ILs [153], this effect could be potentially compensated and decreased by additional interactions between water and ILs (*e.g.* hydrogen bonds formation). Possibilities of hydrogen bonds formation have been reported between acetic [18] and etheric [19] groups and water. The presence of water in IL can also modify the nature of the interface between the metal and the electrolyte. For instance, the formation of an amorphous “gel-like” film on the surface of Mg electrode by hydrated chloro-magnesium complexes with IL was reported to make the interface passive at open circuit but conductive under anodic polarization [135].

Despite the clear interest of the water - ionic liquids mixtures, very little is known about the behavior of Mg alloys in such electrolytes and the role of the cations and anions of IL in electrochemical processes. Considering Mg reactivity in water – IL mixtures, the question of the existence of the NDE in these electrolytes is completely unexplored, at least we were not able to find any mention of the presence or the absence of the anomalous hydrogen evolution on Mg in ILs or water - IL mixtures. If present, the NDE can however play a significant role for both practical applications and fundamental understanding of Mg behavior in such electrolytes. Although some knowledge is accumulated about the effect of small organic anions on Mg corrosion in aqueous electrolytes, this is not the case for the organic cations. The later can contain some functional groups potentially influencing the interaction of Mg with water and affect hydrogen evolution. The existence of the effect in different ILs needs hence to be verified and the role of IL composition for activation or not of the NDE in water-IL mixtures needs to be understood. The

present work is the first attempt in this direction. It compares the reactivity of commercially available pure Mg (Mg 99,9% purity, 280 ppm of Fe) and AZ61 alloy in two new hydrophilic ILs containing 10 weight % of water, demonstrating that only in one electrolyte the NDE is present. Both ILs were formed with acetate (OAc^-) anion, chosen because of the previously reported inhibiting effect of carboxylic acids on the NDE in aqueous solutions. The choice of two different cations based on quaternary nitrogen with different substitutions is based on the expected difference in the capacity of aliphatic and etheric functional groups to interact with Mg surface and leached magnesium ions. Aliphatically substituted BMPyr^+ is expected to be inert for both, water and Mg, while polar etheric groups in $\text{mPEG}_7\text{MPyrr}^+$ could probably participate in the formation of complexes and hence modify reactivity of the system. The water content of 10 wt. % was chosen in order to have sufficient conductivity and because close optimal water contents were studied in some other water - IL systems for Mg anodes applications [134], [135]. The main objectives of the work are:

- 1) to check if the NDE exists in the new water-IL mixtures
- 2) to verify if there is an effect of the IL cation on the HER
- 3) to compare reactivity of two alloys in the new electrolytes.

2. *Materials and methods*

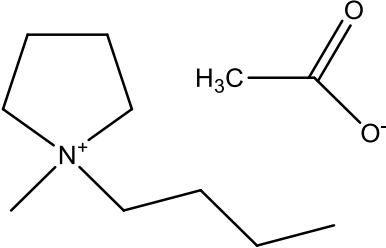
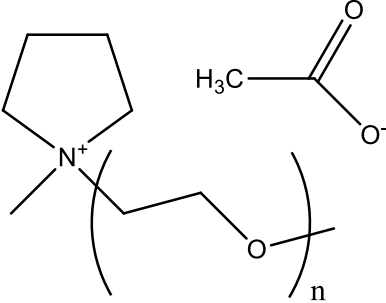
The compositions of the alloys are presented in **Table 4.1**. Foils with area of 1×1 cm were grinded by 800, 1200, 2400, 4000 SiC polishing paper grits using absolute ethanol as a lubricant, rinsed with ethanol and dried.

Table 4.1. Composition of Mg alloys used in this work.

Sample name	Al ppm	Zn ppm	Mn ppm	Si ppm	Fe ppm	Ca ppm	Mg wt. %
CP Mg	70	<20	170	50	280	-	Balance
AZ61	62,000	7,400	2,300	40	40	1.3	Balance

The chemical formulas of the ILs and the characterization methods used to confirm their structures are presented in **Table 4.2**.

Table 4.2. Graphical structures of used ILs, their acronyms, identification methods.

Ionic liquid (Name)	Graphical formula	Identified by
[BMPyr]OAc (aliphatic)		¹ H, ¹³ C NMR; MALDI-TOF
[mPEG _n MPyr]OAc* (etheric)		¹ H, ¹³ C NMR; MALDI-TOF

*n – means variable numbers of etheric groups found by MALDI-TOF, $4 \leq n \leq 16$ with an average value $\langle n \rangle = 7$.

General procedure of the ILs synthesis is published elsewhere [140,141]

All the electrochemical experiments were made in the IL-water mixtures containing 10 weight % of Milli-Q water (18.2 Ω).

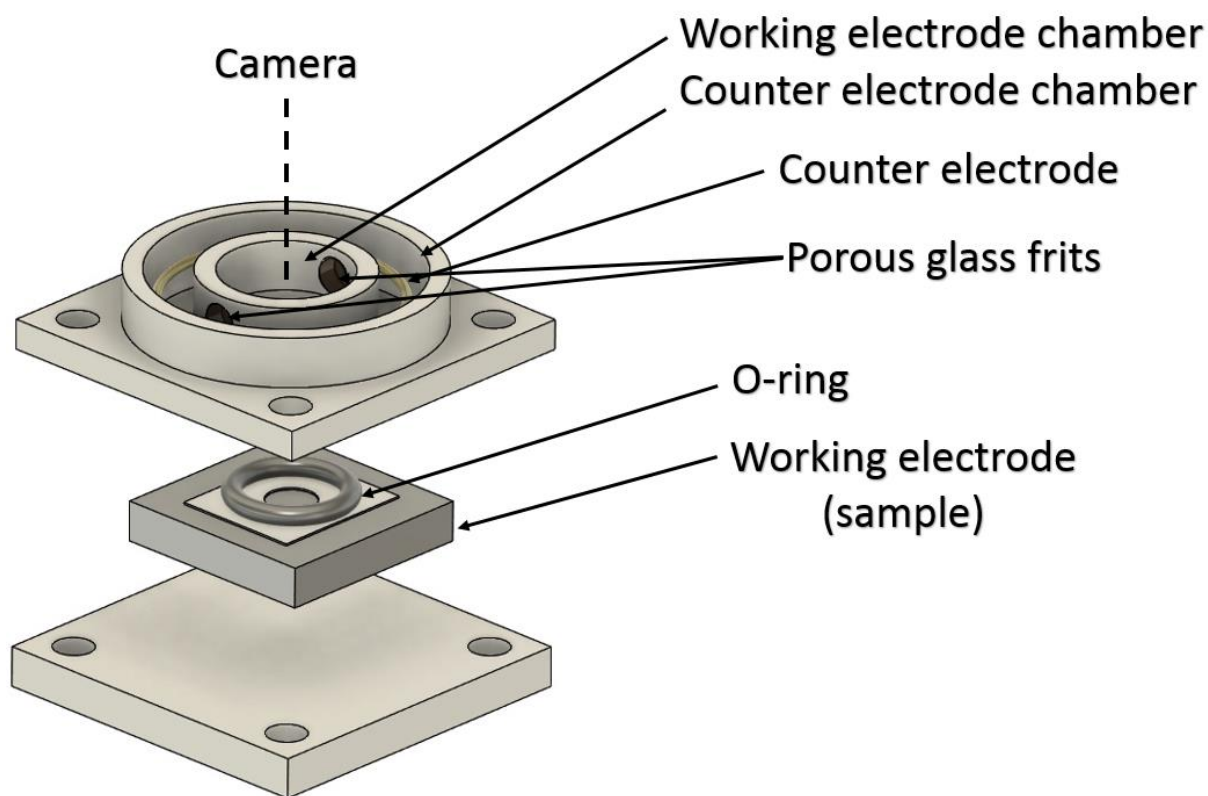


Fig. 4.1. Schematic representation of electrochemical cell.

A three-electrodes home-made electrochemical cell was designed and printed by 3D-printer using inert PLA (polylactic acid) filament (**Fig. 4.1**). The working electrode chamber was filled with 0.6 ml of water-ionic liquids solutions. Since ionic liquids contained 10 wt. % of water, we assumed that it permits to employ aqueous-based electrolyte (0.5 M magnesium acetate, $\text{Mg}(\text{OAc})_2$) in the counter electrode chamber. The counter electrode chamber communicated with the working electrode chamber via glass frits membrane. The separation was necessary to be able to observe the surface of the working electrode without perturbations due to the reaction products formed on the counter electrode, in particular to avoid the hydrogen gas bubbles not formed on the working electrode. The cell geometry, with the reference electrode into the counter electrode chamber, results in a junction potential between two phases (IL – water). Junction potentials between the chambers, defined as the potential difference between two identical platinum wires, were 36 mV for $[\text{BMPyr}]\text{OAc}^- - \text{H}_2\text{O} // 0.5\text{M } \text{Mg}(\text{OAc})_2\text{-H}_2\text{O}$ and 49 mV for $[\text{mPEG}_n\text{MPyr}]\text{OAc}^- - \text{H}_2\text{O} // 0.5\text{M } \text{Mg}(\text{OAc})_2\text{-H}_2\text{O}$ junctions.

Mg alloys were used as working electrode (exposed geometric area 0.196 cm^2 was delimited by PortHoles electrochemical sample mask), platinum rounded wire ($S \approx 1.23 \text{ cm}^2$) as a counter electrode and aqueous AgCl/Ag (in saturated KCl) reference electrode. Electrical contact with the working electrode was realized by a single sided copper tape.

All the electrochemical experiments were performed on Gamry 3000 potentiostat at room temperature and under ambient atmosphere. Reactivity was studied at open circuit (OC) and under anodic polarization in potentiostatic and potentiodynamic conditions. Potentiodynamic anodic polarization curves were recorded after 30 minutes of OC potential (E_{oc}) measurement within the potential range from 0 to +1200 mV vs E_{oc} (scan rate of 1 mV/s). Additionally, cyclic potentiostatic polarizations were performed. The cycle started after stabilizing the E_{oc} within one hour. Cycles consisted of three polarizations at +700 mV vs E_{oc} , then 3 polarizations at +1 V vs E_{oc} . Each polarization lasted 20 minutes and was followed by 15 minutes of E_{oc} measurement. Two potentials + 700 mV and +1000 mV vs OCP were chosen in order to (1) ensure a sufficient polarization to evidence visually the enhancement or not of the hydrogen evolution under anodic polarization when compared to open circuit condition and (2) verify the effect of applied anodic potential and cycling on the current stability.

Hydrogen evolution at open circuit and under anodic polarization was surveyed in situ by time lapse microscopy (TLM). HD USB microscope with 2 MP CMOS detector and a 4000 K white LED enlightenment was coupled with the electrochemical cell. Images were taken every 30 seconds during the experiments.

Raman spectroscopy was used to analyze the surface chemistry and confirm the presence of corrosion products and surface films. The presence of IL containing film was verified thanks to specific peaks typical for functional groups (**Table 4.3**)

Table 4.3. Selected Raman shift peaks of (a) [BMPyr]OAc and (b) [mPEG_nPyr]OAc.**[BMPyr]OAc (a)**

N ^o of peak (Raman shift, cm ⁻¹)	Bond	Attribution	Ref.
10 (1452)	C-H	bending, CH ₂ , pyrrolidinium	[157]
9 (1396)	COO	symmetric stretching, acetate	[158]
8 (1331)	C-H	bending, CH ₃ , acetate	[36]
7 (1317)	C-H	observed in Pyr ₁₃ I	[159]
6 (1122)	C-H	observed in Pyr ₁₃ I	[159]
5 (1061)	C-H	observed in Pyr ₁₄ Br	[160]
4 (908)	C-C	ring / stretching, C-C, pyrrolidinium / acetate	[157,158,161]
3 (825)	C-C / C-H	bending, C-C and CH ₂ , butyl	[157]
2 (735)	C-H	observed in Pyr ₁₃ I	[159]
1 (644)	COO	bending, acetate	[158,161]

[mPEG_nMPyr]OAc (b)

N ^o of peak (Raman shift, cm ⁻¹)	Bond	Type of vibration / comments	Ref.
14 (1473)	C-H	bending, CH ₂ , PEG	[162]
13 (1452)	C-H	bending / bending, CH ₂ , pyrrolidinium / PEG	[157,162]
12 (1397)	COO	symmetric stretching, acetate	[158]
11 (1336)	C-H	bending, CH ₃ , acetate	[158]
10 (1285)	C-H	bending, CH ₂ , PEG	[163]
9 (1243)	C-H	bending, CH ₂ , PEG	[163]
8 (1136)	C-O / C-C	bending, C-O, C-C, PEG	[162,163]
7 (1049)	C-C / C-H	stretching / bending, C-C / CH ₂ , PEG	[163]
6 (995)		observed in MPEG ₇ PyrTFSI	[136]
5 (913)	C-O / C-C / C-H	bending, C-O, C-C, CH ₃ acetate	[157,158,161]
4 (902)	C-H / C- C	bending / ring / stretching, symmetric ring breathing, CH ₂ , C-C, pyrrolidinium	[158]
3 (845), Broad	C-O-C	stretching, C-O-C, PEG	[164]
2 (719)	???		
1 (643)	COO	bending, acetate	[158,161]

The presence and the distribution of $\text{Mg}(\text{OH})_2$ was also studied because its formation was reported to correlate with an extensive hydrogen evolution reaction in aqueous solutions [144]. A_{1g} O-H stretch vibration (peak at 3652 cm^{-1}) was used for the $\text{Mg}(\text{OH})_2$ detection.

Raman spectroscopy and mapping were made with a Renishaw Confocal Raman Microscope InVia using red laser (HeNe, 633 nm, 17 mW power). Illumination and observation of the surface were performed through a microscope objective Leica of $\times 50$ magnification and numerical aperture (NA) of 0.75. The exposure time was 3 seconds, and 50 spectra were recorded at each point. The mapping was made in the spectral range of $3300\text{--}3900\text{ cm}^{-1}$. Typical area of one map was $7000\text{ }\mu\text{m}^2$ for Mg GF/[BMPyr]OAc- H_2O , $6000\text{ }\mu\text{m}^2$ for CP Mg/[mPEG_nMPyr]OAc- H_2O (with the step of $10\text{ }\mu\text{m}$); $7840\text{ }\mu\text{m}^2$ for AZ61/[BMPyr]OAc and AZ61/[mPEG_nMPyr]OAc (with step of $7\text{ }\mu\text{m}$). For mapping, the peak area at 3652 cm^{-1} was normalized on its maximum value, which was selected among all the results obtained on Mg GF surface immersed in [BMPyr]OAc solution.

3. Results and discussion.

3.1. In situ magnesium reactivity in two electrolytes

3.1.1. Potentiodynamic polarization

Fig. 2 (a) represents anodic potentiodynamic polarization curves for CP Mg (dashed lines) and AZ61 (solid lines) in [BMPyr]OAc- H_2O (black) and [mPEG_nMPyr]OAc- H_2O (red) electrolytes.

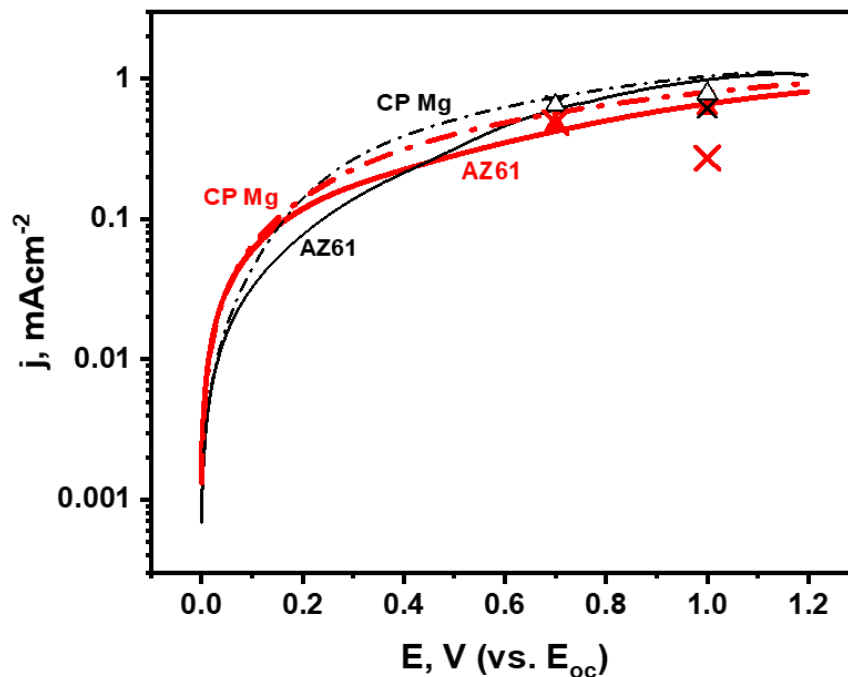


Fig. 4.2. Typical anodic polarization curves of CP Mg (dashed dot lines) and AZ61 (solid lines) in [BMPyr]OAc-H₂O (black) and [mPEG_nMPyr]OAc-H₂O (red) electrolytes. For comparison symbols indicate anodic current densities registered under the same potential at the last minutes of the third potentiostatic polarization cycle for CP Mg (triangles) and AZ 61 (crosses). The same color code indicates the electrolytes.

At potentials lower than + 200 mV vs E_{oc} the current measured for both alloys in [mPEG_nMPyr]OAc-H₂O electrolyte (red curves) is slightly higher than in [BMPyr]OAc-H₂O (black curves). This initial difference in the reactivity cannot be explained by a slight difference in conductivity, κ , which is lower for [mPEG_nMPyr]OAc-H₂O ($\kappa = 1.8 \text{ mS}\cdot\text{cm}^{-1}$) compared with [BMPyr]OAc-H₂O ($\kappa = 2.2 \text{ mS}\cdot\text{cm}^{-1}$) because of long substituted side chain in the cation for the first compound [165]. The measured currents reflect hence higher intrinsic reactivity of Mg alloys in [mPEG_nMPyr]OAc-H₂O than in [BMPyr]OAc-H₂O. At polarizations higher than + 500 mV vs E_{oc}, current seems to stabilize which can be interpreted by a formation of a surface film. Therefore, the measured currents reflect the film

properties. In this region the reactivity of both alloys in [mPEG_nMPyr]OAc-H₂O electrolyte (red curves) is slightly lower than in [BMPyr]OAc-H₂O (black curves), indicating stronger passivation in [mPEG_nMPyr]OAc-H₂O. The TLM images taken within the experiments are assembled in the videos (accelerated 100 times) presented in supplementary materials (<https://doi.org/10.1016/j.corsci.2022.110178>).

<link to the video 100x_CP Mg_ILA_pol_curve.gif>

<link to the video 100x_AZ61_ILA_pol_curve.gif>

For both alloys in [BMPyr]OAc-H₂O electrolyte almost no hydrogen gas was visible by TLM during the E_{oc} measurement, but the bubbles appeared under anodic polarization. The hydrogen evolution increased with applied potential thus demonstrating the NDE. In this water - IL mixture containing aliphatic cation and acetic anion both alloys demonstrated hence the behavior similar to that reported in aqueous solutions.

For CP Mg and AZ61 in [mPEG_nMPyr]OAc-H₂O solution (red curves in **Fig. 4.2**) the current density is lower than in [BMPyr]OAc-H₂O. It reaches +0.92 mA/cm² and +0.81 mA/cm² under anodic polarization E = 1.2 V vs. E_{oc} for CP Mg (red dashed line) and AZ61 (red solid line) respectively. The corresponding TLM images assembled in the video are also shown in supplementary materials (<https://doi.org/10.1016/j.corsci.2022.110178>).

<link to the video 100x_CP Mg_ILE_pol_curve.gif>

<link to the video 100x_AZ61_ILE_pol_curve.gif>

Surprisingly, in the [mPEG_nMPyr]OAc-H₂O mixture, which contains etheric cation and acetate anion, the gas formed on both alloys at E_{oc} measurement, but its formation decreased and even disappeared under anodic polarization. Thus, in contrast to [BMPyr]OAc-H₂O solution, the NDE was not observed in [mPEG_nMPyr]OAc-H₂O.

3.1.2. Cyclic potentiostatic polarization

The shape of polarization curve with stabilization and even slight reduction of current under anodic polarization indicated possible passivation of the interface. This means that the behavior of the system can significantly vary with time. In order to explore the stability of the system, a cyclic polarization alternating the OC reactivity with potentiostatic anodic polarization in the domain in which a possible passivation is suspected was applied (3 cycles with applied potential of +0.7 mV followed by 3 cycles with +1.0 V vs. E_{oc}). The graphs in **Figures 4.3** and **4.4** represent the evolution of the electrochemical potential (left axis, lower curve) and the current density (right axis, upper curve) during cycling of CP Mg (a) and AZ61 alloy (b) in [BMPyr]OAc- H_2O and [mPEG_nMPyr]OAc- H_2O mixtures respectively.

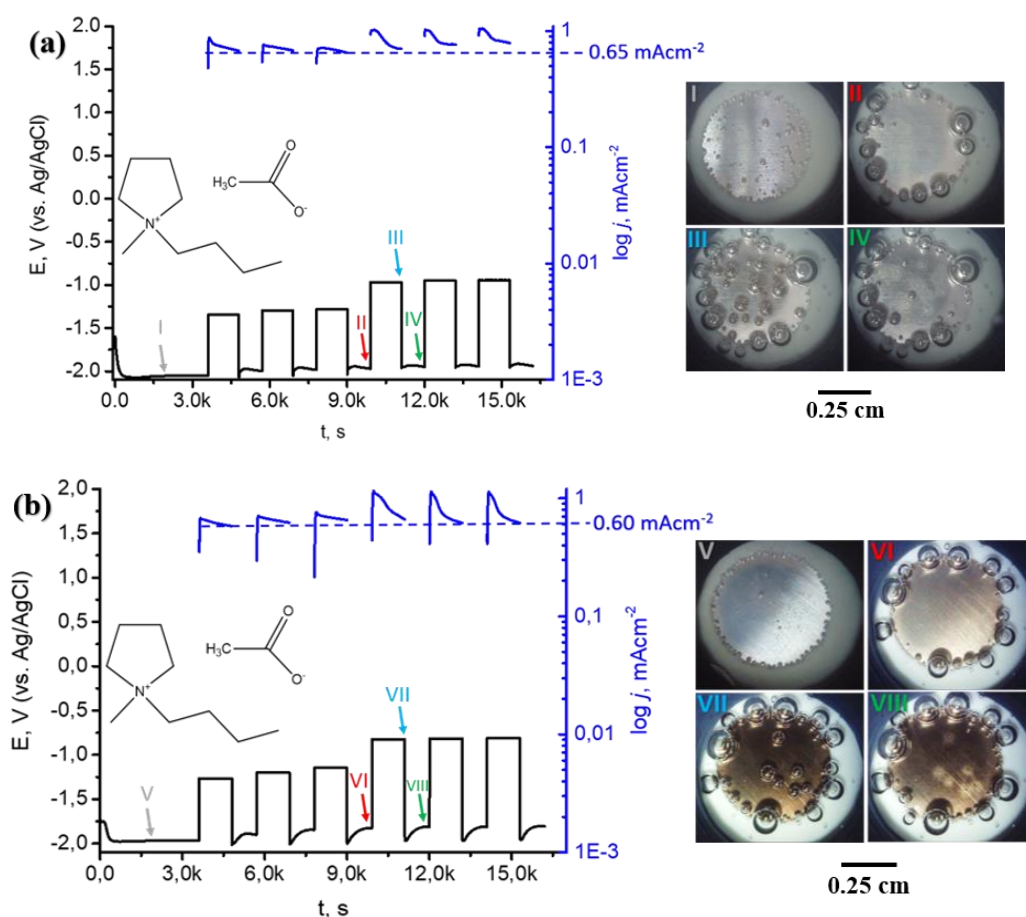


Fig. 4.3. Electrochemical response of (a) CP Mg and (b) AZ61 in [BMPyr]OAc – H_2O mixture and typical TLM images of the surface taken during the experiments. The times at which the selected images were taken is indicated by arrows (I-VIII) on the potential evolution curve.

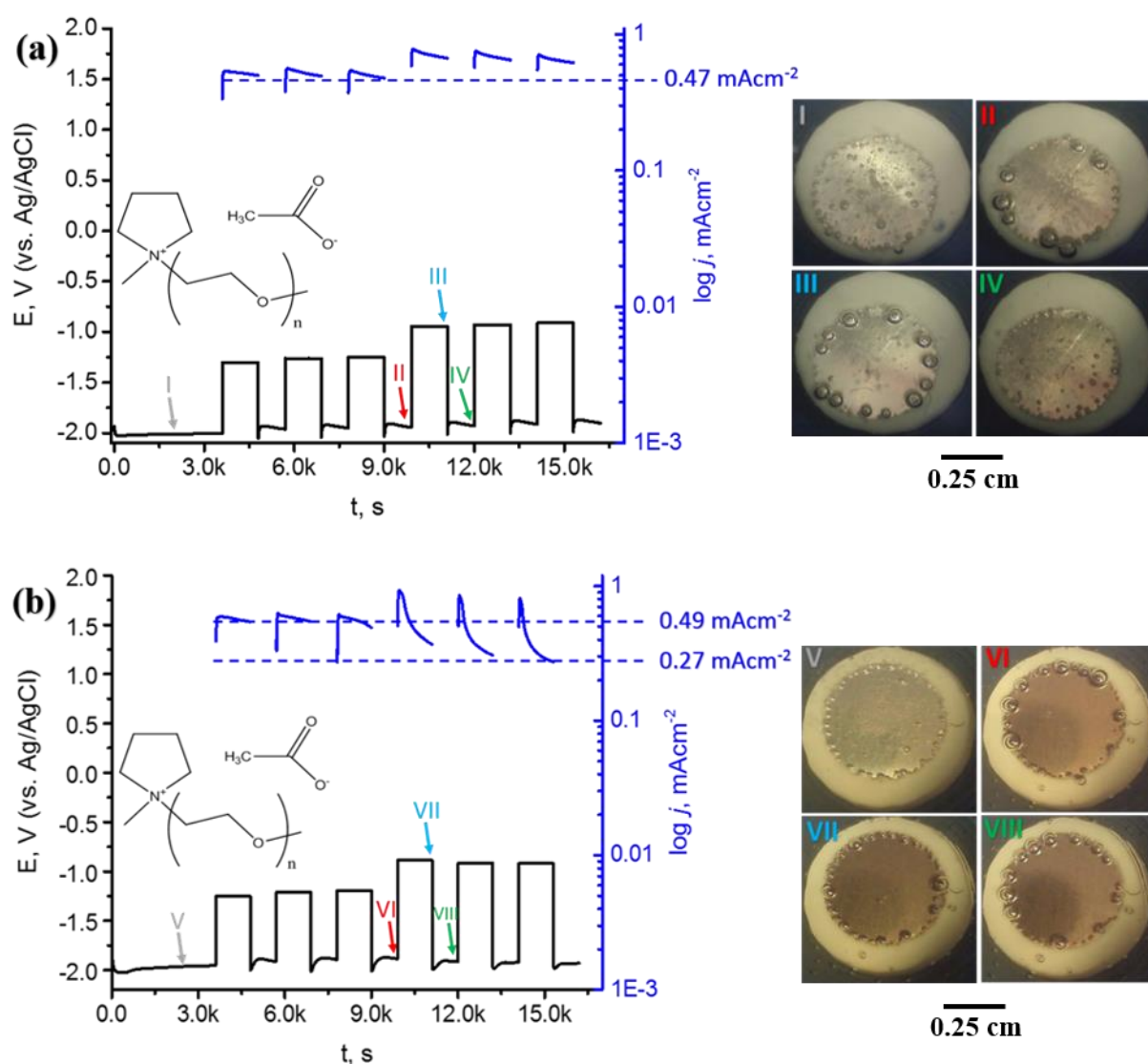


Fig. 4.4. Electrochemical response of (a) CP Mg and (b) AZ61 in [mPEG_nMPyr]OAc – H₂O mixture and typical TLM images of the surface taken during the experiments. The times at which the selected images were taken is indicated by arrows (I-VIII) on the potential evolution curve.

Some typical images of the surface, taken at the characteristic steps of the cycle, are also shown and the moments at which the images were taken are indicated by numbered arrows in the graphs. The initial evolution of the open circuit potential (E_{oc}) indicates the dissolution of an initially present passive film (expected to be MgO and Mg(OH)₂ [166,167]). Approximately within 30 minutes, the E_{oc} reaches a quasi-steady state at around -2.0 V for both materials in both electrolytes. The stream of tiny bubbles, attributed to hydrogen evolution reaction (2) [7], is also visible

during the first E_{oc} measurement (before anodic polarization) for both alloys in both electrolytes (images I and V in **Fig. 4.3** for [BMPyr]OAc-H₂O, images I and V in **Fig. 4.4 a** for [mPEG_nMPyr]OAc-H₂O).

For both materials exposed in the [BMPyr]OAc-H₂O mixture, the anodic current density stabilizes at approximately +0.6 mA/cm² under applied anodic polarization at $E = +0.7$ V vs. E_{oc} (**Fig. 4.3 a, b**). Increasing applied potential did not lead to a significant increase of the quasi-steady state current. It can be seen from the figures, that at $E = +1.0$ V vs. E_{oc} the current density stays at approximately 0.78 mA/cm² for CP Mg (**Fig. 4.3 a**) and at approximately +0.65 mA/cm² for AZ61 (**Fig. 3b**). The “quasi steady-state” currents measured in cycling experiment are compared with the currents measured in potentiodynamic polarization at the same potentials in the right graph in Fig. 2 (points shown by symbols). The values are different, and the difference evolves between two applied potentials, implying that the interface significantly changes under polarization and justifying the cyclic experiment.

Tiny bubble stream, clearly seen before polarization (**Fig. 4.3**, images I and V), is replaced by more intensive hydrogen evolution with formation of big bubbles under anodic polarization in [BMPyr]OAc-H₂O (**Fig. 4.3**, images III and VII). Once anodic polarization is relaxed, the gas formation is stopped, and it reappears only under anodic polarization for both materials (compare images III and IV in **Fig. 4.3a** for CP Mg and images VII and VIII in **Fig. 4.3 b** for AZ61). This behavior is typical for the NDE: the hydrogen evolution is enhanced under anodic polarization. To sum up, as in potentiodynamic polarization experiment, the NDE is observed for both alloys in the [BMPyr]OAc - H₂O electrolyte, which contains aliphatic substitution in the cation.

Graphs in **Fig. 4.4 a** and **4.4 b** illustrate the current densities evolution, measured under cyclic anodic polarization in the [mPEG_nMPyr]OAc - H₂O mixture. The current densities of both materials are lower in the [mPEG_nMPyr]OAc - H₂O mixture than in the [BMPyr]OAc - H₂O electrolyte. For Mg CP (**Fig. 4 a**), the current

density stabilizes at around $+0.48 \text{ mA cm}^{-2}$ under polarization at $+0.7 \text{ V vs. } E_{oc}$ and at $+0.62 \text{ mA cm}^{-2}$ at $+1.0 \text{ V vs. } E_{oc}$. These values do not significantly change with cycling. In the $[\text{mPEG}_n\text{MPyr}]\text{OAc} - \text{H}_2\text{O}$ electrolyte, tiny bubble stream is still visible on CP Mg during the open circuit measurement after polarization (**Fig. 4 a**, images II-IV). The gas evolution however significantly decreases under polarization (**Fig. 4 a**, image III). Such a behavior seems to be “normal”: cathodic hydrogen evolution decreases with anodic polarization.

As it can be seen in **Fig. 4.4 b**, for AZ61 polarized at $+0.7 \text{ V vs. } E_{oc}$ the current density reaches $+0.49 \text{ mA cm}^{-2}$ and it slightly decreases with polarization cycling. In $[\text{mPEG}_n\text{MPyr}]\text{OAc} - \text{H}_2\text{O}$ the quasi-steady state current under potentiostatic polarization differs from the values measured from the polarization curve (see comparison in **Fig. 4.2**) even more than in the electrolyte with aliphatic cations. Polarization at $+1.0 \text{ V vs. } E_{oc}$ results in significant current decrease, reaching the values as low as $+0.27 \text{ mA cm}^{-2}$ (**Fig. 4.4**) This passivation correlates with the formation of a visible dark film observed by TLM and suppression of hydrogen evolution (**Fig. 4.4**, photos VI-VIII). The illustration can be also seen in the online version of the article in the videos assembled from the Time Lapse images, taken under cycling OCP - polarization at $+1.0 \text{ V (vs. } E_{oc})$ (speed x100) (<https://doi.org/10.1016/j.corsci.2022.110178>).

<link to the video x100_Summ CP Mg ILA.gif>

<link to the video x100_Summ AZ61 ILA.gif>

<link to the video x100_Summ CP Mg ILE.gif>

<link to the video x100_Summ AZ61 ILE.gif>

To sum up, the steady state polarization cycling confirmed the results of the potentiodynamic polarization experiment. The NDE is present on both alloys in the electrolyte containing aliphatic cation ($[\text{BMPyr}]\text{OAc} - \text{H}_2\text{O}$) and it is lower in the electrolyte containing etheric cation ($[\text{mPEG}_n\text{MPyr}]\text{OAc} - \text{H}_2\text{O}$). Additionally, TLM

demonstrated the formation of a visible film under anodic polarization which coincided with the reactivity decrease. The film formation can be regarded hence as one of the possible reasons of the NDE decrease in [mPEG_nMPyr]OAc - H₂O.

3.1.3. Scratch experiment under potentiostatic anodic polarization

In order to verify if the hydrogen evolution is decreased by the formed film, an additional scratch experiment was made. After the full cycling the sample was polarized once more at + 1.0 V vs. E_{oc} for approximately 2500 s and during the polarization the surface was scratched by a plastic tip.

Fig. 5 shows the current density evolution during this additional polarization, the moment of scratching is indicated in the figure by a vertical line. Both, the current density evolution (upper figure) and the surface appearance (image I) indicate that the surface is significantly passivated during the first 1000 seconds. Immediately after scratching, the stream of bubbles appears from the damaged area (**Fig. 4.5**, image III). At the same moment, the current suddenly increases (**Fig. 4.5**, point III). However, the film restores in about 1000 seconds (**Fig. 4.5**, point IV and image IV).

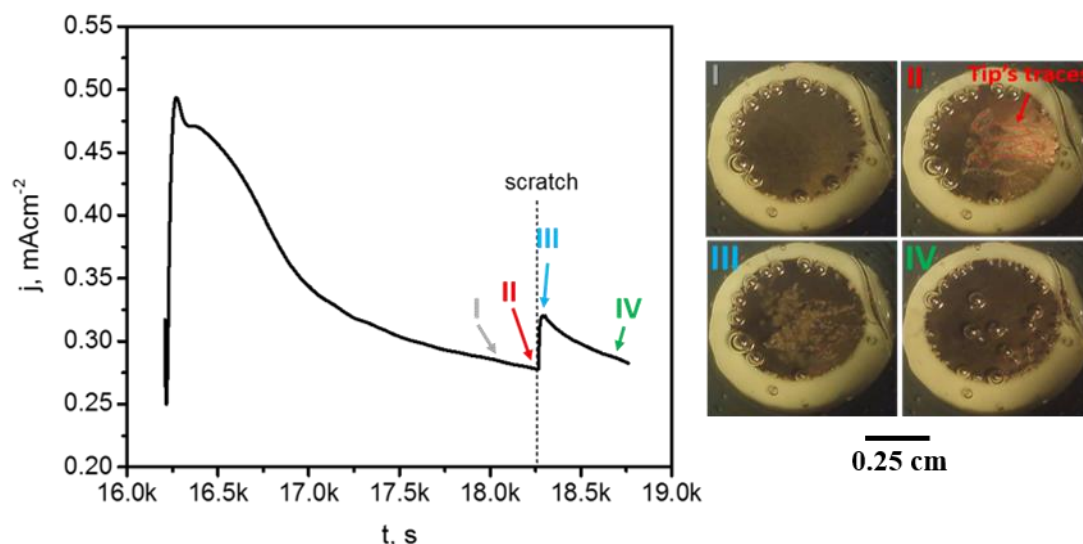


Fig. 4.5. Anodic current evolution (left) and examples of TLM images of the surface during scratch test of the surface of AZ61 in the [mPEG_nMPyr]OAc – H₂O mixture during potentiostatic polarization at 1 V vs. E_{oc}. The moments, at which the selected images were taken, are indicated on the curve by arrows (I-IV).

Morphology of the reacted area under the film demonstrated intergranular attack (see **Appendix 1, Fig. 3S**). Interestingly, if the samples after the experiment were rinsed with water, the film and related color change disappeared. The surface became brilliant but in long contact with air the humid surface darkened. The film seems hence to be protective but not strongly adherent.

Similar results of the scratch experiment (cathodic reactivity in the scratch under anodic polarization, which healed with time) were obtained for CP Mg. The low adherent film formed and healed in scratch experiments under anodic polarization of Mg and its alloys. This film seems hence to decrease hydrogen evolution reaction.

3.2. Magnesium surface state from Confocal Raman microscopy.

The wet surfaces after the potentiostatic cycling experiments were characterized by vibrational spectroscopy. The advantage of vibrational spectroscopy in the case of the low-adherent and easily washable films observed in the present work is that it allows to analyze wet surfaces, which composition could be very different from the dry state analyzed by many high vacuum surface analytical technics (X-ray

photoelectron spectroscopy, electron microscopy, time of flight secondary ion mass-spectrometry, ...). Typical confocal Raman spectra recorded in [BMPyr]OAc-H₂O and in [mPEG_nMPyr]OAc-H₂O electrolytes are shown in **Figs. 4.6 a** and **4.6 b** respectively. Reference spectra of the unreacted water-IL mixtures are shown in blue. The bulk spectra of ILs after the reaction did not change and are not shown. All the characteristic for the electrolyte's peaks are clearly visible on the surface, however, the positions of the characteristic peaks of acetate and etheric groups are shifted if compared with the initially used ILs-water solution, especially on the surface of AZ61 (areas shown by shadow in **Fig. 4.6**). This indicates some modifications in the chemical environment of the selected groups which can be interpreted as bond formations at the interface or in the film. The shifts are different for CP Mg and AZ61. The latter can be explained by the formation of different products because of possible participation of alloying elements (Al, Zn) in the film formation. Indeed, both Al and Mg are dissolved from an alloy in aqueous environment and can participate in the formation of the surface film [48,168,169] and, hence, also participate in the formation of complexes with organic groups.

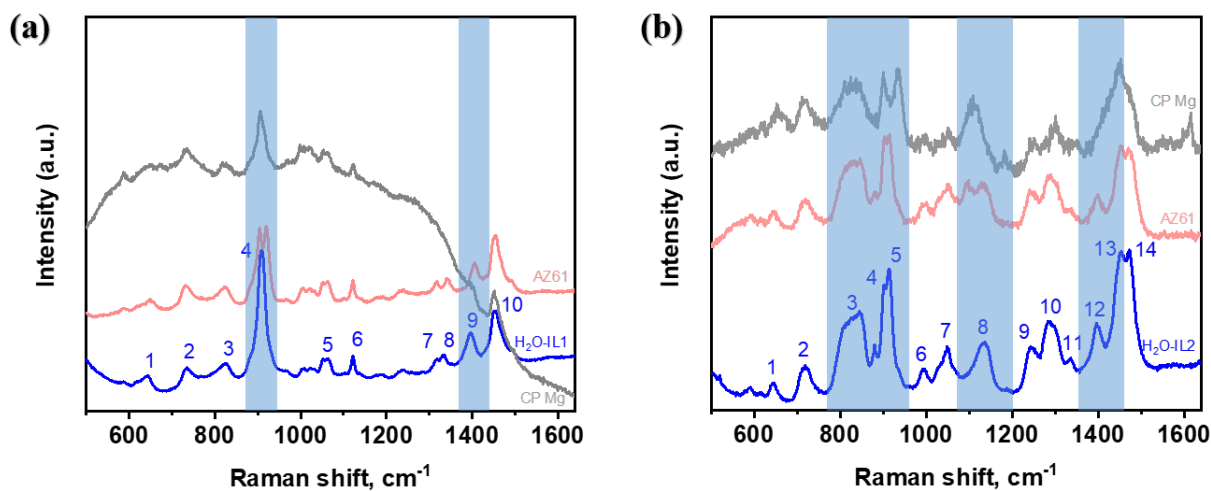


Fig. 4.6. Typical Raman spectra recorded on the surfaces of CP Mg and AZ61 after electrochemical experiment in [BMPyr]OAc – H₂O (here IL1) (a), [mPEG_nMPyr]OAc – H₂O (here IL2) (b). Red: spectrum recorded on the surface of AZ61, grey: spectrum recorded on the surface of CP Mg, blue: spectra of ionic liquids – H₂O mixtures. Zones, characteristic for the Raman shifts of acetate ion and C-O-C groups (see table 3) are shown in blue shadowing.

Some fluorescent background was present on all wet surfaces after the electrochemical experiment, however strong fluorescence between 500 and 1400 cm^{-1} appeared mainly on the surface of CP Mg in [BMPyr]OAc - H_2O . Generally, fluorescence indicates conjugated organic systems or metallic complexes. The chemistry of the ILs ions is not conjugated so the hypothesis of metallic complexes seems to be logical. The intensity of the fluorescence is proportional to the concentration so the highest fluorescence of CP Mg in [BMPyr]OAc - H_2O is coherent with the highest anodic currents observed in this system and the expected highest quantity of leached Mg-ions. Leached Mg ions can either stay in a soluble form or participate in the surface film formation. In the presence of water, the film is expected to contain not only the complexes with the organic molecules but also magnesium oxides and hydroxides.

Confocal Raman spectra (**Fig. 4.7 a, b**) in the region of O-H vibrations of $\text{Mg}(\text{OH})_2$ demonstrated that magnesium hydroxide formed on the surface of CP Mg but not on the AZ61 in both water-IL mixtures. Mapping of large surfaces confirmed the homogeneous distribution of $\text{Mg}(\text{OH})_2$ on CP Mg (**Fig. 4.7 a, b**) and its absence on AZ61 (**Fig. 4.8 a, b**) after the electrochemical experiments in both electrolytes. The presence of $\text{Mg}(\text{OH})_2$ on CP Mg and its absence on AZ61 in both electrolytes and its absence on AZ 61 was confirmed by ATR-FTIR spectra (**Appendix 1, Figs. S1, S2**).

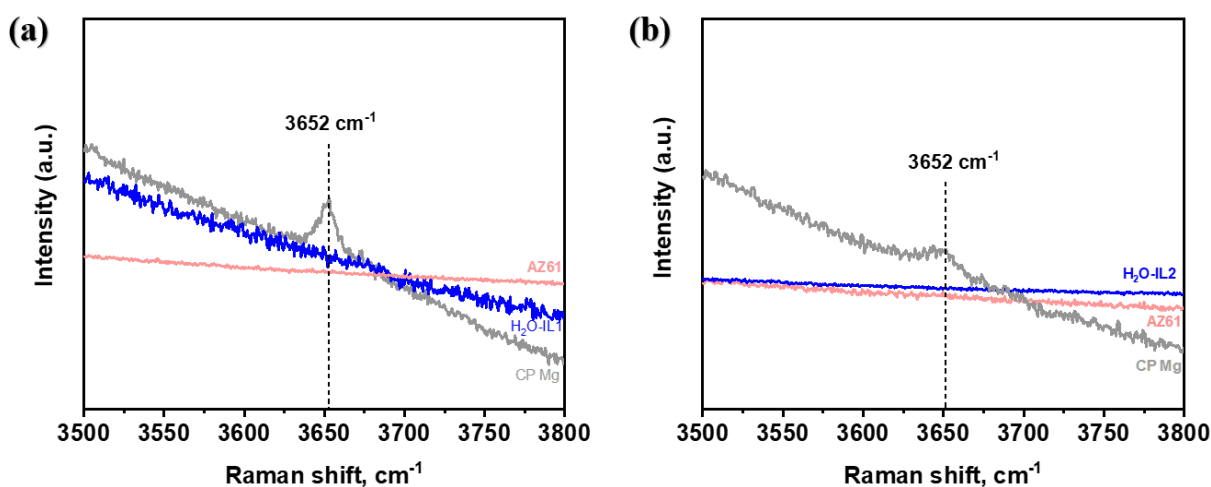
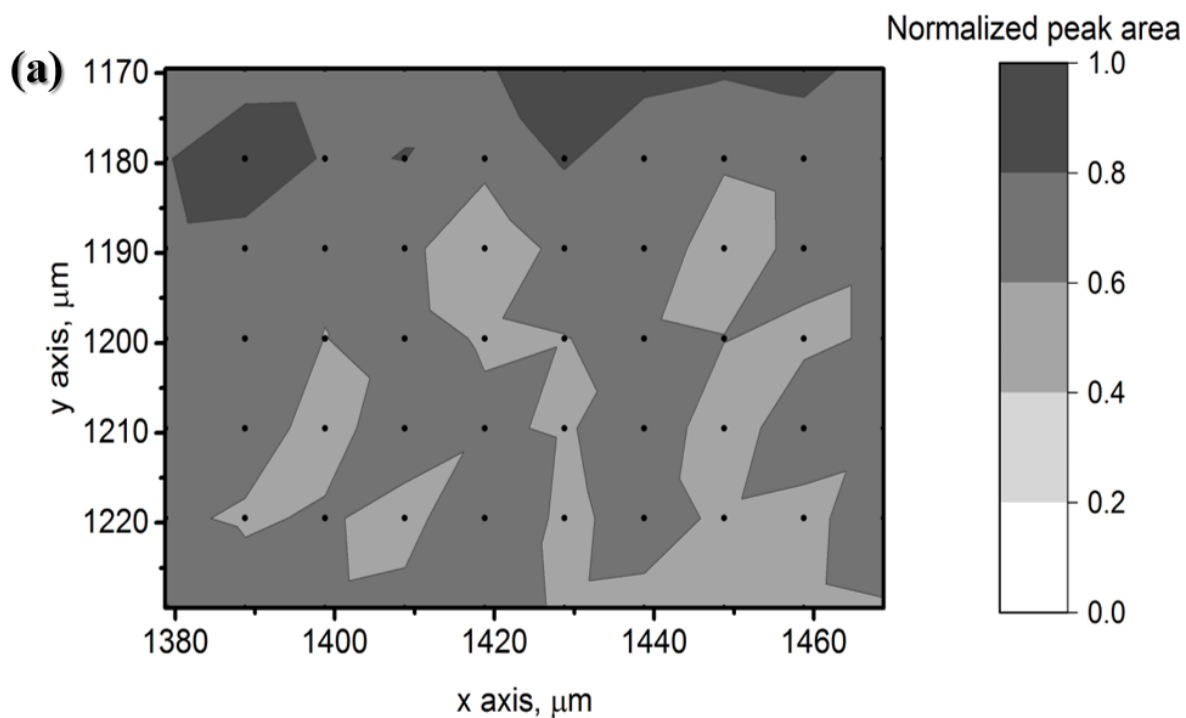


Fig. 4.7. Typical Raman spectra in the region of A_{g1} O-H ($Mg(OH)_2$) vibration recorded on the surfaces of CP Mg and AZ61 after electrochemical experiment in (a) [BMPyr]OAc – H_2O mixture (here IL1) and (b) [mPEG_nMPyr]OAc – H_2O mixture (here IL2). Red: spectrum recorded on the surface of AZ61, black: spectrum recorded on the surface of CP Mg, blue: spectra of the electrolyte (IL – H_2O mixture).



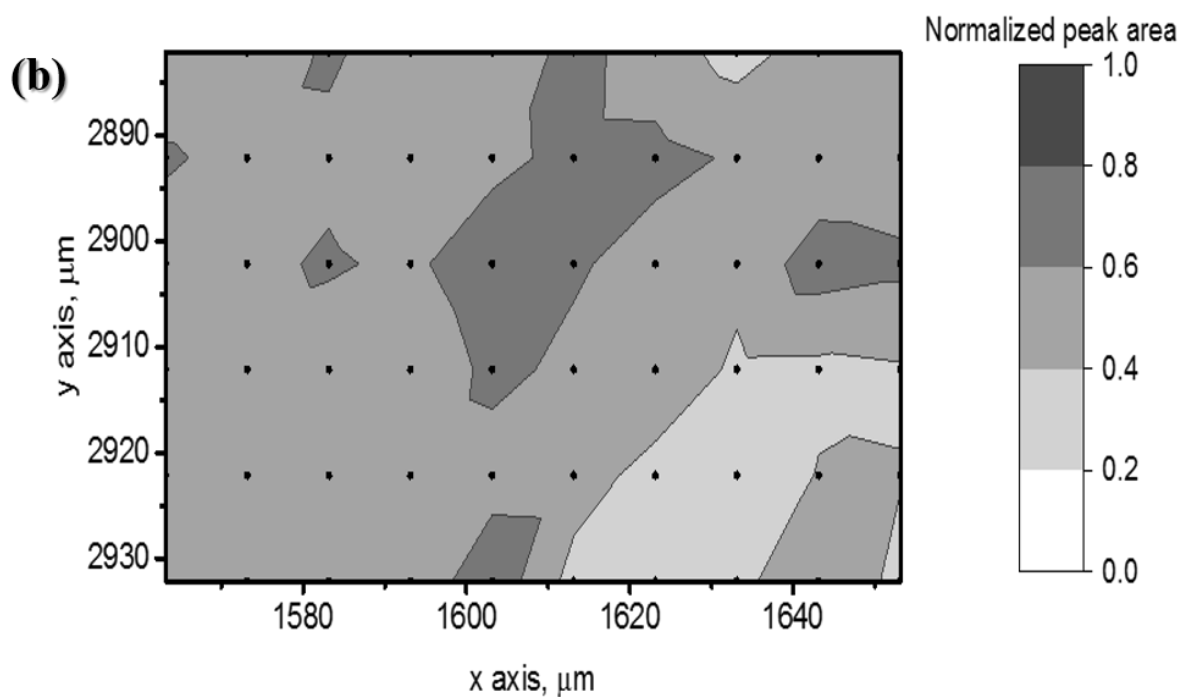


Fig. 4.8. Confocal Raman mapping of 3652 cm^{-1} peak area (normalized) on the surface of CP Mg after polarization in (a) [BMPyr]OAc- H_2O and (b) [mPEG_nMPyr]OAc- H_2O .

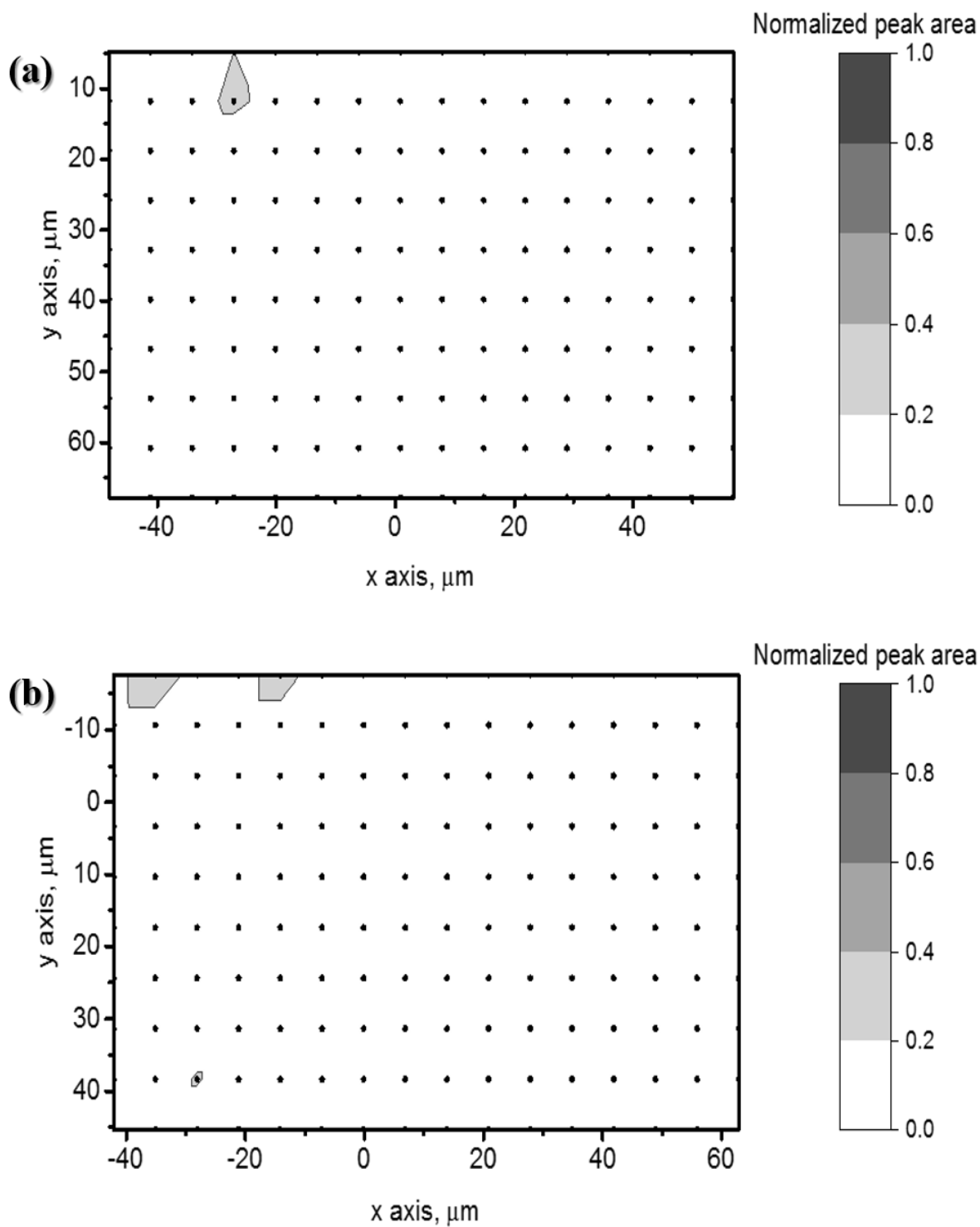


Fig. 4.9. Confocal Raman mapping of 3652 cm⁻¹ peak area (normalized) on the surface of AZ61 after polarization in (a) [BMPyr]OAc-H₂O and (b) [mPEG_nMPyr]OAc-H₂O.

To sum up, acetate was present on the surfaces of both alloys after exposures in both electrolytes, while Mg(OH)₂ film formation correlated with the alloy

composition but did not depend on the used electrolyte. Neither the action of the acetate, nor the presence of $\text{Mg}(\text{OH})_2$ film cannot hence explain the differences observed for magnesium reactivity in two electrolytes. The presence and the absence of the NDE should be hence correlated with the nature of the organic cation – clear NDE in the mixture with aliphatic cation and no NDE observed in the mixture with etheric cation. The shifts of the etheric peaks positions in the Raman spectra favors the hypothesis that these groups are responsible for the modification of the surface film properties. Further detailed surface characterization is in progress and will be published soon.

3.3 Discussion: hydrogen evolution on Mg in hybrid water – IL electrolytes

Our results demonstrate that for both CP Mg and AZ61 the hydrogen evolution is strongly enhanced by anodic polarization in the $[\text{BMPyr}]\text{OAc} - \text{H}_2\text{O}$ electrolyte and reduced (or even suppressed) in the $[\text{mPEG}_n\text{MPyr}]\text{OAc} - \text{H}_2\text{O}$ solution. The hydrogen evolution in both mixtures is expected to occur by water reduction (reaction (2)). The morphology of hydrogen bubbles in water – IL mixtures, illustrated in **Figs. 4.3-4.5** and in the supplementary materials (videos) (see online version of the article), can be interpreted on the basis of the work [65], which described the hydrogen bubbles formed on Mg corroding in aqueous solutions. Initial (before anodic polarization) fine bubbles “hydrogen stream” observed on both freshly polished alloys during the first immersion in both electrolytes seems to be similar with the bubbles observed on corrosion front in aqueous solutions on the surface areas free from the surface film. This “hydrogen stream” disappeared after the anodic polarization cycle, indicating a probable film formation under anodic potential. Big isolated bubbles grown under anodic polarization in $[\text{BMPyr}]\text{OAc} - \text{H}_2\text{O}$ electrolyte look similar to the observed on the cathodic sites (intermetallics) in aqueous electrolytes, supporting the idea of cathodic activation under anodic polarization. Thus, the observed morphological features indicate that the anodic hydrogen evolution on Mg in the mixed electrolytes is still cathodically activated.

In [mPEG_nMPyr]OAc-H₂O, the behavior differs between CP Mg and AZ61 alloys. On CP Mg medium size bubbles grow on extended cathodically active corroded regions during E_{oc} measurements and their growth decreases under anodic polarization. Hydrogen evolution on AZ61 is almost completely suppressed after the first anodic polarization, which is coherent with the formation of a surface film. The anodic current evolution also shows different trends: on AZ61 it decreases with polarization potential and polarization time, which is coherent with the growth of a surface film, limiting mass and/or charge transport, but on CP Mg it slightly increases with polarization potential, which is not expected for the diffusion limited systems. Such a difference can be interpreted as an indication of multiple mechanisms which can be involved in the inhibition of the water reduction on Mg alloys by [mPEG_nMPyr]OAc.

Our results do not permit to verify all the discussed in the literature mechanisms of NDE in aqueous electrolytes, which have been recently reviewed for instance in the work [13]. They could however help to propose the first hypotheses about which mechanisms could be blocked by ILs and how it could occur. **Table 4.4** displays the summary of NDE features obtained in this work.

Table 4.4. Summary of NDE features.

Material / electrolyte	anodic hydrogen	Mg(OH) ₂ on the surface
CP Mg / [BMPyr]OAc-H ₂ O	Yes, more than at OC, big bubbles	Yes
CP Mg / [mPEG _n MPyr]OAc-H ₂ O	No (except residual from OC)	Yes
AZ61 / [BMPyr]OAc-H ₂ O	Yes, more than at OC, big bubbles	No
AZ61 / [mPEG _n MPyr]OAc-H ₂ O	No	No

No NDE was found on the CP Mg and AZ61 immersed in [mPEG_nMPyr]OAc-H₂O. However, the same alloys behave differently in [BMPyr]OAc-H₂O. Hence, the

HER blocking cannot be considered as a consequence of the presence of carboxylic anion, expected from the knowledge accumulated in aqueous corrosion, and it is significantly affected by the mPEG-containing cation (further mPEG in the text). Clearly, because of the presence of $\text{Mg}(\text{OH})_2$ on the surface of CP Mg in both cases, with and without NDE, if the enhanced hydrogen evolution is considered by galvanic coupling with catalytic corrosion products, this mechanism is not the one which is inhibited by mPEG group. Similarly, the Fe impurities content [34,40] is very different in two materials, but the mPEG-containing cation decreases NDE for both of them. There is neither any reason that the presence of mPEG could modify the formation of the hydrides (MgH_2 [27,35]) under the interface. Possible interactions between etheric mPEG group and Mg-ions have previously been reported in the literature [136,137]. The inclusion of Mg-ions in the mPEG-containing IL film could be regarded as “incomplete film mechanism” [26], however, none of our results could support the oxidation state of Mg(I) in the formed complexes. We could not confirm or exclude other theories, but the shifts in the IL groups positions in Raman spectra of the Mg / electrolyte interface still suggests that after anodic polarization the chemical environment of mPEG containing groups close to the metallic surface is modified. The later could probably lead to a formation of a conductive film, as it was in the work [135], levelling the potential distribution over the surface. The fact that hydrogen bubbling increases on CP Mg but not on AZ61 when the potential is returned to the OC condition after the anodic polarization indicates that the nature of the film is affected by the presence of Al and/or Zn and that probably other factors are important for the NDE inhibition. Weak adherence of the film (easily washed by water and removed by a plastic tip) also requires further understanding. Finally, not only the surface, but the water activity in the electrolyte can be affected by possible hydrogen bonds formation with acetic [18] and etheric [19] groups. The exact nature of the surface films formed on CP Mg and AZ61 in two electrolytes and the effect of the IL on water activity will be explored in our further works.

Conclusions

In this work, the reactivity of commercially available Mg alloys (CP Mg and AZ61) in hydrophilic room temperature ionic liquids mixed with water was investigated. Results revealed that Mg alloys could dissolve in these electrolytes at reasonable potential and relatively high current. Negative difference effect was observed for both alloys exposed in [BMPyr]OAc-H₂O electrolyte. However, in [mPEG_nMPyr]OAc-H₂O the NDE was suppressed, and hydrogen evolution decreased on CP Mg. Hydrogen evolution was completely blocked on AZ61 by the low adherent passivating film which formed and healed under anodic polarization. The nature of this film should be deeper understood.

Raman microscopy of the surface after exposure in both electrolytes confirmed that chemically bound acetate is present on the surface, while homogeneously distributed Mg(OH)₂ film formed on CP Mg but no Mg(OH)₂ was detected on AZ61 independently of the used electrolyte. This indicates that in the water-IL mixtures the presence or not of the NDE cannot be correlated neither with the action of the acetate anions nor with the presence of corrosion products. In contrast, NDE seems to be present if the IL cation contains aliphatic chain but suppressed if the IL cation is substituted with the etheric chain.

Thus, the interaction between magnesium and water in water-IL mixtures seems to be different than in inorganic aqueous solutions. Alternative hypotheses including a formation of a conductive film leveling the interface potential and possible water activity reduction in the presence of PEG-containing cation can be advanced and need verification. However, the detailed role of the etheric-substituted cation in water – IL mixtures should be also further studied.

Chapter 4:

Influence of PEG-containing cation on molecular state of water in water – acetate based ionic liquids mixtures

This chapter answers the questions “How does water interact with cation and anion in selected hydrophilic RTILs (with and without PEG-substitution in the cation)? How do these interactions influence basic properties of the electrolyte?”

*The results of this chapter are prepared in the form of article submitted to
Journal of Molecular Liquids.*

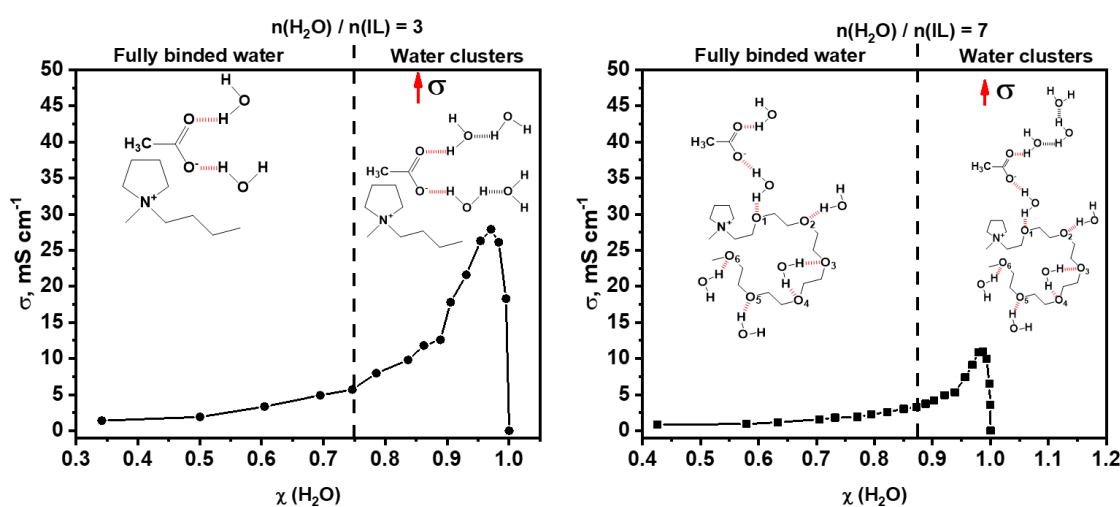
Influence of PEG-containing cation on molecular state of water in water – acetate based ionic liquids mixtures.

D. Kurchavov^a, U. Rustambek^a, M. Haddad^b, A. Ottochian^c, G. Lefèvre^a, I. Ciaffini^c, V. Lair^a, P. Volovitch^{a*}

^a Chimie ParisTech, PSL University, CNRS, Institut de Recherche de Chimie Paris (IRCP), F-75005 Paris, France

^b PSL University, Chimie ParisTech, CNRS UMR 8060, Institute of Chemistry for Life and Health Sciences, CSB2D team, 75005 Paris, France

^c PSL University, Chimie ParisTech, CNRS UMR 8060, Institute of Chemistry for Life and Health Sciences, TCM team, 75005 Paris, France



Keywords: acetate ionic liquids, PEGylated, aliphatic, water, ATR-FTIR, MD

Abstract

Two acetate ionic liquids (ILs) based on N-methyl-pyrrolidinium cation with etheric (mPEG_n-) and aliphatic (butyl-) substitutions were synthesized. Electrochemical potential windows (EPW) were measured on a glassy carbon electrode. The results revealed that introduction of etheric group in the IL structure constricts the EPW if compared with aliphatic substitution. The binary mixtures of ILs with water were characterized by Raman, Attenuated Total Reflectance Fourier Transform Infrared (ATR-FTIR) spectroscopies and Molecular Dynamics (MD) simulations. Intermolecular hydrogen bonds between acetate anions and etherically substituted cations have been found. Detailed analysis of molecular state of water in these mixtures by ATR-FTIR and MD simulations indicates that water clustering process

starts when ratio $n(\text{H}_2\text{O}) / n(\text{IL})$ is more than 3 for [BMPyr]OAc and more than 7 for [mPEG_nMPyr]OAc. The evolution of specific conductivity of water-ILs mixtures well correlates with modification of water state.

1. Introduction

Room temperature ionic liquids (RTILs or ILs) are compounds which entirely consist of ions and exist in liquid state at the temperatures below 100 °C. They have attracted enormous interest from researchers because of a wide range of possible applications, from organic synthesis and catalysis to analytical chemistry and electrochemical applications thanks to a high solubility of a wide range of inorganic, organic and polymeric materials in them [101,170,171]. One of the key employments of RTILs is as an electrolyte for electrochemical applications [95,96] because they improved electrochemical and thermal stability [16,89,97], have relatively high conductivity [9], low volatility [99] and are not flammable [100]. The disadvantages of RTILs as electrolytes are their relatively high viscosity and relatively narrow liquid state temperature [172].

Many physico-chemical RTIL properties, for example, conductivity or viscosity can be adjusted by varying cations and anions [88–92]. This could be however unsuitable for task-specific RTILs which should contain special functional groups in the cation or anion. In this case another suitable approach to improve RTIL properties is an addition of conventional organic solvents or water. Indeed, viscosity decreases, and room temperature conductivity increases even by slight dilution of RTILs with common organic solvents [17,155,173]. Nevertheless, considering RTILs applications as “green” solvents, their dilution with toxic organic solvents seems to be undesirable [174]. Water, as an environmentally friendly solvent, looks more attractive, especially for the applications in water-based systems and biochemistry [104,175].

The influence of water content on physicochemical properties of RTILs was studied in numerous works. It has been shown that a higher water fraction decreases

viscosity [110–112]. It was also reported that conductivity of RTIL-water mixtures increases but the electrochemical potential window (EPW) reduces [112,113] with water content. Water decomposition can be however suppressed if water electrochemical reactivity is reduced either by its low concentration or by strong interactions with IL, for example, intermolecular hydrogen bonding [114,115]. Understanding the interactions between water and ILs is therefore important for numerous applications. To achieve this understanding, the nature of IL is primordial.

In relation with water contents, two types of ILs can be distinguished: 1) hydrophobic ILs which pick up minimum of water and saturate at low water concentration; 2) hydrophilic ILs which are infinitely miscible with water [108]. Using Molecular Dynamic (MD) simulations it was established that their hydrophilicity is determined by the nature of ions and interactions between them [121–124]. Briefly, the interactions between water and IL anions and between IL anions and cations play crucial role in the hydrophilicity [121,125,176,177]. In the work of Koishi, four ILs based on 1-butyl-3-methylimidazolium (BMIm^+) cation with two hydrophilic (NO_3^- and BF_4^-) and two hydrophobic (PF_6^- and $(\text{CF}_3\text{SO}_2)_2\text{N}^-$) anions in the mixture with water were simulated [126]. The results revealed that nitrate and tetrafluoroborate anions connected with water as anion-water-anion through hydrogen bonds and H_2O molecules did form water-clusters. But in PF_6^- and $(\text{CF}_3\text{SO}_2)_2\text{N}^-$ ILs water was rather bonded with itself. These results are in agreement the with experiments of Dominguez-Vidal et al. [127]. It was also reported that long aliphatic tails in cations form nonpolar domains in solution and increase hydrophobicity [125].

Water – IL anion interactions have been successfully studied by nuclear magnetic resonance (NMR) [112,178], small-angle X-ray scattering and small-angle neutron scattering (SAXS/SANS) [179], infrared (ATR-IR, FTIR) [116,119] and near infrared spectroscopies (NIRS) [118]. Although in water/IL mixtures water can form nanoheterogeneity (called “water-pockets”) in water-rich regions and water-clusters at high water concentration [179], they also form intermolecular hydrogen

bonds with anions of ILs. These water-anion hydrogen bonds can be even stronger than cation-anion interactions [112,116–118], e. i. with anions containing fluorine ($F\cdots H-OH$ bond with BF_4^- , SbF_6^- , PF_6^- , etc) and with oxygen atoms in the anions ($O\cdots H-OH$ bond with NO_3^- , ClO_4^- etc.). Kazarian et al. [116] studied ILs with water absorbed from air (low concentrations) using ATR-IR spectroscopy and reported that water molecules are present mostly not in a self-associated state but form H-bonded complexes with two anions (anion $\cdots HOH\cdots$ anion). Strong H-bonding was reported between water and $CF_3CO_2^-$ anion due to its high basicity. Water molecules can exist in double donor (DD) state, with the ratio one water molecule for two molecules of IL (1 H_2O : 2 IL), and a single donor (SD, with one water molecule per one IL molecule: 1 H_2O : 1 IL) state [119], which was also confirmed for hydrophilic ionic liquids [107]. Recently, some evidence of hydrogen bonds formation between water and hydrophilic 1-butyl-1-methyl-pyrrolidinium cation were reported [128]. The amount of free water (which does not form hydrogen bonds with ILs moieties) in imidazolium ionic liquids was reported to depend on the temperature, concentration of ILs and nature of anions [118]. The authors reported that 1-3-dimethylimidazolium chloride has the greatest capacity to bind the water molecules. *Ab initio* MD revealed, that at moderate water content in mixtures of 1-ethyl-3-methylimidazolium acetate with water [129], acetate anions are coordinated to the same water molecule forming bridges ($AcO^-\cdots HOH\cdots OAc$).

To sum up, although the effect of RTIL anions on the water state in water-RTIL mixtures was a subject of thorough investigations, water-cation interactions are not intensively studied. The fact that water interactions with the cation of RTIL are usually disregarded can be due to the expected weaker hydrogen bonding of water with organic cations than with anions. The situation can be however different if hydrophilic groups, for example, etheric groups in the substituted chains in the cations, are present. To the best of our knowledge, no systematic study of the effect of hydrophilic groups in the cation on the water - RTIL interactions has been published. Involving hydrophilic groups into the structure of cations of ILs can be

however very interesting because it can improve water absorption capacity. Design of new water-miscible RTILs can hence be improved by tailored modification of the substituted chains in IL cation. One of the promising candidates can be the cation with a poly-etheric groups containing substitution, which can form intermolecular hydrogen bonds with water [180]. Polyethylene glycols (PEG) are considered as biodegradable and biocompatible compounds which are widely used in cosmetics and pharmaceutical industry and in nanochemistry [181–183]. For electrochemical applications polyetheric chains can be interesting because they improve transport properties of ILs [184] and can complex metallic cations, such as Li^+ [164,184], Mg^{2+} [136–138] and Na^+ [185]. Understanding interactions of PEG-substituted RTIL cations with water in water –RTIL mixtures and the effect of water content in the mixture on these interactions is hence of high interest for smart design of new water-miscible RTILs with desired physico-chemical properties.

Thus, the main objective of this work is to explore the influence of PEG-substituted cation in N-methyl-pyrrolidinium (MPyr) acetate (OAc) ILs on the molecular state of water in water – IL mixtures from experimental and theoretical points of view. This is achieved via several intermediate goals:

a) **to synthesize** two acetic ionic liquids with hydrophilic poly-etheric ($-\text{O}-\text{CH}_2-\text{CH}_2-$)_n) substituted cation ($[\text{mPEG}_n\text{Pyr}]\text{OAc}$), further named as etheric IL or **ILE**) and hydrophobic aliphatically (butyl ($-\text{C}_4\text{H}_9$)) substituted cation ($[\text{BMPyrr}]\text{OAc}$, further named as aliphatic IL or **ILA**) ;

b) **to characterize** their electrochemical properties, particularly specific conductivity and electrochemical potential window;

c) **to compare the effect of water content** on the molecular state of water in water-RTIL binary mixtures in a wide composition range (from several % to more than 90 % of water) using vibrational spectroscopies;

d) to provide MD simulations of pure ionic liquids and their mixtures with water in order to understand the effect of mPEG_n-substitution in the cation on the molecular state of water in the mixtures.

2. Experimental

2.1. Synthesis of RTILs

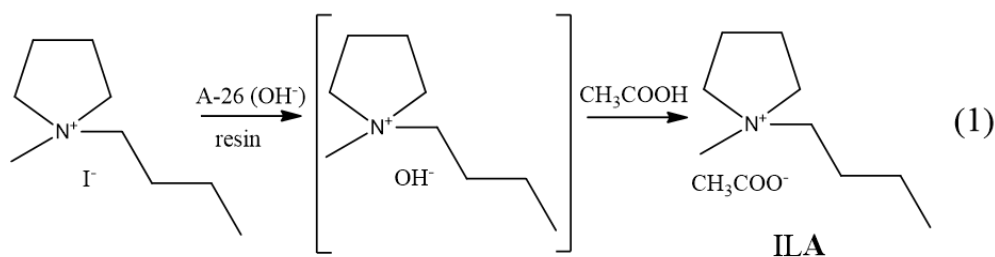
2.1.1. Materials for synthesis

The following commercially available compounds were used for synthesis: Methoxy-terminated poly(ethylene glycol) (mPEG₇, CAS no. 9004-74-4, M.W. 350), 4-toluenesulfonyl chloride (TsCl, CAS no. 98-59-9, 99%), 4-dimethylaminopyridine (DMAP, CAS no. 1122-583, 99%), triethylamine (CAS no. 121-44-8, 99.5%), anhydrous potassium iodide (KI, CAS no. 7681-11-0, 99%), N-methylpyrrolidine (CAS no. 120-94-5, 97%), silver nitrate (AgNO₃ CAS no. 7761-88-8, ≥99%), ethyl acetate (CAS no. 141-78-6, ≥99.5), toluene (CAS no. 108-88-3, 99.8%), 1-butyl-1-methyl-pyrrolidinium iodide (CAS no. 56511-17-2) supplied by Sigma-Aldrich. Acetone (CAS no. 67-64-1), chloroform (CAS no. 67-66-3), methanol (CAS no. 67-56-1), cyclohexane (CAS no. 110-82-7), acetic acid (CAS no. 64-19-7, ≥99.7%) supplied by VWR. All chemicals were used as received.

2.1.2. Synthesis procedure

Synthesis of 1-Butyl-1-methyl-pyrrolidinium acetate (ILA) is presented in **Scheme 5.1**. Four-step synthesis of 1-poly(ethylene-glycol)-1-methyl-pyrrolidinium acetate (ILE) is shown in **Scheme 5.2**.

Synthesis of ILA.



Scheme 5.1. Synthesis of [BMPyr]OAc (ILA).

Aqueous solution of 1-butyl-1-methyl-pyrrolidinium iodide (6 g, 0.022 mol) was passed dropwise through a chromatography column packed with Amberlyst A-26 hydroxide form (40 g). One equivalent amount of acetic acid was added to the resulting solution. Neutral pH was controlled with pH meter. The water was removed by evaporation under vacuum using rotary evaporate at 60 °C. The iodide content of ionic liquid was determined by means of 0.1 M AgNO₃ aqueous solution (solubility of AgI is 3·10⁻⁷ g/100mL at 20 °C). Hence, the concentration of I⁻ in corresponding ionic liquids revealed to be inferior to this value.

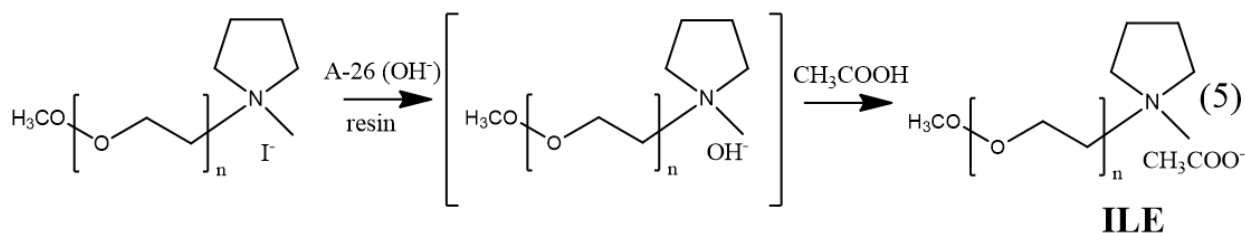
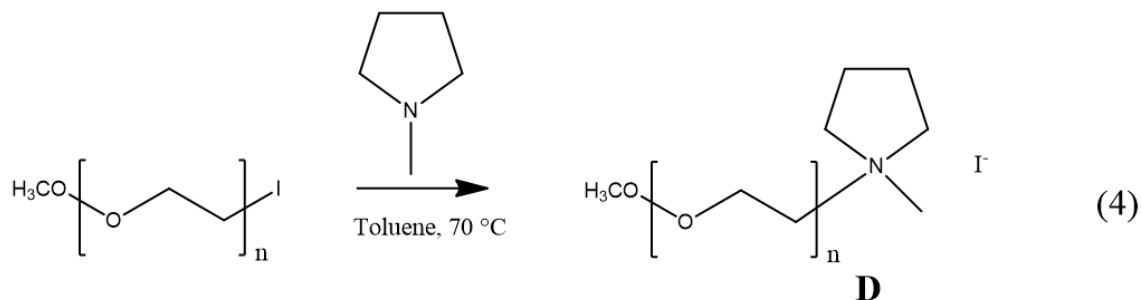
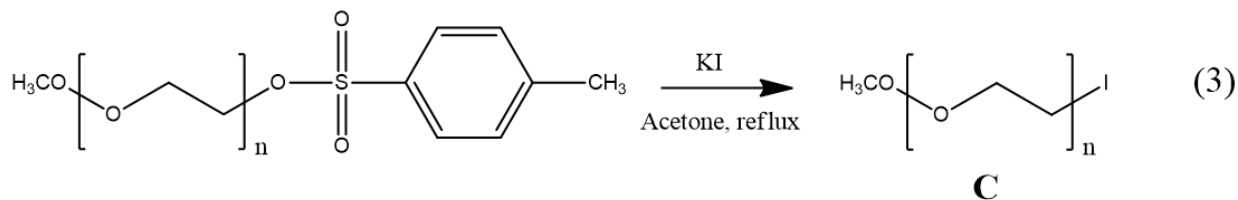
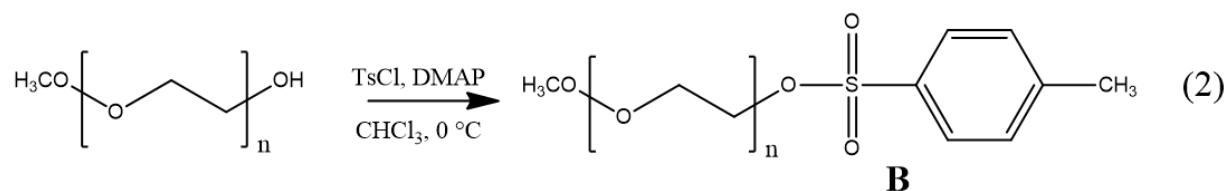
The structure of compound ILA, [BMPyr]OAc was confirmed by ¹H, ¹³C-Nuclear Magnetic Resonance (NMR) and high resolution mass spectrometry (HRMS). The positive mass over charge ratios m/z detected in atmospheric pressure chemical ionization (APCI-Orbitrap) (+) were: m/z = 202.1807 (C₁₁H₂₄NO₂⁺), m/z = 142.1590 (C₉H₂₀N⁺). The detected NMR signals are listed below:

¹H NMR (400 MHz, CDCl₃) δ 3.73 – 3.51 (br m, 4H), 3.43 – 3.37 (br m, 2H), 3.13 (s, 3H), 2.22 – 2.11 (br m, 4H), 1.80 (s, 3H), 1.70 – 1.60 (br m, 2H), 1.40 – 1.27 (m, J = 36 Hz, 2H), 0.91 (t, J = 8 Hz, 3H)

¹³C NMR (101 MHz, CDCl₃) δ 176.6, 77.4, 63.9, 63.7, 48.1, 25.7, 25.4, 21.5, 19.7, 13.6

Water content in as synthesized ILA was 4.44 wt. % as determined by Karl Fischer (KF) coulometric titration (C20, Mettler Toledo).

Synthesis of ILE (**scheme 5.2**). General procedure was already published in the literature [140,141].



Scheme 5.2. Synthesis of [mPEG_nMPyr]OAc (**ILE**) and [mPEG_nMPyr]ClO₄ (**ILEP**)

The first step (reaction 2) was preparation of compound **B** by tosylation reaction. A solution of alcohol (15 g, 0.043 mol), trimethylamine (8.67 g, 0.086 mol) and 4-dimethylaminopyridine (0.3 g, 0.025 mol) in chloroform (100 mL) was cooled to 0°C (ice bath). Tosylchloride (12.26 g, 0.064 mol) diluted in chloroform (100 mL) was added dropwise and the solution was allowed to warm to room temperature under stirring for 12 hrs. Saturated NaHCO₃ (50 mL) was added, and the solution was extracted, washed with H₂O (100 mL), dried over Na₂SO₄, and filtered. The solvent was removed under vacuum (rotary evaporator), and the crude product was purified by flash chromatography starting with cyclohexane/ethyl acetate (80/20) in order to eliminate the excess of 4-toluenesulfonyl chloride followed by

dichloromethane/MeOH (90/10) to recover the pure tosylated alcohol (compound **B**) as a colorless oil: 17.73 g (82 % yield). The product was identified by ^1H , ^{13}C -NMR and mass spectrometry. APCI (+) HRMS: major $m/z = 495.2262$ ($\text{C}_{22}\text{H}_{39}\text{O}_{10}\text{S}^+$).

^1H NMR (400 MHz, CDCl_3) δ 7.79 – 7.75 (d, $J = 8$ Hz, 2H), 7.34 – 7.29 (d, $J = 12$, 2H), 4.16 – 4.10 (br m, 2H), 3.67 – 3.64 (br m, 2H), 3.63 – 3.57 (br m, 19H), 3.56 – 3.54 (br m, 4H), 3.53 – 3.50 (br m, 2H), 3.35 (s, 3H), 2.42 (s, 3H).

^{13}C NMR (101 MHz, CDCl_3) δ 144.9, 133.1, 129.9, 128.0, 72.0, 70.8, 70.6, 69.3, 68.7, 59.1, 21.7

The next step was the synthesis of compound **C** by nucleophilic substitution (3). Tosylated alcohol (17.73 g, 0.035 mol) was diluted in dry acetone (100 mL) and placed in a round bottom flask equipped with a refrigerating apparatus. Potassium iodide (11.62 g, 0.07 mol) was added, and the system was placed in dark (aluminum foil). The solution was refluxed for 24 hrs. Resulting mixture was filtered through celite, diluted with H_2O (100 mL), and extracted twice with CH_2Cl_2 . Organic layer was dried over Na_2SO_4 , filtered, and the solvent was evaporated under vacuum to give the iodide compound (12.62 g, 75%) as a yellowish viscous oil (compound **C**) which was used without further purification. The later was identified by ^1H , ^{13}C -NMR and mass spectrometry. APCI (+) HRMS: major $m/z = 451.1189$ ($\text{C}_{15}\text{H}_{32}\text{O}_7\text{I}^+$).

^1H NMR (400 MHz, CDCl_3) δ 3.73 – 3.67 (br m, 2H), 3.64 – 3.56 (br m, 21H), 3.52 – 3.47 (br m, 2H), 3.32 (s, 3H), 3.23 – 3.18 (br m, 2H)

^{13}C NMR (101 MHz, CDCl_3) δ 71.9, 71.9, 70.6, 70.6, 70.2, 59.0, 3.0

Synthesis of compound **D** was made using quaternization reaction (reaction (4)). Iodide compound (12.62 g, 0,027 mol) and 1-methylpyrrolidine (2.52 g, 0,03 mol) were diluted in a round bottom flask and dissolved in toluene (100 mL). The mixture was stirred at 70 °C for 48 hours. Two separated liquid layers were observed. The resulting $m\text{PEG}_n\text{MePyrI}$ salt was separated from toluene phase and washed with toluene (3×20 ml) and diethyl ether (3×20 ml). The residual product was

successfully identified by ^1H , ^{13}C -NMR and mass spectrometry as compound **D**. MALDI-TOF (matrix HCCA) (+) MS: major $m/z = 408.29$ ($\text{C}_{20}\text{H}_{42}\text{NO}_7^+$). MALDI-TOF (matrix DHB) (-) MS: $m/z = 126.90$ (I^-).

^1H NMR (400 MHz, CDCl_3) δ 3.99 – 3.85 (br m, 6H), 3.84 – 3.75 (br m, 2H), 3.69 – 3.63 (br m, 2H), 3.63 – 3.54 (br m, 19H), 3.53 – 3.47 (br m, 2H), 3.34 (s, 3H), 3.30 (s, 3H), 2.34 – 2.15 (br m, 4H)

^{13}C NMR (101 MHz, CDCl_3) δ 72.0, 70.6, 70.3, 65.8, 65.5, 63.3, 59.1, 49.4, 21.6

Finally, **ILE** was obtained by anion exchange via reaction (5) (**Scheme 2**). Anion exchange reaction was realized as mentioned above for $[\text{BMPyr}]\text{OAc}$. Aqueous solution of $m\text{PEG}_n\text{MePyrI}$ (6.17 g, 0,011 mol) was passed through a chromatography column packed with 40 g Amberlyst A-26 hydroxide (OH^- form) dropwise. Equimolar amount of acetic acid (0.65 g, 0,011 mol) was added to the resulting solution. Neutral pH was controlled with pH meter Mettler Toledo. The water was carefully removed under vacuum using rotary vapor at 60 °C during for few hours. Absence of residual iodide was controlled by AgNO_3 test. The product was identified as $[\text{mPEG}_n\text{MPyr}]\text{OAc}$ (compound **ILE**) and by ^1H , ^{13}C -NMR and mass spectrometry. APCI (+) HRMS: major $m/z = 468.3149$ ($\text{C}_{22}\text{H}_{45}\text{NO}_9^+$). Water content in as synthesized **ILE** was 2.73 wt. % as determined by Karl Fischer coulometric titration.

^1H NMR (400 MHz, CDCl_3) δ 3.97 – 3.87 (br, 4H), 3.86 – 3.76 (br m, 2H), 3.72 – 3.63 (br m, 2H), 3.61 – 3.50 (br m, 23H), 3.49 – 3.43 (br m, 2H), 3.32 – 3.26 (m, 3H), 3.20 (s, 3H), 2.25 – 2.05 (br m, 4H), 1.85 (s, 3H)

^{13}C NMR (101 MHz, CDCl_3) δ 177.2, 77.2, 70.5, 70.4, 70.2, 70.1, 65.6, 65.1, 63.0, 59.0, 48.3, 25.4, 21.4

2.1.3. RTIL identification.

Mass analysis of the compounds **B**, **C** and **ILE** by MALDI-TOF mass-spectrometry was hindered due to the close mass of certain compounds. Firstly, mass

analysis of initial alcohol (mPEG_nOH) revealed that it exists as an extended population of monomers n (4 < n < 14, where n = -CH₂-CH₂-O-), the difference of molecular masses is 44.0262 Da. Products **B** (mPEG_nOTs) and **C** (mPEG_{n-1}I) (scheme 2) differs by 0.0829 Da, hence, their distinguishing is difficult. Thus, we provided an analysis by high resolution mass spectrometry (HRMS) atmospheric pressure chemical ionization (APCI-Orbitrap) which allowed to more precisely identify products with high resolution masses and correctly observe anions in ionic liquids.

2.2. Water- RTIL mixtures

Water-RTIL mixtures in a very large range of water concentration were studied both in experimental work and by modelling. For the experimental characterization the mixtures were prepared gravimetrically using freshly prepared Milli-Q water (18.2 MΩ) and “as synthesized” ILs in ratios shown in **Tables 5.1 a and 5.1 b**.

Table 5.1. Composition of water - RTIL mixtures studied experimentally or by modeling (marked by *): **(a)** water – ILA

(a)

Mass fraction of H ₂ O in ILA, $\omega(\text{H}_2\text{O})$, %	Molar fraction of ILA	Molar fraction of water, $\chi(\text{H}_2\text{O})$	$n(\text{H}_2\text{O}) / n(\text{ILA})$
0*	1*	0*	0*
4.44	0.658	0.342	0.519
6.25	0.573	0.427	0.744
8.22*	0.500*	0.500*	1.000*
8.23	0.500	0.500	1.001
12.05	0.396	0.604	1.530
14.96	0.337	0.663	1.964
15.19*	0.333*	0.667*	2.000*
16.92	0.305	0.695	2.274
20.87	0.253	0.747	2.945
24.70	0.215	0.785	3.663
31.46	0.163	0.837	5.126
35.92	0.138	0.862	6.259
41.77	0.111	0.889	8.010
46.17	0.095	0.905	9.578
50.00*	0.082*	0.918*	11.167*
51.45	0.078	0.922	11.834
54.63	0.069	0.931	13.446
56.41	0.065	0.935	14.451
64.92	0.046	0.954	20.665
74.84	0.029	0.971	33.216
84.11	0.017	0.983	59.108
94.78	0.005	0.995	202.754
100	0	1	--

Table 5.1. (b) Composition of water - RTIL mixtures studied experimentally or by modeling (marked by *): **(b)** water – ILE

(b)

Mass fraction of H ₂ O in ILE, $\omega(\text{H}_2\text{O})$, %	Molar fraction of ILE	Molar fraction of water, $\chi(\text{H}_2\text{O})$	$n(\text{H}_2\text{O}) / n(\text{ILE})$
0*	1*	0*	0*
2.73	0.574	0.426	0.742
4.30*	0.462*	0.538*	1.166*
4.55	0.447	0.553	1.237
5.04	0.421	0.579	1.377
6.25	0.336	0.634	1.730
8.24*	0.300*	0.700*	2.330*
8.43	0.295	0.705	2.388
9.53	0.268	0.732	2.733
11.47	0,229	0.771	3.361
12.93	0.206	0.794	3.853
15.09	0,178	0.822	4.611
17.96	0.150	0.850	5.680
20.90	0.127	0.873	6.855
21.22*	0.125*	0.875*	6.988*
23.43	0.112	0.888	7.939
26.36	0.097	0.903	9.316
26.42*	0.097*	0.903*	9.287 *
28.29	0.089	0.911	10.235
30.94	0.079	0.921	11.624
32.82	0.073	0.927	12.675
37.08	0,061	0.939	15.290
40.00*	0.055*	0.945*	17.296*
45.77	0,044	0.956	21.897
50.00*	0.037*	0.963*	25.944*
54.59	0.031	0.969	31.189
64.66	0.021	0.979	47.469
74.66	0.013	0.987	76.441
84.86	0.007	0.993	145.419
95.20	0.002	0.998	514.565
96.97	0.001	0.999	830.308
98.98	$4.000 \cdot 10^{-4}$	0.9996	2517.629
100	0	1	--

ω – mass fraction, %; χ – molar fraction; $n(\text{IL}) / n(\text{H}_2\text{O})$ – molar ratio.

2.3. Electrochemical characterization.

The ionic conductivity of RTILs and their aqueous mixtures was measured by electrochemical impedance spectroscopy (EIS) method using a Solartron Modulab potentiostat with ECS software interface in a home-made dip-type conductivity cell

having a cell constant of $3.78 \pm 0.05 \text{ cm}^{-1}$ with two parallel platinum electrodes at 10 mV amplitude vs. E_{oc} within the frequency range 100 MHz – 100 Hz. The cell constant was determined by measuring the impedance of 0.01 M KCl aqueous solution ($\sigma = 1.408 \text{ mS/cm}$ at 25°C). All the measurements were conducted at least 5 times in a Faraday cage and at temperature $25 \pm 0.2^\circ\text{C}$.

Electrochemical potential windows (EPWs) of RTILs were investigated by cyclic voltammetry (CV) method using a Solartron Modulab potentiostat with ECS software interface in home-made three-electrode system. Glassy carbon disk ($S=0.0314 \text{ cm}^2$), Pt-wires and pseudo-Ag/AgCl electrode were used as working, counter and reference electrodes respectively. Pseudo-reference Ag/AgCl electrode was calibrated using 0.01 M $\text{K}_3[\text{Fe}(\text{CN})_6]$. This calibration solution was selected because of the previously reported instability of ferrocene and its analogous in RTILs [142]. The potentials of oxidation/reduction pair of $\text{K}_3[\text{Fe}(\text{CN})_6]$ were determined as $V_{(\text{FeIII}/\text{FeII})} = -0.54 \text{ V}$ and $V_{(\text{FeIII}/\text{FeII})} = -0.395 \text{ V}$ in ILA and ILE respectively (appendix 2, **Fig. 4S**). CV measurements for the EPW were conducted with the scan rate of 50 mVs^{-1} .

2.4 Chemical characterization by vibrational spectroscopy.

Raman spectra were recorded with a Renishaw Confocal Raman Microscope InVia using red laser (HeNe, 633 nm, 17 mW power). The samples were deposited as a droplet ($\approx 15 \mu\text{l}$) on a support (Si-plate) and covered by a transparent microscope glass cover. Laser beam was focused on the liquid phase between the Si-plate and glass. The focus was reached using a microscope objective Leica of $\times 50$ magnification and numerical aperture (NA) of 0.75. The exposure time was 10 seconds, and 25 spectra were recorded for each sample.

Attenuated Total Reflection Fourier Transform Infrared (ATR-FTIR) spectra were recorded using Thermo Scientific Nicolet 6700 FTIR spectrometer equipped with a mercury cadmium telluride detector cooled at 77 K by liquid nitrogen. The ATR accessory was a horizontal ZnSe crystal coated with diamond ($A=2.54 \text{ mm}^2$)

with single reflection and an angle of incidence of 45° (Smart Miracle from PIKE). The spectra were recorded with resolution 2 cm^{-1} and were averaged from 64 scans in order to minimize duration of contact of samples with air and corrected by corresponding refractive index. Although some absorption of moisture from the air is possible during measurement, we assume that its effect can be neglected if compared with the initial water content which was several wt. % even for the less concentrated in water samples (see **Table 5.1**). A droplet of the sample was placed on the diamond ATR crystal and recording was started immediately; each concentration was recorded 5 times. OMNIC software was used for the data collection and treatment. Further deconvolution of the spectra has been done using OriginPro 2018b using the following base line correction parameters: constant $Y = 0$; number of peaks: 4; fitting function: Gaussian; any other parameters were not fixed; R-square was more than 0.999 for all fitted spectra.

2.5. MD modeling methodology

All the compounds used for simulations were drawn using Gauss View 6 [186] and a calculation with Gaussian 16 [187] in junction with Antechamber module [188,189] was performed to assign the Restrained Electrostatic Potential (RESP) charges of each atom. As the protocol requires [190] Gaussian optimizations were carried out at Hartree Fock level standard 6-31* basis.

We performed different simulations of one hundred pairs of IL cations and acetate anions, and an opportune number of water molecules were added to reproduce $\chi(\text{H}_2\text{O}) = 0.500; 0.667; 0.918$ of water concentrations for ILA and $\chi(\text{H}_2\text{O}) = 0.538; 0.700; 0.875; 0.903; 0.954; 0.963$ for ILE (**Appendix 2, Table 1S**). The starting configurations were created with the PACKMOL package [191].

The molecular dynamic simulations were instead carried out with Large-Scale Atomic/Molecular Massively Parallel Simulator (LAMMPS) package [192,193]. The equilibration, 1 ns long or even more, was calculated at ambient conditions ($T = 298.15\text{ K}$ or 25°C) in a NVT ensemble with volume reflecting the real densities

values founded experimentally. Production runs, in NVE ensemble, were performed for at least 1 ns. The total energy drift $E_{\text{tot}} / E_{\text{tot}}$ was checked to be less than 10^{-6} in the worst case. All the thermodynamic outputs were treated using OriginPro 2018b.

Structural characterization was realized through the observation of radial distribution function, $G(r)$, of the distance between the selected atoms. Its definition for the two atom α and β is given by following formula:

$$G_{\alpha,\beta}(r) = \frac{1}{N_{\alpha} \cdot N_{\beta}} \langle \sum_{i,j}^{N_{\alpha}, N_{\beta}} \delta(r_{ij} - r) \rangle \quad (6)$$

where the $\langle \dots \rangle$ indicates the usual ensemble average, and $\delta(x)$ is the Dirac delta function, r_{ij} is the distance between an α and β atoms whereas N_{α} and N_{β} are respectively their number in the sample box. Strong hydrogen bonds can be considered if the distance between the oxygen of RTIL and hydrogen of water ($\text{O}(\text{RTIL}) \cdots \text{H}(\text{H}_2\text{O})$) is less than 2 Å, weak hydrogen bonds can be considered for the $\text{O}(\text{IL}) \cdots \text{H}(\text{H}_2\text{O})$ distances up to 3 Å [194].

3. Results

3.1. Electrochemical Potential Window. To the best of our knowledge, although, some works with mPEG_n-N-methylpyrrolidinium ILs were carried out [136], the experimental electrochemical stability of this cation, especially with acetate anion, has never been studied. **Fig. 5.1** shows voltammograms of as synthesized **ILA** and **ILE**, containing 0.342 and 0.426 molar fraction of water respectively. Determined from these polarization curves the electrochemical potential windows are: $\text{EPW} \approx 2.26$ V for **ILE** and $\text{EPW} \approx 2.88$ V for **ILA**. Especially, for **ILE** the EPW is narrowed at cathodic (negative) potentials. Such difference in the EPW of two ionic liquids can be explained by lower electrochemical stability of etheric bonds in substituted tail compared to the alkyl group because of their electrochemical reduction [195]. Similar effects have been previously reported for phosphonium and piperidinium cations [92,196–198]. The difference between the oxidation potentials **ILA** and **ILE** stays unclear.

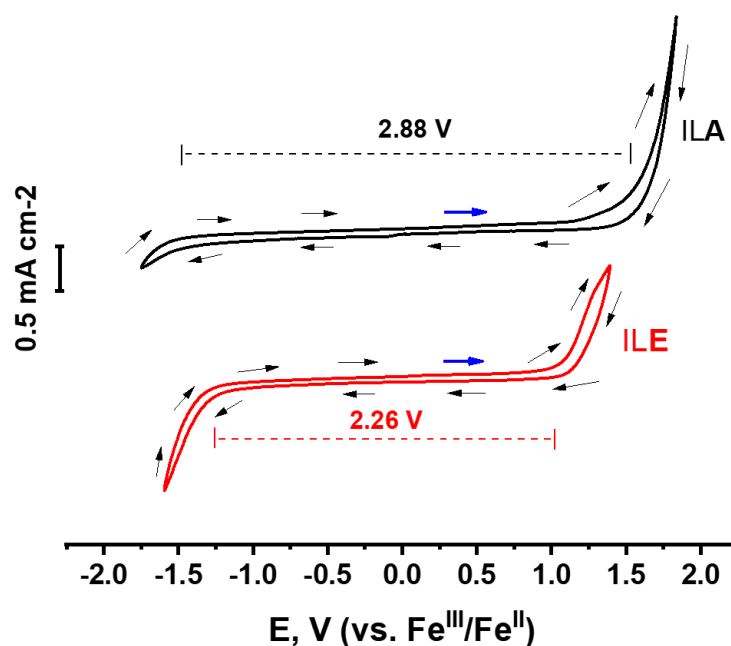


Fig. 5.1. Cyclic voltammograms recorded on glassy carbon disk electrode of “as synthesized” ILA and ILE, as indicated. Arrows indicate potential scanning direction starting from the blue one. Scan rate 50 mVs^{-1} . Electrochemical potential window is also shown by dash lines; the limits are determined at $0.1 \text{ mA}\cdot\text{cm}^{-2}$ current density cut off.

3.2. Specific conductivity.

Specific conductivity of the electrolytes is one of their key-properties for the electrochemical applications. In some works, it has been shown that dilution of ILs by conventional electrolytes increases conductivity [17,172,199]. **Fig. 5.2** represents specific conductivity (σ , $\text{mS}\cdot\text{cm}^{-1}$) of water - ILA and water - ILE mixtures as a function of the water content (molar fraction). As it can be seen from the figure, the conductivity of ILA is systematically higher than that of ILE, which can be explained by a shorter length of the substituted tail resulting in higher ionic mobility. The conductivity increases with the water content and has a maximum of $27.9\pm 0.1 \text{ mS}\cdot\text{cm}^{-1}$ at $\chi(\text{H}_2\text{O}) = 0.971$. On the contrary, for ILE the maximum of specific conductivity is observed at $\chi(\text{H}_2\text{O}) = 0.987$ with the only at 11.0 ± 0.1

$\text{mS}\cdot\text{cm}^{-1}$ which is more than two times lower than for ILA. Conductivity growth with dilution can be explained by two factors: a) viscosity decrease which leads to the higher mobility of ions; b) formation of water clusters which allow ions to move freely [84]. Since, ILA and ILE have the same anion – acetate, the substituted chains at nitrogen atoms play a crucial role in the conductivity evolution. Sharp decrease of conductivity at very high water contents is similar to the expected for diluted aqueous solutions in which only isolated hydrated ions ensure conductivity, so less is the fraction of ions, lower conductivity. One could consider hence that starting from the concentration corresponding to the maximal conductivity, the interactions between IL ions could be neglected if compared with the interactions with water molecules.

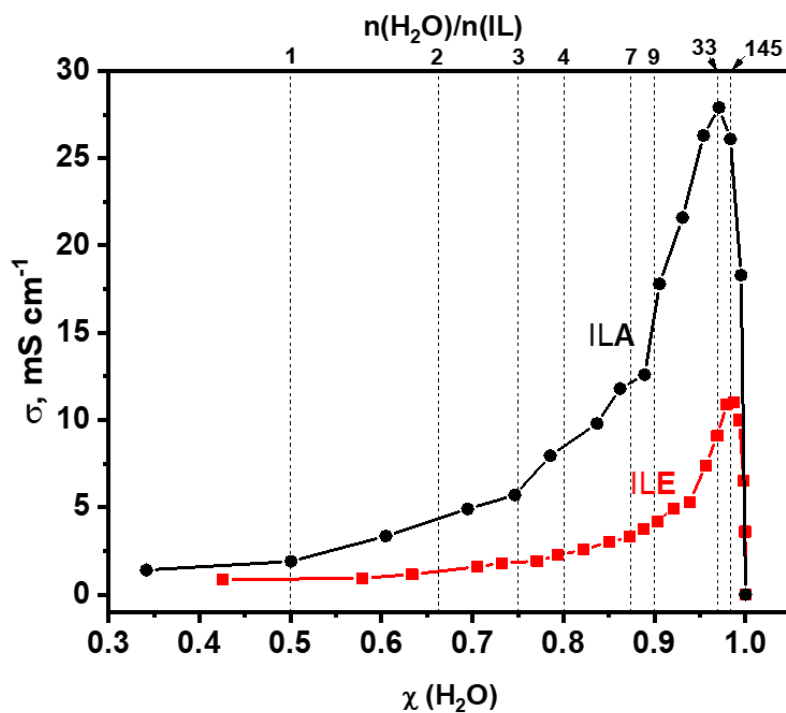


Fig. 5.2. Specific conductivity of water-ILA and water-ILE mixtures, σ , as a function of molar water content $\chi(\text{H}_2\text{O})$. Vertical lines show fractions for some selected molar ratios between water molecules and IL molecules $n(\text{H}_2\text{O})/n(\text{IL})$ as indicated.

3.3 Raman spectroscopy of water-RTIL mixtures.

Fig. 5.3 displays typical Raman spectra of water-RTIL mixtures for ILA (**a**) and ILE (**b**) as a function of water content. Detailed attribution of the peak positions is given in supplementary information (**Appendix 2, Table 2S**). As it can be seen from **Fig. 5.3 (a)** the Raman peaks at 637, 906, 1325, 1387 cm^{-1} shift to higher wavenumbers with increasing of water content. These peaks are usually attributed to acetate anion vibrations [158]. The band nearby 905 cm^{-1} on the spectra of ILA (**a**) and ILE (**b**) containing 0.342 and 0.426 water molar fraction respectively consists of two peaks attributed to pyrrolidinium ring [157], acetate anion [161] and are not distinguishable. Growth of the water content leads to the formation of a shoulder and then to the bifurcation of the peak. The second peak nearby 914 cm^{-1} appears at $\chi(\text{H}_2\text{O}) = 0.747$ and $\chi(\text{H}_2\text{O}) = 0.794$ for ILA and ILE respectively. These observations indicate that water molecules strongly interact with acetic group in both ionic liquids, which is coherent with the previously reported results [18,200,201]. Additionally, for ILE (**Fig. 5.3 b**) the form of the broad peak attributed to C-O-C vibration (770-867 cm^{-1} with the maximum nearby 850 cm^{-1}) slightly changes with dilution, which can be attributed to the changing of etheric-groups conformation due to interaction with water [202].

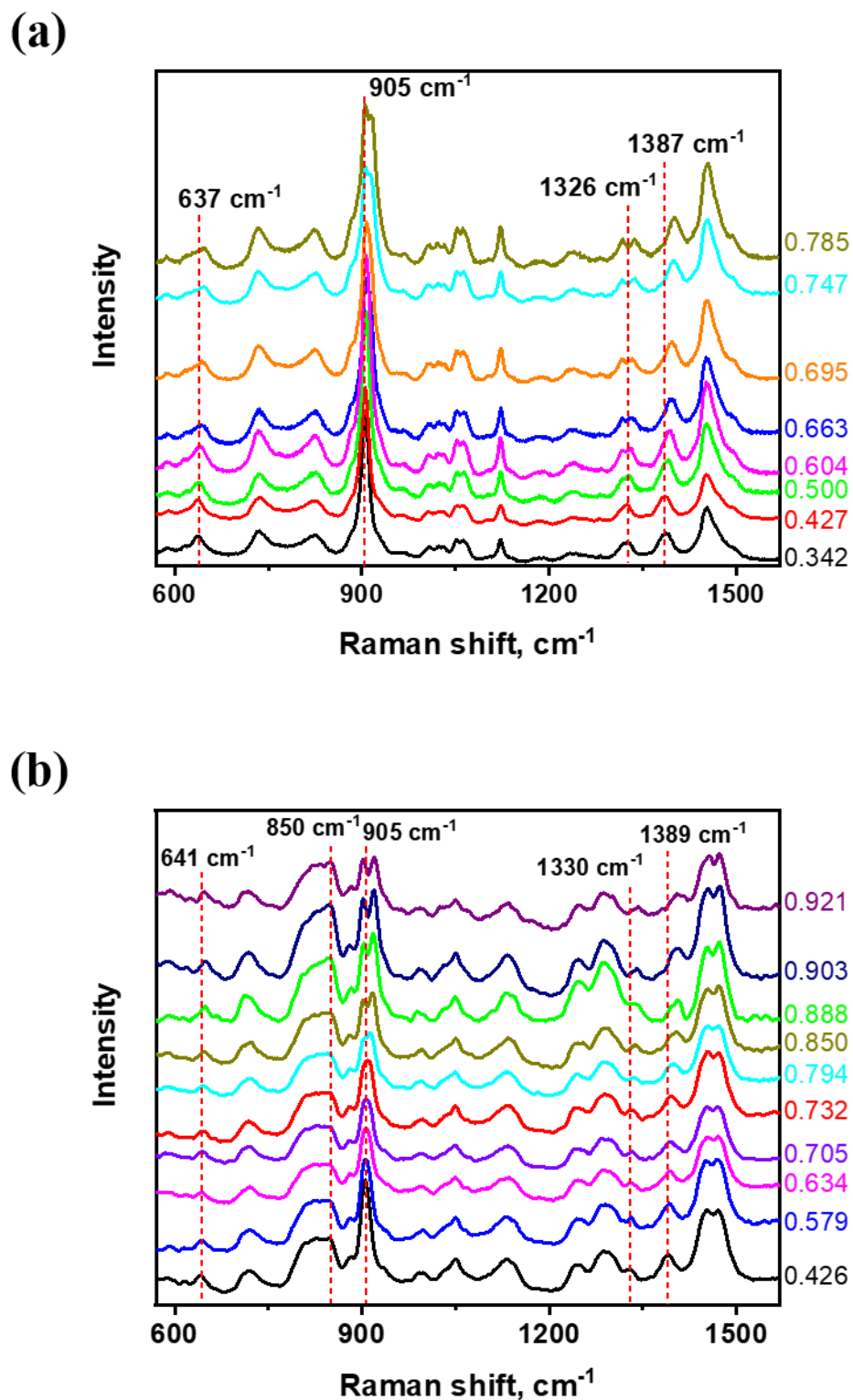


Fig. 5.3. Typical Raman spectra of water mixtures with ILA **(a)** and ILE **(b)** with different molar fractions of water (as indicated at right of each spectrum). On **(a)** all noted shifts are attributed to acetate groups vibrations. On **(b)** 850 cm^{-1} is attributed to C-O-C vibrations, the others – to acetate group.

3.4 ATR-FTIR spectra of water-RTIL mixtures.

Fig. 4 (a, b) displays ATR-FTIR spectra of ILA and ILE within the range of 750-3800 cm^{-1} . Peaks attribution is shown in Tables 5.2 a and 5.2 b.

Table 5.2. FTIR peaks attribution of “as prepared” ILA (a) and ILE (b) within the range 900-3800 cm^{-1} .

(a) ILA

Experimental wavenumbers, cm^{-1} (intensity)	Type of vibration	Group attribution	Reference
3371 (weak)	O-H, stretching	OH, H ₂ O	[203]
3017 (weak)	C-H, stretching	CH ₂ , CH ₃ , C ₄ H ₉ , acetate, pyrrolidinium	[161]
2963 (medium)	C-H, stretching	CH ₂ , CH ₃	[161]
2877 (weak)	C-H, stretching	CH ₂ , CH ₃	[128]
1650 (weak)	O-H, bending	OH	[203]
1583 (very strong)	O-C, as. stretching	COO, acetate	[18,161]
1468 (weak)	C-H, bending	CH ₂ , CH ₃	[204] / [205]
1429 (weak)	C-H, bending	CH ₃ , acetate	[18]
1379 (medium)	C-H, bending	CH ₃ , acetate	[18]
1323 (weak)	C-O, symmetric	COO, acetate	[18]
1307 (weak)	C-H, twisting	CH ₂ , C ₄ H ₉	[204]
1122 (weak)	C-H, twisting	CH ₂ , C ₄ H ₉	[204]
1050 (weak)	C-H, rocking	CH ₃ of acetate / C-C ring mode	[161] / [204]
1032 (weak)	C-H, wagging	CH ₂ , C ₄ H ₉	[204]
1004 (weak)	C-H, wagging / rocking	CH ₂ , C ₄ H ₉ CH ₃ , acetate	[161] / [204]
967 (weak)	C-N, stretching	CN, pyrrolidinium	[204]
932 (weak)	C-C, stretching	C-C ring breathing, pyrrolidinium	[161] / [204]
906 (weak)	C-C, stretching	O-C-O, acetate C-C, ring breathing pyrrolidinium	[161] / [204]

(b) ILE

Wavenumbers, cm ⁻¹ (intensity)	Type of vibration	Group	Reference
3471 (weak)	O-H, stretching	OH, H ₂ O	[203]
2873 (medium)	C-H, stretching	CH ₂ , CH ₃ , ether, acetate, pyrrolidinium	[128]
1649 (weak)	O-H, bending	OH, H ₂ O	[203]
1580 (medium)	O-C, stretching	COO, Acetate	[18,161]
1460 (weak)	C-H, bending	CH ₂ , ether	[183,206]
1429 (weak)	C-H, bending	CH ₃ , acetate	[18]
1380 (medium)	C-H	CH ₃ , bending	[130]
1351 (weak)	C-H, wagging / scissoring	CH ₂ , ether	[161]
1325 (weak)	C-O, symmetric	COO, acetate	[18]
1301 (weak)	C-H, twisting	CH ₂ , pyrrolidinium, C ₄ H ₉	[183,207]
1248 (weak)	C-O, stretching	COC, ether	[183]
1199 (weak)			
1107 (strong)	C-O-C, stretching	COC, ether	[183]
1041 (weak)	C-H, bending	CH ₃ , acetate	[18]
1000 (weak)	C-H, bending	CH ₃ , acetate	[18]
941 (weak)	C-N, stretching	CN, pyrrolidinium	[204]
904 (weak)	C-C, stretching	O-C-O, acetate C-C, ring breathing pyrrolidinium	[161] / [204]

It is obvious from **Fig. 5.4** that higher is the water content, higher are O-H absorbance peaks (3000-3700 cm⁻¹) and lower are the peaks corresponding to ILEs absorbance. Similar to Raman spectra, positions of some peaks change with dilution. As can be seen from the **Fig. 5.4 b**, peaks nearby 1379 cm⁻¹ and 1583 cm⁻¹ suffer blue and red shifts respectively. These peaks are attributed to C-O and C-H vibrations of acetic groups [18,161]. It also should be noted that on the spectra of ILE these shifts (for peaks at 1380 cm⁻¹ and 1583 cm⁻¹) are also observed. Less intensive peaks attributed to acetic groups nearby 906 cm⁻¹, 1004 cm⁻¹, 1323 cm⁻¹ and 904 cm⁻¹, 1325 cm⁻¹ for ILA and ILE respectively (noted in the figures) are also shifted. For water - ILE mixtures, the positions of the peaks with the maximum at 1107 cm⁻¹

¹ and 1248 cm⁻¹, which are attributed to C-O-C etheric group [183], also shift with dilution (**Fig. 5.4 d**).

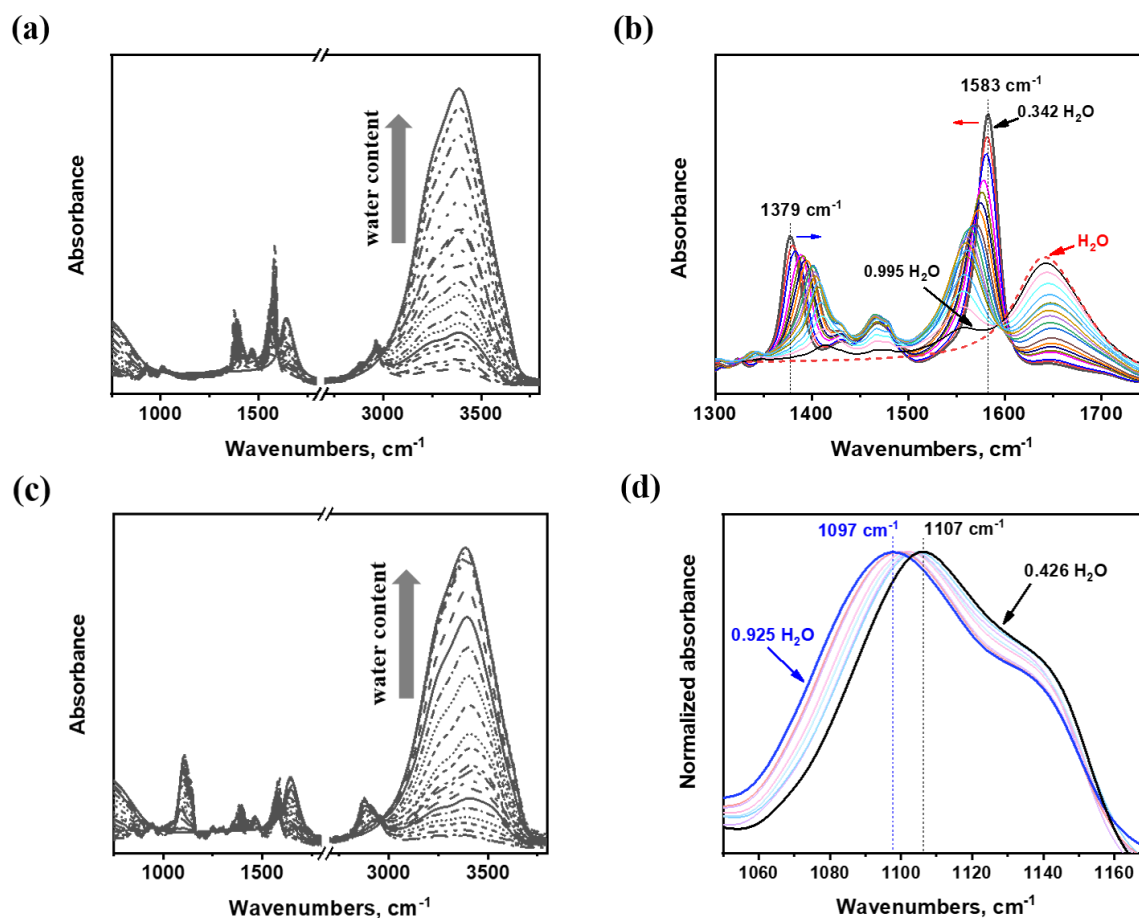


Fig. 5.4. Evolution of ATR-FTIR spectra of ILA (**a, b**) and ILE (**c, d**) as a function of water content. For ILA water molar fraction $\chi(\text{H}_2\text{O})$ are: 0.342, 0.427, 0.500, 0.605, 0.663, 0.695, 0.747, 0.786, 0.837, 0.862, 0.889, 0.905, 0.922, 0.931, 0.954, 0.971, 0.983, 0.995, 1 (pure water);

For ILE water molar fraction $\chi(\text{H}_2\text{O})$ are: 0.426, 0.553, 0.579, 0.634, 0.705, 0.732, 0.794, 0.873, 0.888, 0.903, 0.911, 0.939, 0.956, 0.969, 0.979, 0.987, 0.993, 0.998, 0.999, 0.9996, (pure water).

Typical ATR-IR spectra in C-O (acetic) region of ILA (**b**) and in C-O-C etheric region of ILE (**d**) as a function of water content. For (**d**) water molar fraction $\chi(\text{H}_2\text{O})$ are: 0.426, 0.705, 0.794, 0.850, 0.873, 0.903, 0.911, 0.925.

3.5. Radial distribution function for hydrogen bonds in water - RTILs mixtures from MD simulation

Fig. 5.5 represents typical configurations of ILs molecules with the closest water molecules, extracted from the MD calculations for the models with approximate water molar fraction $\chi(\text{H}_2\text{O}) = 0.918$ for **ILA** and $\chi(\text{H}_2\text{O}) = 0.903$ for **ILE**. The closest distances between the water hydrogen atoms and acetate oxygen atoms are indicated. Oxygen atoms numbering in etheric groups is also shown (the distance for $\text{O4}\cdots\text{H}_2\text{O}$ is indicated). The shortest distances between H-atom from water and O atom from ionic liquid are also indicated. Normally the distance between O and H atoms less than 3 \AA is attributed to a hydrogen bond formation [194], so the results shown in **Fig. 5.5a-b** indicate the formation of H-bonds between water and acetate anion and also etheric oxygens in case of **ILE**. In the model with **ILA**, water clusters are formed at this concentration. In contrast, the model with **ILE** shows only some embryos of water-clusters formations.

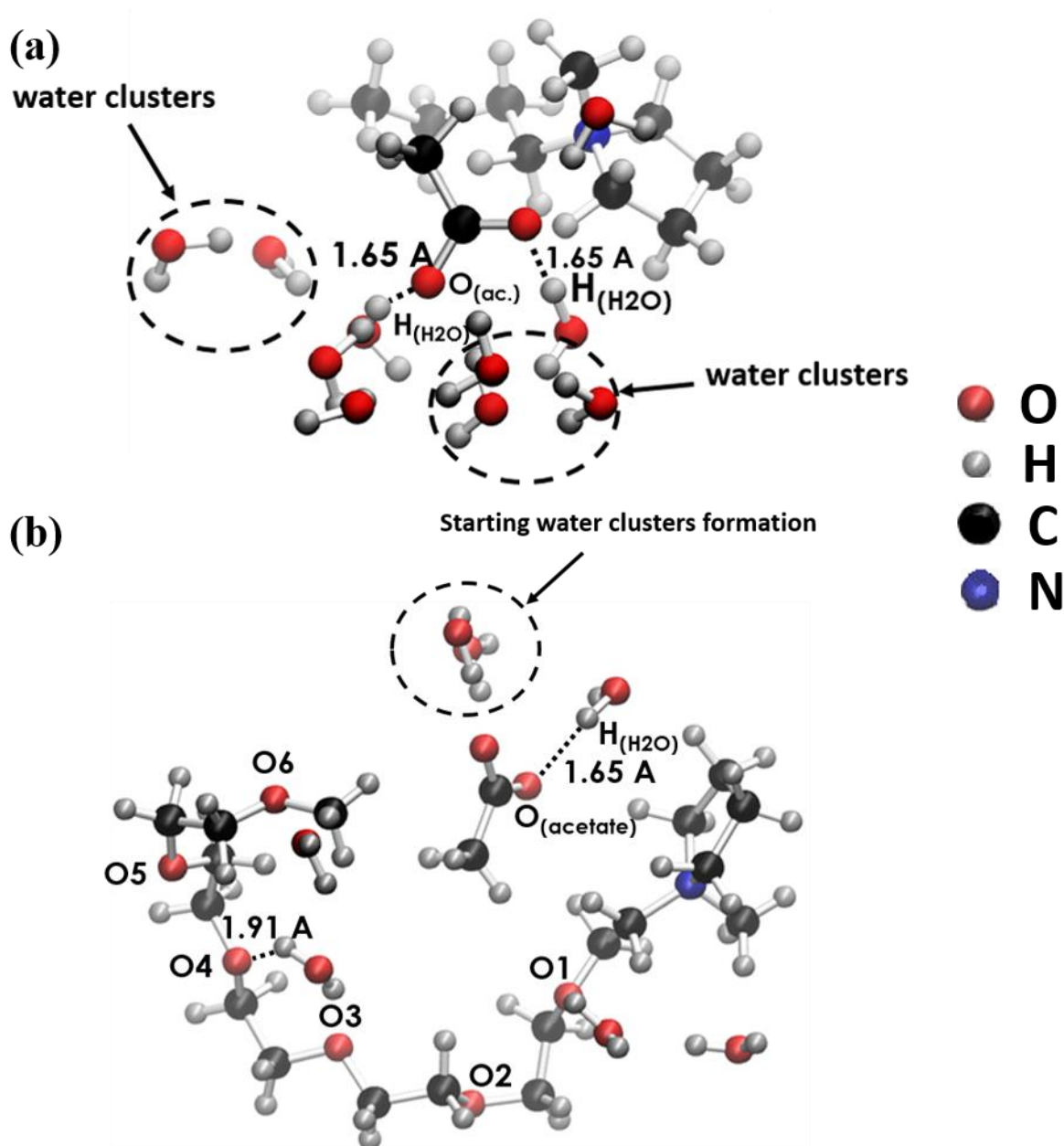


Fig. 5.5. Representation of models ILA containing $\chi(\text{H}_2\text{O}) = 0.918$ ($n(\text{H}_2\text{O}) / n(\text{ILA}) \approx 11$) – (a); ILE model representation $\chi(\text{H}_2\text{O}) = 0.903$ ($n(\text{H}_2\text{O}) / n(\text{ILE}) \approx 9$) – (b).

These extracted structures are however only illustrations, more quantitative description of H-bonding can be obtained by analysis of radial distribution function (RDF), $G(r)$, shown in **Fig. 5.6**. Presented in the figure $G(r)$ graphs describe the probability of finding a hydrogen atom from water molecule at a distance r (measured in Å). Due to dynamical movement, liquids do not maintain a constant

structure, so at large distances the molecules are independent and the distribution returns to the bulk density ($G(r)=1$). However, at low distances the first peak indicates the first coordination sphere, so if there are specific interactions between atoms, *e.g.* hydrogen bonds between acetate anion, O_{acetate} , and water hydrogen atom $H_{\text{H}_2\text{O}}$, a peaks at low distance should occur on the radial distribution function $G(O_{\text{acetate}}/H_{\text{water}})$. **Figs. 5.6 a and b** represent the $G(r_{O_{\text{acetate}}\cdots H_{\text{water}}})$ for the distance between the acetate oxygen and water hydrogen in **ILA** and **ILE** mixtures with water for different water contents. They are characterized by 2 peaks nearby 1.65 Å and 2.97 Å. The intensity of both peaks decreases with dilution, indicating that H-bonding becomes less probable with increasing water concentration. The $G(r_{O_{\text{etheric}}\cdots H_{\text{water}}})$, representing the length distribution between etheric oxygen and hydrogen of water also revealed 2 peaks nearby 1.92 Å and 4.90 Å (**Fig. 5.7**, only at ≈ 1.92 Å is shown). Interestingly, different etheric oxygen atoms showed different intensities of the first peak, indicating different affinity to H-bonding (**Fig. 5.8**).

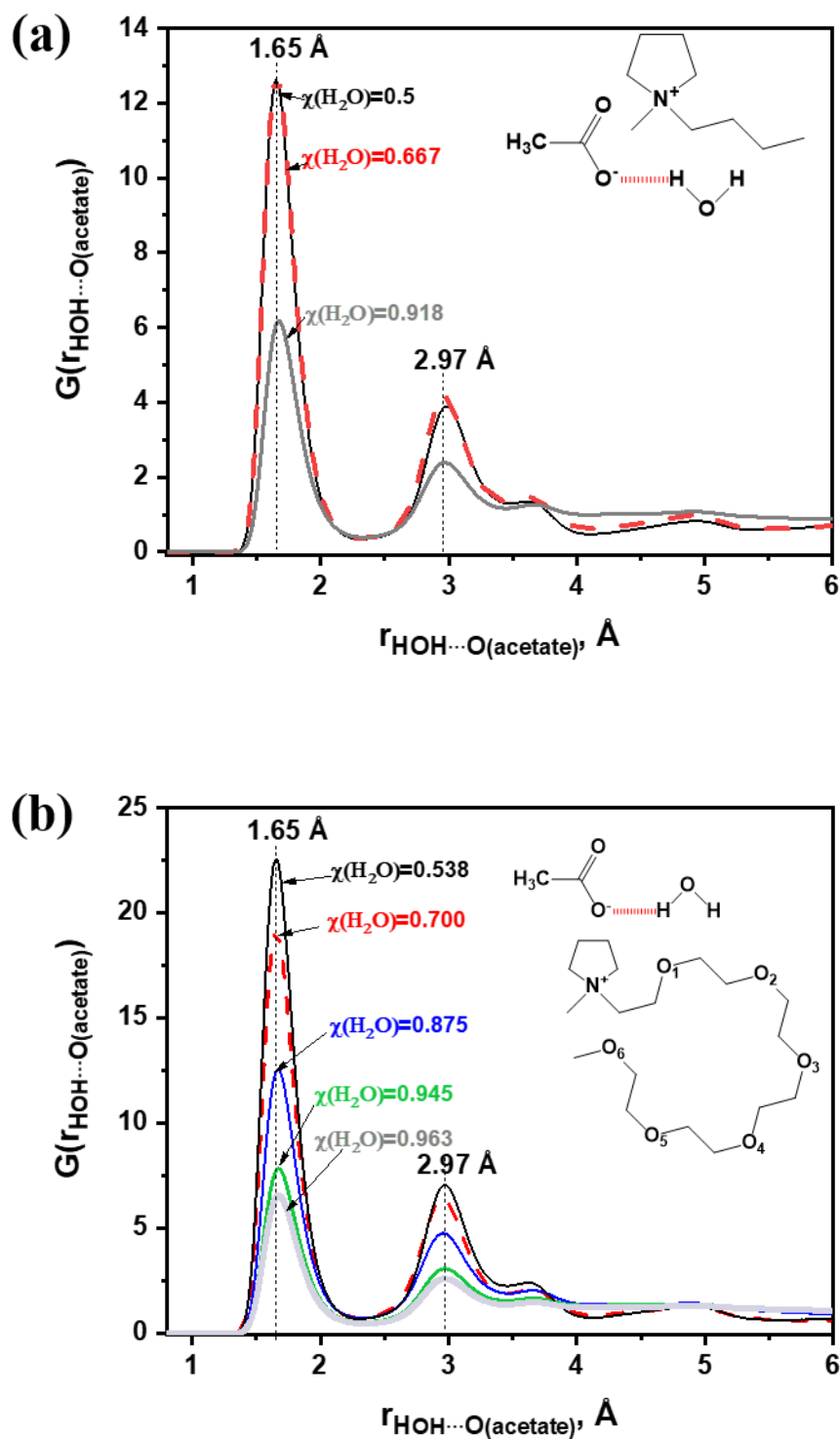


Fig. 5.6. Radial distribution function $G(r_{\text{HO-H}\cdots\text{O}(\text{acetate})})$ of the distances between water hydrogen and acetate oxygen, $r_{\text{HO-H}\cdots\text{O}(\text{acetate})}$, for water mixtures with ILA (a) and ILE (b) with selected water molar fractions $\chi(\text{H}_2\text{O})$, as indicated.

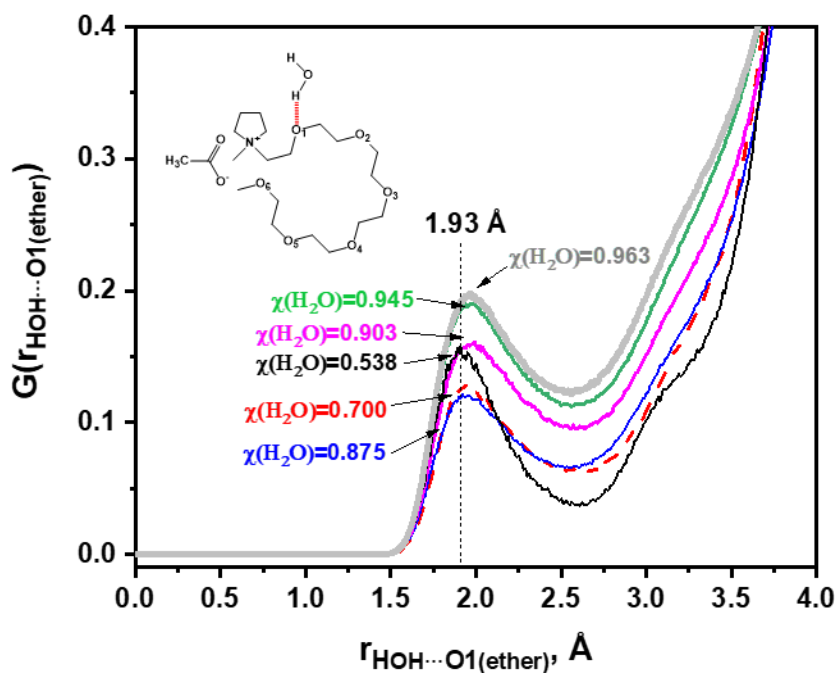


Fig. 5.7. Radial distribution function $G(r_{\text{HOH}\cdots\text{O1(ether)}})$ of the distances between water hydrogen and first etheric oxygen, $r_{\text{HOH}\cdots\text{O(etheric)}}$, for water mixtures ILE with selected water molar fractions $\chi(\text{H}_2\text{O})$ as indicated.

Detailed analysis of the RDFs evolution suggests that the probability of intermolecular interactions between water and acetic moiety decreases upon dilution while the probability of hydrogen bonds between water and etheric oxygen increases (**Fig. 5.8-5.9**). At concentration $\chi(\text{H}_2\text{O}) = 0.538$ the highest intensity of RDF characterizing the length of $\text{H}_{(\text{water})}\text{-O}_{(\text{etheric})}$ bonds is observed for O1 and O3 (counting from N^+), at the same time water molecules interact with acetic group (**Fig. 5.8 b**). Thus, it can be assumed that water is confined between acetate and etheric oxygens (O_1, O_3), forming $\text{AcO}\cdots\text{HOH}\cdots\text{O}_{(\text{etheric})}$ segregations, which are sterically the closest to acetate. This is also supported by the fact that RDF intensities of $\text{O1}_{(\text{etheric})}\text{-H}_{(\text{water})}$ does not change significantly with water fraction in the mixture (**Fig. 5.8**). Another interesting observation is a rapid increase of RDF intensities $\text{O}_{(\text{etheric})}\text{-H}_2\text{O}$ for O2-O6 starting from the water fraction $\chi(\text{H}_2\text{O}) = 0.875$, whereas

peaks area ratios start to change rapidly (**Fig. 5.9 b**). Might be, it indicates a start of water-clusters formation.

Thereby, we assume that this graph can be divided into 3 regions. Within the first region ($\chi(\text{H}_2\text{O}) = 0.442 - 0.702$) water molecules are strongly bonded to acetate moieties ($\text{AcO}\cdots\text{HOH}\cdots\text{OAc}$). The second region ($\chi(\text{H}_2\text{O}) = 0.702 - 0.872$) is characterized by the existence of $\text{AcO}\cdots\text{HOH}$ and $\text{O}_{(\text{etheric})}\cdots\text{HOH}$ and H-bonds. The third region ($\chi(\text{H}_2\text{O}) = 0.872 - 1$) represents the domain in which water clusters present and continuously grow. All of these conclusions were supported by dynamic boxes, in which the first hint of water-clusters appearance was observed at $\chi(\text{H}_2\text{O}) = 0.872$ (**Appendix 2, Table 2S**).

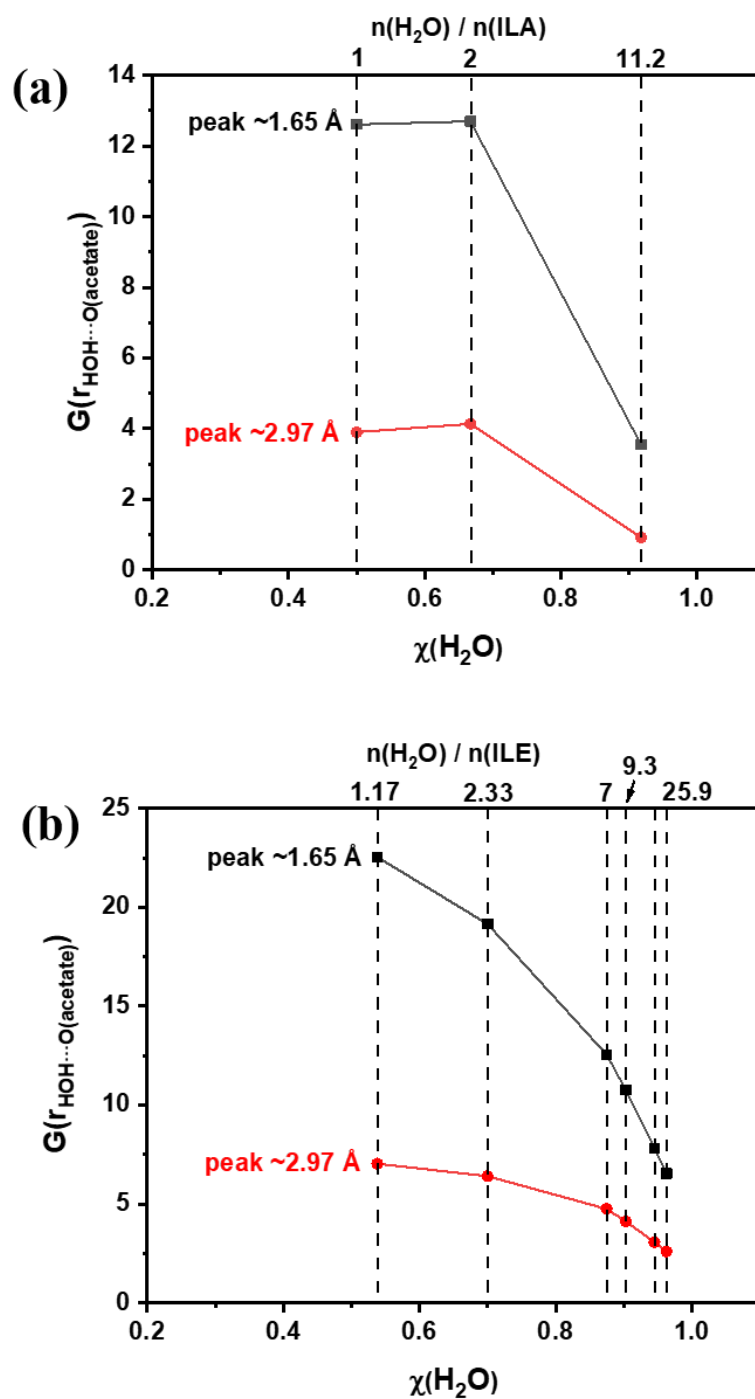


Fig. 5.8. Evolution of the intensities of the first two peaks of RDF for the distances $r_{\text{HO}\cdots\text{O}(\text{acetate})}$ between the hydrogen from water and the oxygen from the acetate anion as a function of water molar fraction in water mixtures with ILA (a) and ILE (b). Vertical dash lines indicates selected molar ratios of water to ILs, $n(\text{H}_2\text{O}) / n(\text{ILA})$ and $n(\text{H}_2\text{O}) / n(\text{ILE})$, as indicated.

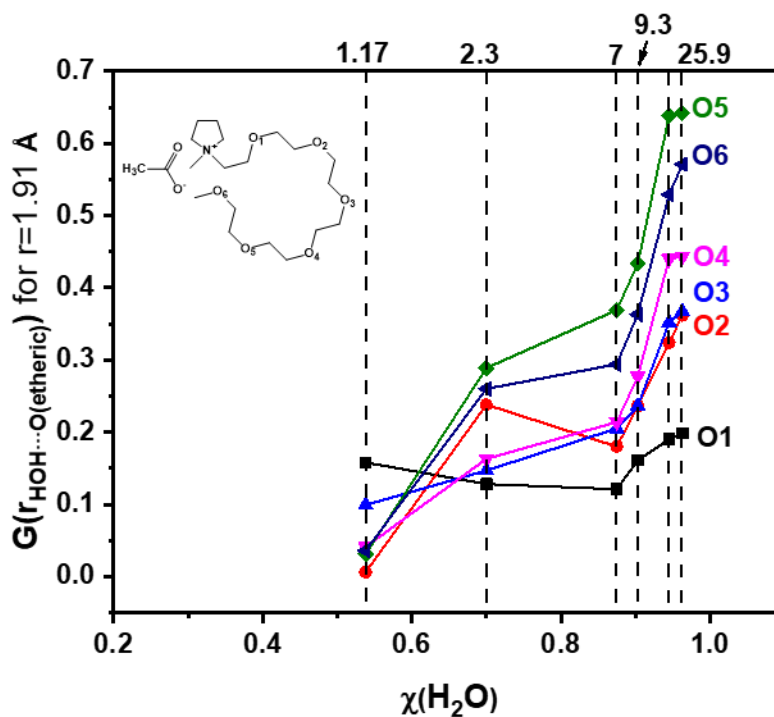


Fig. 5.9. Evolution of the intensities of the RDF at $r_{\text{HOH}\cdots\text{O}(\text{etheric})}=1.91$ Å (the closest distance between the hydrogen from water and the etheric oxygen atoms) as a function of water molar fraction in water mixtures with ILA (a) and ILE (b).

Vertical dash lines indicates selected molar ratios of water to ionic liquids:

$$n(\text{H}_2\text{O}) / n(\text{ILE}).$$

4. Discussion.

4.1. Effect of water content on molecular structure of water-RTIL mixtures for aliphatic and etheric substituted MPyrOAc RTILs

In order to understand water state in various solutions, the literature suggests to explore the evolution of infrared spectra in the region of O-H vibrations ($3000\text{--}3700\text{ cm}^{-1}$) [119,208–211]. **Fig. 5.9** compares the spectra of pure water with the spectra of water-ILA and water-ILE mixtures in the close to 1:1 water to IL molar ratios (molar water fraction $\chi(\text{H}_2\text{O}) = 0.427$ and $\chi(\text{H}_2\text{O}) = 0.426$ for ILA and ILE respectively). For both mixtures the peak's width at half-height is smaller than for pure water, which evidences that water molecules are separated from each other [208]. Additionally, in the water-ILE mixture an additional shoulder appears at

nearby 3757 cm^{-1} , but not in water-ILA mixture (**Fig. 5.9**). Appearance of this additional vibration peak at 3757 cm^{-1} can be tentatively explained by the observed in MD simulation structures in which water is confined between acetate and etheric oxygens (O_1, O_3), forming $\text{AcO}\cdots\text{HOH}\cdots\text{O}_{(\text{etheric})}$ segregations, which are sterically the closest to acetate (see section 3.5).

To quantify the evolution of the molecular structure, the spectra of all mixtures were reproducibly decomposed into 4 single Gaussian functions (A, B, C, D) as illustrated on the examples shown in **Fig. 5.10 a, b**. Unfortunately, there is no unique model describing infrared peak deconvolution of liquid water in mixtures, in different works these peaks are decomposed into 3, 4 [212,213]; 5 or 6 bands [119,211,214]. In theory, hydrogen bonding should decrease vibrational mobility of H-atom, so the vibration frequency modifications and peak splitting can be expected. An exact attribution of the observed vibration wavenumbers is however very complex even with the help of modelling and requires multiple a priori for cluster structures and symmetries even for pure water [213]. For this reason, the present work is limited to an empirical 4-component decomposition which fitted well for all the studied spectra.

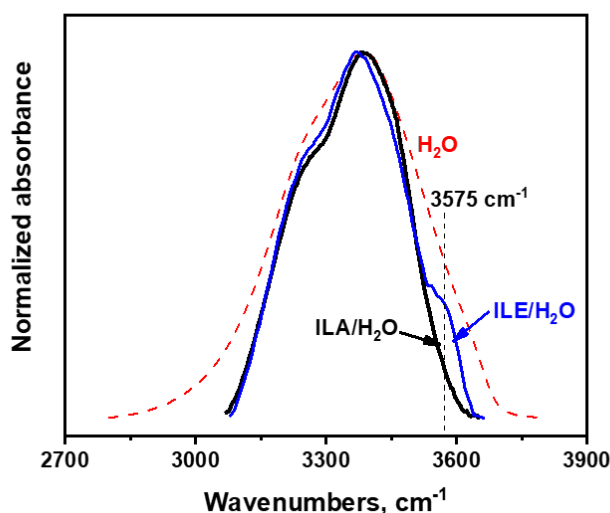
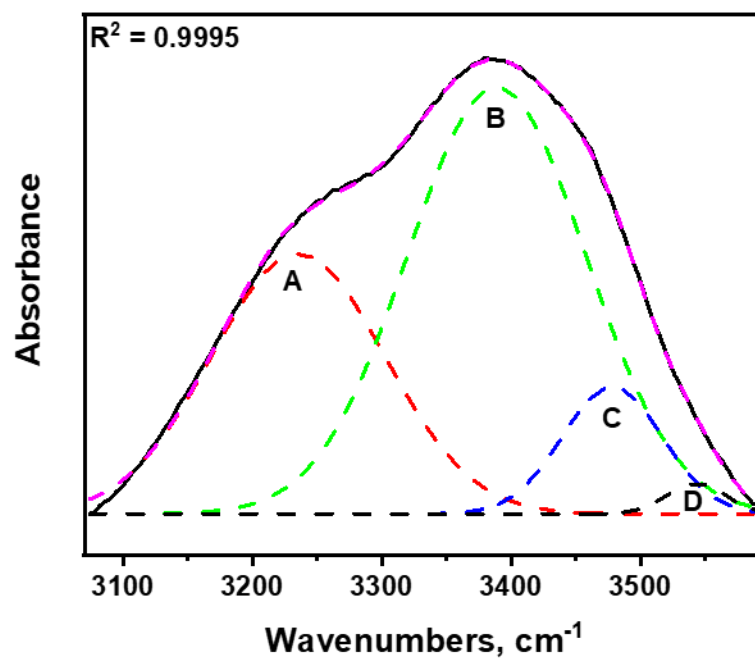


Fig. 5.9. FTIR spectra of ILA ($\chi(\text{H}_2\text{O}) = 0.427$) - black, ILE ($\chi(\text{H}_2\text{O}) = 0.426$) – blue, and pure H_2O – dash red.

(a)



(b)

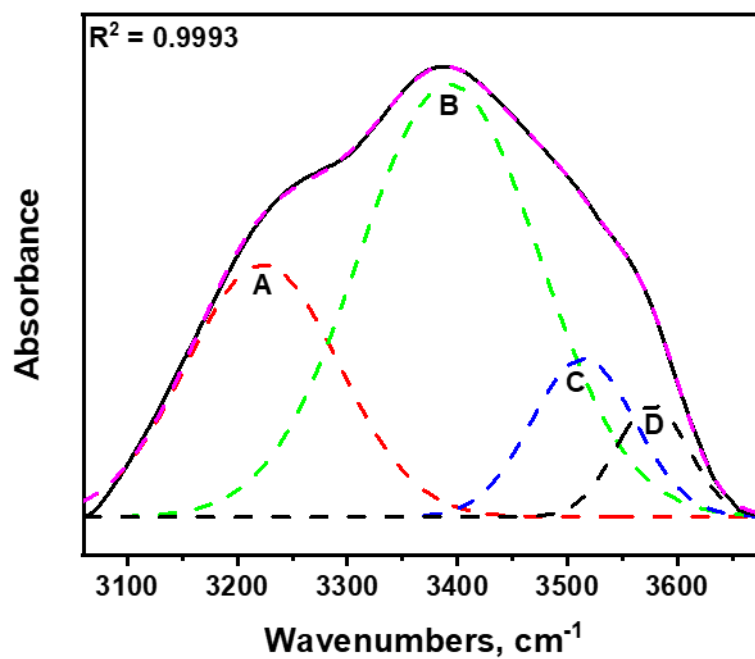


Fig. 5.10. Typical decomposed FTIR spectrum of ILA containing ($\chi(\text{H}_2\text{O}) = 0.427$) – **a**, ILE containing ($\chi(\text{H}_2\text{O}) = 0.705$) – **b**.

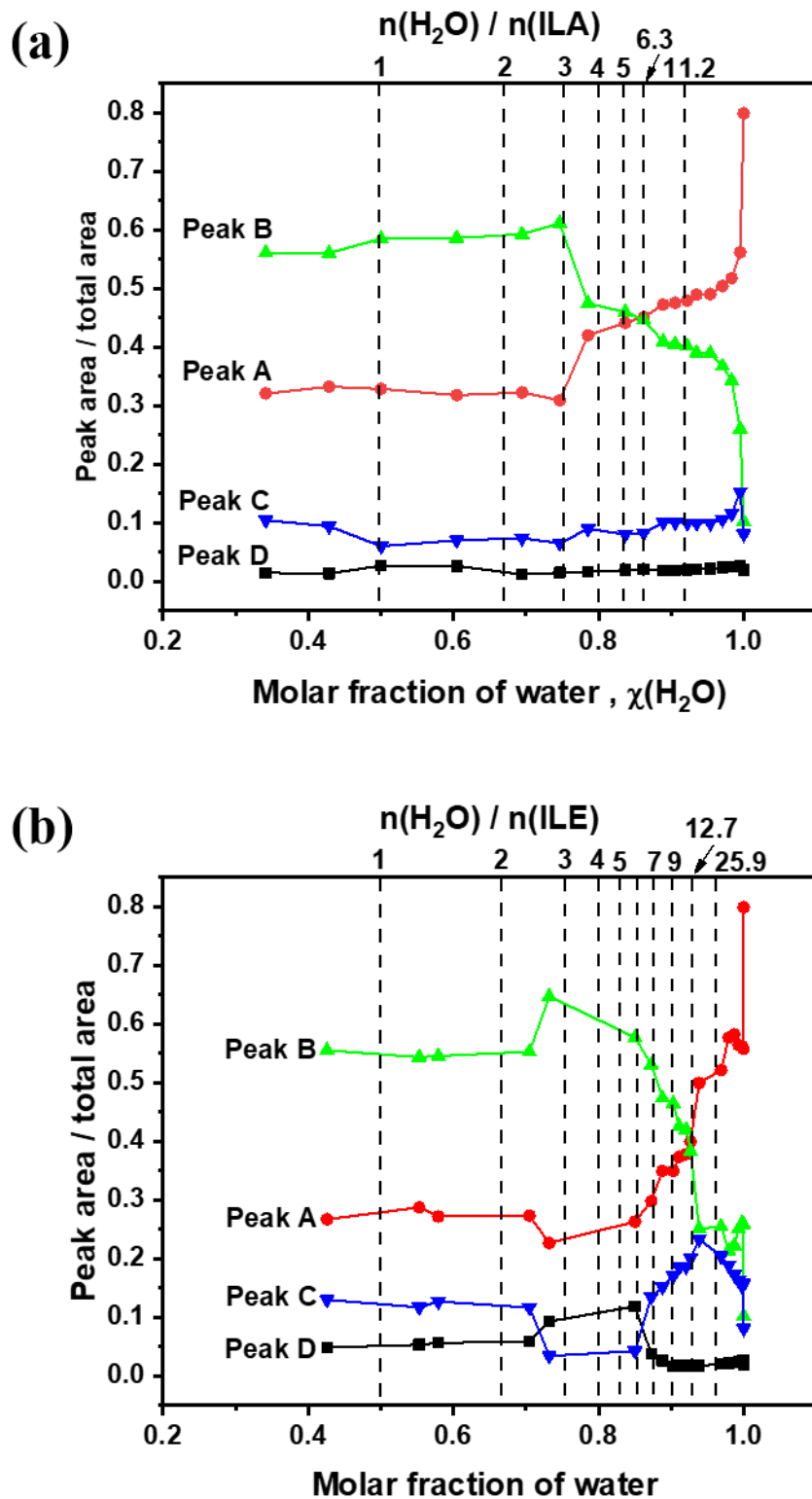


Fig. 5.11. Ratios of area of decomposed bands to total area as a function of water content for ILA – a, ILE – b.

Fig. 5.11 displays the results of the decomposition of water bands, in which the area fraction of each peak (A, B, C and D) is shown as a function of molar water

fraction in the water mixtures with ILA (**Fig. 5.11a**) and ILE (**Fig. 11 b**). Additional top x-axis represents the ratio between the molar concentrations of water and ILs, which is useful to compare experimental and modelling results. As can be seen from the figure, at least 2 regions can be noticed for ILA. At water molar fractions below $\chi(\text{H}_2\text{O}) = 0.747$, corresponding to the ratio of $n(\text{H}_2\text{O}) / n(\text{ILA}) = 3$, the contribution of all the peak areas A-D do not change and are very different from the contributions detected for pure water ($\chi(\text{H}_2\text{O}) = 1$). This indicates similar water state for all water-ILA mixtures where not more than 2 water molecules per one acetate ion is present ($n(\text{H}_2\text{O}) / n(\text{ILA}) = 2$) and probably even for the first water molecule at the second sphere bounded to these AcO-HOH structures. This is coherent with the formation of hydrogen bonds with acetate $\text{R-C}(\text{O})\text{O}\cdots\text{HOH}$ (ratio $n(\text{H}_2\text{O}) / n(\text{ILA}) = 1$) and $\text{R-C}(\text{=O})\cdots\text{HOH})\text{O}\cdots\text{HOH}$ (ratio $n(\text{H}_2\text{O}) / n(\text{ILA}) = 2$) (see **Table 5.3 a**). Similar results were already reported for imidazolium-based acetate ILs [129]. For higher water concentrations the peak A contribution becomes visibly higher and stays more or less constant up to enough high water contents. In this domain acetate ions are expected to be already saturated by water so they cannot form new H-bonds. This should lead to water clustering with more than one sphere ($\text{AcO}\cdots\text{H-OH}\cdots\text{HOH}\cdots\text{OH}_2$). Finally, for molar water fractions $\chi(\text{H}_2\text{O}) > 0.85$ the peak A strongly increases and the peak B decreases, both rapidly reaching the contributions similar to the measured in pure water, indicating that the mixture can be considered as an aqueous solution with a percolating water cluster and isolated organic moieties.

It seems hence that the evolution of the peaks contributions reflects the evolution of the water structure in the mixture: bound water for molar ratios of water and ILA up to 2, water clusters for ratios starting from ratios 3 - 4 and transition to isolated IL ions in aqueous solution for water molar fraction more than 0.85. These speculations are supported by the discussed in section 3.5. evolution of the RDF for the $\text{H}_{\text{H}_2\text{O}}\text{-O}_{\text{acetate}}$ distance (**Fig. 5.8 a**), showing significant loss of the probability to find an H-atom in the vicinity of O(acetate) with dilution.

Application of a similar approach to the water-ILE mixtures reveals some

interesting observations. The increase of the contribution of peak the A starts only after the molar ratios $n(\text{H}_2\text{O}) / n(\text{ILE})$ higher than 7, indicating that the formation of water clusters in ILE requires significantly higher water content. Interestingly, in the domain of molar ratios $n(\text{H}_2\text{O}) / n(\text{ILE})$ between 3 and 7 the contribution of the peak D, attributed to the presence of $\text{AcO}\cdots\text{HOH}\cdots\text{O}_{(\text{etheric})}$ structures, increases about twice and after this it decreases to zero. This is coherent with the idea that once the acetate anion is saturated with water, the excess water molecules are still bounded with IL, in this case with the cation via etheric oxygen (**Table 5.3**). Such a bonding reduces probability of water clustering, and hence water phase formation and its mobility.

MD simulations illustrate different structures expected for selected water contents in ILA and ILE as can be seen in dynamic boxes and RDF results (**Appendix 2 Table 5S**). Indeed, both, the first water pockets and percolating water clusters appear at higher water contents for water-ILE mixtures.

Table 5.3. Proposed structures for molecular state of water in aqueous mixtures of: ILA – (a). Intermolecular hydrogen bonds IL \cdots H $_2$ O are in red, H $_2$ O \cdots H $_2$ O in black.

(a)

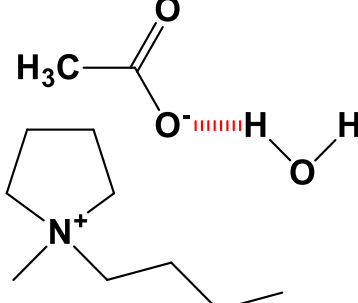
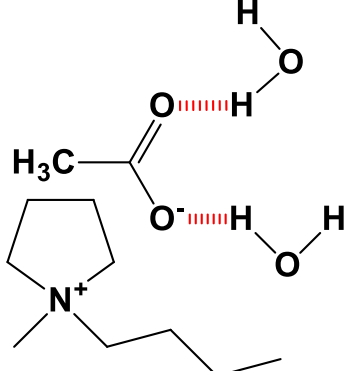
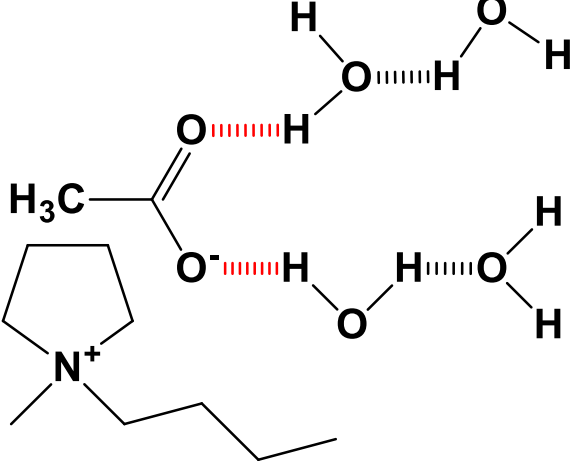
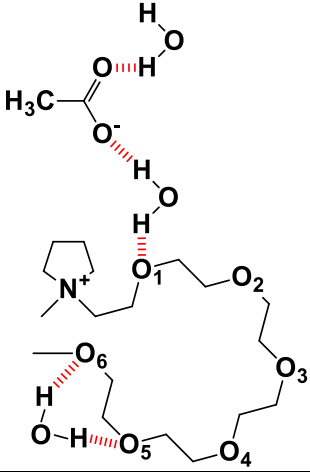
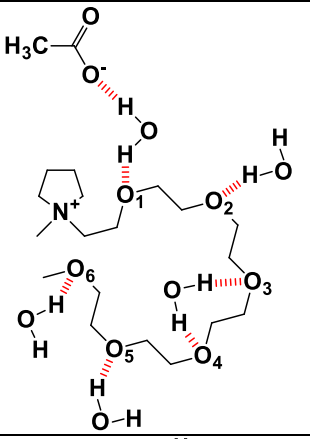
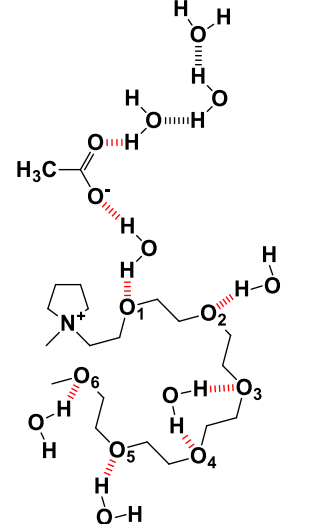
n(H $_2$ O) / n (ILA)	Examples of proposed structures
1 $\chi(\text{H}_2\text{O}) \approx 0.50$	
2 $\chi(\text{H}_2\text{O}) \approx 0.69$	
≥ 3 $\chi(\text{H}_2\text{O}) \geq 0.74$	

Table 5.3. Proposed structures for molecular state of water in aqueous mixtures of: ILE – (b). Intermolecular hydrogen bonds IL \cdots H $_2$ O are in red, H $_2$ O \cdots H $_2$ O in black.

(b)

n(H $_2$ O) / n (ILE)	Examples of proposed structures
3 $\chi(\text{H}_2\text{O}) \approx 0.50$	
5 $\chi(\text{H}_2\text{O}) \approx 0.69$	
≥ 7 $\chi(\text{H}_2\text{O}) \geq 0.87$	

4.2. Influence of molecular structure of water-RTIL mixtures on their conductivity

The proposed speculative model of water organization in mixtures with ILA and ILE fits well with the observed in **Fig. 5.2** specific conductivity evolution. Indeed, the conductivity increase with water content starts earlier and grows quicker for ILA than for ILE. Its decrease at high water contents arrives also quicker in water mixtures with ILA than with ILE. To understand this, some schematic illustrations of the water state in the mixtures are presented in **Table 5.3**. All the water molecules can be H-bounded to IL cations or anions at water to IL molar ratios lower than 3 for ILA and lower than 7 for ILE. Ionic mobility is therefore limited, and conductivity variation is very small. For higher water to IL ratios “free” water pockets appear by clustering, which are more mobile, less viscous and can also transport acetate ions. This results in a modification of conductivity. Finally, at water to IL ratios of 33 (and higher) for ILA and 145 (and higher) for ILE the solutions can be considered as diluted aqueous solutions in which hydrated IL anions ensure the charge transport.

Table 5.3 also illustrates the difference between water behavior in mixtures with ILE and ILA, explained by the water coordination with etheric oxygen. The latter was confirmed by the increase of the fraction of peak D for water to ILE molar ratios between 3 and 7, shown in **Fig. 5.11**, and by increase of the probability of H-bonds between water and etheric oxygen, shown in **Fig. 5.8**. Considering bidentate acetate anion, for molar ratios water to IL ratios up to 2 ($\chi(\text{H}_2\text{O}) = 0.500\text{-}0.667$) water molecules should be strongly bonded to acetate moieties ($\text{AcO}\cdots\text{HOH}$) in both IL. At ratios between 2 and 3 ($\chi(\text{H}_2\text{O}) = 0.667\text{-}0.750$) the water molecules in ILA can be bound to acetate only in the second coordination sphere ($\text{AcO}\cdots\text{HOH}\cdots\text{O}(\text{H}_2\text{O})$). Thus, starting from this moment, the increase of the water fraction should rapidly result in the formation of H-bonding between multiple water molecules, thus creating “free” water. In contrast, in ILE, even if acetate anions are saturated, up to 5 additional water molecules can be strongly coordinated by the

cation via etheric oxygen atoms ($\text{HOH}\cdots\text{O}_{(\text{etheric})}$). As a result, in ILE water pockets are not expected up to molecular water fractions about $\chi(\text{H}_2\text{O}) = 0.82\text{-}0.85$. Similarly, much higher number of water molecules will be necessary to isolate hydrated ions of ILE necessary to describe the behavior of the mixture as diluted aqueous solution.

Conclusions

This work illustrates in detail the interactions between water and cations of ionic liquid in water miscible ionic liquids with a wide range of water concentrations. Two new water miscible acetate-based ionic liquids with aliphatic substituted and etheric substituted cation ($[\text{BMPyr}]\text{OAc}$ and $[\text{mPEG}_n\text{MPyr}]\text{OAc}$) were proposed and synthesized. Electrochemical potential window of as prepared electrolytes was established as 2.88 V for $[\text{BMPyr}]\text{OAc}$ and 2.26 V for $[\text{mPEG}_n\text{MPyr}]\text{OAc}$. Molecular state of water in water – IL mixtures in a wide concentration range was characterized with help of ATR-FTIR spectroscopy, MD modeling and compared with specific conductivity. The results demonstrated that water molecules can strongly interact not only with acetate anions but also with etheric-substituted MPyr cations. Molecular organization of the electrolyte and its conductivity strongly depend on the water content and this dependence differs between ILs with aliphatic and etheric substituted cation. More in details:

1) For molecular ratios between water and ionic liquid $n(\text{H}_2\text{O}) / n(\text{IL}) \leq 3$ both ATR-FTIR spectra evolution with water dilution and MD simulations indicate strong preferential H-bonding of water molecules to acetate anion. In this concentration range the conductivity of the electrolyte does not vary significantly with water content.

2) For molecular ratios between water and ionic liquid $n(\text{H}_2\text{O})/n(\text{IL}) > 3$ both infrared spectra and MD simulations suggest different molecular structure evolution for ionic liquids with etheric substituted and aliphatic substituted cation.

In [mPEG_nMPyr]OAc water molecules stay coordinated by oxygen atoms of etheric groups in the cation which can create H-bonds with up to 5-6 molecules. These H-bonds are initially less probable than water-acetate H-bonds, however, in contrast to the water - acetate, their relative probability increases with dilution. As a result, water pockets do not form up to $n(\text{H}_2\text{O}) / n(\text{ILE})=7-8$. This is coherent with a very insignificant conductivity increase with dilution of [mPEG_nMPyr]OAc for this domain.

In contrast, in mixtures of water with aliphatic substituted [BMPyr]OAc, probability of H-bonding between water molecules ($\text{HOH}\cdots\text{O}_{(\text{H}_2\text{O})}$) increases and H-bonding between water and acetate ($\text{HOH}\cdots\text{OAc}$) decreases with dilution. This is expected to result in the formation of water clusters starting from $n(\text{H}_2\text{O})/n(\text{IL})=3$. This correlates with the experimentally observed conductivity growth with dilution in this concentrations range.

Water clusters form hence at significantly higher water contents in [mPEG_nMPyr]OAc than in [BMPyr]OAc because of water-cation interactions.

3) Once “free” water phase with water-water hydrogen bonds is formed, it very rapidly grows in both ILs, which is expected decrease viscosity and hence increase conductivity. In the formed water clusters charge transfer is ensured only by hydrated ions (mainly acetate anion because of its relatively higher mobility if compared to the cation), which should lead to the observed conductivity decrease at high dilutions. Transition from the conductivity increase with water (behavior expected for slightly water diluted IL) to the conductivity decrease (behavior typical for diluted aqueous solutions with H₂O fraction increase) occurs at molar water to IL ratios $n(\text{H}_2\text{O}) / n(\text{IL})=33$ for aliphatic substituted [BMPyr]OAc and at $n(\text{H}_2\text{O}) / n(\text{IL})=145$ for [mPEG_nMPyr]OAc.

Finally, etheric substitution in IL cation can significantly modify molecular structure of water - IL mixtures and this structure permanence versus dilution.

Chapter 6:

Synergic effect of ionic liquid (IL) cation and anion inhibits negative difference effect on Mg in water - IL mixtures

This chapter answers the questions “What are the mechanisms of the NDE or of its inhibition in water-hydrophilic IL mixtures?”

*The results of this chapter are prepared in the form of the article submitted to
Corrosion science.*

Synergistic effect of ionic liquid (IL) cation and anion inhibits negative difference effect on Mg in water - IL mixtures

D. Kurchavov^a, U. Rustambek^a, A. Ottochian^b, G. Lefèvre^a, A. Seyeux^a, I. Ciaffini^b, P. Marcus^a, V. Lair^a, P. Volovitch^{a*}

^a *Chimie ParisTech, PSL University, CNRS, Institut de Recherche de Chimie Paris (IRCP), F-75005 Paris, France*

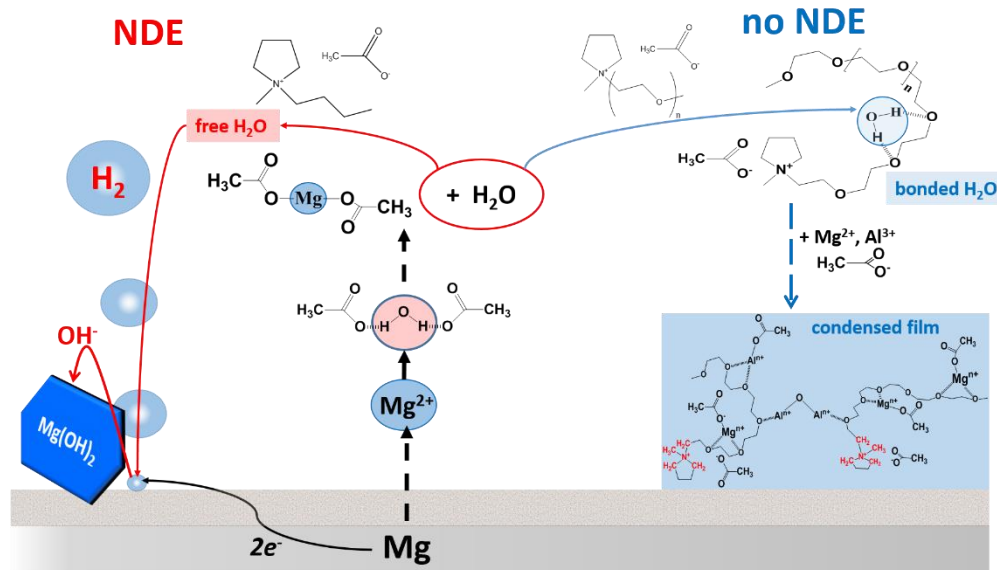
^b *PSL University, Chimie ParisTech, CNRS UMR 8060, Institute of Chemistry for Life and Health Sciences, CSB2D team, 75005 Paris, France*

*Corresponding author.

E-mail addresses: polina.volovitch@chimieparistech.psl.eu (P. Volovitch)

Abstract:

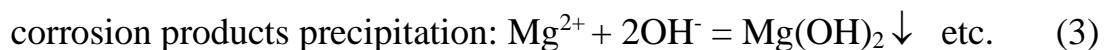
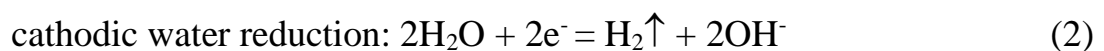
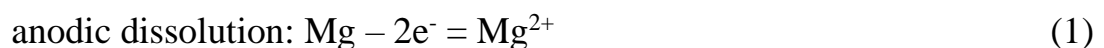
Electrochemical measurements and live imaging demonstrated strong negative difference effect (NDE) on Mg alloys in [mPEG_nMPyr]ClO₄-H₂O and [BMPyr]OAc-H₂O but not in [mPEG_nMPyr]OAc-H₂O mixtures. Role of [mPEG_nMPyr]⁺ and its synergy with OAc⁻ for Mg reactivity in water-ionic liquid mixtures was detailed combining surface analysis by ToF-SIMS, surface and solution analysis by vibration spectroscopy and molecular dynamics (MD) simulation. Two complementary mechanisms of inhibition were proposed: (1) etheric oxygen in [mPEG_nMPyr]⁺ bounds free water, liberated from HO-H...OAc⁻ complexes by leached Mg²⁺; (2) condensed film, formed by [mPEG_nMPyr]⁺ and OAc⁻ coordinated with Mg²⁺ and Al³⁺, reduces its transport to the surface.



Keywords: *Mg alloys, ionic liquids, PEG, acetate, Negative Difference Effect (NDE), mechanisms*

1. Introduction

Control of Mg reactivity in the presence of liquid films is essential for multiple applications (engineering, biomedicine, energy storage, etc...) [4–6], because its poor corrosion resistance and high electrochemical reactivity determines the service time. Corrosion of Mg is usually described by at least three parallel processes: anodic dissolution, cathodic hydrogen evolution reaction (HER) (2) and precipitation of corrosion products (3) [37].



While following the theory of electrochemical kinetics, Butler-Volmer equation, rate of cathodic reactions decreases exponentially with increasing anodic potential [9], Mg alloys in aqueous media exhibit the opposite behavior: HER increases with anodic polarization (vs. open circuit potential, E_{oc}) [23]. This phenomenon was called Negative Difference Effect (NDE) or anomalous hydrogen evolution (HE).

This uncontrolled cathodic activity under anodic polarization could be particularly harmful for Mg-based energy storage systems. Formed corrosion products passivate the metallic surface and increase the anode's volume. Hydrogen reduction leads to the significantly high mass loss to that calculated from Faraday's law for 2 electron transfer process and, therefore, to the loss of the utilization efficiency of Mg anodes [216].

Numerous models have been proposed to elucidate this phenomenon in aqueous electrolytes (see for instance recent review of Song et al. [13]), however there is no generally accepted universal theory describing the mechanism of the NDE. The existing proposed NDE theories include: partially protective surface film [24], uni-positive Mg^+ ion [25,26], Mg hydride formation by a chemical reaction (MgH_2) [27,28], particle undermining [29], incomplete film containing univalent Mg^+ ion [30], self-corrosion [31], enhanced cathodic catalytic activity [32], the impurity particle cathode [8,32–34] and Mg^*H and Mg^*OH catalysts [35].

While the literature is abundant about NDE in aqueous electrolytes, it is not largely discussed in non-aqueous electrolytes, such as ionic liquids (ILs). ILs are potentially interesting for Mg alloys applications, particularly for energy storage. Normally, ILs consist of organic cations and organic or inorganic anions and are considered as environmentally friendly compounds with large electrochemical window, high flash point and low vapor pressure [14–16]. Thus, they seem to be good candidates to employ as electrolyte in Mg-based energy storage systems [217]. The interest of ILs is that their physico-chemical properties can be adjusted by the variation of ions combination. Additionally, the use of non-aqueous electrolytes reduces corrosion rate of the anode [131,132] and is expected to prevent HE on the anode and its passivation because of formation of Mg oxides and hydroxydes. Anhydrous electrolytes based on ILs, especially ILs containing etheric groups, were reported to support the most important reaction of secondary batteries, Mg stripping, with high columbic efficiency [136,137].

Practical application of anhydrous ILs is however limited by their high viscosity and low conductivity (generally, few mS/cm). Moreover, some ILs are unstable in humid atmospheres. So, application of stable water-miscible ILs can be interesting in order to decrease viscosity and improve conductivity of the electrolyte. Dilution of several sustainable ILs by small amount of water did not result in significant decrease of electrochemical stability window [113,153–156]. Lower viscosity and higher conductivity of IL-water mixtures is expected to increase Mg reactivity. However, in some H₂O diluted ILs, hydrogen evolution on Mg similar to aqueous solutions has been reported [134]. But HE and the concentrations above which it occurs have never been studied in detail.

In our previous work [218], we have shown that even for relatively high water content (10 wt. %), the NDE can be suppressed or even blocked depending of the nature of IL's cation and alloy matrix. In the mixture of hydrophilic aliphatically (butyl (-C₄H₉)) substituted N-methylpyrrolidinium acetate ([BMPyr]OAc) with 10 wt. % of H₂O, commercially pure Mg (CP Mg) and AZ61 revealed cathodic hydrogen evolution similar to aqueous electrolytes. However, the same alloys in hydrophilic poly-etheric (-O-CH₂-CH₂-)_n) substituted cation ([mPEG_nPyr]OAc) with 10 wt. % H₂O, showed suppressed NDE on CP Mg and HE blocked on AZ61 at E_{oc} and under anodic polarization. At the same time, Mg(OH)₂ was detected after the experiment on commercially pure Mg in both electrolytes, but not on AZ61 alloy. The particular role of the cation and anion in corrosion mechanism and the role of Al alloying element remains unclear.

The most intuitive hypothesis, which could explain the NDE inhibition inherited from aqueous corrosion, is related to the modification of the metallic surface via formation of adsorbed films and/or dissolution of noble impurities or corrosion products. For example, for molecules containing carboxylate anions, a high inhibiting efficiency was assigned to the blocking of microgalvanic coupling due to the dissolution of metallic and oxide heterogeneities by the formation of soluble Mg and Fe complexes [70]. Formation of soluble Fe and Mg carboxylate

complexes was confirmed by in situ vibration spectroscopy [72]. Adsorption of organic molecules on the $\text{Mg}(\text{OH})_2$ crystals was proposed to reduce crystal growth, leading to compact films, thus explaining the observed decrease of Mg corrosion by sodium salts of carboxylic acids [72] and sodium dodecyl sulfate (SDS) [219]. In the presence of 2,5 pyridine carboxylate (PDCA) inhibition was correlated with the formation of a conjugated film coordinated by leached Mg^{2+} ions [72]. Corrosion inhibition of Mg was attributed to the formation of thin self-assembling adsorbed films in the presence of sodium diethyldithiocarbamate and sodium acetate [74], 6-ring organic compounds containing N-heteroatom [220], SDS [75] and sodium dodecylbenzenesulfate (SDBS) in ethylene glycol solutions [76]. In these works, chemisorption of polar groups and formation of a hydrophobic barrier of alkyl chain, limiting diffusion, were considered. Similar inhibition mechanisms were reported for other surfactants based on carboxylic acids (R-COO^-), phosphonic acids (R-PO_3^{2-}), sulfonic (R-SO_3^-) anions [71,221]. For Al-containing alloys, which surface can be enriched by Al and its oxides [169], specific interactions of organic molecules with Al could play an important role. Stable Al complexes with carboxylates were reported for Al [34], which explains high passivating effect of carboxylic acids on Al corrosion [223]. In alkaline solutions the inhibition efficiency increases with the number of carboxylic groups in the molecule [224] and with the carbon chain length [225]. Inhibition action of quaternary amines on Al is also known [226].

On the basis of this knowledge, one can expect that the surface film, formed on commercially pure Mg (CP Mg) and AZ61 alloy in water-IL mixtures, can significantly differ from the surface film, formed in aqueous solutions. It's composition and structure can be very complex and they can be present in very different forms as adsorbed monolayers, like described for tensioactifs [76], as surface complexes [34], or as thicker low adherent condensed film, coordinated by leached cations, like in case of PDCA [72], or even as precipitated $\text{Mg}(\text{OH})_2$ film modified by organic molecules [72,227]. A detailed surface analysis is therefore

necessary to define the nature of the surface film and to verify the role of organic cation and organic anion in its inhibiting action. In the previous work [218] we have used Raman spectroscopy to access $\text{Mg}(\text{OH})_2$ distribution and to prove the presence of both, anions and cations of IL in the humid surface film. The detailed analysis of the film composition only by vibration spectroscopy needs however to be completed, in particular because its spatial resolution in depth is insufficient to verify the film thickness and the evolution of its in depth composition. Previously, surface analytical technics such as Time-of-flight secondary ion mass spectrometry (ToF-SIMS) were successfully applied to detail the nature of the surface films formed during corrosion and degradation of metallic materials and to understand the inhibition mechanisms, especially for Mg-alloys [39,133,145,146]. These surface sensitive technique is therefore selected to complete the surface characterizations in the present work.

Another hypothesis, explaining NDE decreasing in water – IL mixtures, can be more specific for organic solutions, in which water electrochemical reactivity can be affected by strong interaction between water and ILs moieties. For instance, hydrogen bonds, can alter the reaction of cathodic water reduction (2). Usually, water molecules interact predominantly with anions of ILs [116]. For substituted acetate anions, the strongest H-bonding was found for trifluoroacetate (CF_3CO_2^-). Hydrogen bonding (H-bonding) between acetic anions and water [129,200] is well known, however, some evidence of weak H-bonding between water and aliphatic cation was also reported [128]. Insertion of etheric groups in the structure of cation can be also followed by formation of hydrogen bonds between oxygen of etheric groups water molecules [19]. In our previous work [**Chapter 5**] we have demonstrated by ATR-FTIR spectroscopy, conductivity measurement and molecular dynamic (MD) modelling, that water molecules can create H-bonds with acetate anions and etheric groups of the cation in the studied ILs. Thus, ambivalent function of etheric substituted chain of the cation might be expected: complexation

of releasing Mg (or even Al) ions and water binding through the intermolecular hydrogen bonds.

Finally, the role of cation and anion in the above discussed mechanisms (surface film formation, water bonding and complexation of metallic leached cations) need experimental and theoretical verification.

The main objective of the present work is to understand the differences in the behavior of AZ61 and CP Mg in aliphatic substituted and etheric substituted MPyr acetate and to understand the role of cation and anion in the NDE and the NDE inhibition. To reach this, the formulated above hypotheses of the mechanism of the NDE suppression via formation of a surface film and via the electrolyte modification are verified. In particular,

- 1) the nature of the surface films formed on different alloys in two different ILs is detailed with ToF-SIMS;
- 2) the importance of cation and anions synergistic effect for the NDE suppression is verified by additional experiments in the mixture of water with etheric substituted cation and perchlorate anion [mPEG_nMPyr]ClO₄ - 10 wt.% H₂O;
- 3) the interactions of water and the IL cations and anions in presence of released Mg²⁺ are described with Molecular Dynamics Simulations;
- 4) two complementary mechanisms of the NDE suppression are proposed.

2. Materials and methods

2.1 Materials

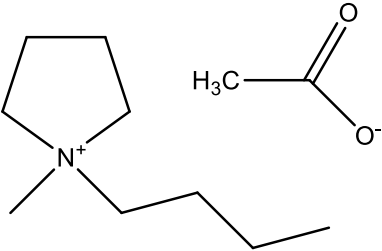
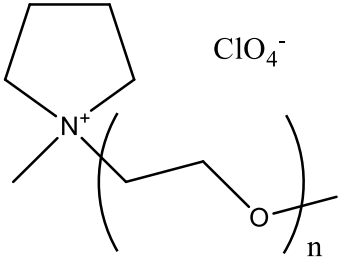
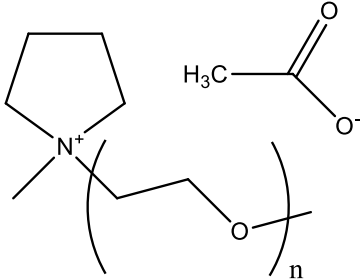
General procedure of the ILs synthesis is published in our previous work and elsewhere [140,141].

All the electrochemical experiments were made in the IL-water mixtures containing 10 weight (wt.) % of Milli-Q water (18.2 Ω).

The work considers the mixture of 10 wt. % water with three different ionic liquids presented in **Table 6.1**.

In order to clarify if the NDE inhibition reported in [218] is governed only by the etheric substituted cation or a synergic effect of anion and cation is important, additionally to the previously discussed [BMPyr]OAc and [mPEG_nMPyr]OAc, similar to the reported in [218] experiments were conducted in the mixture of [mPEG_nMPyr]ClO₄-H₂O. Perchlorate anion was selected as an inorganic anion with low donor number and forming weak hydrogen bonds with water [139,210]. Its bonding with Mg-ions as well as hydrogen bonding with H₂O molecules are supposed to be negligible.

Table 6.1. Graphical structures of used ILs.

Ionic liquid (short name)	Verified hypotheses	Graphical formula
[BMPyr]OAc	Effect of acetate anion	
[mPEG _n MPyr]ClO ₄	Effect of etheric cation	
[mPEG _n MPyr]OAc	Synergistic effect of etheric cation and acetate anion	

*n – means variable numbers of etheric groups found by MALDI-TOF, $4 \leq n \leq 16$ with an average value $\langle n \rangle = 7$.

The compositions of the alloys used in this and previous work are presented in **Table 6.2**. Commercial purity Al and Mg were used to verify the effect of alloying elements on the reactivity. Foils with area of 1×1 cm were grinded by 800, 1200, 2400, 4000 SiC polishing paper grits using absolute ethanol as a lubricant, rinsed with ethanol and dried. CP Mg and CP Al foils were supplied by GoodFellow.

Table 6.2. Metallic materials used in the work.

Sample name	Al ppm	Zn ppm	Mn ppm	Si ppm	Fe ppm	Ca ppm	Mg wt. %
CP Mg	70	<20	170	50	280	-	Balance
AZ61	62.000	7.400	2.300	40	40	1.3	Balance
CP Al	Balance	Cu- 0.3	-	0.8	0.3	-	1.2

2.2 Electrochemical experiments

Electrochemical experiments and setup design are described in [218]. A three-electrodes home-made electrochemical cell was designed and printed using inert PLA (polylactic acid) filament. The working electrode chamber was filled by the IL electrolyte containing 10 wt.% of water. Counter electrode chamber was filled by 0.5 M of Mg salts with the same anion as the anion in the tested IL. Working electrode and counter electrode chamber were separated by glass frits. The junction potential for perchlorate containing electrolyte [mPEG_nMPyr]ClO₄ - H₂O // 0.5M Mg(ClO₄)₂-H₂O) was measured as 86 mV.

For CP Al the cycling started after the open circuit potential (E_{oc}) measurements within one hour. Cycles consisted of three polarizations at potential $E=+400$ mV (vs. E_{oc}). Each polarization lasted 20 minutes and was followed by 15 minutes of the E_{oc} measurement.

Mg alloys (CP Mg and AZ61) and pure Al were used as working electrodes (geometric exposed area 0.196 cm² was delimited by PortHoles electrochemical sample mask (supplied by Gamry), aqueous AgCl/Ag (in saturated KCl) reference

electrode and platinum rounded wire ($S \approx 1.23 \text{ cm}^2$) as a counter electrode. Electrical contact with the working electrode was ensured by a single sided copper tape.

All the electrochemical experiments were conducted using Gamry 3000 potentiostat at room temperature and ambient atmosphere for at least 3 times. Hydrogen evolution at open circuit and under anodic polarization was surveyed in situ by time lapse microscopy (TLM). HD USB microscope with 2 MP CMOS detector and a 4000 K white LED enlightenment was coupled with the electrochemical cell. Images were taken every 30 seconds during the experiments.

2.3 Chemical characterization by Raman spectroscopy.

Raman spectra were made with a Renishaw Confocal Raman Microscope InVia using red laser (HeNe, 633 nm, 17 mW power) and WiRE 4.2 software. Illumination and observation of the surface were performed through a microscope objective Leica of $\times 50$ magnification and numerical aperture (NA) of 0.75. The analysis of ILs, droplet of samples (approximately 15 μl) was placed on Si-plate support and covered by a transparent glass. Laser beam was focused on the liquid phase. The exposure time was 10 seconds and 25 spectra were recorded of each sample.

For each combination of the material and the electrolyte, the characterizations were made at least on 3 different samples. The results were reproducible and for simplicity only one spectrum for each combination is shown in the next sections.

2.4 ToF-SIMS

The measurements were provided using a ToF-SIMS V spectrometer (ION-TOF GmbH, Muenster, Germany). The operation pressure in the chamber was around 10^{-9} mbar (ultra-high vacuum, UHV). Ion mass spectra (MS) and depth profiles were recorded. A Bi^+ pulsed primary ions gun with a 45° angle to the surface was used for analysis. The surface sputtering was done using a Cs^+ gun, also oriented with a 45° angle to the surface. Atomic and molecular ions (secondary ions),

characteristic of the surface composition, were emitted and analyzed. Their mass/charge (m/z) ration is measured by their time of flight to reach the detector.

Three different types of analysis were carried out: positive and negative ions mass spectra (MS) on the top surface and negative ions depth profile. Negative and positive MS were obtained by scanning a $500 \times 500 \mu\text{m}^2$ area using a 20 keV Bi^+ ion beam delivering 1.2 pA current. Negative ions depth profiles were conducted using the spectrometer in dual beam mode, meaning that Bi analyzing gun and Cs sputtering gun scan successively the surface. Thus, for generating the $300 \times 300 \mu\text{m}^2$ crater, the 2keV Cs^- ion beam delivering 100 nA was used. The analysis was realized by sputtering a $100 \times 100 \mu\text{m}^2$ area at the bottom of the crater using a 20keV Bi^+ ion beam delivering 1.2 pA current. The spectra were calibrated using, at least, 5 well identified peaks in the MS. In depth profiles, the intensities of all compounds are plotted versus sputtering time. Data treatment and post processing were carried out using the Ion-Spec software (version 6.9).

2.5 Modeling methodology

All the compounds used for simulations were drawn using Gauss View 6 [186]. A calculation with Gaussian 16 [187] in junction with Antechamber module [188,189] was performed to assign the Restrained Electrostatic Potential (RESP) charges of each atom. As the protocol requires [190], Gaussian optimizations were carried out at Hartree Fock level standard 6-31* basis.

Different simulations of one hundred ions pairs of IL cations and anions with a various number of water molecules and Mg^{2+} ions were performed (**Appendix 3, Table 3S**). The electroneutrality of the systems was reached by addition OH^- anions in a molar ratio $n(\text{OH}^-) / n(\text{Mg}^{2+}) = 2:1$. The starting configuration were created with the PACKMOL package [191].

The molecular dynamic simulations were instead carried out with Large-Scale Atomic/Molecular Massively Parallel Simulator (LAMMPS) package [192,193]. The equilibration, 1 ns long or even more, was made at ambient conditions ($T =$

298.15 K or 25 °C) in a canonical NVT ensemble (amount of the substance N, volume V and temperature T are conserved) with volume reflecting the real densities values, found experimentally. Production runs, in NVE canonical ensemble (amount of the substance N, constant energy E, constant volume E) were performed for at least 1 ns. The total energy drift $E_{\text{tot}} / E_{\text{tot}}$ was checked to be less than 10^{-6} in the worst case.

Structural characterization was realized through the observation of radial distribution function G(r) of selected atoms. Its definition for the two atom α and β is given by following formula:

$$G_{\alpha,\beta}(r) = \frac{1}{N_{\alpha} \cdot N_{\beta}} \langle \sum_{i,j}^{N_{\alpha}, N_{\beta}} \delta(r_{ij} - r) \rangle \quad (4)$$

where the $\langle \dots \rangle$ indicates the usual ensemble average, and $\delta(x)$ is the Dirac delta function, r_{ij} is the distance between an α and β atoms whereas N_{α} and N_{β} are respectively their number in the sample box.

3. Results

3.1 Magnesium reactivity in $[m\text{PEG}_n\text{MPyr}]\text{ClO}_4$

3.1.1 In situ reactivity of CP Mg and AZ61 from electrochemical measurements and live imaging in $[m\text{PEG}_n\text{MPyr}]\text{ClO}_4\text{-H}_2\text{O}$ mixture

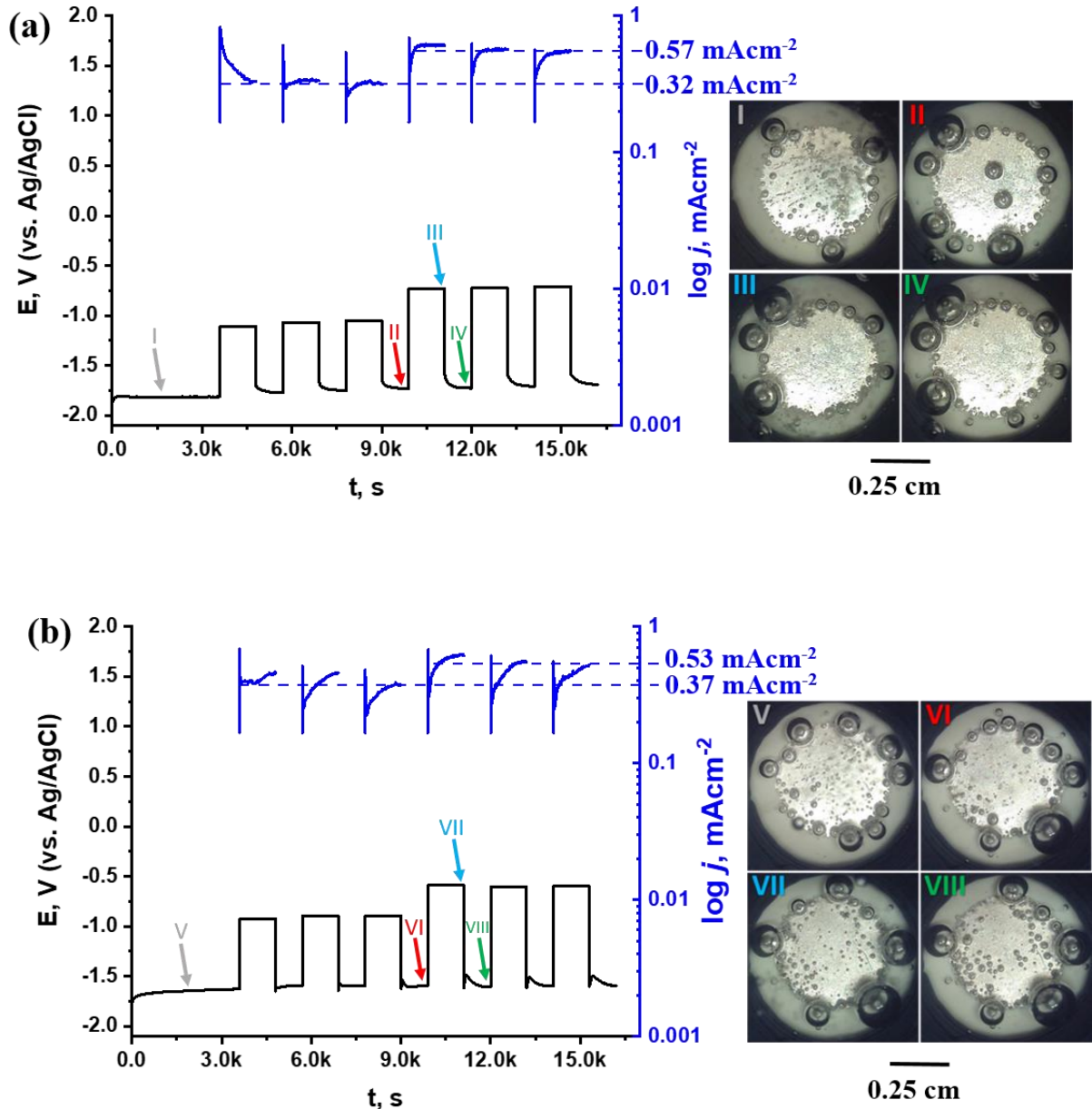


Fig. 6.1. Electrochemical response of (a) CP Mg and (b) AZ61 in $[m\text{PEG}_n\text{MPyr}]\text{ClO}_4\text{-H}_2\text{O}$ mixture and typical TLM images of the surface taken during the experiments. The time at which the selected images were taken is indicated by arrows (I-VIII) on the potential evolution curve.

The E_{oc} reaches a quasi-steady state within 10 minutes of the experiment. $E_{oc} = -1.81$ V and $E_{oc} = -1.64$ V vs. Ag/AgCl for CP Mg and AZ61, which is significantly higher than the values, previously observed in [mPEG_nMPyr]AcO-H₂O mixtures ($E_{oc} \approx -2.0$ V for both materials [218]).

Anodic current density stabilizes at 0.32 mAcm^{-2} and 0.37 mAcm^{-2} for CP Mg and AZ61 respectively under anodic polarization at applied potential $E = +0.7$ V vs E_{oc} and even higher at $E = +1$ V vs. E_{oc} (0.57 and 0.53 mAcm^{-2} for CP Mg and AZ61 respectively). However, the surface of AZ61 seems to be activated with polarization time, which was not the case in [mPEG_nMPyr]OAc-H₂O mixture. The presence of acetic anion therefore significantly modifies anodic reactivity.

Images I and V in **Fig. 6.1 a** and **Fig. 6.1 b**, captured during E_{oc} measurement for CP Mg and AZ61 respectively, display abundant hydrogen bubbles. This behavior is similar to the observed in [mPEG_nMPyr]OAc-H₂O. The images taken under anodic polarization (**Fig. 1 a** images II – IV and **Fig. 1 b** images VI – VIII) indicate non-intensive but still visible, in particular in the dynamic mode (see videos, will be presented), bubbles release under both E_{oc} measurement and anodic polarization. The NDE is hence not suppressed in this electrolyte. In contrast to the observed in [mPEG_nMPyr]OAc-H₂O) formation of a dark film, no film is detected in the [mPEG_nMPyr]ClO₄-H₂O mixture.

<video: x100_CPMg_mPEGMPyrClO4.gif>

<video: x100_AZ61_mPEGMPyrClO4.gif>

3.1.2 Surface state of CP Mg and AZ61 from vibrational spectroscopy after electrochemical experiments in $[m\text{PEG}_n\text{MPyr}]\text{ClO}_4\text{-H}_2\text{O}$

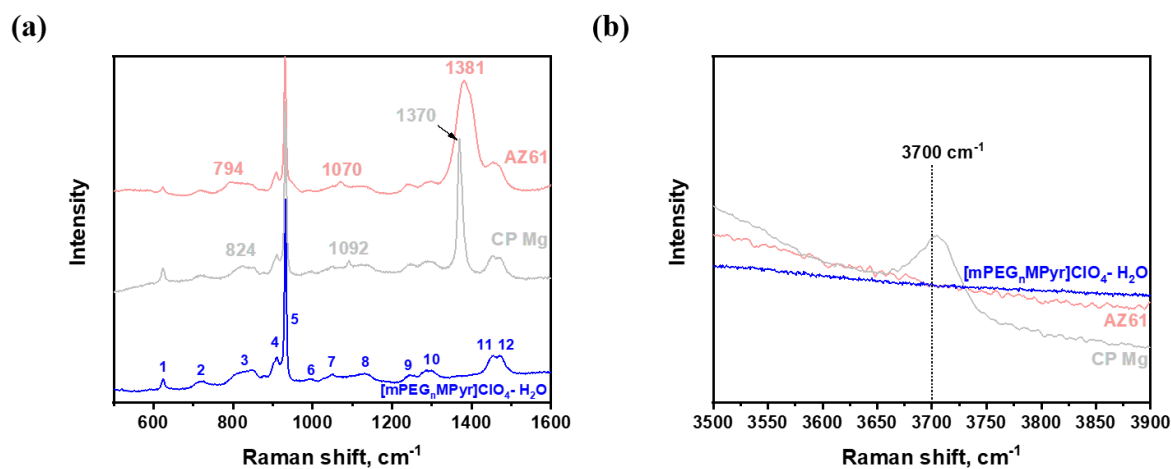


Fig. 6.2. Typical Raman spectra recorded on the surfaces of CP Mg and AZ61 (as indicated) after electrochemical experiment in $[m\text{PEG}_n\text{MPyr}]\text{ClO}_4 - \text{H}_2\text{O}$ within $500\text{-}1600\text{ cm}^{-1}$ (a), $3500\text{-}3900\text{ cm}^{-1}$ (b). The spectrum of $[m\text{PEG}_n\text{MPyr}]\text{ClO}_4 - \text{H}_2\text{O}$ mixture is shown for comparison.

Fig. 6.2 a represents Raman spectra recorded on the surface of CP Mg and AZ61 within the range $500\text{-}1600\text{ cm}^{-1}$. Attribution of the band is detailed in **Table S5** in **Appendices 3**. First of all, all the peaks typical of IL are visible and a slight modification of peak $780\text{-}860\text{ cm}^{-1}$ attributed to C-O-C stretching vibrations of PEG-fragment of the cation [136,164], is visible. On AZ61 the maximum of this band shifts to 794 cm^{-1} . On CP Mg this signal narrows and the maximum is at 824 cm^{-1} . At the same time, low intensive new bands at 1070 cm^{-1} and 1092 cm^{-1} appear on AZ61 and CP Mg respectively. These bands are between peaks 7 and 8 (on the blue spectra, 1049 and 1136 cm^{-1}) which are attributed to C-C, C-O and C-H bending vibrations of PEG (see **Table S6** in **Appendices 3**). Thus, some interaction would exist between the etheric groups and the surface (or the ions released during anodic polarization). Similar evolution presents on both CP Mg and AZ61 (new bands at 1099 cm^{-1} and 1109 cm^{-1} on AZ61 and CP Mg respectively).

The position of intensive peaks at 1381 cm^{-1} and 1370 cm^{-1} on AZ61 and CP Mg respectively correlates with the position of the C=O group vibration, however its origin needs further study. It has been previously reported that etheric group in

the presence of Mg^{2+} -ions can undergo nucleophilic attack by OH^- ions and produce carboxylic, carbonyl or ester groups [20]. The fact that no other intrinsic bands have been observed can be interpreted as the formed $C=O$ groups are probably present as adsorbed species and other vibrations becomes inactive because of the symmetry modifications (see for instance [228]). Such an explanation stays however insufficient because these bands were not observed on the surface of the same alloys after the electrochemical experiments in $[mPEG_nMPyr]OAc-H_2O$. If the hypothesis of the electrolyte attack by leached Mg^{2+} is accepted for $[mPEG_nMPyr]ClO_4 - H_2O$, the absence of such an attack in $[mPEG_nMPyr]OAc-H_2O$ can be regarded as an indication of a protective action of OAc^- for etheric groups, probably thanks to the strong binding of Mg^{2+} in $Mg(OAc)^+$ and $Mg(OA)_2$ complexes.

Similarly, to acetate ILs [218], **Fig. 6.2 b** evidences $Mg(OH)_2$ on the CP Mg and its absence on the AZ61. The peak position at 3710 cm^{-1} indicates that $Mg(OH)_2$ is nanocrystalline [144]. These observations are also supported by ATR-FTIR spectroscopy (see **Appendices 3 Fig. S5, Table S7**).

3.2 In situ reactivity of CP Al from electrochemical measurements coupled with live imaging in $[mPEG_nMPyr]OAc-H_2O$ and $[mPEG_nMPyr]ClO_4-H_2O$ mixtures

In order to understand the effect of the alloy composition, in particular of Al alloying in AZ61, similar electrochemical experiments were repeated on CP Al in $[mPEG_nMPyr]OAc-H_2O$ and $[mPEG_nMPyr]OAc-ClO_4$. **Fig. 6.3** displays the electrochemical response of CP Al in $[mPEG_nMPyr]OAc-H_2O$ and $[mPEG_nMPyr]ClO_4-H_2O$ mixtures and live images taken during the experiments (**Fig. 6.3** images IX-XIV). As can be seen from the figure, the reactivity of CP Al is completely blocked under E_{oc} conditions and under anodic polarization at $E=+0.4\text{ V}$ (vs. E_{oc}) in $[mPEG_nMPyr]OAc-H_2O$. In $[mPEG_nMPyr]ClO_4-H_2O$ CP Al stays reactive. Abundant hydrogen evolution under anodic polarization is also observed. The probable reason of these differences is the difference in the surface state, such as formation of stable Al-acetate complexes [223]. This hypothesis is also supported

by Raman spectra recorded after the electrochemical experiment in $[\text{mPEG}_n\text{MPyr}]\text{OAc-H}_2\text{O}$. Raman shifts nearby 650 cm^{-1} , 917 cm^{-1} , 1407 cm^{-1} attributed to acetic group vibrations are slightly shifted when compared to the electrolyte, indicating a possible chemisorption (**Appendix 3, Fig. S6**). Attributions of other Raman shifts can be found in supplementary information and [218].

Thus, the electrochemical results clearly demonstrate that not only the etheric substitution in the IL cation, but a synergistic effect of etheric substituted cation and acetic anions plays a crucial role in the NDE suppression on Mg-alloys in water – IL mixtures.

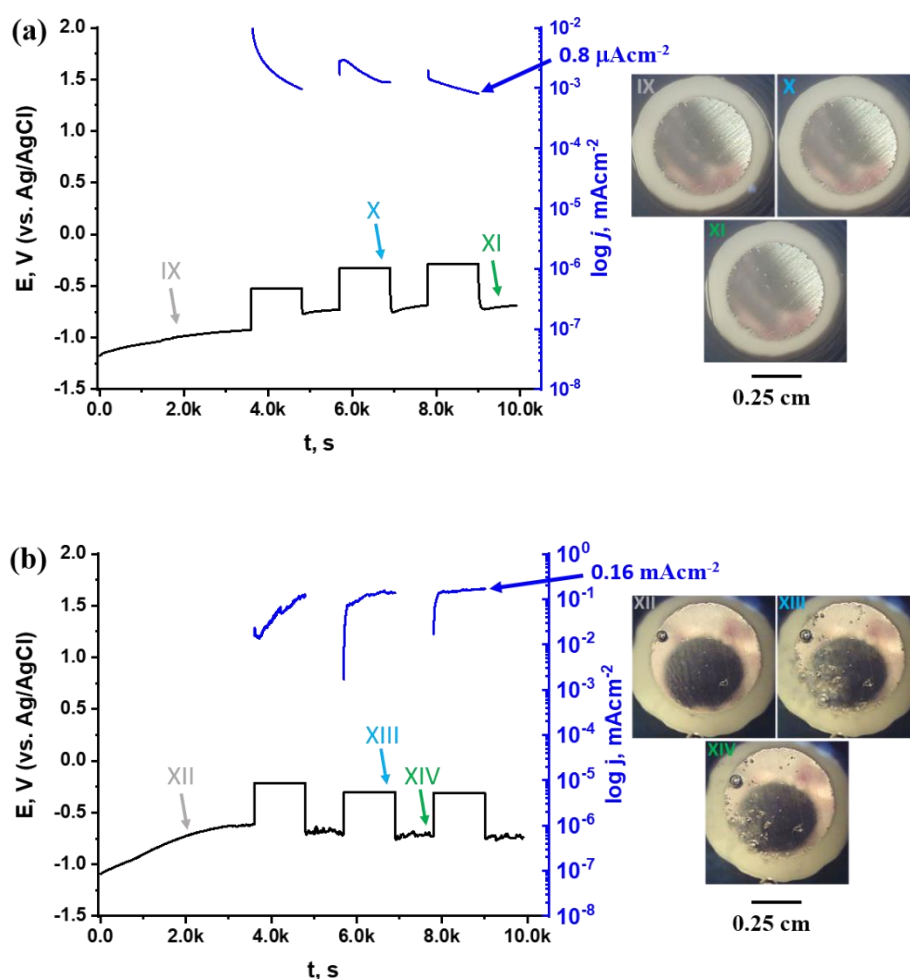


Fig. 6.3. Electrochemical response of CP Al in: $[\text{mPEG}_n\text{MPyr}]\text{OAc-H}_2\text{O}$ – (a); $[\text{mPEG}_n\text{MPyr}]\text{ClO}_4\text{-H}_2\text{O}$ – (b) mixture and typical TLM images of the surface taken during the experiments. The time at which the selected images were taken is indicated by arrows (IX-XIV) on the potential evolution curve.

3.3. Surface film analysis by ToF-SIMS.

Positive and negative MS of the surfaces after the electrochemical experiments are presented in **Appendix 3, Figs. S7**. The observed in positive MS peaks mainly reflect the presence of the $[\text{mPEG}_n\text{MPyr}]^+$ cation. The interpretation of negative ion MS is much more complex. The structures and the correspondent masses, proposed for the interpretation of negative ions MS are detailed in **Appendices 3** in **Tables S6, S7**. Briefly, the presence of carboxylate and etheric complexes is confirmed on the top surface. Detailed analysis of the film structure can be made on the basis of the negative ions depth profiles of selected ions, presented in **Fig. 6.4**.

Specifically, the signals of MgO^- ($m/z=39.97$), AlO^- ($m/z=42.97$), $\text{MgO}(\text{OH})^-$ ($m/z=57$) and OH^- ($m/z=17$) can be used to detect oxides and hydroxides, the signal of CN^- ($m/z=26$) as a marker of the heteroatom in the cation. Etheric groups are revealed by the C_2O^- ($m/z=39.99$) fragment and specific complexes can be also verified by the moieties of MgOAc^- ($m/z=83$) and $\text{C}_2\text{H}_4\text{MgO}^-$ ($m/z=68$), $\text{Mg}(\text{OAc})_2^-$ ($m/z=141$), $\text{Al}(\text{OAc})_3^-$ ($m/z=204$) and structures **2, 5** in the **Table S6 (Appendix 3)**.

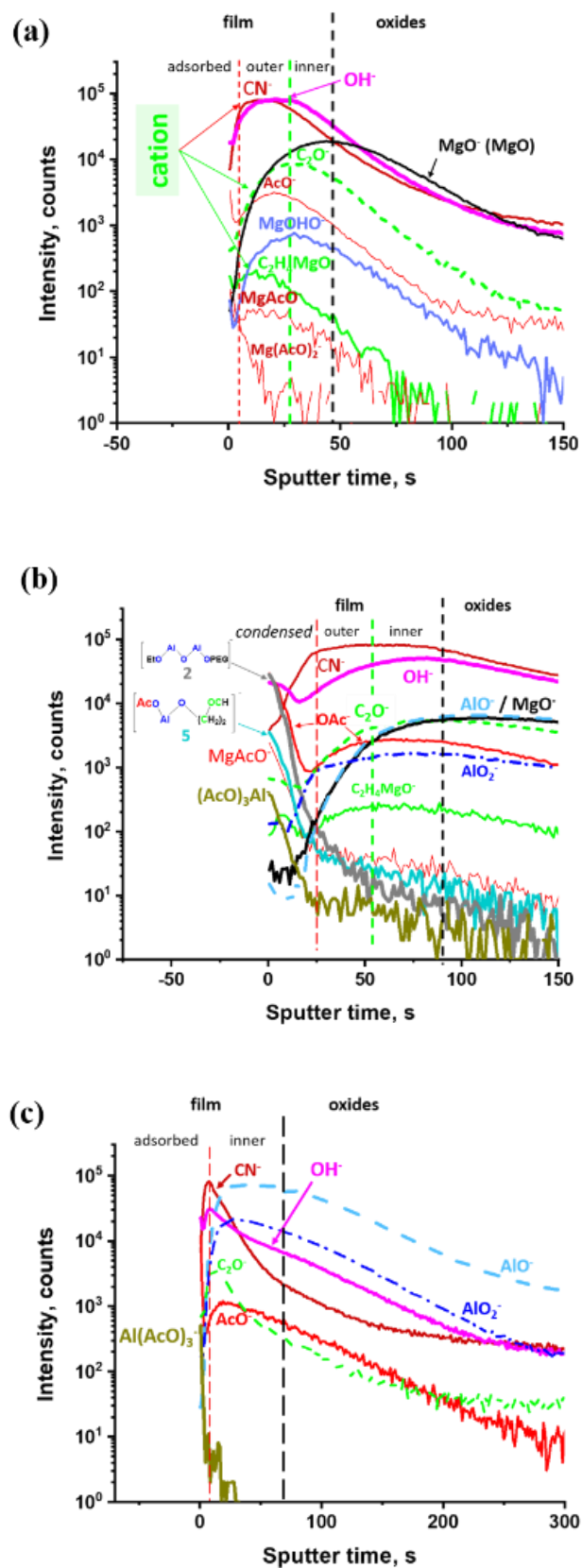


Fig. 6.4. Typical ToF-SIMS depth negative ions profile obtained after electrochemical experiments in $[\text{mPEG}_n\text{MPyr}]\text{OAc}-\text{H}_2\text{O}$ electrolyte on (a) CP Mg, (b) AZ61 and (c) CP Al.

Fig. 6.4 a displays profiles obtained on CP Mg. Two layers can be distinguished on the profile: a relatively thin surface film rich in organic moieties and eroded in about 50 s and a thicker oxide film close to the metal, identified thanks to the position of MgO^- . The surface film consists of inner and outer sublayers, and very thin adsorbed sublayer. The inner layer represents by maximum of peaks of MgO_2H^- and C_2O^- signals, which can be assumed as the fragments of $\text{Mg}(\text{OH})_2$ and etheric group respectively, also observed on Raman and ATR-FTIR spectra. This allows us to suspect that cations of IL are adsorbed on the crystals of $\text{Mg}(\text{OH})_2$. The outer sublayer is characterized by the signals of OH^- , CN^- and $\text{C}_2\text{H}_4\text{MgO}^-$. Three last signals can be also attributed to the fragments of the cation of IL. The presence of $\text{C}_2\text{H}_4\text{MgO}^-$ fragments evidences the complexation of Mg-ions by etheric groups as it has been reported previously for dry PEG-containing ionic liquids [137]. Taking into account the difference in the peak maximum positions for CN^- and C_2O^- , the cation of ILs seems to be oriented to the surface by etheric groups. The composition of adsorbed layer is predominantly represented by the signals of $\text{C}_4\text{H}_6\text{O}_4\text{Mg}^-$ ($\text{Mg}(\text{OAc})^-$), MgOAc^- which are Mg acetate and AcO^- ($m/z=59$). Further detailed analysis of the adsorbed layer is provided by the positive and negative MS in supporting information (**Appendix 3 Fig. S7, S8, Table S6 and S7**).

Fig. 6.4 b represents negative ions profile of AZ61. Two principal layers are also distinguishable: the organic moieties containing film and the oxide. Oxide layer contain Al and Mg oxides, marked by AlO^- and MgO^- fragments. The surface film can be divided into three sublayers. The inner sublayer closest to the oxide is characterized by the peaks of AlO_2^- , $\text{C}_2\text{H}_4\text{MgO}^-$, C_2O^- , OH^- signals. The intensity of OH^- detected on AZ61 is significantly lower (more than 1.5 times) than those observed on CP Mg, which is in agreement with the absence of $\text{Mg}(\text{OH})_2$ – signal in the Raman and FTIR spectra. However, it is impossible to exclude a very thin layer of a hydroxide ($\text{Mg}(\text{OH})_2$ or $\text{Al}(\text{OH})_3$). As on CP Mg, the outer part of the film corresponds to the maximums of the signals of CN^- , AcO^- ($m/z=59$), $\text{C}_2\text{H}_4\text{MgO}^-$ indicating the presence of cation in complex with Mg. The maximum of the CN^-

signal is however reached at much longer times than for CP Mg, indicating much thicker external layer on AZ61. This layer, marked with the signals of some Al complexes (structures **2 and 5 in Table S6 in Appendix 3**) and aluminum and magnesium acetates ($\text{Al}(\text{AcO})_3^-$ and MgAcO^-) can be considered as a condensed layer formed by an associated structure of metal-organic complexes which can be responsible for the dark film visible by TLM during anodic polarization. This film can block water diffusion and hence hydrogen evolution reaction during E_{oc} measurement and under anodic polarization (NDE).

Fig. 6.4 c displays negative ions profile of CP Al after the electrochemical experiment in $[\text{mPEG}_n\text{MPyr}]\text{OAc-H}_2\text{O}$, in which almost no reactivity has been observed. The analysis revealed that there are at least two principal layers: film and oxides. The oxide layer is represented by the peaks of AlO^- and AlO_2^- signals. The film contains both C_2O^- and AcO^- which indicates the presence of IL. The maximum of the signals of $\text{Al}(\text{AcO})_3^-$, CN^- and OH^- are close to the external top surface. The maximum of AcO^- is deeper in the profile than the maximum of C_2O^- which is the opposite on CP Mg and AZ61. The orientation of the cation of IL is however the same on all the substrate - etheric groups are oriented to the metallic surface as can be assumed from the maximum positions of the signals of CN^- and C_2O^- . The complexes of Al detected on CP Al are similar to that, observed on AZ61 (Appendix 3, **Fig. S7 c, S8 b, table S6, S7**). The comparison of the depth profiles of AZ61, CP Mg and CP Al illustrates that both Mg and Al participate in the formation of the complexes with anions and cations in the surface film, and that the thick condensed film is formed only if the combination of both metallic cations is present. This film also contains complexes with both cation and anion.

Considering the results of ToF-SIMS depth profiles, Raman and ATR-FTIR spectra, a tentative schematics of the surface film, formed in $[\text{mPEG}_n\text{MPyr}]\text{OAc-H}_2\text{O}$ electrolyte on the Mg substrates can be proposed (**Fig. 6.5**). This schematics underlines that the surface of CP Mg at some points is similar to that in aqueous electrolytes: metallic surface is covered by MgO which is followed by $\text{Mg}(\text{OH})_2$

[61]. Mg acetate and etheric groups are adsorbed on the hydroxide and the external cation head is responsible for the adsorption of acetate counter ions.

Mg(OH)₂ is practically absent on AZ61, which can be related to the oxide modification by Al [47,48]. In contrast, after the internal layer, in which IL cations are fixed to the oxide by etheric groups, a relatively thick layer Al- and Mg-complexes with cations and anions of ILs is condensed on the top of the external heterocycle oriented surface in place of adsorbed counter ions.

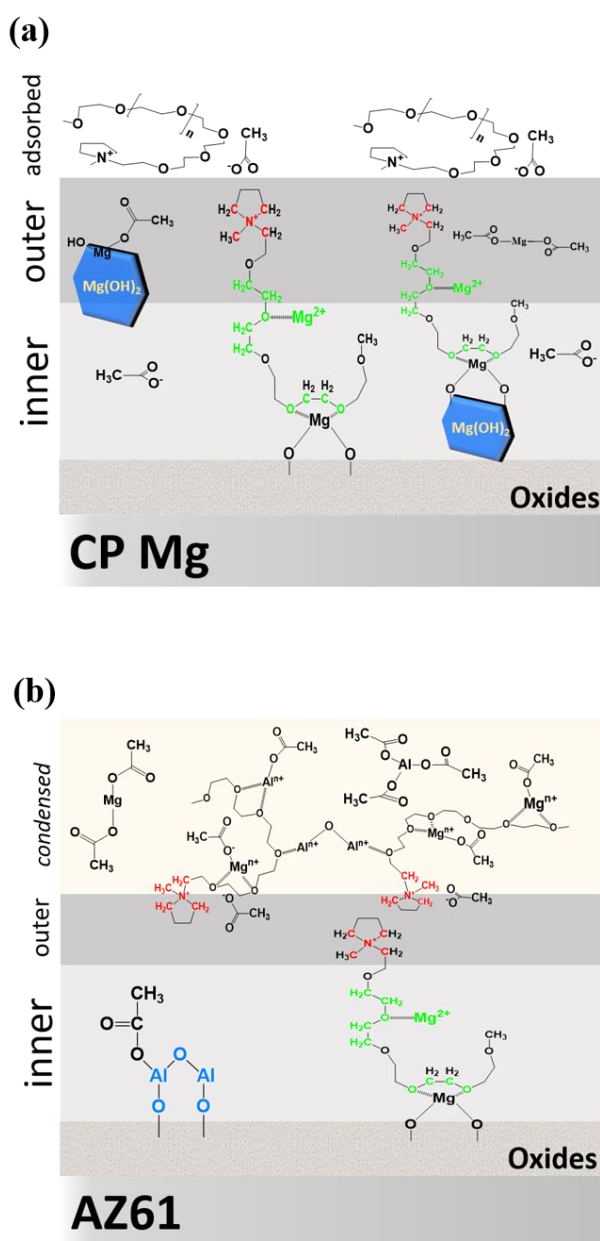


Fig. 6.5. Tentative schematics of surface profiles for (a) CP Mg, (b) AZ61.

3.4 Molecular state of water molecules by ATR-FTIR

Molecular state of water in H₂O - IL mixture can be understood by the evolution of the ATR-FTIR spectra in the region 3000 – 3700 cm⁻¹. All the spectra are normalized by their maximum of intensity (I_{\max}) in this region. **Fig. 6** illustrates typical ATR-FTIR spectra of O-H vibration regions on the wet surfaces of CP Mg and AZ61 compared with the spectra of pure water and the used electrolyte before and after the electrochemical experiments. In our previous work [**Chapter 5**], we have demonstrated that in the spectra of solutions the shoulder nearby ≈ 3520 cm⁻¹ was absent for pure water and [BMPyr]OAc-H₂O mixtures for all concentrations, while it was characteristic for [mPEG_nMPyr]OAc-H₂O mixtures. Therefore, it was attributed to specific interactions (H-bonds) connecting water molecule with both acetic anion and etheric oxygen of the PEG-substituted cation. In the spectrum of [mPEG_nMPyr]ClO₄-H₂O (**Fig. 6.6 c**, blue spectrum) which doesn't contain acetate in the structure, the peak maximum at ≈ 3534 cm⁻¹ is hence attributed to ClO₄⋯HOH⋯O_{etheric} H-bonding. It should be stressed that weaker interaction between water and ClO₄⁻ than between water and acetate can contribute in O-H vibrations of water leading to slight changing of the peak center [210].

Evolution of ATR-FTIR spectra, recorded on the wet surfaces of the both alloys after the electrochemical experiments in [BMPyr]OAc-H₂O and [mPEG_nMPyr]OAc-H₂O, indicates that water molecules interact with IL. In case of [mPEG_nMPyr]OAc-H₂O, the shoulder nearby ≈ 3520 cm⁻¹ remains indicating water and etheric groups interaction. This bonding of water can reduce its mobility and block penetration to the metallic surface. Interestingly, on CP Mg this seems to be more pronounced than on AZ61. On the contrast, significant evolution of the spectra in O-H region (if compared with the used electrolyte) is observed on the metallic surfaces after the electrochemical experiments in [mPEG_nMPyr]ClO₄-H₂O. Especially on CP Mg, the spectrum become closer to the spectrum of pure water and the interactions between water and etheric groups disappears. Thus, it can be assumed that leaching Mg-ions expel H₂O molecules from etheric oxygens water to

break H-bondings and to form water-clusters. Another possible reason of these circumstances is the decomposition of etheric groups [20].

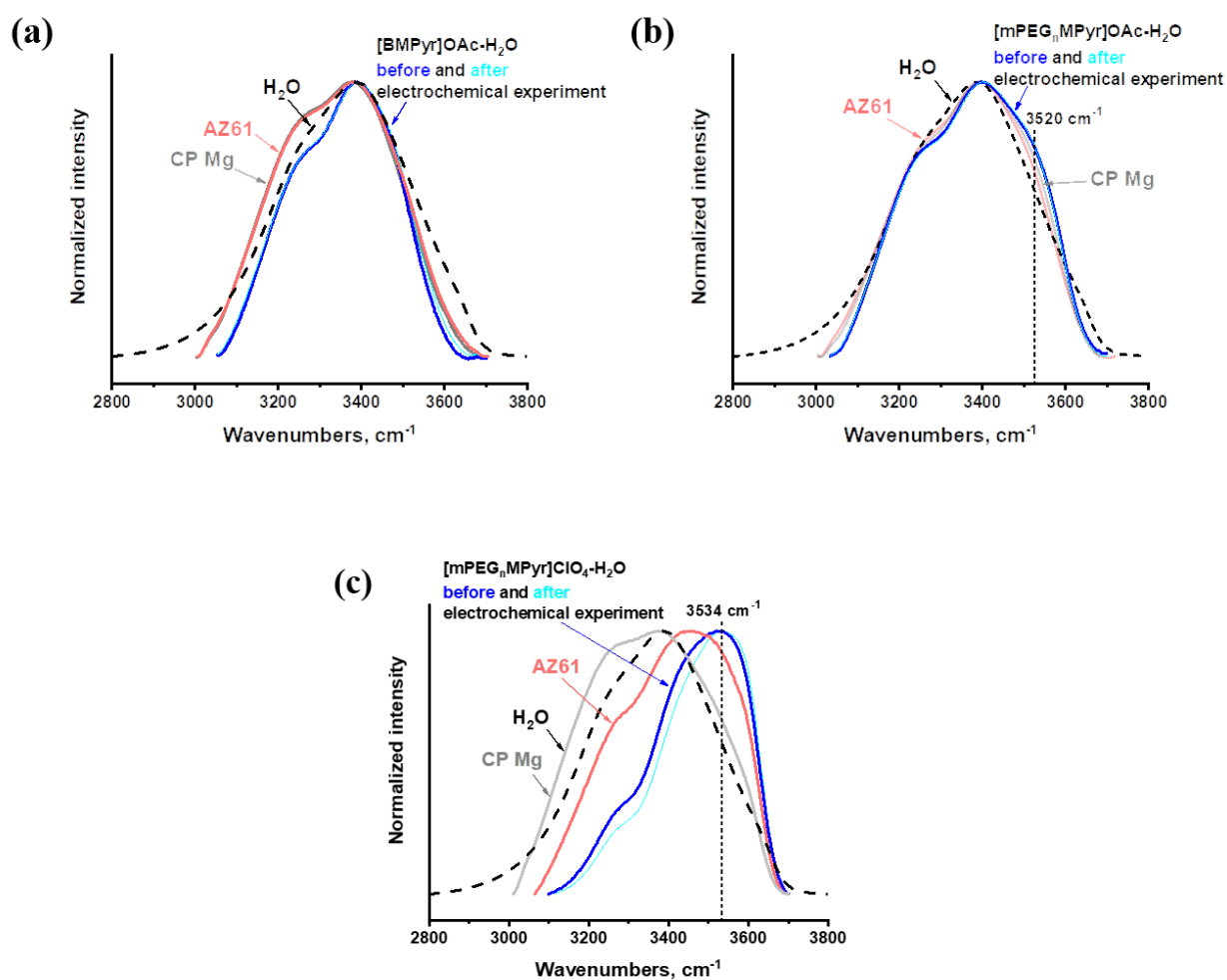


Fig. 6.6. Superposition of OH-vibration regions of ATR-FTIR spectra recorded on wet surfaces of CP Mg and AZ61 after the experiment in (a) - [BMPyr]OAc-H₂O; (b) - [mPEG_nMPyr]OAc-H₂O electrolyte; (c) – [mPEG_nMPyr]ClO₄-H₂O, as indicated. The spectra of pure water and of the electrolyte before and after the experiment are shown for comparison.

3.5 Molecular state of water molecules from MD simulations

ATR FTIR spectroscopy demonstrated for all the studied systems that the fraction of free water at the interface is higher than in the bulk electrolyte in both systems. In order to understand this, MD simulation was made.

Preliminary MD simulation demonstrated that acetic anions form strong intermolecular H-bonds with water, which is expected to prevent formation of free water phase [Chapter 5] and hence to reduce hydrogen evolution in both [BMPyr]OAc-H₂O and [mPEG_nMPyr]OAc-H₂O. H-bonds were also demonstrated with etheric groups of the PEG substituted cation, but their probability for low water to IL molar ratios ($n(\text{H}_2\text{O}) / n(\text{IL}) \leq 3$) was lower than for acetate anion. The probability of H-bonds between water molecules and acetate rapidly decreased with dilution, which could explain the effect of dilution on the NDE. However, the experiments in this work were made with a fixed water to IL molar ratio $n(\text{H}_2\text{O}) / n(\text{IL}) \leq 3$, at which water bonding with acetate anion and hence the NDE suppression could be expected in both studied mixtures. The fact, that it is not the case at the interface, can be regarded as an indication that other species present in the electrolyte could interact with both, IL and water, and interfere with water-IL interactions. The most probable of them could be the Mg²⁺ ions leached by anodic dissolution (reaction 1).

This hypothesis was verified by considering the effect of Mg²⁺ on the stability of H-bonds between water and IL cation and anion in MD simulation. [BMPyr]OAc-H₂O and [mPEG_nMPyr]OAc-H₂O mixtures are simulated in four different configurations: with and without addition of Mg²⁺ (in the form of Mg(OH)₂ to ensure electro-neutrality). In total 50 Mg²⁺ ions and 100 OH⁻ ions were added into the system containing 100 molecules of IL. 100 or 200 water molecules were considered to simulate the molar ratios between water and IL $n(\text{H}_2\text{O}) / n(\text{IL}) = 1$ and 2 respectively.

Mg(OH)₂ as the source of Mg²⁺ in the simulation was selected because it is a common corrosion products of Mg-alloys, which is often naturally present in the outer layer on the metallic surface. Moreover, this product was detected by Raman and IR spectroscopies on CP Mg in all studied electrolytes. Slightly lower H₂O content than the experimentally used in the bulk electrolyte (theoretical molar ratio $n(\text{H}_2\text{O}) / n(\text{IL}) = 2.9$ for [mPEG_nMPyr]OAc 10 wt. % H₂O) was selected assuming

a possible consumption of H₂O by reaction (2) in during open circuit periods and limited diffusion of water to the interface.

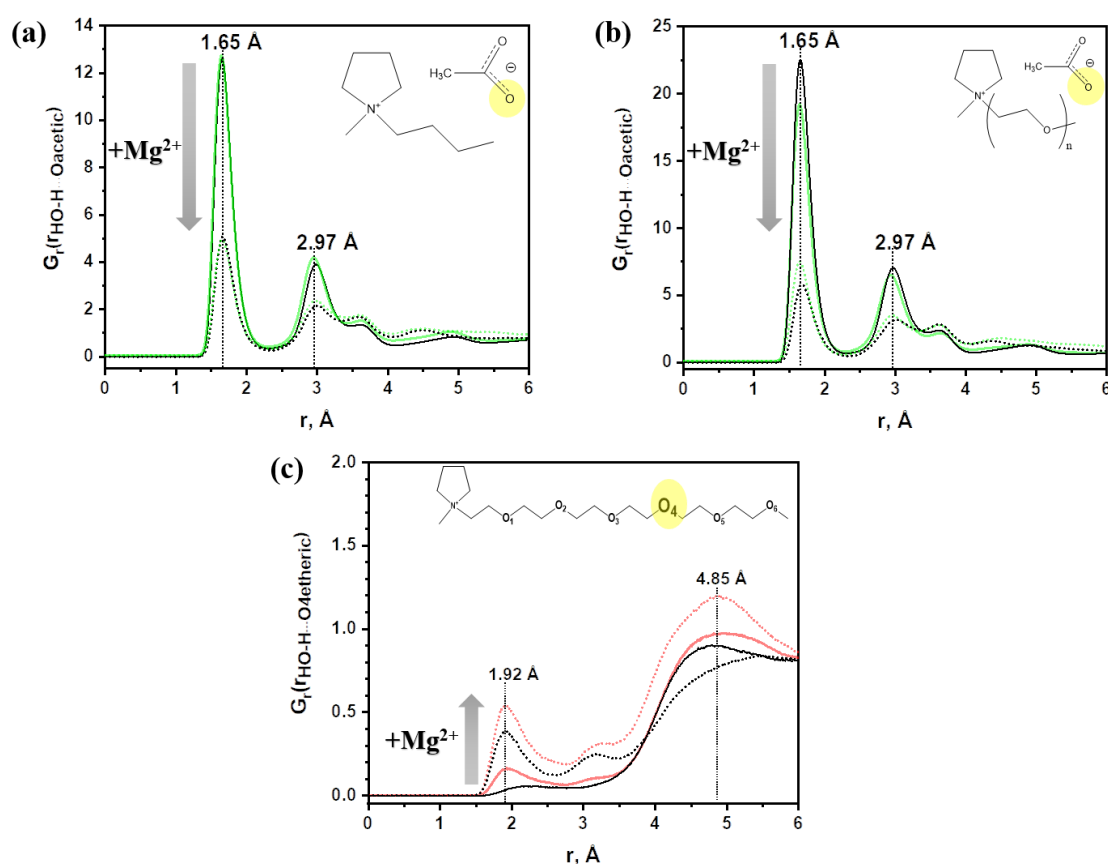


Fig. 6.7. Radial distribution function $G_r(r_{\text{HO-H...Oacetate}})$ (a, b) and $G_r(r_{\text{HO-H...O4etheric}})$ (c) of the distances, r , between acetate oxygen or etheric oxygen 4 (shown in the insets) and the closest water hydrogen, calculated for water – [BMPyr]OAc (a) and water - [mPEG_nMPyr]OAc (b, c) mixtures without (solid lines) and with (dot lines) Mg²⁺ ions in solution. Examples of the mixtures with molar ratios between water and IL $n(\text{H}_2\text{O}) / n(\text{IL})=1$ (black) and $n(\text{H}_2\text{O}) / n(\text{IL})=2$ (red) are presented.

The results of modelling are shown in **Fig. 6.7**. Radial distribution functions $G(r)$, calculated in different conditions, describe the probability to find a hydrogen atom from water molecule at a distance r (measured in Å) to a specified oxygen atom from the IL. At large distances the molecules are independent and $G(r)=1$. If there are some specific interactions between atoms, *e.g.* hydrogen bonds between acetate anion, O_{acetate}, and water hydrogen atom H_{H₂O}, a peak at low distance should occur

on the radial distribution function (in the present example on **Fig. 8 a and b**). **Figs. 6.7 a and b** represent the $G_r(r_{\text{HO-H}\cdots\text{O}_{\text{acetate}}})$ in [BMPyr]OAc-H₂O and [mPEG_nMPyr]OAc-H₂O mixtures, calculated with and without Mg²⁺. They are characterized by 2 peaks nearby 1.65 Å and 2.97 Å. The intensity of both peaks decreases with dilution and with addition of Mg²⁺, which could be due to the formation of Mg-acetate complexes.

In **Fig. 6.7 c**, the RDF of the 4th oxygen in the polymeric chain are shown as an example of $G_r(r_{\text{HO-H}\cdots\text{O}_{\text{etheric}}})$. It is clear from the picture, that in contrast to $G_r(r_{\text{HO-H}\cdots\text{O}_{\text{acetate}}})$, for the $G_r(r_{\text{HO-H}\cdots\text{O}_{\text{etheric}}})$ the addition of Mg²⁺ increases the probability of H-bonding (increase of $G_r(r \approx 1.92 \text{ \AA})$). Thus, it can be assumed that water molecules, expelled by Mg²⁺ from acetic anions, form hydrogen bonds with oxygen atoms of etheric groups of IL cation.

To illustrate the effect of Mg on all the etheric oxygen atoms, the difference of maximums of RDF intensities with and without Mg-ions respectively ΔG_r were subtracted and plotted as a function of water content. **Fig. 6.8** represents the histograms of $\Delta G_r(r)$ for $\text{O}_{(\text{acetate})}$ and $\text{H}_{(\text{H}_2\text{O})}$ in [BMPyr]OAc-H₂O, [mPEG_nMPyr]OAc-H₂O and $\text{O}_{(\text{etheric})}$ and $\text{H}_{(\text{H}_2\text{O})}$. Negative values of $\Delta G_r(r_{\text{HO-H}\cdots\text{O}_{\text{acetate}}})$ (**a, b**) for selected HO-H \cdots O distances r designate decreasing H-bonding probability with Mg²⁺, positive values of $\Delta G_r(r_{\text{HO-H}\cdots\text{O}_{\text{etheric}}})$ (**c**) indicate growing H-bonding probability with Mg²⁺

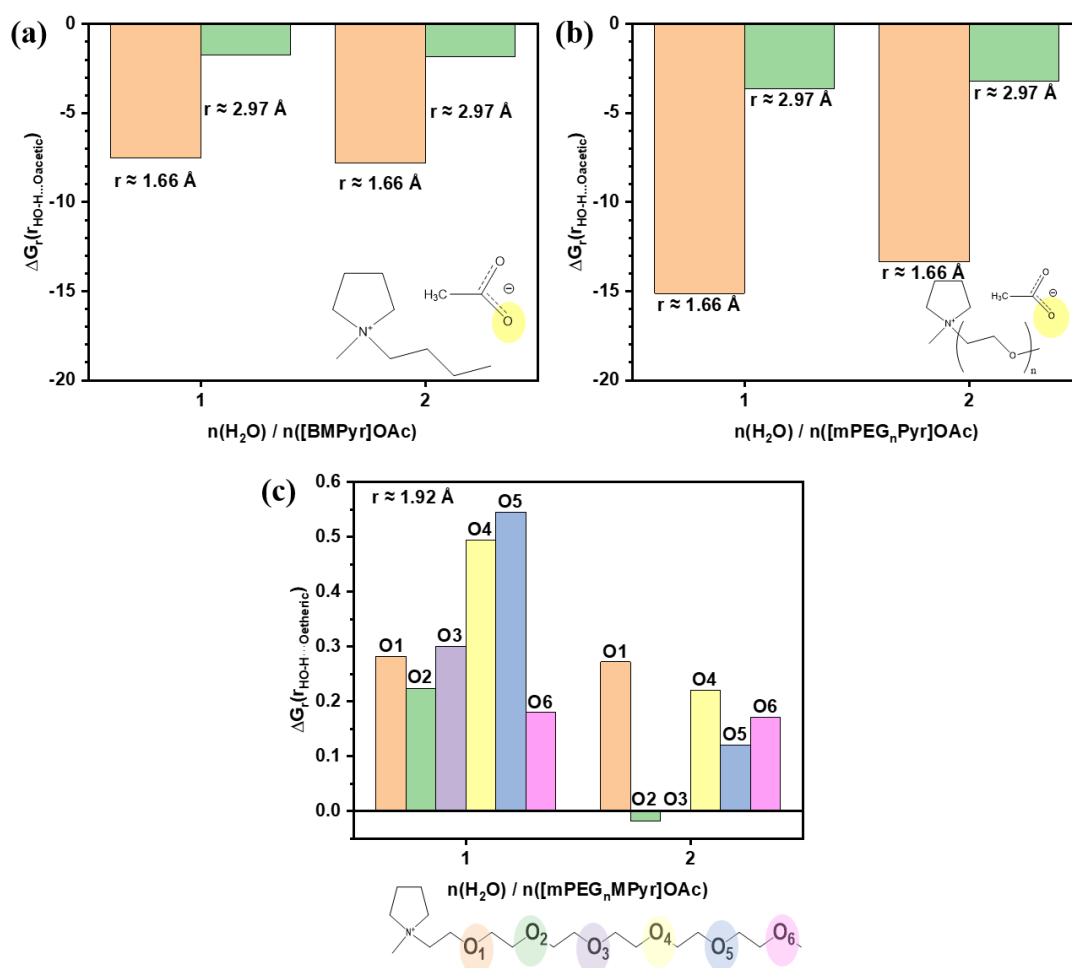


Fig. 6.8. Effect of leached Mg^{2+} ions in solution on the probability of water coordination by H-bonding with acetic (a, b) and etheric (c) oxygen atoms in water mixtures with different IL and molar water to IL ratios $n(\text{H}_2\text{O})/n(\text{IL})$ as indicated.

4. Discussion: Mechanisms of NDE and NDE-suppression on Mg alloys in H_2O -ILs mixtures

Whatever mechanisms of the NDE is considered, it requires water reduction reaction (2) which needs the presence of mobile (not coordinated with IL) free water phase. Comparing the ATR-FTIR and molecular dynamic simulations results, one can conclude that water molecules in the bulk electrolytes can be strongly H-bonded by acetate anions in both [BMPyr]OAc- H_2O and [mPEG_nMPyr]OAc- H_2O mixtures with water to IL ratios $n(\text{H}_2\text{O}) / n(\text{IL})$ up to 3 (**Chapter 5**). The probability of $\text{HO}\cdots\text{H}\cdots\text{O}_{\text{acetate}}$ bonds is expected however to be strongly weakened at the metal / solution interface because of accumulation of leached by anodic dissolution Mg^{2+} . As a

result, in [BMPyr]OAc-H₂O mixture, free water phase is liberated at the metal / solution interface and is available for hydrogen evolution reaction, and hence the NDE. Moreover, the formed water phase is expected to be highly conductive because of dissolved acetate anions.

In [mPEG_nMPyr]OAc-H₂O mixture the liberated by Mg²⁺ water seems to be immediately coordinated by etheric groups in the PEG-substituted cation. Moreover, this initially low probable H-bonding seems to be enhanced with Mg²⁺ addition. Thus, water binding by PEG substituted cation can be considered as one of the mechanisms of the NDE inhibition, which is not expected to depend on the alloy composition.

One should note that anodic hydrogen evolution was observed in [mPEG_nMPyr]ClO₄-H₂O mixture (section 3.1), which indicates the synergic effect of both the PEG-substituted cation and the carboxylic anion. The surface characterizations demonstrated partial transformation of etheric oxygen into C=O at the interface, the most probably also under the action of the electrochemically formed Mg²⁺ [20]. Strong bonding between Mg²⁺ and acetate anion can be a factor preventing PEG destabilization at the interface in [mPEG_nMPyr]OAc-H₂O electrolyte.

Finally, an additional NDE inhibition mechanism can be proposed on the basis of ToF-SIMS, Raman and ATR-FTIR surface analysis, which includes the formation of a condensed surface film which alters mobility of water to the interface and hence the NDE. This film formation also requires the presence of both acetic anion and etherically substituted cation. The film composition and properties are also affected by the presence of both, Al and Mg, in the alloy.

It seems therefore that the NDE inhibition in [mPEG_nMPyr]OAc-H₂O electrolyte cannot be attributed to a solely anion or cation but is a result of a complex combination of synergistic effects of both ions of the IL.

Figs. 6.9 a and b illustrate schematically the proposed NDE mechanism on CP Mg and AZ61 alloys in [BMPyr]OAc-H₂O electrolyte. Dissolved Mg²⁺ ions

expel H₂O molecules from acetic anions and liberated “free” water molecules tend to form water-clusters involved in hydrogen reduction reaction (**Fig. 6.9 a, b**).

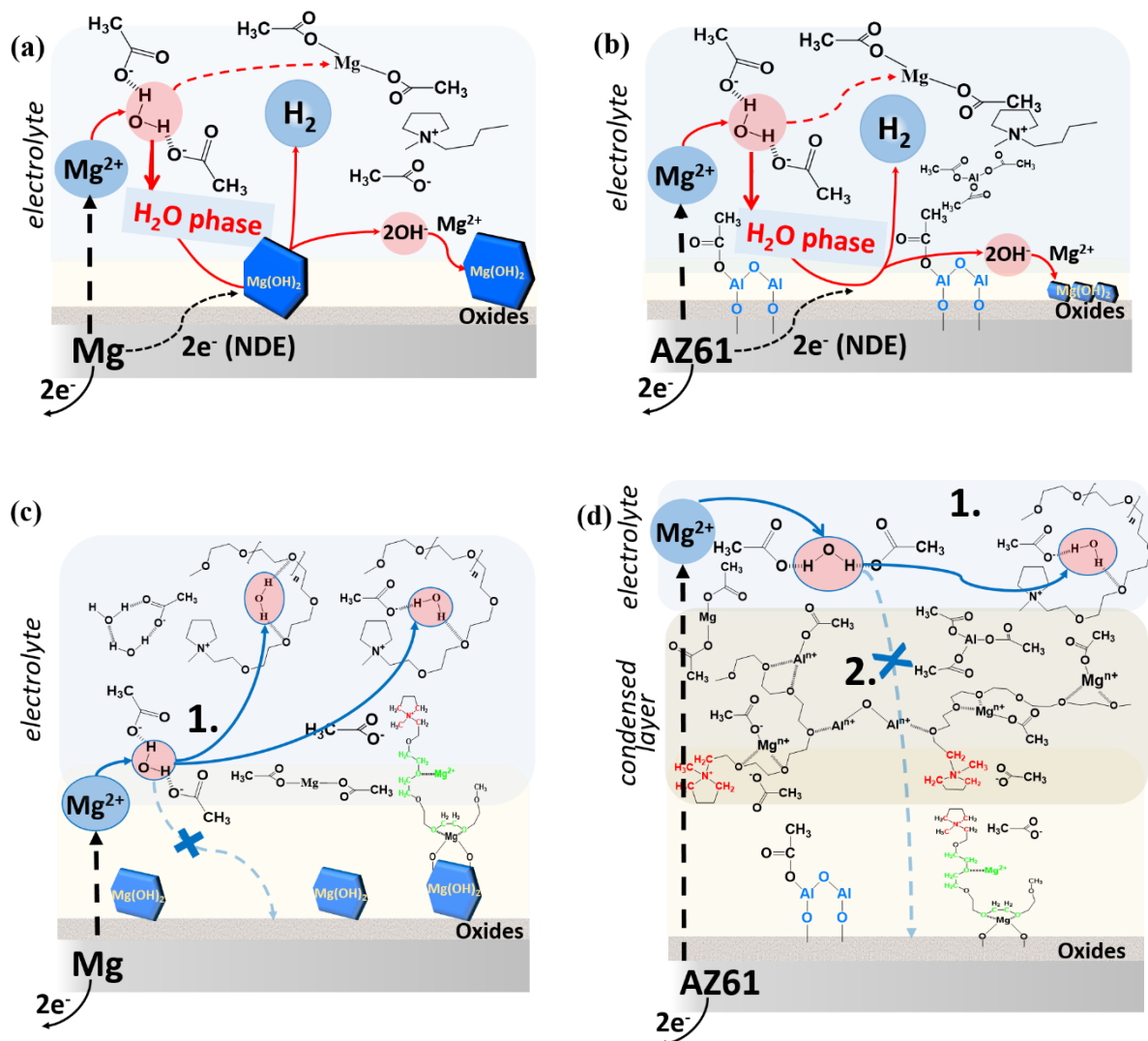


Fig. 6.9. Schematic mechanisms of NDE in [BMPyr]OAc-H₂O (**a, b**) and NDE inhibition in [mPEG_nMPyr]OAc-H₂O on CP Mg (**a, c**) and AZ61 (**b, d**). Numbers 1 and 2 indicate synergic inhibition mechanisms: 1. bonding by [mPEG_nMPyr]⁺ of free water phase, ejected from acetate-water H-bonded complexes by leached Mg²⁺; 2. barrier effect of the condensed film, in which [mPEG_nMPyr]⁺ and OAc⁻ moieties are coordinated by initially leached Mg²⁺ and Al³⁺ ions.

In contrast, in [mPEG_nMPyr]OAc-H₂O (**Fig. 6.9 c, d**) the liberated H₂O molecules form intermolecular hydrogen bonds with etheric oxygens of PEG-

moieties, while liberated Mg^{2+} participate in the formation of surface film, which can be enough thick in the presence of Al^{3+} . Formation of the condensed layer also impedes penetration of H_2O to the metallic surface. In addition, this film can level the electrochemical potential on the surface preventing the formation of microgalvanic couplings on the surface.

The proposed synergistic inhibition mechanisms are shown schematically by numbers 1 and 2 in **Fig. 6.9**. These mechanisms are: 1. bonding by $[\text{mPEG}_n\text{MPyr}]^+$ of free water phase, ejected from acetate-water H-bonded complexes by leached Mg^{2+} ; 2. barrier effect of the condensed film, in which $[\text{mPEG}_n\text{MPyr}]^+$ and OAc^- moieties are coordinated by initially leached Mg^{2+} and Al^{3+} ions. Additional (not shown in the figure) synergic effect is stabilization of $[\text{mPEG}_n\text{MPyr}]^+$ versus its oxidation in the presence of Mg^{2+} due to the Mg ions binding with acetate.

5. Conclusions

In this work the role of cation and anion of ionic liquid for corrosion mechanism and the negative difference effect inhibition in water-ionic liquid mixtures was studied in detail on the example of Mg alloys in $[\text{mPEG}_n\text{MPyr}]\text{ClO}_4\text{-H}_2\text{O}$, $[\text{BMPyr}]\text{OAc-H}_2\text{O}$ and $[\text{mPEG}_n\text{MPyr}]\text{OAc-H}_2\text{O}$ mixtures. The NDE was observed on CP Mg and AZ61 in two first mixtures but was blocked on both alloys in $[\text{mPEG}_n\text{MPyr}]\text{OAc-H}_2\text{O}$, demonstrating a synergistic action of $[\text{mPEG}_n\text{MPyr}]^+$ and OAc^- .

The results of surface analysis by ToF-SIMS, surface and solution analysis by vibration spectroscopy and molecular dynamics (MD) simulation, allow to propose several complementary mechanisms explaining the observed synergistic effect:

(1) Effects in the electrolyte:

Although water is H-bonded to the acetic anion in bulk electrolyte, free water can be liberated from $\text{HO-H}\cdots\text{OAc}^-$ complexes by leached Mg^{2+} . Thanks to the H-bonds between the liberated water and etheric oxygen in $[\text{mPEG}_n\text{MPyr}]^+$ its mobility and

hence electrochemical activity at the interface remains limited. The $[\text{mPEG}_n\text{MPyr}]^+$ is however unstable under anodic polarization because of nucleophilic attack in the presence of Mg^{2+} . OAc^- anions bound leached Mg^{2+} in strong acetate complexes, stabilizing m-PEG substituted cation.

(2) Effects in the surface film:

On AZ61, a condensed film can be formed by $[\text{mPEG}_n\text{MPyr}]^+$ and OAc^- coordinated with Mg^{2+} and Al^{3+} . This film is mobile, but reforms spontaneously and can contribute to the reduced water transport to the surface.

To conclude, the synergistic effects of acetic anion and ether-substituted pyrrolidinium cation can prevent the NDE on Mg alloys in water–IL mixture.

Part 5. Conclusions and perspectives

Chapter 7:

Results and perspectives

Mg behavior in water – hydrophilic ionic liquids mixtures

The results presented in this PhD work bring a new knowledge in several connected but still well distinct areas:

- (1) Design of new hydrophilic room temperature ILs potentially interesting for Mg applications and first exploration of Mg reactivity in their mixtures with water.
- (2) Understanding of molecular state and reactivity of water in the new electrolytes and the role of the poly-etheric substituted tail in the cation.
- (3) Detailed understanding of the chemistry at alloy – solution interface and precision of the role of cation and anion in IL for the NDE inhibition in new hybrid electrolytes.

The main conclusions in each of these domains are summarized below.

(1) Preliminary discovery of Mg reactivity in water-hydrophilic IL mixtures.

Two hydrophilic acetate-based ionic liquids (1-butyl-1-methylpyrrolidinium acetate, [BMPyr]OAc, and 1-methoxy-polyethylenglycol-1-methylpyrrolidinium acetate, [mPEG_nMPyr]OAc) have been proposed and their synthesis verified. To the best of our knowledge, [mPEG_nMPyr]OAc **has been synthesized for the first time.**

Electrochemical experiments and Time Lapse Microscopy reveal that different **Mg alloys (CP Mg and AZ61) dissolve in ILs containing 10 wt. % H₂O at reasonable potential and relatively high current**, making the new electrolytes potentially interesting if commercial Mg alloy is used as the anode material.

Negative difference effect (NDE) was observed for both alloys exposed in [BMPyr]OAc-H₂O electrolyte, indicating the behavior similar to the observed in aqueous solutions. In contrast, the NDE was suppressed on CP Mg and hydrogen evolution was completely blocked on AZ61 in [mPEG_nMPyr]OAc-H₂O, on which a low adherent gel-like film formed and healed under anodic polarization.

Raman microscopy and Attenuated Total Reflectance Fourier Transform Infrared Spectroscopy of the surface after the exposure in both electrolytes confirmed that chemically bound acetate is present on the surface, indicating that **the presence or absence of carboxylate does not correlate with the absence or presence of the NDE, as it could be expected from the inhibiting properties of carboxylates known in aqueous corrosion.** Independently on the NDE, a homogeneously distributed Mg(OH)₂ film was detected in all electrolytes on CP Mg while no Mg(OH)₂ was detected on AZ61, showing that, in contrast to aqueous corrosion, **in the water - IL mixtures the NDE cannot be explained by the presence and breakdown of Mg corrosion products.** For both alloys the NDE suppression was observed if the IL cation is mPEG-substituted, while the NDE was strong in the mixtures in which the IL cation was aliphatic-substituted. This preliminary knowledge allowed to demonstrate **the importance of the IL cation chemistry for the control of Mg reactivity in water – hydrophilic IL mixtures** with high IL content.

(2) Understanding the interactions between water and IL moieties, in particular the capacity of the cation to form intermolecular hydrogen bonds and its effect on molecular state and reactivity of water.

Molecular interactions in H₂O-IL mixtures were characterized in a wide concentration range of water content (from 0 to 100 wt.%) with the help of Raman and ATR-FTIR spectroscopy and Molecular Dynamic (MD) simulations. The evolution of the liquid structure was compared with the evolution specific conductivity. The results demonstrated that **water molecules form H-bonds not only with acetate anions but also with etheric-substituted MPyr⁺ cation.**

Molecular organization of the electrolyte and its conductivity strongly depend on the water content. Water structure evolves from H-bonded to IL (isolated water molecules) through finite “water pockets” to the percolating “free water” phase. Critical molar water fractions, which should be achieved for the transition between these structural organizations, are very different for the ILs with aliphatic and etheric substituted cation.

For molecular ratios between water and ionic liquid $n(\text{H}_2\text{O}) / n(\text{IL}) \leq 3$ only isolated water molecules H-bonded mainly to acetate anion are present in both ILs. For the higher water contents ($n(\text{H}_2\text{O}) / n(\text{IL}) > 3$) in the aliphatic substituted [BMPyr]OAc, the probability of H-bonding between water molecules ($\text{HOH} \cdots \text{O}_{(\text{H}_2\text{O})}$) increases and the probability of H-bonding between water and acetate ($\text{HOH} \cdots \text{OAc}$) decreases with dilution. This is expected to result in **a rapid growth of water phase clusters starting from $n(\text{H}_2\text{O}) / n(\text{IL}) = 3$.**

In contrast, in [mPEG_nMPyr]OAc-H₂O, the molecules of water remain coordinated by oxygen atoms of etheric groups of PEG-substituted cation, which can create H-bonds with up to 5-6 molecules. As a result, **water pockets do not form up to $n(\text{H}_2\text{O}) / n(\text{IL}) = 7-8$.**

Finally, once “free” water phase with water-water hydrogen bonds is formed, **specific conductivity very rapidly grows in both ILs.**

Significant difference in the composition of the mixture, starting from which the water phase clusters are formed, seems to correlate well with the results of conductivity measurements (**Fig. 5.2**). Indeed, significant conductivity growth in [BMPyr]OAc-H₂O mixtures starts from relatively low water contents and the modification of the tangent can be seen around $n(\text{H}_2\text{O}) / n(\text{IL}) = 3$, while in [mPEG_nMPyr]OAc-H₂O specific conductivity stays much less affected by the water content and the slope modification seems to be closer to $n(\text{H}_2\text{O}) / n(\text{IL}) = 7-9$.

Finally, a transition from conductivity increases with water content (behavior expected for slightly water diluted IL) to conductivity decrease with water content

(behavior typical for diluted aqueous solutions) occurs in both electrolytes but at very different water contents. This **transition from conductivity growth to its decrease, indicating that the solvent (percolating phase) is changed, occurs at molar water to IL ratios $n(\text{H}_2\text{O}) / n(\text{IL}) = 33$ for aliphatic substituted [BMPyr]OAc and at $n(\text{H}_2\text{O}) / n(\text{IL}) = 145$ for [mPEG_nMPyr]OAc.**

(3) Detailed understanding of the chemistry of Mg alloy – hybrid electrolyte interfaces and of the role of specific functional groups in the cation and the anion, tentative reactivity mechanisms.

The roles of cation and anion of ionic liquid in the modification of corrosion behavior and the NDE inhibition in the new hybrid electrolytes was studied in detail on the example of Mg alloys in [mPEG_nMPyr]ClO₄-H₂O, [BMPyr]OAc-H₂O and [mPEG_nMPyr]OAc-H₂O mixtures.

The results demonstrated **synergistic effects of acetic anion and ether-substituted pyrrolidinium cation on Mg alloys corrosion mechanisms and on the inhibition of the NDE on Mg in water–IL mixture.** This synergy seems to act by **several complementary mechanisms.**

(a) Electrolyte modification. Although water is H-bonded to the acetic anion in the bulk electrolyte, formation of acetate complexes of Mg²⁺ prevails the formation of water-acetate H-bonds near the interface. As a result, **free water is liberated from HO-H···OAc⁻ agglomerates by leached in corrosion process Mg²⁺.** This effect explains the observed NDE in the [BMPyr]OAc-H₂O mixtures.

The mobility of water and the formation of free water phase are however still limited thanks to the increasing probability of the H-bonds formation with etheric oxygen in [mPEG_nMPyr]⁺. As a result, **water electrochemical activity at the interface stays inhibited if [mPEG_nMPyr]⁺ cation is stable.** The [mPEG_nMPyr]⁺ is however unstable under anodic polarization on Mg surface because of nucleophilic attack in the presence of Mg²⁺, which explains

the NDE still observed in [mPEG_nMPyr]ClO₄-H₂O. In contrast, as previously noted, OAc⁻ anions bound leached Mg²⁺ in strong acetate complexes, stabilizing mPEG substituted cations.

(b) Formation of surface films. On AZ61, additional effect can be attributed to the formation of a condensed film, containing both [mPEG_nMPyr]⁺ and OAc⁻ coordinated with leached by corrosion process Mg²⁺ and Al³⁺. This film is mobile, but reforms spontaneously and **can contribute to the reduced water transport to the surface.**

Perspectives

This work is a very first study of a completely new system – Mg alloy in water miscible ionic liquid mixed with water. Although a lot of new knowledge has been accumulated during the work, even more stays to do. Further research could either lead to a deeper understanding of the obtained results and detailed verification of all the formulated hypotheses or on the optimization and development of the setups, IL design and alloy matrices as well as screening of possible applications.

Concerning the obtained results:

- 1) The exact chemical reaction and the products of decomposition of [mPEG_nMPyr]ClO₄ on Mg electrode should be investigated;
- 2) The influence of water content on the evolution of the electrochemical potential window should be investigated;
- 3) Bigger volumes of the electrolyte need to be prepared for additional and more precise characterizations of the IL properties (viscosity, density, ...);
- 4) The hypothesis of the modification of the electrochemical activity of water in hybrid electrolytes could be verified on an inert electrode;
- 5) Quantitative description of HER can be interesting.

Concerning the last point, either a high volume of the electrolyte should be available, or the electrochemical setup can be improved in order to be able to measure the volume of the released bubbles. This work reveals only qualitative data

of H₂ reduction, however, the quantitative results can open new possibilities to compare with aqueous-based electrolytes and for further comprehensive and argumentated discussions.

Going further in the completely unexplored directions, IL design can be modified regarding to the application. The amount of different combinations of cations and anions of RTILs are inexhaustible. It seems to be promising to involve some other anions recognized as inhibitors for Mg-corrosion and for the NDE in the IL structure.

It seems also interesting to test the new electrolytes with newly developed alloys. For instance, more recent work reports new Mg-Ca alloys exhibiting almost no hydrogen evolution during anodic polarization in aqueous-based electrolytes [55]. Since in this work it is shown that the NDE can be suppressed or completely blocked depending on the alloy matrix, the behavior of these new alloys can be also of interest.

Bibliography

- [1] S. Jayasathyakawin, M. Ravichandran, N. Baskar, C.A. Chairman, R. Balasundaram, Mechanical properties and applications of Magnesium alloy – Review, *Mater. Today Proc.* 27 (2020) 909–913. <https://doi.org/10.1016/j.matpr.2020.01.255>.
- [2] S.K. Panigrahi, K. Kumar, N. Kumar, W. Yuan, R.S. Mishra, R. DeLorme, B. Davis, R.A. Howell, K. Cho, Transition of deformation behavior in an ultrafine grained magnesium alloy, *Mater. Sci. Eng. A.* 549 (2012) 123–127. <https://doi.org/10.1016/j.msea.2012.04.017>.
- [3] V.M. Garamus, W. Limberg, M. Serdechnova, D. Mei, S. V. Lamaka, T. Ebel, R. Willumeit-Römer, Degradation of titanium sintered with magnesium: Effect of hydrogen uptake, *Metals (Basel)*. 11 (2021) 1–12. <https://doi.org/10.3390/met11040527>.
- [4] S. Sankaranarayanan, M. Gupta, Emergence of god’s favorite metallic element: Magnesium based materials for engineering and biomedical applications, *Mater. Today Proc.* 39 (2020) 311–316. <https://doi.org/10.1016/j.matpr.2020.07.220>.
- [5] J. Tan, S. Ramakrishna, Applications of magnesium and its alloys: A review, *Appl. Sci.* 11 (2021). <https://doi.org/10.3390/app11156861>.
- [6] R. Mohtadi, O. Tutusaus, T.S. Arthur, Z. Zhao-Karger, M. Fichtner, The metamorphosis of rechargeable magnesium batteries, *Joule*. 5 (2021) 581–617. <https://doi.org/10.1016/j.joule.2020.12.021>.
- [7] G. Song, A. Atrens, Understanding magnesium corrosion. A framework for improved alloy performance, *Adv. Eng. Mater.* 5 (2003) 837–858. <https://doi.org/10.1002/adem.200310405>.
- [8] S. Thomas, N. V. Medhekar, G.S. Frankel, N. Birbilis, Corrosion mechanism and hydrogen evolution on Mg, *Curr. Opin. Solid State Mater. Sci.* 19 (2015) 85–94. <https://doi.org/10.1016/j.cossms.2014.09.005>.
- [9] E.J.F. Dickinson, A.J. Wain, The Butler-Volmer equation in electrochemical theory: Origins, value, and practical application, *J. Electroanal. Chem.* 872 (2020) 114145. <https://doi.org/10.1016/j.jelechem.2020.114145>.
- [10] B. Vaghefinazari, D. Höche, S. V. Lamaka, D. Snihirova, M.L. Zheludkevich, Tailoring the Mg-air primary battery performance using strong complexing agents as electrolyte additives, *J. Power Sources*. 453 (2020). <https://doi.org/10.1016/j.jpowsour.2020.227880>.
- [11] S. Sathyanarayana, N. Munichandraiah, A new magnesium - air cell for long-life applications, *J. Appl. Electrochem.* 11 (1981) 33–39. <https://doi.org/10.1007/BF00615319>.
- [12] L. Wang, D. Snihirova, M. Deng, C. Wang, D. Höche, S. V. Lamaka, M.L. Zheludkevich, Indium chloride as an electrolyte additive for primary aqueous Mg batteries, *Electrochim. Acta.* 373 (2021) 137916. <https://doi.org/10.1016/j.electacta.2021.137916>.
- [13] J. Huang, G.L. Song, A. Atrens, M. Dargusch, What activates the Mg surface—A comparison of Mg dissolution mechanisms, *J. Mater. Sci. Technol.* 57 (2020) 204–220. <https://doi.org/10.1016/j.jmst.2020.03.060>.

- [14] M.J. Earle, J.M.S.S. Esperança, M.A. Gilea, J.N.C. Lopes, L.P.N. Rebelo, J.W. Magee, K.R. Seddon, J.A. Widegren, The distillation and volatility of ionic liquids, *Nature*. 439 (2006) 831–834. <https://doi.org/10.1038/nature04451>.
- [15] P. Bonhôte, A.P. Dias, N. Papageorgiou, K. Kalyanasundaram, M. Grätzel, Hydrophobic, Highly Conductive Ambient-Temperature Molten Salts, *Inorg. Chem.* 35 (1996) 1168–1178. <https://doi.org/10.1021/ic951325x>.
- [16] N. DeVos, C. Maton, C. V. Stevens, Electrochemical Stability of Ionic Liquids: General Influences and Degradation Mechanisms, *ChemElectroChem*. 1 (2014) 1258–1270. <https://doi.org/10.1002/celec.201402086>.
- [17] A. Jarosik, S.R. Krajewski, A. Lewandowski, P. Radzimski, Conductivity of ionic liquids in mixtures, *J. Mol. Liq.* 123 (2006) 43–50. <https://doi.org/10.1016/j.molliq.2005.06.001>.
- [18] M. Thomas, M. Brehm, O. Hollóczki, Z. Kelemen, L. Nyulászki, T. Pasinszki, B. Kirchner, Simulating the vibrational spectra of ionic liquid systems: 1-Ethyl-3-methylimidazolium acetate and its mixtures, *J. Chem. Phys.* 141 (2014). <https://doi.org/10.1063/1.4887082>.
- [19] E.E. Fenn, D.E. Moilanen, N.E. Levinger, M.D. Fayer, Water Dynamics and Interactions in Water–Polyether Binary Mixtures, *J. Am. Chem. Soc.* 131 (2009) 5530–5539. <https://doi.org/10.1021/ja809261d>.
- [20] Y. Yu, A. Baskin, C. Valero-Vidal, N.T. Hahn, Q. Liu, K.R. Zavadil, B.W. Eichhorn, D. Prendergast, E.J. Crumlin, Instability at the electrode/electrolyte interface induced by hard cation chelation and nucleophilic attack, *Chem. Mater.* 29 (2017) 8504–8512. <https://doi.org/10.1021/acs.chemmater.7b03404>.
- [21] C. Wang, D. Mei, G. Wiese, L. Wang, M. Deng, S. V Lamaka, M.L. Zheludkevich, High rate oxygen reduction reaction during corrosion of ultra-high-purity magnesium, *Npj Mater. Degrad.* 4 (2020) 42. <https://doi.org/10.1038/s41529-020-00146-1>.
- [22] M. Strebl, M. Bruns, S. Virtanen, Editors’ Choice—Respirometric in Situ Methods for Real-Time Monitoring of Corrosion Rates: Part I. Atmospheric Corrosion, *J. Electrochem. Soc.* 167 (2020) 021510. <https://doi.org/10.1149/1945-7111/ab6c61>.
- [23] W. Beetz, XXXIV. On the development of hydrogen from the anode, London, Edinburgh, Dublin Philos. Mag. J. Sci. 32 (1866) 269–278. <https://doi.org/10.1080/14786446608644179>.
- [24] Y.L. G. Song, A. Atrens, D. Stjohn, J. Nairn, The electrochemical corrosion of pure magnesium in 1N NaCl, 39 (1997) 855–875. [https://doi.org/https://doi.org/10.1016/S0010-938X\(96\)00172-2](https://doi.org/https://doi.org/10.1016/S0010-938X(96)00172-2).
- [25] G. Song, A. Atrens, Understanding Magnesium Corrosion—A Framework for Improved Alloy Performance, *Adv. Eng. Mater.* 5 (2003) 837–858. <https://doi.org/10.1002/adem.200310405>.
- [26] Y. Li, Z. Shi, X. Chen, A. Atrens, Anodic hydrogen evolution on Mg, *J. Magnes. Alloy.* (2021). <https://doi.org/10.1016/j.jma.2021.09.002>.
- [27] W.D. Mueller, H. Hornberger, The influence of MgH₂ on the assessment of electrochemical data to predict the degradation rate of Mg and Mg alloys, *Int. J. Mol. Sci.* 15 (2014) 11456–11472. <https://doi.org/10.3390/ijms150711456>.
- [28] J. Chen, J. Dong, J. Wang, E. Han, W. Ke, Effect of magnesium hydride on the corrosion behavior of an AZ91 magnesium alloy in sodium chloride solution, *Corros. Sci.* 50 (2008) 3610–3614. <https://doi.org/10.1016/j.corsci.2008.09.013>.
- [29] G.L. Makar, J. Kruger, Corrosion Studies of Rapidly Solidified Magnesium Alloys, *J. Electrochem. Soc.* 137 (1990) 414–421. <https://doi.org/10.1149/1.2086455>.

- [30] G.L. Song, A. Atrens, Corrosion mechanisms of magnesium alloys, *Adv. Eng. Mater.* 1 (1999) 11–33. [https://doi.org/10.1002/\(SICI\)1527-2648\(199909\)1:1<11::AID-ADEM11>3.0.CO;2-N](https://doi.org/10.1002/(SICI)1527-2648(199909)1:1<11::AID-ADEM11>3.0.CO;2-N).
- [31] A. Atrens, G.L. Song, F. Cao, Z. Shi, P.K. Bowen, Advances in Mg corrosion and research suggestions, *J. Magnes. Alloy.* 1 (2013) 177–200. <https://doi.org/10.1016/j.jma.2013.09.003>.
- [32] S. Fajardo, G.S. Frankel, Effect of impurities on the enhanced catalytic activity for hydrogen evolution in high purity magnesium, *Electrochim. Acta.* 165 (2015) 255–267. <https://doi.org/10.1016/j.electacta.2015.03.021>.
- [33] G. Williams, H. Neil McMurray, Localized Corrosion of Magnesium in Chloride-Containing Electrolyte Studied by a Scanning Vibrating Electrode Technique, *J. Electrochem. Soc.* 155 (2008) C340. <https://doi.org/10.1149/1.2918900>.
- [34] D. Höche, C. Blawert, S. V. Lamaka, N. Scharnagl, C. Mendis, M.L. Zheludkevich, The effect of iron re-deposition on the corrosion of impurity-containing magnesium, *Phys. Chem. Chem. Phys.* 18 (2015) 1279–1291. <https://doi.org/10.1039/c5cp05577f>.
- [35] J.A. Yuwono, C.D. Taylor, G.S. Frankel, N. Birbilis, S. Fajardo, Understanding the enhanced rates of hydrogen evolution on dissolving magnesium, *Electrochem. Commun.* 104 (2019) 106482. <https://doi.org/10.1016/j.elecom.2019.106482>.
- [36] M.P. Gomes, I. Costa, N. Pébère, J.L. Rossi, B. Tribollet, V. Vivier, On the corrosion mechanism of Mg investigated by electrochemical impedance spectroscopy, *Electrochim. Acta.* 306 (2019) 61–70. <https://doi.org/10.1016/j.electacta.2019.03.080>.
- [37] M. Esmaily, J.E. Svensson, S. Fajardo, N. Birbilis, G.S. Frankel, S. Virtanen, R. Arrabal, S. Thomas, L.G. Johansson, Fundamentals and advances in magnesium alloy corrosion, *Prog. Mater. Sci.* 89 (2017) 92–193. <https://doi.org/10.1016/j.pmatsci.2017.04.011>.
- [38] R.E. McNulty, J.D. Hanawalt, Some Corrosion Characteristics of High Purity Magnesium Alloys, *Trans. Electrochem. Soc.* 81 (1942) 423. <https://doi.org/10.1149/1.3071389>.
- [39] D. Mercier, J. Światowska, E. Protopopoff, S. Zanna, A. Seyeux, P. Marcus, Inhibition of Mg Corrosion by Sulfur Blocking of the Hydrogen Evolution Reaction on Iron Impurities, *J. Electrochem. Soc.* 167 (2020) 121504. <https://doi.org/10.1149/1945-7111/abaf79>.
- [40] D. Mercier, J. Światowska, S. Zanna, A. Seyeux, P. Marcus, Role of Segregated Iron at Grain Boundaries on Mg Corrosion, *J. Electrochem. Soc.* 165 (2018) C42–C49. <https://doi.org/10.1149/2.0621802jes>.
- [41] E. Michailidou, H.N. McMurray, G. Williams, Quantifying the Role of Transition Metal Electrodeposition in the Cathodic Activation of Corroding Magnesium, *J. Electrochem. Soc.* 165 (2018) C195–C205. <https://doi.org/10.1149/2.0251805jes>.
- [42] G. Williams, N. Birbilis, H.N. McMurray, Controlling factors in localised corrosion morphologies observed for magnesium immersed in chloride containing electrolyte, *Faraday Discuss.* 180 (2015) 313–330. <https://doi.org/10.1039/c4fd00268g>.
- [43] T. Cain, S.B. Madden, N. Birbilis, J.R. Scully, Evidence of the Enrichment of Transition Metal Elements on Corroding Magnesium Surfaces Using Rutherford Backscattering Spectrometry, *J. Electrochem. Soc.* 162 (2015) C228–C237. <https://doi.org/10.1149/2.0541506jes>.
- [44] M. Taheri, J.R. Kish, N. Birbilis, M. Danaie, E.A. McNally, J.R. McDermid, Towards a physical description for the origin of enhanced catalytic activity of corroding magnesium surfaces, *Electrochim. Acta.* 116 (2014) 396–403. <https://doi.org/10.1016/j.electacta.2013.11.086>.
- [45] K. Gusieva, C.H.J. Davies, J.R. Scully, N. Birbilis, Corrosion of magnesium alloys: the role of alloying, *Int. Mater. Rev.* 60 (2015) 169–194. <https://doi.org/10.1179/1743280414Y.0000000046>.

- [46] S. Al Bacha, I. Aubert, O. Devos, M. Zakhour, M. Nakhl, J.-L. Bobet, Corrosion of pure and milled Mg₁₇Al₁₂ in “model” seawater solution, *International Journal of Hydrogen Energy*, 45, 32, 2020, 15805-15813, <https://doi.org/10.1016/j.ijhydene.2020.04.030>.
- [47] S. Fajardo, J. Bosch, G.S. Frankel, Anomalous hydrogen evolution on AZ31, AZ61 and AZ91 magnesium alloys in unbuffered sodium chloride solution, *Corros. Sci.* 146 (2019) 163–171. <https://doi.org/10.1016/j.corsci.2018.10.039>.
- [48] P. Volovitch, M. Serdechnova, K. Ogle, Aqueous corrosion of Mg-Al binary alloys: Roles of Al and Mg, *Corrosion*. 68 (2012) 557–570. <https://doi.org/10.5006/i0010-9312-68-6-557>.
- [49] Y.M. Yan, O. Gharbi, A. Maltseva, X.B. Chen, Z.R. Zeng, S.W. Xu, W.Q. Xu, P. Volovich, M. Ferry, N. Birbilis, Investigating the Structure of the Surface Film on a Corrosion Resistant Mg-Li(-Al-Y-Zr) Alloy, *Corrosion*. 75 (2018) 80–89. <https://doi.org/10.5006/2995>.
- [50] S. Luo, Q. Zhang, Y. Zhang, C. Li, X. Xu, T. Zhou, In vitro and in vivo studies on a Mg-Li-X alloy system developed as a new kind of biological metal, *Mater. Sci. Forum.* 747–748 (2013) 257–263. <https://doi.org/10.4028/www.scientific.net/MSF.747-748.257>.
- [51] T.W. Cain, J.P. Labukas, The development of β phase Mg–Li alloys for ultralight corrosion resistant applications, *Npj Mater. Degrad.* 4 (2020). <https://doi.org/10.1038/s41529-020-0121-2>.
- [52] Y. hua SUN, R. chu WANG, C. qun PENG, Y. FENG, M. YANG, Corrosion behavior and surface treatment of superlight Mg–Li alloys, *Trans. Nonferrous Met. Soc. China (English Ed.)* 27 (2017) 1455–1475. [https://doi.org/10.1016/S1003-6326\(17\)60167-5](https://doi.org/10.1016/S1003-6326(17)60167-5).
- [53] R. Wu, Y. Yan, G. Wang, L.E. Murr, W. Han, Z. Zhang, M. Zhang, Recent progress in magnesium-lithium alloys, *Int. Mater. Rev.* 60 (2015) 65–100. <https://doi.org/10.1179/1743280414Y.0000000044>.
- [54] Y. Pan, C. Chen, R. Feng, H. Cui, B. Gong, T. Zheng, Y. Ji, Effect of calcium on the microstructure and corrosion behavior of microarc oxidized Mg-xCa alloys, *Biointerphases*. 13 (2018) 011003. <https://doi.org/10.1116/1.5003320>.
- [55] M. Deng, D. Höche, S. V. Lamaka, D. Snihirova, M.L. Zheludkevich, Mg-Ca binary alloys as anodes for primary Mg-air batteries, *J. Power Sources*. 396 (2018) 109–118. <https://doi.org/10.1016/j.jpowsour.2018.05.090>.
- [56] M. Deng, L. Wang, D. Höche, S. V. Lamaka, C. Wang, D. Snihirova, Y. Jin, Y. Zhang, M.L. Zheludkevich, Approaching “stainless magnesium” by Ca micro-alloying, *Mater. Horizons*. 8 (2021) 589–596. <https://doi.org/10.1039/d0mh01380c>.
- [57] S.J.B. Bin, K.S. Fong, B.W. Chua, M. Gupta, Mg-based bulk metallic glasses: A review of recent developments, *J. Magnes. Alloy.* (2021). <https://doi.org/10.1016/j.jma.2021.10.010>.
- [58] V. Hasannaemi, M. Sadeghilaridjani, S. Mukherjee, Electrochemical and Corrosion Behavior of Metallic Glasses, 2021. <https://library.oapen.org/handle/20.500.12657/47561>.
- [59] F. Cao, B. Xiao, Z. Wang, T. Ying, D. Zheng, A. Atrens, G.L. Song, A Mg alloy with no hydrogen evolution during dissolution, *J. Magnes. Alloy.* (2021). <https://doi.org/10.1016/j.jma.2021.08.024>.
- [60] J.H. Nordlien, S. Ono, N. Masuko, K. Nisancioglu, A tem investigation of naturally formed oxide films on pure magnesium, *Corros. Sci.* 39 (1997) 1397–1414. [https://doi.org/10.1016/S0010-938X\(97\)00037-1](https://doi.org/10.1016/S0010-938X(97)00037-1).
- [61] M. Taheri, R.C. Phillips, J.R. Kish, G.A. Botton, Analysis of the surface film formed on Mg by exposure to water using a FIB cross-section and STEM-EDS, *Corros. Sci.* 59 (2012) 222–228. <https://doi.org/10.1016/j.corsci.2012.03.001>.

- [62] McMurray H., Williams G., Localized Corrosion of Magnesium in Chloride Containing Electrolyte Studied by a Scanning Vibrating Electrode Technique, *J. Electrochem. Soc.* 155 (2008) 340–349. <https://iopscience.iop.org/article/10.1149/1.2918900>
- [63] S.H. Salleh, S. Thomas, J.A. Yuwono, K. Venkatesan, N. Birbilis, Enhanced hydrogen evolution on Mg (OH)₂ covered Mg surfaces, *Electrochim. Acta.* 161 (2015) 144–152. <https://doi.org/10.1016/j.electacta.2015.02.079>.
- [64] K.S. Williams, J.P. Labukas, V. Rodriguez-Santiago, J.W. Andzelm, First Principles Modeling of Water Dissociation on Mg(0001) and Development of a Mg Surface Pourbaix Diagram, *CORROSION.* 71 (2015) 209–223. <https://doi.org/10.5006/1322>.
- [65] Y. Yang, F. Scenini, M. Curioni, A study on magnesium corrosion by real-time imaging and electrochemical methods: Relationship between local processes and hydrogen evolution, *Electrochim. Acta.* 198 (2016) 174–184. <https://doi.org/10.1016/j.electacta.2016.03.043>.
- [66] M.F. Montemor, Functional and smart coatings for corrosion protection: A review of recent advances, *Surf. Coatings Technol.* 258 (2014) 17–37. <https://doi.org/10.1016/j.surfcoat.2014.06.031>.
- [67] M.L. Zheludkevich, S.K. Poznyak, L.M. Rodrigues, D. Raps, T. Hack, L.F. Dick, T. Nunes, M.G.S. Ferreira, Active protection coatings with layered double hydroxide nanocontainers of corrosion inhibitor, *Corros. Sci.* 52 (2010) 602–611. <https://doi.org/10.1016/j.corsci.2009.10.020>.
- [68] N. V. Murillo-Gutiérrez, F. Ansart, J.P. Bonino, M.J. Menu, M. Gressier, Protection against corrosion of magnesium alloys with both conversion layer and sol-gel coating, *Surf. Coatings Technol.* 232 (2013) 606–615. <https://doi.org/10.1016/j.surfcoat.2013.06.036>.
- [69] X.B. Chen, M.A. Easton, N. Birbilis, H.Y. Yang, T.B. Abbott, Corrosion-resistant electrochemical plating of magnesium (Mg) alloys, Woodhead Publishing Limited, 2013. <https://doi.org/10.1533/9780857098962.3.315>.
- [70] S. V. Lamaka, B. Vaghefinazari, D. Mei, R.P. Petrauskas, D. Höche, M.L. Zheludkevich, Comprehensive screening of Mg corrosion inhibitors, *Corros. Sci.* 128 (2017) 224–240. <https://doi.org/10.1016/j.corsci.2017.07.011>.
- [71] Y. Liu, Z. Yu, S. Zhou, L. Wu, Self-assembled monolayers on magnesium alloy surfaces from carboxylate ions, *Appl. Surf. Sci.* 252 (2006) 3818–3827. <https://doi.org/10.1016/j.apsusc.2005.05.072>.
- [72] A. Maltseva, S. V. Lamaka, K.A. Yasakau, D. Mei, D. Kurchavov, M.L. Zheludkevich, G. Lefèvre, P. Volovitch, In situ surface film evolution during Mg aqueous corrosion in presence of selected carboxylates, *Corros. Sci.* 171 (2020) 108484. <https://doi.org/10.1016/j.corsci.2020.108484>.
- [73] B. Vaghefinazari, C. Wang, D. Mercier, D. Mei, A. Seyeux, P. Marcus, C. Blawert, S. V. Lamaka, M.L. Zheludkevich, Adverse effect of 2,5PDC corrosion inhibitor on PEO coated magnesium, *Corros. Sci.* 192 (2021) 109830. <https://doi.org/10.1016/j.corsci.2021.109830>.
- [74] X. Liu, L. Hou, H. Wang, Y. Li, H. Wei, B. Liu, H. Du, Y. Wei, Synergistic inhibition behavior of sodium diethyldithiocarbamate and sodium acetate for AZ31B magnesium alloy in NaCl solution, *Mater. Express.* 9 (2019) 27–41. <https://doi.org/10.1166/mex.2019.1472>.
- [75] X. Lu, Y. Li, P. Ju, Y. Chen, J. Yang, K. Qian, T. Zhang, F. Wang, Unveiling the inhibition mechanism of an effective inhibitor for AZ91 Mg alloy, *Corros. Sci.* 148 (2019) 264–271. <https://doi.org/10.1016/j.corsci.2018.12.025>.
- [76] D. Huang, J. Hu, G.L. Song, X. Guo, Inhibition effect of inorganic and organic inhibitors on the corrosion of Mg-10Gd-3Y-0.5Zr alloy in an ethylene glycol solution at ambient and elevated

- temperatures, *Electrochim. Acta.* 56 (2011) 10166–10178.
<https://doi.org/10.1016/j.electacta.2011.09.002>.
- [77] G. Song, A. Atrens, D. St. John, X. Wu, J. Nairn, The anodic dissolution of magnesium in chloride and sulphate solutions, *Corros. Sci.* 39 (1997) 1981–2004. [https://doi.org/10.1016/S0010-938X\(97\)00090-5](https://doi.org/10.1016/S0010-938X(97)00090-5).
- [78] J. Świątowska, P. Volovitch, K. Ogle, The anodic dissolution of Mg in NaCl and Na₂SO₄ electrolytes by atomic emission spectroelectrochemistry, *Corros. Sci.* 52 (2010) 2372–2378. <https://doi.org/10.1016/j.corsci.2010.02.038>.
- [79] F.W. Richey, B.D. McCloskey, A.C. Luntz, Mg Anode Corrosion in Aqueous Electrolytes and Implications for Mg-Air Batteries, *J. Electrochem. Soc.* 163 (2016) A958–A963. <https://doi.org/10.1149/2.0781606jes>.
- [80] M. Curioni, M. Lyu, A. Cioncolini, F. Scenini, Investigating the Effect of pH on Corroding Magnesium by Dynamic pH Sweep Coupled with Electrochemical Measurements, *Corrosion.* 77 (2020) 148–155. <https://doi.org/10.5006/3593>.
- [81] L. Rossrucker, A. Samaniego, J.-P. Grote, A.M. Mingers, C.A. Laska, N. Birbilis, G.S. Frankel, K.J.J. Mayrhofer, The pH Dependence of Magnesium Dissolution and Hydrogen Evolution during Anodic Polarization, *J. Electrochem. Soc.* 162 (2015) C333–C339. <https://doi.org/10.1149/2.0621507jes>.
- [82] L. Wang, D. Snihirova, M. Deng, C. Wang, B. Vaghefinazari, G. Wiese, M. Langridge, D. Höche, S. V. Lamaka, M.L. Zheludkevich, Insight into physical interpretation of high frequency time constant in electrochemical impedance spectra of Mg, *Corros. Sci.* 187 (2021). <https://doi.org/10.1016/j.corsci.2021.109501>.
- [83] S. Lebouil, O. Gharbi, P. Volovitch, K. Ogle, Mg dissolution in phosphate and chloride electrolytes: Insight into the mechanism of the negative difference effect, *Corrosion.* 71 (2015) 234–241. <https://doi.org/10.5006/1459>.
- [84] W. Silva, M. Zanatta, A.S. Ferreira, M.C. Corvo, E.J. Cabrita, Revisiting ionic liquid structure-property relationship: A critical analysis, *Int. J. Mol. Sci.* 21 (2020) 1–37. <https://doi.org/10.3390/ijms21207745>.
- [85] P. Walden, Molecular weights and electrical conductivity of several fused salts *Bull. Acad. Imper. Sci.* 8 405-422 (1914) - Google Scholar, *Bull. Acad. Imper. Sci.(St. Petersburg).* 8 (1914) 405–422.
- [86] J.S. Wilkes, M.J. Zaworotko, Air and water stable 1-ethyl-3-methylimidazolium based ionic liquids, *J. Chem. Soc. Chem. Commun.* (1992) 965–967. <https://doi.org/10.1039/C39920000965>.
- [87] A.E. Visser, R.P. Swatloski, W.M. Reichert, R. Mayton, S. Sheff, A. Wierzbicki, J. Davis, R.D. Rogers, Task-specific ionic liquids for the extraction of metal ions from aqueous solutions, *Chem. Commun.* (2001) 135–136. <https://doi.org/10.1039/b008041l>.
- [88] S. Jiang, Y. Hu, Y. Wang, X. Wang, Viscosity of Typical Room-Temperature Ionic Liquids: A Critical Review, *J. Phys. Chem. Ref. Data.* 48 (2019). <https://doi.org/10.1063/1.5090486>.
- [89] M. Hayyan, F.S. Mjalli, M.A. Hashim, I.M. AlNashef, T.X. Mei, Investigating the electrochemical windows of ionic liquids, *J. Ind. Eng. Chem.* 19 (2013) 106–112. <https://doi.org/10.1016/j.jiec.2012.07.011>.
- [90] M. Klahn, C. Stüber, A. Seduraman, P. Wu, What determines the miscibility of ionic liquids with water? Identification of the underlying factors to enable a straightforward prediction, *J. Phys. Chem. B.* 114 (2010) 2856–2868. <https://doi.org/10.1021/jp1000557>.
- [91] L.M. Galán Sánchez, J.R. Espel, F. Onink, G.W. Meindersma, A.B. De Haan, Density, viscosity, and

- surface tension of synthesis grade imidazolium,pyridinium, and pyrrolidinium based room temperature ionic liquids, *J. Chem. Eng. Data.* 54 (2009) 2803–2812.
<https://doi.org/10.1021/je800710p>.
- [92] K. Tsunashima, M. Sugiya, Physical and electrochemical properties of low-viscosity phosphonium ionic liquids as potential electrolytes, *Electrochem. Commun.* 9 (2007) 2353–2358.
<https://doi.org/10.1016/j.elecom.2007.07.003>.
- [93] R. Khalil, N. Chaabene, M. Azar, I.B. Malham, M. Turmine, Effect of the chain lengthening on transport properties of imidazolium-based ionic liquids, *Fluid Phase Equilib.* 503 (2020) 112316.
<https://doi.org/10.1016/j.fluid.2019.112316>.
- [94] J. Ma, Y. Wang, X. Yang, B. Wang, *Fast Track to Acetate-Based Ionic Liquids: Preparation, Properties and Application in Energy and Petrochemical Fields*, Springer International Publishing, 2021. <https://doi.org/10.1007/s41061-020-00315-5>.
- [95] D.R. Macfarlane, N. Tachikawa, M. Forsyth, J.M. Pringle, P.C. Howlett, G.D. Elliott, J.H. Davis, M. Watanabe, P. Simon, C.A. Angell, Energy applications of ionic liquids, *Energy Environ. Sci.* 7 (2014) 232–250. <https://doi.org/10.1039/c3ee42099j>.
- [96] S. Caporali, F. Ghezzi, A. Giorgetti, A. Lavacchi, A. Tolstogouzov, U. Bardi, Interaction between an imidazolium based ionic liquid and the AZ91D magnesium alloy, *Adv. Eng. Mater.* 9 (2007) 185–190. <https://doi.org/10.1002/adem.200600250>.
- [97] Z. Xue, L. Qin, J. Jiang, T. Mu, G. Gao, Thermal, electrochemical and radiolytic stabilities of ionic liquids, *Phys. Chem. Chem. Phys.* 20 (2018) 8382–8402. <https://doi.org/10.1039/c7cp07483b>.
- [98] E. Knipping, C. Aucher, G. Guirado, L. Aubouy, Room temperature ionic liquids: Versus organic solvents as lithium-oxygen battery electrolytes, *New J. Chem.* 42 (2018) 4693–4699.
<https://doi.org/10.1039/c8nj00449h>.
- [99] S. Ravula, N.E. Larm, M.A. Mottaleb, M.P. Heitz, G.A. Baker, Vapor pressure mapping of ionic liquids and low-volatility fluids using graded isothermal thermogravimetric analysis, *ChemEngineering.* 3 (2019) 1–12. <https://doi.org/10.3390/chemengineering3020042>.
- [100] D.M. Fox, W.H. Awad, J.W. Gilman, P.H. Maupin, H.C. De Long, P.C. Trulove, Flammability, thermal stability, and phase change characteristics of several trialkylimidazolium salts, *Green Chem.* 5 (2003) 724–727. <https://doi.org/10.1039/b308444b>.
- [101] A. Taheri, B. Lai, C. Cheng, Y. Gu, Brønsted acid ionic liquid-catalyzed reductive Friedel-Crafts alkylation of indoles and cyclic ketones without using an external reductant, *Green Chem.* 17 (2015) 812–816. <https://doi.org/10.1039/c4gc01299b>.
- [102] I.A.M. Asiri, *Applications of Nanotechnology for Green Synthesis*, 2020.
<http://link.springer.com/10.1007/978-3-030-44176-0>.
- [103] M.R. Ehrenburg, E.B. Molodkina, A. Mishchenko, A. V. Rudnev, The promoting effect of water on the electrodeposition of Eu in a dicyanamide ionic liquid, *Electrochim. Acta.* 379 (2021).
<https://doi.org/10.1016/j.electacta.2021.138169>.
- [104] M. Armand, F. Endres, D.R. MacFarlane, H. Ohno, B. Scrosati, Ionic-liquid materials for the electrochemical challenges of the future, *Nat. Mater.* 8 (2009) 621–629.
<https://doi.org/10.1038/nmat2448>.
- [105] S. Chowdhury, R.S. Mohan, J.L. Scott, Reactivity of ionic liquids, *Tetrahedron.* 63 (2007) 2363–2389. <https://doi.org/10.1016/j.tet.2006.11.001>.
- [106] P.W. and T. Welton, *Ionic liquids in synthesis - Wasserscheid & Welton.pdf*, (2003) 360.

- [107] M. López-Pastor, M.J. Ayora-Cañada, M. Valcárcel, B. Lendl, Association of methanol and water in ionic liquids elucidated by infrared spectroscopy using two-dimensional correlation and multivariate curve resolution, *J. Phys. Chem. B.* 110 (2006) 10896–10902. <https://doi.org/10.1021/jp057398b>.
- [108] J.G. Huddleston, A.E. Visser, W.M. Reichert, H.D. Willauer, G.A. Broker, R.D. Rogers, Characterization and comparison of hydrophilic and hydrophobic room temperature ionic liquids incorporating the imidazolium cation, *Green Chem.* 3 (2001) 156–164. <https://doi.org/10.1039/b103275p>.
- [109] Y. Chen, Y. Cao, T. Mu, A new application of acetate-based ionic liquids: Potential usage as drying materials, *Chem. Eng. Technol.* 37 (2014) 527–534. <https://doi.org/10.1002/ceat.201300583>.
- [110] Z. Wang, L. Fu, H. Xu, Y. Shang, L. Zhang, J. Zhang, Density, viscosity, and conductivity for the binary systems of water + dual amino-functionalized ionic liquids, *J. Chem. Eng. Data.* 57 (2012) 1057–1063. <https://doi.org/10.1021/je2007549>.
- [111] K.R. Seddon, A. Stark, M.-J.J. Torres, Influence of chloride, water, and organic solvents on the physical properties of ionic liquids, *Pure Appl. Chem.* 72 (2000) 2275–2287. <https://doi.org/10.1351/pac200072122275>.
- [112] T.A. Fadeeva, P. Husson, J.A. Devine, M.F. Costa Gomes, S.G. Greenbaum, E.W. Castner, Interactions between water and 1-butyl-1-methylpyrrolidinium ionic liquids, *J. Chem. Phys.* 143 (2015) 1–13. <https://doi.org/10.1063/1.4928065>.
- [113] Y. Zhang, R. Ye, D. Henkensmeier, R. Hempelmann, R. Chen, “Water-in-ionic liquid” solutions towards wide electrochemical stability windows for aqueous rechargeable batteries, *Electrochim. Acta.* 263 (2018) 47–52. <https://doi.org/10.1016/j.electacta.2018.01.050>.
- [114] R. Chen, R. Hempelmann, Ionic liquid-mediated aqueous redox flow batteries for high voltage applications, *Electrochem. Commun.* 70 (2016) 56–59. <https://doi.org/10.1016/j.elecom.2016.07.003>.
- [115] S. Chen, R. Lan, J. Humphreys, S. Tao, Effect of cation size on alkali acetate-based ‘water-in-bisalt’ electrolyte and its application in aqueous rechargeable lithium battery, *Appl. Mater. Today.* 20 (2020) 100728. <https://doi.org/10.1016/j.apmt.2020.100728>.
- [116] L. Cammarata, S.G. Kazarian, P.A. Salter, T. Welton, Molecular states of water in room temperature ionic liquids, *Phys. Chem. Chem. Phys.* 3 (2001) 5192–5200. <https://doi.org/10.1039/b106900d>.
- [117] V.H. Paschoal, L.F.O. Faria, M.C.C. Ribeiro, Vibrational Spectroscopy of Ionic Liquids, *Chem. Rev.* 117 (2017) 7053–7112. <https://doi.org/10.1021/acs.chemrev.6b00461>.
- [118] M.I. Barba, M.S. Larrechi, A. Coronas, Quantitative analysis of free water in ionic liquid-water mixtures, *Talanta.* 199 (2019) 407–414. <https://doi.org/10.1016/j.talanta.2019.02.087>.
- [119] T. Köddermann, C. Wertz, A. Heintz, R. Ludwig, The association of water in ionic liquids: A reliable measure of polarity, *Angew. Chemie - Int. Ed.* 45 (2006) 3697–3702. <https://doi.org/10.1002/anie.200504471>.
- [120] J. Gao, N.J. Wagner, Water Nanocluster Formation in the Ionic Liquid 1-Butyl-3-methylimidazolium Tetrafluoroborate ([C4mim][BF4])-D2O Mixtures, *Langmuir.* 32 (2016) 5078–5084. <https://doi.org/10.1021/acs.langmuir.6b00494>.
- [121] H.E. Bailey, Y.L. Wang, M.D. Fayer, The influence of hydrophilicity on the orientational dynamics and structures of imidazolium-based ionic liquid/water binary mixtures, *J. Chem. Phys.* 149 (2018). <https://doi.org/10.1063/1.5038563>.

- [122] W. Jiang, Y. Wang, G.A. Voth, Molecular dynamics simulation of nanostructural organization in ionic liquid/water mixtures, *J. Phys. Chem. B.* 111 (2007) 4812–4818. <https://doi.org/10.1021/jp0671421>.
- [123] J.N. Canongia Lopes, M.F. Costa Gomes, A.A.H. Pádua, Nonpolar, polar, and associating solutes in ionic liquids, *J. Phys. Chem. B.* 110 (2006) 16816–16818. <https://doi.org/10.1021/jp063603r>.
- [124] A.R. Porter, S.Y. Liem, P.L.A. Popelier, Room temperature ionic liquids containing low water concentrations—a molecular dynamics study, *Phys. Chem. Chem. Phys.* 10 (2008) 4240–4248. <https://doi.org/10.1039/b718011j>.
- [125] S. Feng, G.A. Voth, Molecular dynamics simulations of imidazolium-based ionic liquid/water mixtures: Alkyl side chain length and anion effects, *Fluid Phase Equilib.* 294 (2010) 148–156. <https://doi.org/10.1016/j.fluid.2010.02.034>.
- [126] T. Koishi, Molecular Dynamics Study of the Effect of Water on Hydrophilic and Hydrophobic Ionic Liquids, *J. Phys. Chem. B.* 122 (2018) 12342–12350. <https://doi.org/10.1021/acs.jpcc.8b07774>.
- [127] A. Dominguez-Vidal, N. Kaun, M.J. Ayora-Cañada, B. Lendl, Probing intermolecular interactions in water/ionic liquid mixtures by far-infrared spectroscopy, *J. Phys. Chem. B.* 111 (2007) 4446–4452. <https://doi.org/10.1021/jp068777n>.
- [128] O. Palumbo, F. Trequattrini, J.B. Brubach, P. Roy, A. Paolone, Molecular assembling in mixtures of hydrophilic 1-butyl-1-methylpyrrolidinium dicyanamide ionic liquid and water, *Appl. Sci.* 10 (2020). <https://doi.org/10.3390/app10144837>.
- [129] M. Brehm, H. Weber, A.S. Pensado, A. Stark, B. Kirchner, Liquid structure and cluster formation in ionic liquid/water mixtures - An extensive ab initio molecular dynamics study on 1-ethyl-3-methylimidazolium acetate/water mixtures - Part 2, *Zeitschrift Fur Phys. Chemie.* 227 (2013) 177–203. <https://doi.org/10.1524/zpch.2012.0327>.
- [130] M. Brehm, H. Weber, A.S. Pensado, A. Stark, B. Kirchner, Proton transfer and polarity changes in ionic liquid-water mixtures: A perspective on hydrogen bonds from ab initio molecular dynamics at the example of 1-ethyl-3-methylimidazolium acetate-water mixtures - Part 1, *Phys. Chem. Chem. Phys.* 14 (2012) 5030–5044. <https://doi.org/10.1039/c2cp23983c>.
- [131] J.-A. Latham, P.C. Howlett, D.R. MacFarlane, A. Somers, M. Forsyth, Anodising AZ31 in a Phosphonium Ionic Liquid: Corrosion Protection through Composite Film Deposition, *J. Electrochem. Soc.* 159 (2012) C539–C545. <https://doi.org/10.1149/2.015212jes>.
- [132] M. Forsyth, P.C. Howlett, S.K. Tan, D.R. MacFarlane, N. Birbilis, An ionic liquid surface treatment for corrosion protection of magnesium alloy AZ31, *Electrochem. Solid-State Lett.* 9 (2006) 52–55. <https://doi.org/10.1149/1.2344826>.
- [133] P.C. Howlett, T. Khoo, G. Mooketsi, J. Efthimiadis, D.R. MacFarlane, M. Forsyth, The effect of potential bias on the formation of ionic liquid generated surface films on Mg alloys, *Electrochim. Acta.* 55 (2010) 2377–2383. <https://doi.org/10.1016/j.electacta.2009.11.080>.
- [134] A. Shkurankov, S. Zein El Abedin, F. Endres, AFM-assisted investigation of the corrosion behaviour of magnesium and AZ91 alloys in an ionic liquid with varying water content, *Aust. J. Chem.* 60 (2007) 35–42. <https://doi.org/10.1071/CH06305>.
- [135] T. Khoo, P.C. Howlett, M. Tsagouria, D.R. MacFarlane, M. Forsyth, The potential for ionic liquid electrolytes to stabilise the magnesium interface for magnesium/air batteries, *Electrochim. Acta.* 58 (2011) 583–588. <https://doi.org/10.1016/j.electacta.2011.10.006>.
- [136] T. Watkins, A. Kumar, D.A. Buttry, Supporting Information Designer Ionic Liquids for Reversible Electrochemical Deposition / Dissolution of Mg, *J. Am. Chem. Soc.* 138 (2016) 1–9.

<https://doi.org/10.1021/jacs.5b11031>.

- [137] X. Gao, A. Mariani, S. Jeong, X. Liu, X. Dou, M. Ding, A. Moretti, S. Passerini, Prototype rechargeable magnesium batteries using ionic liquid electrolytes, *J. Power Sources*. 423 (2019) 52–59. <https://doi.org/10.1016/j.jpowsour.2019.03.049>.
- [138] M. Kar, O. Tutusaus, D.R. MacFarlane, R. Mohtadi, Novel and versatile room temperature ionic liquids for energy storage, *Energy Environ. Sci.* 12 (2019) 566–571. <https://doi.org/10.1039/c8ee02437e>.
- [139] M. Schmeisser, P. Illner, R. Puchta, A. Zahl, R. Van Eldik, Gutmann donor and acceptor numbers for ionic liquids, *Chem. - A Eur. J.* 18 (2012) 10969–10982. <https://doi.org/10.1002/chem.201200584>.
- [140] L.V.N.R. Ganapatibhotla, J. Zheng, D. Roy, S. Krishnan, PEGylated imidazolium ionic liquid electrolytes: Thermophysical and electrochemical properties, *Chem. Mater.* 22 (2010) 6347–6360. <https://doi.org/10.1021/cm102263s>.
- [141] D. Kasprzak, I. Stępnia, M. Galiński, Acetate- and lactate-based ionic liquids: Synthesis, characterisation and electrochemical properties, *J. Mol. Liq.* 264 (2018) 233–241. <https://doi.org/10.1016/j.molliq.2018.05.059>.
- [142] N. Frenzel, J. Hartley, G. Frisch, Voltammetric and spectroscopic study of ferrocene and hexacyanoferrate and the suitability of their redox couples as internal standards in ionic liquids, *Phys. Chem. Chem. Phys.* 19 (2017) 28841–28852. <https://doi.org/10.1039/c7cp05483a>.
- [143] J. M. Thompson, *Infrared spectroscopy*, Pan Stanford Publishing Pte. Ltd, 2018.
- [144] A. Maltseva, V. Shkirskiy, G. Lefèvre, P. Volovitch, Effect of pH on Mg(OH)₂ film evolution on corroding Mg by in situ kinetic Raman mapping (KRM), *Corros. Sci.* 153 (2019) 272–282. <https://doi.org/10.1016/j.corsci.2019.03.024>.
- [145] M. Finšgar, Surface analysis of the 2-mercaptobenzothiazole corrosion inhibitor on 6082 aluminum alloy using ToF-SIMS and XPS, *Anal. Methods*. 12 (2020) 456–465. <https://doi.org/10.1039/c9ay02293g>.
- [146] M. Esmaily, P. Malmberg, M. Shahabi-Navid, J.E. Svensson, L.G. Johansson, A ToF-SIMS investigation of the corrosion behavior of Mg alloy AM50 in atmospheric environments, *Appl. Surf. Sci.* 360 (2016) 98–106. <https://doi.org/10.1016/j.apsusc.2015.11.002>.
- [147] S. Bender, J. Goellner, A. Heyn, S. Schmigalla, A new theory for the negative difference effect in magnesium corrosion, *Mater. Corros.* 63 (2012) 707–712. <https://doi.org/10.1002/maco.201106225>.
- [148] S. Lebouil, A. Duboin, F. Monti, P. Tabeling, P. Volovitch, K. Ogle, A novel approach to on-line measurement of gas evolution kinetics: Application to the negative difference effect of Mg in chloride solution, *Electrochim. Acta.* 124 (2014) 176–182. <https://doi.org/10.1016/j.electacta.2013.07.131>.
- [149] L. Rossrucker, K.J.J. Mayrhofer, G.S. Frankel, N. Birbilis, Investigating the Real Time Dissolution of Mg Using Online Analysis by ICP-MS, *J. Electrochem. Soc.* 161 (2014) C115–C119. <https://doi.org/10.1149/2.064403jes>.
- [150] G. Baril, G. Galicia, C. Deslouis, N. Pébère, B. Tribollet, V. Vivier, An Impedance Investigation of the Mechanism of Pure Magnesium Corrosion in Sodium Sulfate Solutions, *J. Electrochem. Soc.* 154 (2007) C108. <https://doi.org/10.1149/1.2401056>.
- [151] O. Tutusaus, R. Mohtadi, T.S. Arthur, F. Mizuno, E.G. Nelson, Y. V. Sevryugina, An Efficient Halogen-Free Electrolyte for Use in Rechargeable Magnesium Batteries, *Angew. Chemie - Int. Ed.*

- 54 (2015) 7900–7904. <https://doi.org/10.1002/anie.201412202>.
- [152] N. Amir, Y. Vestfrid, O. Chusid, Y. Gofer, D. Aurbach, Progress in nonaqueous magnesium electrochemistry, *J. Power Sources*. 174 (2007) 1234–1240. <https://doi.org/10.1016/j.jpowsour.2007.06.206>.
- [153] A.M. O'Mahony, D.S. Silvester, L. Aldous, C. Hardacre, R.G. Compton, Effect of water on the electrochemical window and potential limits of room-temperature ionic liquids, *J. Chem. Eng. Data*. 53 (2008) 2884–2891. <https://doi.org/10.1021/je800678e>.
- [154] K.N. Marsh, J.A. Boxall, R. Lichtenthaler, Room temperature ionic liquids and their mixtures - A review, *Fluid Phase Equilib.* 219 (2004) 93–98. <https://doi.org/10.1016/j.fluid.2004.02.003>.
- [155] S. Fendt, S. Padmanabhan, H.W. Blanch, J.M. Prausnitz, Viscosities of acetate or chloride-based ionic liquids and some of their mixtures with water or other common solvents, *J. Chem. Eng. Data*. 56 (2011) 31–34. <https://doi.org/10.1021/je1007235>.
- [156] T. Zhang, Z. Tao, J. Chen, Magnesium-air batteries: From principle to application, *Mater. Horizons*. 1 (2014) 196–206. <https://doi.org/10.1039/c3mh00059a>.
- [157] B. Bednarska-Bolek, R. Jakubas, G. Bator, J. Baran, Vibrational study of the structural phase transition in bis(pyrrolidinium)-chloride-hexachloroantimonate(V) by infrared spectroscopy, *J. Mol. Struct.* 614 (2002) 151–157. [https://doi.org/10.1016/S0022-2860\(02\)00235-1](https://doi.org/10.1016/S0022-2860(02)00235-1).
- [158] M.I. Cabaço, M. Besnard, Y. Danten, J.A.P. Coutinho, Carbon dioxide in 1-butyl-3-methylimidazolium acetate. I. Unusual solubility investigated by Raman spectroscopy and DFT calculations, *J. Phys. Chem. A*. 116 (2012) 1605–1620. <https://doi.org/10.1021/jp211211n>.
- [159] M. Castriota, T. Caruso, R.G. Agostino, E. Cazzanelli, W.A. Henderson, S. Passerini, Raman investigation of the ionic liquid N-methyl-N-propylpyrrolidinium bis(trifluoromethanesulfonyl)imide and its mixture with LiN(SO₂CF₃)₂, *J. Phys. Chem. A*. 109 (2005) 92–96. <https://doi.org/10.1021/jp046030w>.
- [160] T. Fujimori, K. Fujii, R. Kanzaki, K. Chiba, H. Yamamoto, Y. Umebayashi, S. ichi Ishiguro, Conformational structure of room temperature ionic liquid N-butyl-N-methyl-pyrrolidinium bis(trifluoromethanesulfonyl) imide - Raman spectroscopic study and DFT calculations, *J. Mol. Liq.* 131–132 (2007) 216–224. <https://doi.org/10.1016/j.molliq.2006.08.054>.
- [161] K. Ito, H.J. Bernstein, the Vibrational Spectra of the Formate, Acetate, and Oxalate Ions, *Can. J. Chem.* 34 (1956) 170–178. <https://doi.org/10.1139/v56-021>.
- [162] V. V. Kuzmin, V.S. Novikov, L.Y. Ustynyuk, K.A. Prokhorov, E.A. Sagitova, G.Y. Nikolaeva, Raman spectra of polyethylene glycols: Comparative experimental and DFT study, *J. Mol. Struct.* 1217 (2020) 128331. <https://doi.org/10.1016/j.molstruc.2020.128331>.
- [163] L. Koenig, A.C. Angood, Spectra of Poly(ethylene Glycols) in Solution, *J. Polym. Sci. Part A-2*. 8 (1970) 1787–1796. <https://doi.org/10.1002/pol.1970.160081013>.
- [164] D. Brouillette, D.E. Irish, N.J. Taylor, G. Perron, M. Odziemkowski, J.E. Desnoyers, Stable solvates in solution of lithium bis(trifluoromethylsulfone)imide in glymes and other aprotic solvents: Phase diagrams, crystallography and Raman spectroscopy, *Phys. Chem. Chem. Phys.* 4 (2002) 6063–6071. <https://doi.org/10.1039/b203776a>.
- [165] S. Lall-Ramnarine, C. Rodriguez, R. Fernandez, N. Zmich, E. Fernandez, S. Dhiman, J.F. Wishart, The Effect of Lengthening Cation Ether Tails on Ionic Liquid Properties, *ECS Trans.* 75 (2016) 215–232. <https://doi.org/10.1149/07515.0215ecst>.
- [166] J.H. Nordlien, S. Ono, A TEM investigation of naturally formed oxide films on pure magnesium, 39 (1997) 1397–1414. [https://doi.org/10.1016/S0010-938X\(97\)00037-1](https://doi.org/10.1016/S0010-938X(97)00037-1)

- [167] S. Wang, Y. Wang, Q. Ramasse, Z. Fan, The Nature of Native MgO in Mg and Its Alloys, *Metall. Mater. Trans. A Phys. Metall. Mater. Sci.* 51 (2020) 2957–2974. <https://doi.org/10.1007/s11661-020-05740-1>.
- [168] R.M. Asmussen, P. Jakupi, M. Danaie, G.A. Botton, D.W. Shoesmith, Tracking the corrosion of magnesium sand cast AM50 alloy in chloride environments, *Corros. Sci.* 75 (2013) 114–122. <https://doi.org/10.1016/j.corsci.2013.05.022>.
- [169] M. Liu, S. Zanna, H. Ardelean, I. Frateur, P. Schmutz, G. Song, A. Atrens, P. Marcus, A first quantitative XPS study of the surface films formed, by exposure to water, on Mg and on the Mg-Al intermetallics: Al₃Mg₂ and Mg₁₇Al₁₂, *Corros. Sci.* 51 (2009) 1115–1127. <https://doi.org/10.1016/j.corsci.2009.02.017>.
- [170] R.P. Swatloski, S.K. Spear, J.D. Holbrey, R.D. Rogers, Dissolution of cellulose with ionic liquids, *J. Am. Chem. Soc.* 124 (2002) 4974–4975. <https://doi.org/10.1021/ja025790m>.
- [171] D. Freudenmann, S. Wolf, M. Wolff, C. Feldmann, Ionic liquids: New perspectives for inorganic synthesis?, *Angew. Chemie - Int. Ed.* 50 (2011) 11050–11060. <https://doi.org/10.1002/anie.201100904>.
- [172] C. Comminges, R. Barhdadi, M. Laurent, M. Troupel, Determination of viscosity, ionic conductivity, and diffusion coefficients in some binary systems: Ionic liquids + molecular solvents, *J. Chem. Eng. Data.* 51 (2006) 680–685. <https://doi.org/10.1021/je0504515>.
- [173] A. Stoppa, O. Zech, W. Kunz, R. Buchner, The conductivity of imidazolium-based ionic liquids from (-35 to 195) °C. A. variation of cations alkyl chain, *J. Chem. Eng. Data.* 55 (2010) 1768–1773. <https://doi.org/10.1021/je900789j>.
- [174] T. Welton, Ionic liquids: a brief history, *Biophys. Rev.* 10 (2018) 691–706. <https://doi.org/10.1007/s12551-018-0419-2>.
- [175] C. Li, B. Knierim, C. Manisseri, R. Arora, H. V. Scheller, M. Auer, K.P. Vogel, B.A. Simmons, S. Singh, Comparison of dilute acid and ionic liquid pretreatment of switchgrass: Biomass recalcitrance, delignification and enzymatic saccharification, *Bioresour. Technol.* 101 (2010) 4900–4906. <https://doi.org/10.1016/j.biortech.2009.10.066>.
- [176] S.H. Y. Wang, H. Li, A theoretical investigation of the interactions between water molecules and ionic liquids, *J. Phys. Chem. B.* 110 (2006) 24646–24651. <https://doi.org/10.1021/jp064134w>.
- [177] T. Méndez-Morales, J. Carrete, Ó. Cabeza, L.J. Gallego, L.M. Varela, Molecular dynamics simulation of the structure and dynamics of water-1-alkyl-3-methylimidazolium ionic liquid mixtures, *J. Phys. Chem. B.* 115 (2011) 6995–7008. <https://doi.org/10.1021/jp202692g>.
- [178] K. Saihara, Y. Yoshimura, S. Ohta, A. Shimizu, Properties of water confined in ionic liquids, *Sci. Rep.* 5 (2015) 1–10. <https://doi.org/10.1038/srep10619>.
- [179] H. Abe, T. Takekiyo, M. Shigemi, Y. Yoshimura, S. Tsuge, T. Hanasaki, K. Ohishi, S. Takata, J.I. Suzuki, Direct evidence of confined water in room-temperature ionic liquids by complementary use of small-angle X-ray and neutron scattering, *J. Phys. Chem. Lett.* 5 (2014) 1175–1180. <https://doi.org/10.1021/jz500299z>.
- [180] E.E. Fenn, D.E. Moilanen, N.E. Levinger, M.D. Fayer, Water dynamics and interactions in water-polyether binary mixtures, *J. Am. Chem. Soc.* 131 (2009) 5530–5539. <https://doi.org/10.1021/ja809261d>.
- [181] K.K. Jang HJ, Shin CY, Safety Evaluation of Polyethylene Glycol (PEG) Compounds for Cosmetic Use, *Toxicol. Res.* 31 (2015) 105–136. <https://doi.org/10.5487/TR.2015.31.2.105>.

- [182] D. Hutanu, Recent Applications of Polyethylene Glycols (PEGs) and PEG Derivatives, *Mod. Chem. Appl.* 02 (2014) 2–7. <https://doi.org/10.4172/2329-6798.1000132>.
- [183] K. Shamel, M. Bin Ahmad, S.D. Jazayeri, S. Sedaghat, P. Shabanzadeh, H. Jahangirian, M. Mahdavi, Y. Abdollahi, Synthesis and characterization of polyethylene glycol mediated silver nanoparticles by the green method, *Int. J. Mol. Sci.* 13 (2012) 6639–6650. <https://doi.org/10.3390/ijms13066639>.
- [184] K. Yoshii, T. Uto, T. Onishi, D. Kosuga, N. Tachikawa, Y. Katayama, Ether-Functionalized Pyrrolidinium-Based Room Temperature Ionic Liquids: Physicochemical Properties, Molecular Dynamics, and the Lithium Ion Coordination Environment, *ChemPhysChem.* 22 (2021) 1584–1594. <https://doi.org/10.1002/cphc.202100380>.
- [185] L. Garcia-Quintana, F. Chen, N. Ortiz-Vitoriano, Y. Zhang, L.A. O'Dell, D.R. MacFarlane, M. Forsyth, A.M. Bond, P.C. Howlett, C. Pozo-Gonzalo, Unravelling the Role of Speciation in Glyme:Ionic Liquid Hybrid Electrolytes for Na–O₂ Batteries, *Batter. Supercaps.* 4 (2021) 513–521. <https://doi.org/10.1002/batt.202000261>.
- [186] R. Dennington, T.A. Keith, J.M. Millam, GaussView, Version 6, Semichem Inc., Shawnee Mission, KS. (2016).
- [187] M.J. Frisch, G.W. Trucks, H.B. Schlegel, G.E. Scuseria, M.A. Robb, J.R. Cheeseman, G. Scalmani, V. Barone, G.A. Petersson, X. Nakatsuji, H.; Li, M. Caricato, A. V. Marenich, J. Bloino, B.G. Janesko, R. Gomperts, B. Mennucci, D.J. Hratch, Gaussian 16, Revision C.01, Gaussian, Inc., Wallingford CT. (2016).
- [188] J. Wang, W. Wang, K.P. A., D.A. Case, Automatic atom type and bond type perception in molecular mechanical calculations, *J. Mol. Graph. Model.* 25 (2006) 247–260.
- [189] K. Yoshii, T. Uto, N. Tachikawa, Y. Katayama, The effects of the position of the ether oxygen atom in pyrrolidinium-based room temperature ionic liquids on their physicochemical properties, *Phys. Chem. Chem. Phys.* 22 (2020) 19480–19491. <https://doi.org/10.1039/d0cp02662j>.
- [190] C.J. Cramer, *Essentials of Computational Chemistry: Theories and Models*, 2nd ed., John Wiley & Sons, 2013, 2013.
- [191] L. Martínez, R. Andrade, E.G. Birgin, J.M. Martínez, Packmol: A package for building initial configurations for molecular dynamics simulations, *J. Comput. Chem.* 30 (2009) 2157–2164.
- [192] S. Plimpton, Fast Parallel Algorithms for Short-Range Molecular Dynamics, *J. Comput. Phys.* 117 (2008) 1–19.
- [193] LAMMPS web site, <https://www.lammps.org/>
- [194] R. Ludwig, Water: From clusters to the bulk, *Angew. Chemie - Int. Ed.* 40 (2001) 1808–1827. [https://doi.org/10.1002/1521-3773\(20010518\)40:10<1808::AID-ANIE1808>3.0.CO;2-1](https://doi.org/10.1002/1521-3773(20010518)40:10<1808::AID-ANIE1808>3.0.CO;2-1).
- [195] Z. Bin Zhou, H. Matsumoto, K. Tatsumi, Cyclic quaternary ammonium ionic liquids with perfluoroalkyltrifluoroborates: Synthesis, characterization, and properties, *Chem. - A Eur. J.* 12 (2006) 2196–2212. <https://doi.org/10.1002/chem.200500930>.
- [196] S. Fang, Z. Zhang, Y. Jin, L. Yang, S.I. Hirano, K. Tachibana, S. Katayama, New functionalized ionic liquids based on pyrrolidinium and piperidinium cations with two ether groups as electrolytes for lithium battery, *J. Power Sources.* 196 (2011) 5637–5644. <https://doi.org/10.1016/j.jpowsour.2011.02.047>.
- [197] S. Pandian, K.S. Hariharan, S.P. Adiga, S.M. Kolake, Evaluation of Electrochemical Stability and Li-ion Interactions in Ether Functionalized Pyrrolidinium and Phospholanium Ionic Liquids, *J. Electrochem. Soc.* 167 (2020) 070550. <https://doi.org/10.1149/1945-7111/ab8061>.

- [198] M. Moreno, M. Montanino, M. Carewska, G.B. Appetecchi, S. Jeremias, S. Passerini, Water-soluble, triflate-based, pyrrolidinium ionic liquids, *Electrochim. Acta.* 99 (2013) 108–116. <https://doi.org/10.1016/j.electacta.2013.03.046>.
- [199] J. Bowers, C.P. Butts, P.J. Martin, M.C. Vergara-Gutierrez, R.K. Heenan, Aggregation Behavior of Aqueous Solutions of Ionic Liquids, *Langmuir.* 20 (2004) 2191–2198. <https://doi.org/10.1021/la035940m>.
- [200] Y. Chen, Y. Cao, Y. Zhang, T. Mu, Hydrogen bonding between acetate-based ionic liquids and water: Three types of IR absorption peaks and NMR chemical shifts change upon dilution, *J. Mol. Struct.* 1058 (2014) 244–251. <https://doi.org/10.1016/j.molstruc.2013.11.010>.
- [201] C. Laurence, S. Mansour, D. Vuluga, J. Legros, Measurement of the hydrogen bond acceptance of ionic liquids and green solvents by the ^{19}F solvatomagnetic comparison method, *Green Chem.* 23 (2021) 1816–1822. <https://doi.org/10.1039/d0gc04104a>.
- [202] K. Matsuura, H. Fukuhara, Conformational analysis of poly(oxyethylene) chain in aqueous solution as a hydrophilic moiety of nonionic surfactants, *J. Mol. Struct.* 126 (1985) 251–260. [https://doi.org/10.1016/0022-2860\(85\)80118-6](https://doi.org/10.1016/0022-2860(85)80118-6) ([https://doi.org/10.1016/0022-2860\(85\)80118-6](https://doi.org/10.1016/0022-2860(85)80118-6)).
- [203] M. Falk, T.A. Ford, Infrared Spectrum and Structure of Liquid Water, *Can. J. Chem.* 44 (1966) 1699–1707. <https://doi.org/10.1139/v66-255>.
- [204] O.B. Babushkina, Phase Behaviour and FTIR Spectra of Ionic Liquids: The Mixtures of 1-Butyl-1-methylpyrrolidinium Chloride and TaCl_5 , *Zeitschrift Fur Naturforsch. - Sect. A J. Phys. Sci.* 63 (2008) 66–72. <https://doi.org/10.1515/zna-2008-1-212>.
- [205] P. Garidel, A. Blume, W. Hübner, A Fourier transform infrared spectroscopic study of the interaction of alkaline earth cations with the negatively charged phospholipid 1,2-dimyristoyl-sn-glycero-3-phosphoglycerol, *Biochim. Biophys. Acta - Biomembr.* 1466 (2000) 245–259. [https://doi.org/10.1016/S0005-2736\(00\)00166-8](https://doi.org/10.1016/S0005-2736(00)00166-8).
- [206] O. Stan, M. Todica, L. Olar, I. Papuc, R. Stefan, IR and Fluorescence Investigation of Some PEG-Water Systems, *Mater. Today Proc.* 5 (2018) 15923–15928. <https://doi.org/10.1016/j.matpr.2018.06.065>.
- [207] A.R. Polu, R. Kumar, Impedance spectroscopy and FTIR studies of PEG - Based polymer electrolytes, *E-Journal Chem.* 8 (2011) 347–353. <https://doi.org/10.1155/2011/628790>.
- [208] N. Yaghini, J. Pitawala, A. Matic, A. Martinelli, Effect of water on the local structure and phase behavior of imidazolium-based protic ionic liquids, *J. Phys. Chem. B.* 119 (2015) 1611–1622. <https://doi.org/10.1021/jp510691e>.
- [209] P. Bharmoria, H. Gupta, V.P. Mohandas, P.K. Ghosh, A. Kumar, Temperature invariance of NaCl solubility in water: Inferences from salt-water cluster behavior of NaCl, KCl, and NH_4Cl , *J. Phys. Chem. B.* 116 (2012) 11712–11719. <https://doi.org/10.1021/jp307261g>.
- [210] L. Cammarata, S.G. Kazarian, P.A. Salter, T. Welton, Molecular states of water in room temperature ionic liquids Electronic Supplementary Information available. See <http://www.rsc.org/suppdata/cp/b1/b106900d/>, *Phys. Chem. Chem. Phys.* 3 (2001) 5192–5200. <https://doi.org/10.1039/b106900d>.
- [211] P. Laurson, P. Raudsepp, H. Kaldmäe, A. Kikas, U. Mäeorg, The deconvolution of FTIR-ATR spectra to five Gaussians for detection of small changes in plant-water clusters, *AIP Adv.* 10 (2020) 085214. <https://doi.org/10.1063/5.0011700>.

- [212] K.B. Møller, R. Rey, J.T. Hynes, Hydrogen bond dynamics in water and ultrafast infrared spectroscopy: A theoretical study, *J. Phys. Chem. A*. 108 (2004) 1275–1289. <https://doi.org/10.1021/jp035935r>.
- [213] G. Li, Y.Y. Zhang, Q. Li, C. Wang, Y. Yu, B. Zhang, H.S. Hu, W. Zhang, D. Dai, G. Wu, D.H. Zhang, J. Li, X. Yang, L. Jiang, Infrared spectroscopic study of hydrogen bonding topologies in the smallest ice cube, *Nat. Commun.* 11 (2020) 2–7. <https://doi.org/10.1038/s41467-020-19226-6>.
- [214] C. Boissière, J.B. Brubach, A. Mermet, G. Marzi De, C. Bourgaux, E. Prouzet, P. Roy, Water confined in lamellar structures of AOT surfactants: An infrared investigation, *J. Phys. Chem. B*. 106 (2002) 1032–1035. <https://doi.org/10.1021/jp012724i>.
- [215] T. Watkins, A. Kumar, D.A. Buttry, Supporting Information Designer Ionic Liquids for Reversible Electrochemical Deposition / Dissolution of Mg, (n.d.) 1–9.
- [216] M. Deng, L. Wang, B. Vaghefinazari, W. Xu, C. Feiler, S. V. Lamaka, D. Höche, M.L. Zheludkevich, D. Snihirova, High-energy and durable aqueous magnesium batteries: Recent advances and perspectives, *Energy Storage Mater.* 43 (2021) 238–247. <https://doi.org/10.1016/j.ensm.2021.09.008>.
- [217] G. Vardar, A.E.S. Sleightholme, J. Naruse, H. Hiramatsu, D.J. Siegel, C.W. Monroe, Electrochemistry of magnesium electrolytes in ionic liquids for secondary batteries, *ACS Appl. Mater. Interfaces*. 6 (2014) 18033–18039. <https://doi.org/10.1021/am5049064>.
- [218] D. Kurchavov, M. Haddad, V. Lair, P. Volovitch, Mg-alloys in water – hydrophilic ionic liquid mixtures: is there a negative difference effect?, *Corros. Sci.* (2022) 110178. <https://doi.org/10.1016/j.corsci.2022.110178>.
- [219] Y. Cui, T. Zhang, F. Wang, New understanding on the mechanism of organic inhibitors for magnesium alloy, *Corros. Sci.* (2022) 110118. <https://doi.org/10.1016/j.corsci.2022.110118>.
- [220] E. Slavcheva, G. Schmitt, Screening of new corrosion inhibitors via electrochemical noise analysis, *Mater. Corros.* 53 (2002) 647–655. [https://doi.org/10.1002/1521-4176\(200209\)53:9<647::AID-MACO647>3.0.CO;2-L](https://doi.org/10.1002/1521-4176(200209)53:9<647::AID-MACO647>3.0.CO;2-L).
- [221] A. Mahapatro, T.D. Matos Negrón, A. Nguyen, Spectroscopic evaluations of interfacial oxidative stability of phosphonic nanocoatings on magnesium, *J. Spectrosc.* 2015 (2015). <https://doi.org/10.1155/2015/350630>.
- [222] P.C. Hidber, T.J. Graule, L.J. Gauckler, Citric acid - A dispersant for aqueous alumina suspensions, *J. Am. Ceram. Soc.* 79 (1996) 1857–1867. <https://doi.org/10.1111/j.1151-2916.1996.tb08006.x>.
- [223] R. Solmaz, G. Kardaş, B. Yazici, M. Erbil, Citric acid as natural corrosion inhibitor for aluminium protection, *Corros. Eng. Sci. Technol.* 43 (2008) 186–191. <https://doi.org/10.1179/174327807X214770>.
- [224] J. Wysocka, M. Cieslik, S. Krakowiak, J. Ryl, Carboxylic acids as efficient corrosion inhibitors of aluminium alloys in alkaline media, *Electrochim. Acta.* 289 (2018) 175–192. <https://doi.org/10.1016/j.electacta.2018.08.070>.
- [225] M.N. Moussa, M.M. El-Tagoury, A.A. Radi, S.M. Hassan, Carboxylic acids as corrosion inhibitors for aluminium in acidic and alkaline solutions, *Anti-Corrosion Methods Mater.* 37 (1990) 4–8. <https://doi.org/10.1108/eb007262>.
- [226] P.S.D. Brito, C.A.C. Sequeira, Organic inhibitors of the anode self-corrosion in aluminum-air batteries, *J. Fuel Cell Sci. Technol.* 11 (2014) 1–10. <https://doi.org/10.1115/1.4025534>.

- [227] K.A. Yasakau, A. Maltseva, S. V. Lamaka, D. Mei, H. Orvi, P. Volovitch, M.G.S. Ferreira, M.L. Zheludkevich, The effect of carboxylate compounds on Volta potential and corrosion inhibition of Mg containing different levels of iron, *Corros. Sci.* 194 (2022) 109937.
<https://doi.org/10.1016/j.corsci.2021.109937>.
- [228] G. Lefèvre, T. Preočanin, J. Lützenkirchen, Attenuated Total Reflection - Infrared Spectroscopy Applied to the Study of Mineral - Aqueous Electrolyte Solution Interfaces: A General Overview and a Case Study, *Infrared Spectrosc. - Mater. Sci. Eng. Technol.* (2012).
<https://doi.org/10.5772/36459>.
- [229] Y. Chen, Y.H. Zhang, L.J. Zhao, ATR-FTIR spectroscopic studies on aqueous LiClO₄, NaClO₄, and Mg(ClO₄)₂ solutions, *Phys. Chem. Chem. Phys.* (2004) 537–542.
<https://doi.org/10.1039/b311768e>.

Appendix 1

Supplementary materials for the article “Mg-alloys in water – hydrophilic ionic liquid mixtures: is there a negative difference effect?”

Raman spectroscopy results were completed by Attenuated Total Reflectance Fourier Transform Infrared spectroscopy (ATR-FTIR). The spectra were measured for wet surfaces of Mg samples after the experiment and for the ILs before and after the electrochemical experiments using a Thermo Scientific Nicolet 6700 FTIR spectrometer equipped with a mercury cadmium telluride detector cooled by liquid nitrogen at 77 K. The ATR accessory was a horizontal ZnSe crystal coated with diamond ($A = 2.54 \text{ mm}^2$) with single reflection and an angle of incidence of 45° (Smart Miracle from PIKE). The droplets of ILs samples ($\sim 7 \mu\text{L}$) were placed on the crystal and spectra recording was started immediately. The Mg samples were pressed against the ATR crystal by dynamometric tool. The spectra were recorded with resolution of 2 cm^{-1} and were averaged from 64 scans. OMNIC software was used for the data collection and treatment.

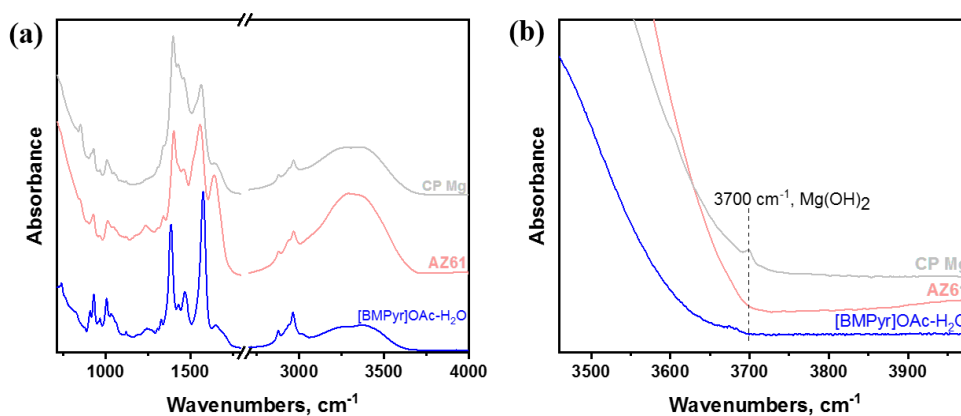


Fig. S1. ATR-FTIR spectra of Mg-alloys surface after electrochemical experiments in [BMPyr]OAc-H₂O. Grey curve – CP Mg, red curve – AZ61, blue – [BMPyr]OAc-H₂O.

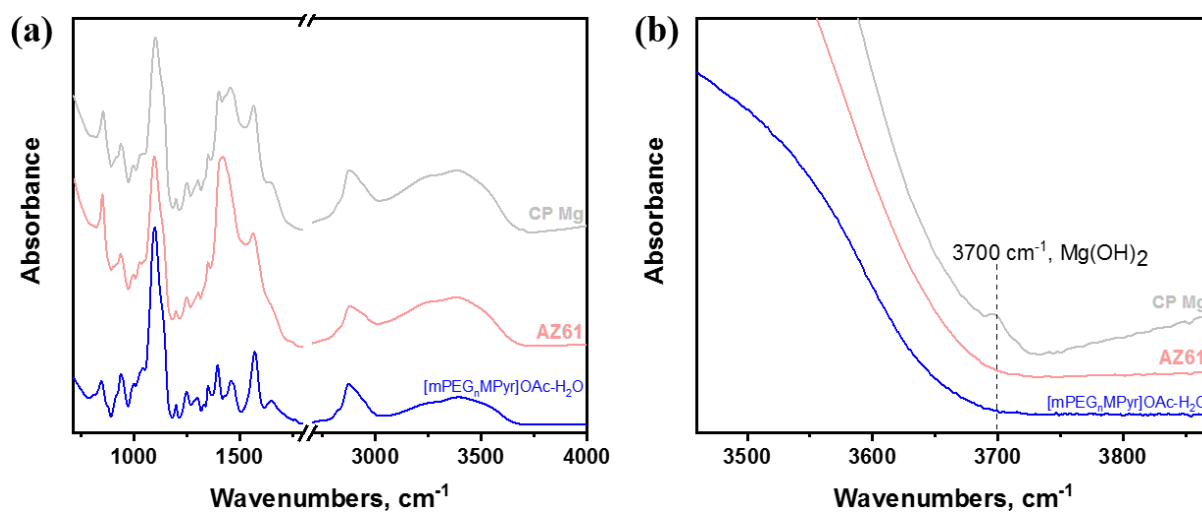


Fig. S2. ATR-FTIR spectra of Mg-alloys surface after electrochemical experiments in [BMPyr]OAc-H₂O. Grey curve – CP Mg, red curve – AZ61, blue – [mPEG_nMPyr]OAc-H₂O.

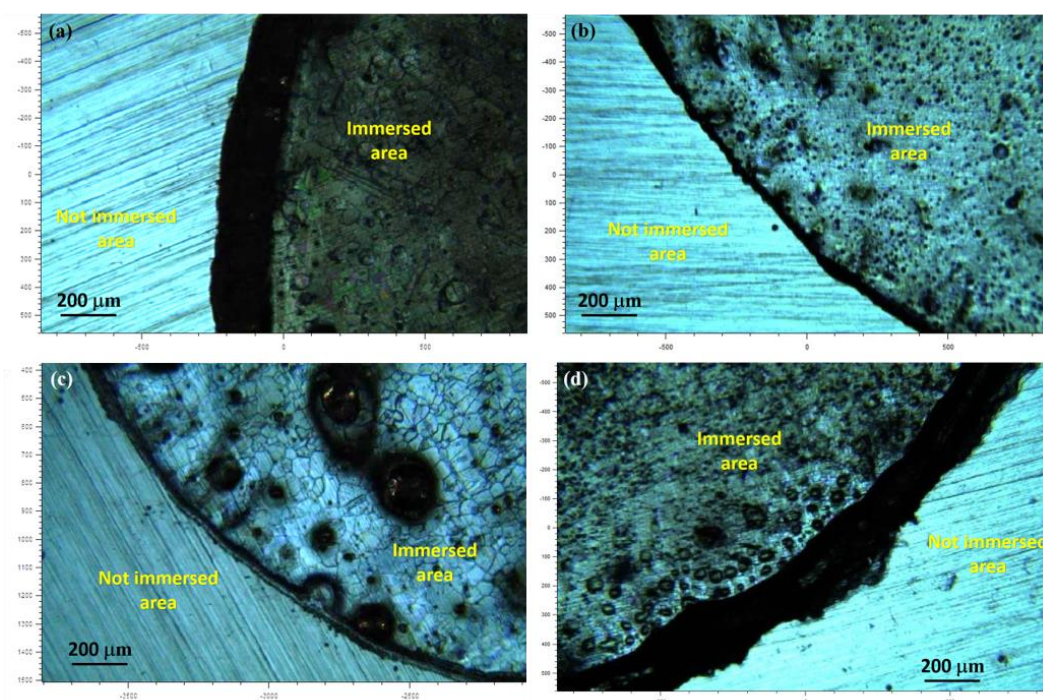


Fig. S3. Corrosion morphology of Mg samples: (a) CP Mg and (b) AZ61 immersed in [BMPyr]OAc-H₂O; (c) CP Mg and (d) AZ61 immersed in [mPEG_nMPyr]OAc-H₂O.

Appendix 2

*Supplementary materials for the article
“Influence of PEG-containing cation on
molecular state of water in water – acetate
based ionic liquids mixtures”*

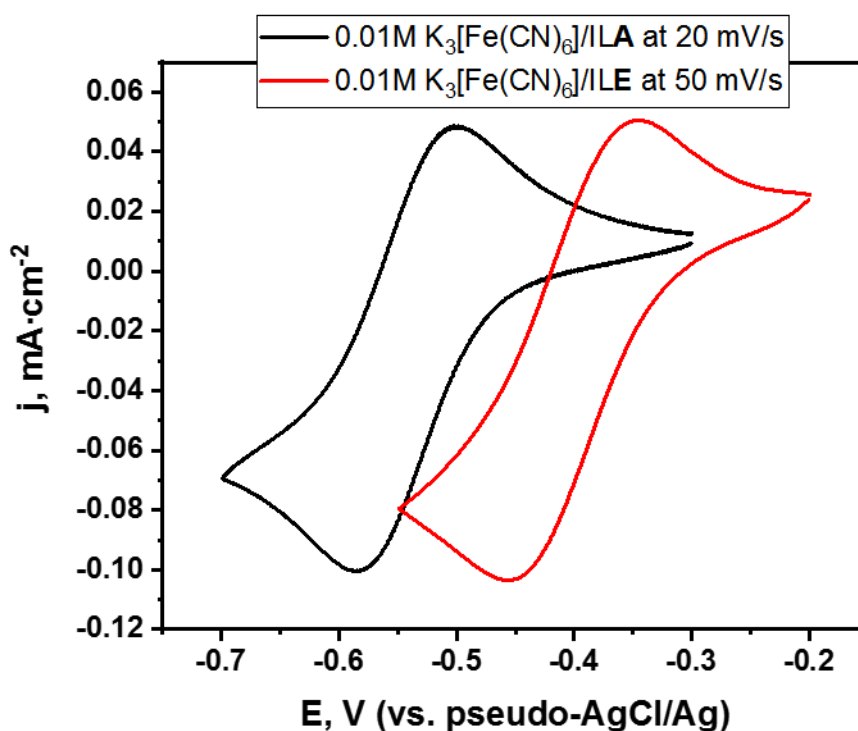
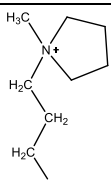
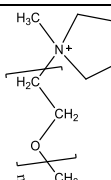


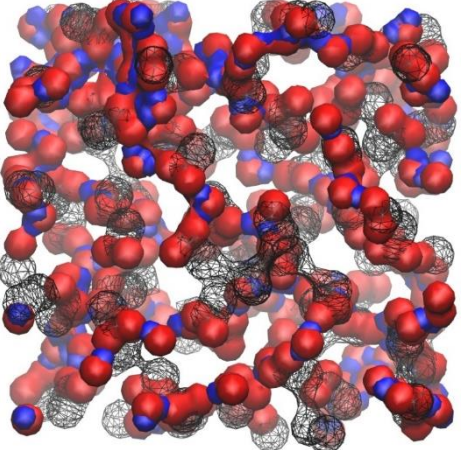
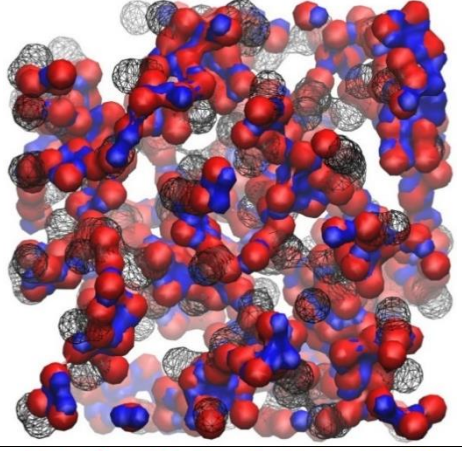
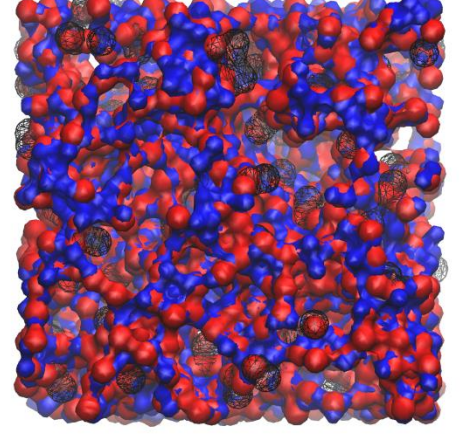
Fig. S4. Voltammograms recorded on glassy carbon electrode in 0.01M solution K₃[Fe(CN)₆]/ILA at 20 mV/s – black curve; for 0.01M solution K₃[Fe(CN)₆]/ILE at 50 mV/s – red curve.

Table S1. Composition of mixtures used for simulations.**Composition and characteristics of used models for simulation purposes**

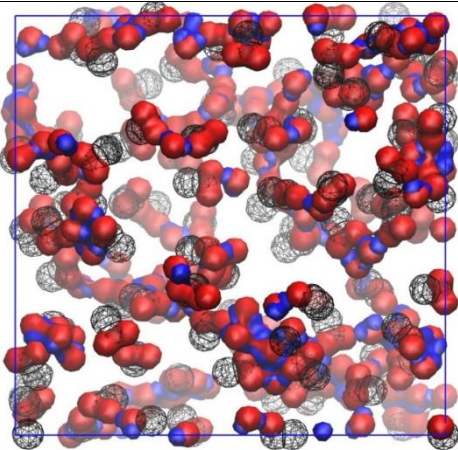
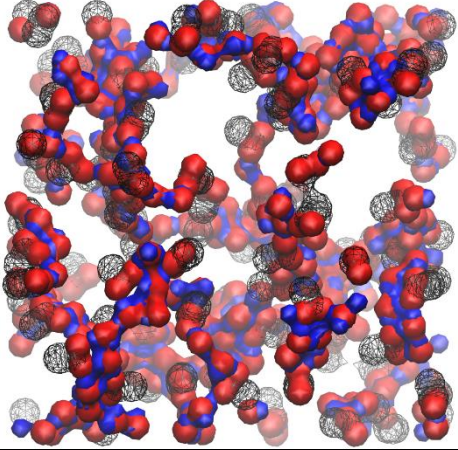
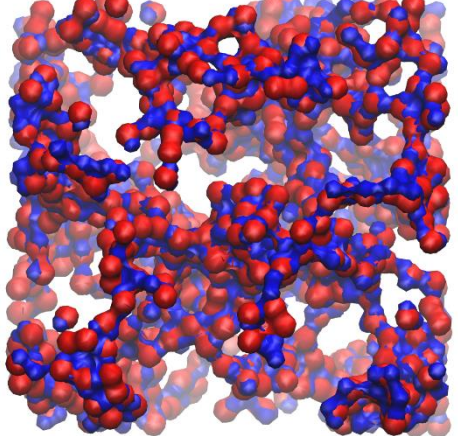
Nº of Models	Type of IL cation	N of IL cations	N of CH ₃ CO ₂ ⁻	Nº of H ₂ O	ω (H ₂ O) [%]	ρ (EXP) [g/cm ³]	V [Å ³]	a [Å]
1		100	100	-	-	1.1444	29209.23	30.80
2		100	100	100	8.22	1.0490	34717.13	32.62
3		100	100	200	15.19	0.9710	40586.31	34.36
4		100	100	1117	50	0.9734	68670.41	40.96
5		100	100	-	-	1.1421	61581.02	39.48
6		100	100	100	4.30	1.1278	65012.64	40.20
7		100	100	200	8.24	1.1140	68504.54	40.92
8		100	100	600	21.22	1.0726	82304.48	43.50
9		100	100	800	26.42	1.0548	89364.56	44.70
10		100	100	1485	40	1.0093	113697.0	48.44
11		100	100	2228	50	0.976	140356.2	51.96

Explanation: for the convenience of visualization, the figures show only the atoms of Water and Acetate ions responsible for the formation of hydrogen bond between them. **Hydrogen atoms surfaces of water molecules are in blue. Oxygen atoms surfaces of Acetate ions and Water molecules are in red. Carbon atoms of acetate are framed in black.**

Mass fraction of H ₂ O in ILA, $\omega(\text{H}_2\text{O})$	Molar fraction of ILA	Molar fraction of water, $\chi(\text{H}_2\text{O})$	$n(\text{H}_2\text{O}) / n(\text{ILA})$
0*	1*	0*	0*
8.22*	0.500*	0.500*	1.000*
15.19*	0.333*	0.667*	2.000*
50.00*	0.0822*	0.918*	11.167*

Mass fraction of H ₂ O in ILA, $\omega(\text{H}_2\text{O})$	Dynamic boxes
8.22*	
15.19*	
50.00*	

Mass fraction of H ₂ O in ILE, $\omega(\text{H}_2\text{O})$	Molar fraction of ILE	Molar fraction of water, $\chi(\text{H}_2\text{O})$	$n(\text{H}_2\text{O}) / n(\text{ILE})$
0*	1*	0*	0*
4.3*	0.462*	0.538*	1.166*
8.24*	0.300*	0.700*	2.330*
21.22*	0.125*	0.875*	6.988*
26.42*	0.097*	0.903*	9.287*
40.00*	0.0547*	0.945*	17.296*
50*	0.037*	0.963*	25.944*

Mass fraction of H ₂ O in ILA, $\omega(\text{H}_2\text{O})$	Dynamic boxes
4.3*	
8.24*	
21.22*	

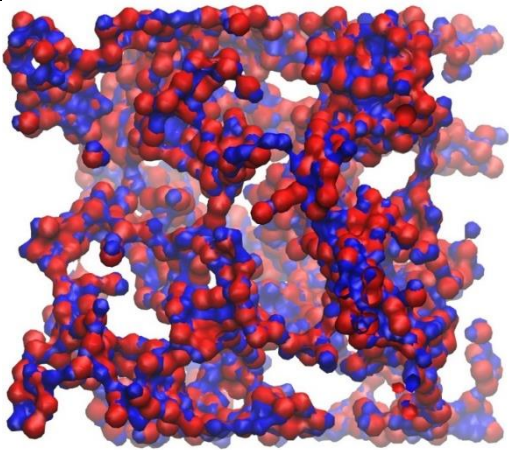
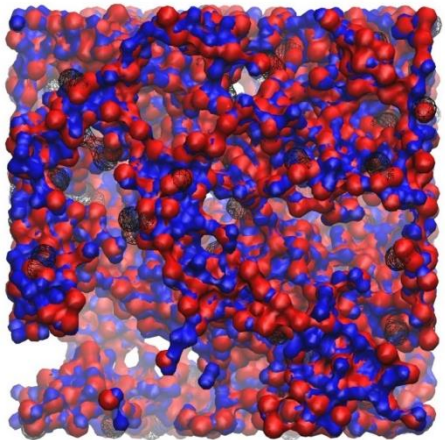
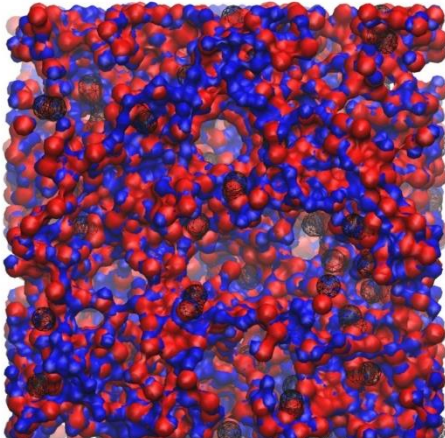
26.42*	
40.00*	
50*	

Table S2. Selected Raman shift peaks of [BMPyr]OAc (a), [mPEG_nPyr]OAc (b).**[BMPyr]OAc (a)**

No of peak (Raman shift, cm ⁻¹)	Bond	Attribution	Ref.
1452	C-H	bending, CH ₂ , pyrrolidinium	[1]
1396	COO	symmetric stretching, acetate	[2]
1331	C-H	bending, CH ₃ , acetate	[2]
1317	C-H	observed in Pyr ₁₃ I	[3]
1122	C-H	observed in Pyr ₁₃ I	[3]
1061	C-H	observed in Pyr ₁₄ Br	[4]
908	C-C	ring / stretching, C-C, pyrrolidinium / acetate	[1,2,5]
825	C-C / C-H	bending, C-C and CH ₂ , butyl	[1]
735	C-H	observed in Pyr ₁₃ I	[3]
644	COO	bending, acetate	[2,5]

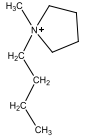
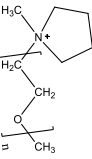
[mPEG_nMPyr]OAc (b)

No of peak (Raman shift, cm ⁻¹)	Bond	Type of vibration / comments	Ref.
1473	C-H	bending, CH ₂ , PEG	[6]
1452	C-H	bending / bending, CH ₂ , pyrrolidinium / PEG	[1,6]
1397	COO	symmetric stretching, acetate	[2]
1336	C-H	bending, CH ₃ , acetate	[2]
1285	C-H	bending, CH ₂ , PEG	[7]
1243	C-H	bending, CH ₂ , PEG	[7]
1136	C-O / C-C	bending, C-O, C-C, PEG	[6,7]
1049	C-C / C-H	stretching / bending, C-C / CH ₂ , PEG	[7]
995		observed in MPEG ₇ PyrTFSI	[8]
913	C-O / C-C / C-H	bending, C-O, C-C, CH ₃ acetate	[1,2,5]
902	C-H / C- C	bending / ring / stretching, symmetric ring breathing, CH ₂ , C-C, pyrrolidinium	[2]
845 Broad	C-O-C	stretching, C-O-C, PEG	[9]
719	???		
643	COO	bending, acetate	[2,5]

Appendix 3

*Supplementary materials for the article
“Synergic effect of ionic liquid (IL) cation
and anion inhibits negative difference effect
on Mg in water - IL mixtures”*

Table 3S. Composition and characteristics of used models for simulation purpose.

N _o of Models	Type of IL cation	N of IL cations	N of acetic ions	N _o of H ₂ O	N of OH	N _o of Mg ²⁺	$\omega(\text{H}_2\text{O})$ [%]	$\chi(\text{H}_2\text{O})$	n(H ₂ O) / n(IL)	ρ_{EXP} [g/cm ³]	V [Å ³]	a [Å]
1		100	100	0	100	50	0	0	0	1.1017	34736.36	32.62
2		100	100	100	100	50	7.26	0.400	1	1.0633	38806.63	33.86
3		100	100	200	100	50	13.53	0.571	2	0.9939	44523.46	35.44
4		100	100	0	100	50	0	0	0	1.1697	64266.80	40.06
5		100	100	100	100	50	3.50	0.400	1	1.1368	68754.98	40.96
6		100	100	200	100	50	6.77	0.571	2	1.0625	76379.33	42.42

Notes: $\omega \text{ H}_2\text{O}$ [%] – mass fraction of H₂O in IL; $\chi (\text{H}_2\text{O})$ – molar fraction of water in IL; ρ_{exp} [g/cm³] – experimental density; V [Å³] – dynamic box volume, a [Å] – dynamic box radius

Table S4. Attribution of Raman shifts of [mPEG_nMPyr]ClO₄.

№ of peak (Raman shift, cm ⁻¹), experimental	Bond	Type of vibration / comments	Ref.
12 (1471)	C-H	bending, CH ₂ , PEG	[6]
11 (1451)	C-H	bending / bending, CH ₂ , pyrrolidinium / PEG	[1,6]
10 (1286)	C-H	bending, CH ₂ , PEG	[7]
9 (1242)	C-H	bending, CH ₂ , PEG	[7]
8 (1136)	C-O / C-C	bending, C-O, C-C, PEG	[6,7]
7 (1049)	C-C / C-H	stretching / bending, C-C / CH ₂ , PEG	[7]
6 (995)		observed in MPEG ₇ PyrTFSI and mPEG _n MPyrOAc	[8]
5 (932)	Cl-O	stretching, ClO ₄	[10]
4 (909)	C-H / C-C	bending / ring / stretching, symmetric ring breathing, CH ₂ , C-C, pyrrolidinium	[2]
3 (845), broad	C-O-C	stretching, C-O-C, PEG	[9]
2 (719)		observed in mPEG _n MPyrOAc	
1 (624)	Cl-O	stretching, ClO ₄	[10]

The ATR-FTIR measurements of wet surfaces after electrochemical experiments and ionic liquids were provided using a Thermo Scientific Nicolet 6700 FTIR spectrometer equipped with a mercury cadmium telluride detector cooled at 77 K by liquid nitrogen. The ATR accessory was a horizontal ZnSe crystal coated with diamond ($A = 2.54 \text{ mm}^2$) with single reflection and an angle of incidence of 45° (Smart Miracle from PIKE). The droplets of ILs samples (~7 μL) were placed on the crystal and spectra recording was started immediately to avoid water adsorption from air. The Mg samples were pressed against the ATR crystal by dynamometric tool. The spectra were recorded with resolution of 2 cm⁻¹ and were averaged from 64 scans. OMNIC software was used for the data collection and treatment.

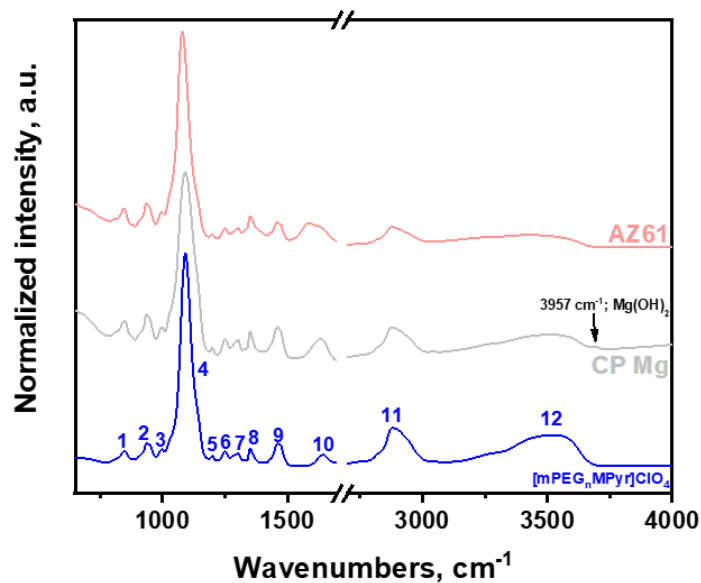


Fig. S5. Typical ATR-FTIR spectra of [mPEG_nMPyr]ClO₄-H₂O – blue, wet surface of CP Mg – grey, wet surface of AZ61 – red. The spectra of surfaces have been recorded after electrochemical experiment in [mPEG_nMPyr]ClO₄-H₂O.

Table S5. Attribution of wavenumbers ATR-FTIR for [mPEGMPyr]ClO₄-H₂O

Nº of peak (Wavenumbers, cm ¹), experimental	Bond / Type of vibration	Functional group / comments	Ref.
12 (3527), broad	O-H, stretching	H ₂ O	[11]
11 (2877), broad	C-H, stretching	CH ₂ , CH ₃ , ether, pyrrolidinium	[12]
10 (1641)	O-H, bending	OH, H ₂ O	[11]
9 (1463)	C-H, bending	CH ₂ , PEG	[13,14]
8 (1350)	C-H, wagging / scissoring	CH ₂ , PEG	[5]
7 (1301)	C-H, twisting	CH ₂ , pyrrolidinium	[13,15]
6 (1250)	C-O, stretching	COC, PEG	[13]
5 (1200)			
(~1115)	Cl-O	ClO ₄ , hidden under 1091 cm ⁻¹ peak	[10]
4 (1091)	C-O-C, stretching	COC, ether	[13]
3 (999)			
2 (937)	C-N, stretching	CN, pyrrolidinium	[16]
1 (848)			

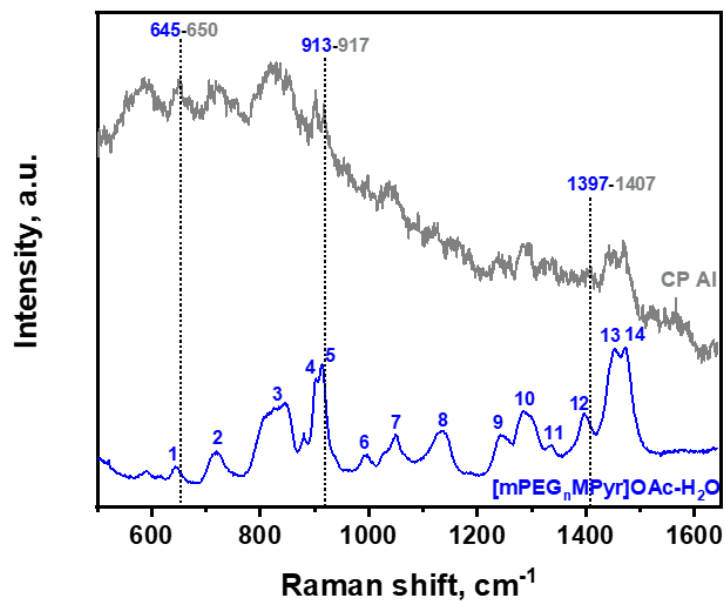
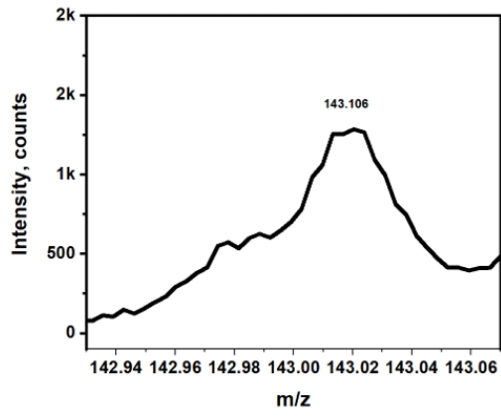
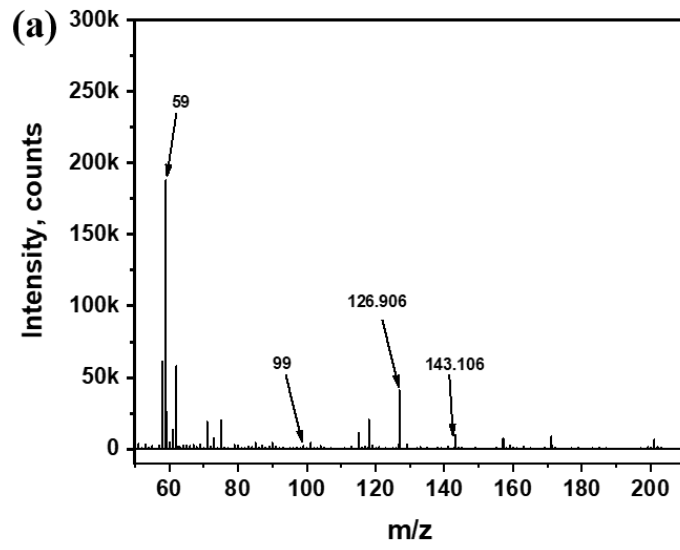


Fig. S6. Typical Raman spectra recorded on CP Al after electrochemical experiment in [mPEG_nMPyr]OAc-H₂O. Grey: spectrum recorded on the wet surface of CP Al, blue: spectra of ionic [mPEG_nMPyr]OAc – H₂O mixture.



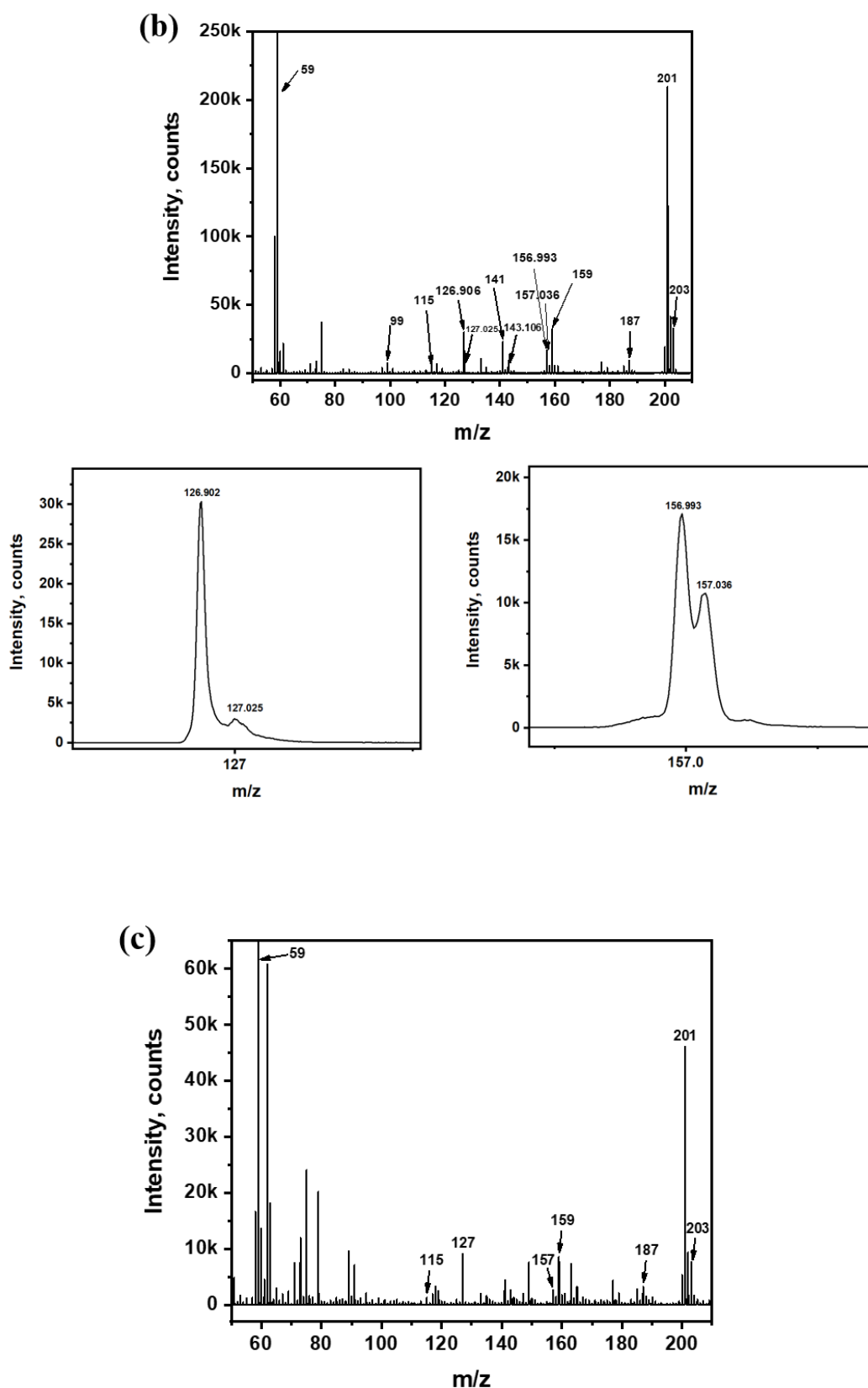


Fig. S7. ToF-SIMS negative ions mass spectra obtained on the surface of (a) CP Mg and (b) AZ61, (c) CP Al after electrochemical experiments in [mPEG_nMPyr]OAc-H₂O electrolyte.

Table S6. Proposed graphical structures of selected peaks observed on ToF-SIMS negative ions mass spectra on the surface of CP Mg and AZ61 after electrochemical experiments in [mPEG_nMPyr]OAc-H₂O electrolyte.

m/z (experimental)	Chemical formula / Number	Proposed graphical structures
203	$C_6H_8AlO_6^-$ 1	
201	$C_6H_{11}Al_2O_4^-$ 2	
156.993	$C_4H_7Al_2O_3^-$ 3	
187	$C_5H_9Al_2O_4^-$ 4	
159	$C_5H_8AlO_4^-$ 5	
143.106	$C_4H_7MgO_4^-$ 6	

157.036	$C_5H_9MgO_4^-$ 7	
115	$C_4H_8AlO_2^-$ 8	
127.025	$C_4H_7MgO_3^-$ 9	
141	$C_4H_5MgO_4^-$ 10	
99	$C_2H_3MgO_3^-$ 11	
59	$C_2H_3O_2^-$ 12	
126.902	I 13	

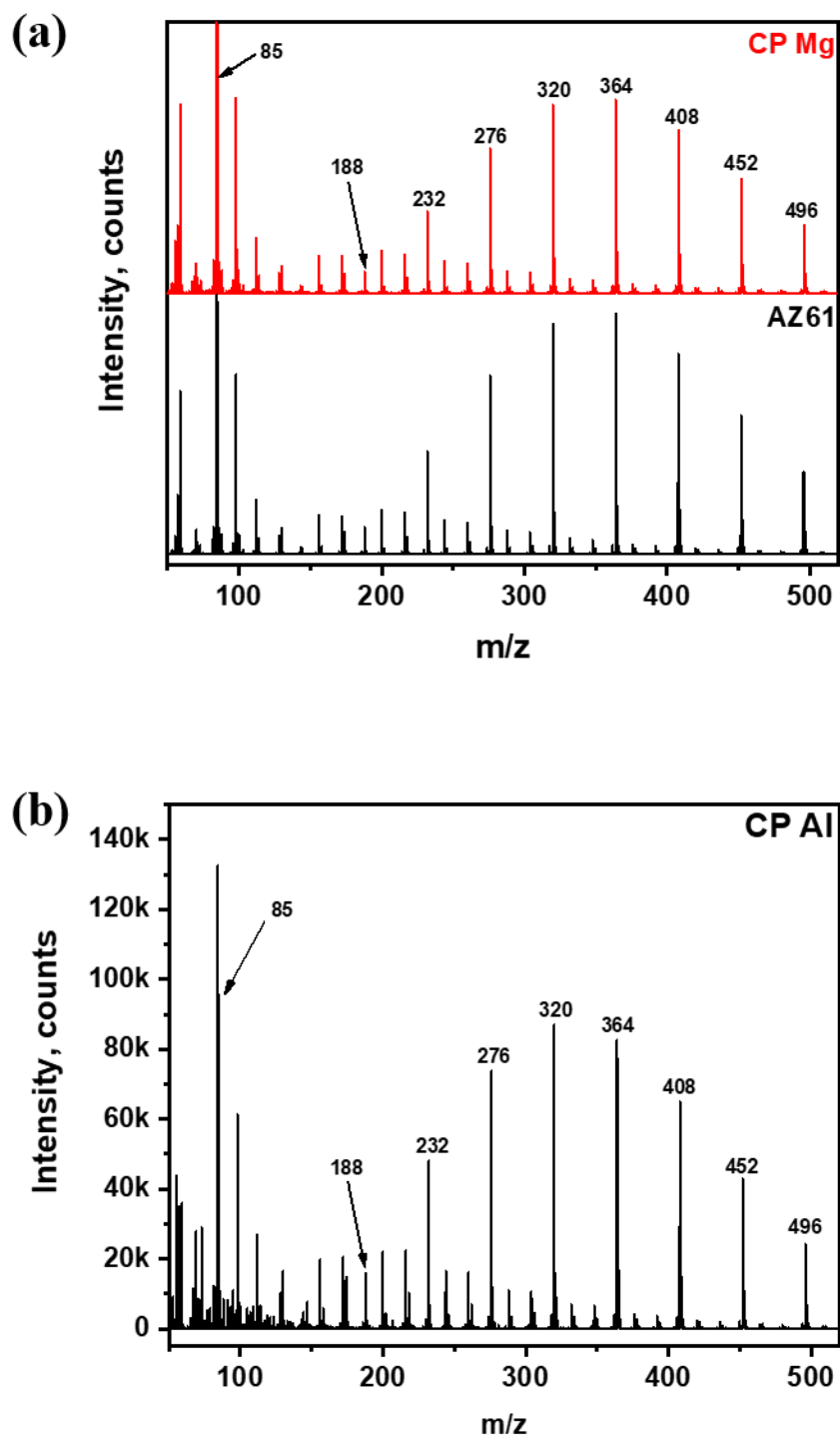
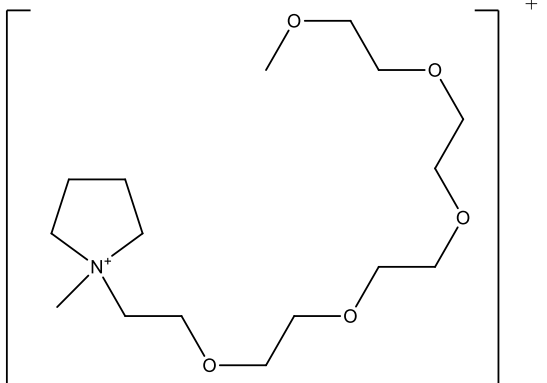
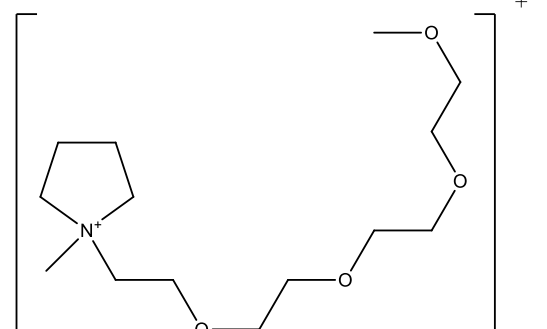
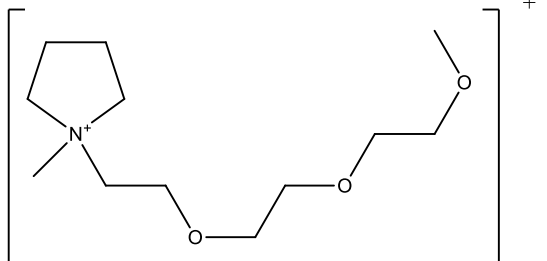
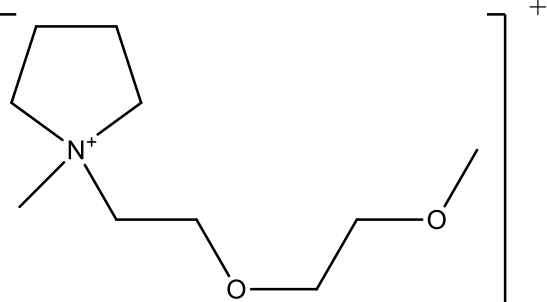
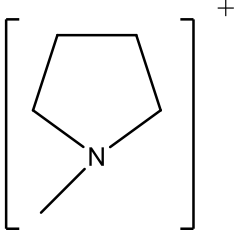


Fig. S8. ToF-SIMS positive ions mass spectra obtained on the surface of: (a) CP Mg – red, AZ61 – black; (b) – CP Al after electrochemical experiments in [mPEG_nMPyr]OAc-H₂O electrolyte.

Table S7. Proposed graphical structures of selected peaks observed on ToF-SIMS positive ions mass spectra on the surface of CP Mg and AZ61 after electrochemical experiments in [mPEG_nMPyr]OAc-H₂O electrolyte.

m/z (experimental)	Chemical formula / Number	Proposed graphical structures
496	C ₂₄ H ₅₀ O ₉ N ⁺ 12	
452	C ₂₂ H ₄₆ O ₈ N ⁺ 13	
408	C ₂₀ H ₄₂ O ₇ N ⁺ 14	
364	C ₁₈ H ₃₈ O ₆ N ⁺ 15	

320	$C_{16}H_{34}O_5N^+$ 16	
276	$C_{14}H_{30}O_4N^+$ 17	
232	$C_{12}H_{26}O_3N^+$ 18	
188	$C_{10}H_{22}O_2N^+$ 19	
85	$C_5H_{11}N^+$ 20	

References

- [1] B. Bednarska-Bolek, R. Jakubas, G. Bator, J. Baran, Vibrational study of the structural phase transition in bis(pyrrolidinium)-chloride-hexachloroantimonate(V) by infrared spectroscopy, *J. Mol. Struct.* 614 (2002) 151–157. [https://doi.org/10.1016/S0022-2860\(02\)00235-1](https://doi.org/10.1016/S0022-2860(02)00235-1).
- [2] M.I. Cabaço, M. Besnard, Y. Danten, J.A.P. Coutinho, Carbon dioxide in 1-butyl-3-methylimidazolium acetate. I. Unusual solubility investigated by Raman spectroscopy and DFT calculations, *J. Phys. Chem. A*. 116 (2012) 1605–1620. <https://doi.org/10.1021/jp211211n>.
- [3] M. Castriota, T. Caruso, R.G. Agostino, E. Cazzanelli, W.A. Henderson, S. Passerini, Raman investigation of the ionic liquid N-methyl-N-propylpyrrolidinium bis(trifluoromethanesulfonyl)imide and its mixture with LiN(SO₂CF₃)₂, *J. Phys. Chem. A*. 109 (2005) 92–96. <https://doi.org/10.1021/jp046030w>.
- [4] T. Fujimori, K. Fujii, R. Kanzaki, K. Chiba, H. Yamamoto, Y. Umebayashi, S. Ichi Ishiguro, Conformational structure of room temperature ionic liquid N-butyl-N-methylpyrrolidinium bis(trifluoromethanesulfonyl) imide - Raman spectroscopic study and DFT calculations, *J. Mol. Liq.* 131–132 (2007) 216–224. <https://doi.org/10.1016/j.molliq.2006.08.054>.
- [5] K. Ito, H.J. Bernstein, the Vibrational Spectra of the Formate, Acetate, and Oxalate Ions, *Can. J. Chem.* 34 (1956) 170–178. <https://doi.org/10.1139/v56-021>.
- [6] V. V. Kuzmin, V.S. Novikov, L.Y. Ustynyuk, K.A. Prokhorov, E.A. Sagitova, G.Y. Nikolaeva, Raman spectra of polyethylene glycols: Comparative experimental and DFT study, *J. Mol. Struct.* 1217 (2020) 128331. <https://doi.org/10.1016/j.molstruc.2020.128331>.
- [7] L. Koenig, A.C. Angood, Spectra of Poly(ethylene Glycols) in Solution, *J. Polym. Sci. Part A-2*. 8 (1970) 1787–1796. <https://doi.org/10.1002/pol.1970.160081013>.
- [8] T. Watkins, A. Kumar, D.A. Buttry, Supporting Information Designer Ionic Liquids for Reversible Electrochemical Deposition / Dissolution of Mg, (n.d.) 1–9.
- [9] D. Brouillette, D.E. Irish, N.J. Taylor, G. Perron, M. Odziemkowski, J.E. Desnoyers, Stable solvates in solution of lithium bis(trifluoromethylsulfone)imide in glymes and other

- aprotic solvents: Phase diagrams, crystallography and Raman spectroscopy, *Phys. Chem. Chem. Phys.* 4 (2002) 6063–6071. <https://doi.org/10.1039/b203776a>.
- [10] Y. Chen, Y.H. Zhang, L.J. Zhao, ATR-FTIR spectroscopic studies on aqueous LiClO₄, NaClO₄, and Mg(ClO₄)₂ solutions, *Phys. Chem. Chem. Phys.* (2004) 537–542. <https://doi.org/10.1039/b311768e>.
- [11] M. Falk, T.A. Ford, Infrared Spectrum and Structure of Liquid Water, *Can. J. Chem.* 44 (1966) 1699–1707. <https://doi.org/10.1139/v66-255>.
- [12] O. Palumbo, F. Trequatrini, J.B. Brubach, P. Roy, A. Paolone, Molecular assembling in mixtures of hydrophilic 1-butyl-1-methylpyrrolidinium dicyanamide ionic liquid and water, *Appl. Sci.* 10 (2020). <https://doi.org/10.3390/app10144837>.
- [13] K. Shameli, M. Bin Ahmad, S.D. Jazayeri, S. Sedaghat, P. Shabanzadeh, H. Jahangirian, M. Mahdavi, Y. Abdollahi, Synthesis and characterization of polyethylene glycol mediated silver nanoparticles by the green method, *Int. J. Mol. Sci.* 13 (2012) 6639–6650. <https://doi.org/10.3390/ijms13066639>.
- [14] O. Stan, M. Todica, L. Olar, I. Papuc, R. Stefan, IR and Fluorescence Investigation of Some PEG-Water Systems, *Mater. Today Proc.* 5 (2018) 15923–15928. <https://doi.org/10.1016/j.matpr.2018.06.065>.
- [15] A.R. Polu, R. Kumar, Impedance spectroscopy and FTIR studies of PEG - Based polymer electrolytes, *E-Journal Chem.* 8 (2011) 347–353. <https://doi.org/10.1155/2011/628790>.
- [16] O.B. Babushkina, Phase Behaviour and FTIR Spectra of Ionic Liquids: The Mixtures of 1-Butyl-1-methylpyrrolidinium Chloride and TaCl₅, *Zeitschrift Fur Naturforsch. - Sect. A J. Phys. Sci.* 63 (2008) 66–72. <https://doi.org/10.1515/zna-2008-1-212>.

Résumé de la thèse

Contexte et objectifs de l'étude

Le magnésium (Mg) et ses alliages sont considérés comme des matériaux attrayants pour de nombreuses applications dans les industries aérospatiale, automobile et biomédicale en raison de leur rapport résistance/poids élevé, de leur biocompatibilité, de leur grande abondance et de leur non-toxicité [1-5]. Sur le plan électrochimique, le Mg possède un potentiel d'oxydo-réduction standard relativement faible ($E_0 = -2,37$ V vs. ESH) et des capacités volumétrique et gravimétrique élevées (jusqu'à $3833 \text{ mAh}\cdot\text{cm}^{-3}$ et $2205 \text{ mAh}\cdot\text{cm}^{-3}$ respectivement) [6]. Ainsi, de nos jours, il est également considéré comme un matériau d'avenir pour les batteries Mg à anodes métalliques. Cependant, de nombreuses applications du Mg sont limitées par son taux de corrosion élevé dans les électrolytes aqueux ou même dans les électrolytes hybrides contenant des traces d'eau, ainsi que par l'existence de films de surface partiellement protecteurs et de produits de corrosion conduisant à une corrosion incontrôlée et fortement localisée. Les mécanismes, complexes et non complètement compris actuellement peuvent conduire à la formation de gaz d'hydrogène. La compréhension et le contrôle de la réactivité du Mg dans différents électrolytes sont donc nécessaires pour la recherche fondamentale et l'utilisation pratique des alliages de Mg.

Il est communément admis que dans les électrolytes aqueux, la réactivité des alliages de Mg est caractérisée par au moins trois processus : la dissolution anodique du Mg, la réduction cathodique de l'eau et la formation de produits de corrosion sur la surface du Mg [7,8]. Certaines caractéristiques spécifiques intéressantes du comportement électrochimique des alliages de Mg sont l'autocorrosion (taux de corrosion croissant après polarisation anodique) et l'effet de différence négative (EDN) ou évolution anormale de l'hydrogène (EH). Ce dernier indique que la vitesse de la réaction de réduction cathodique de l'eau s'accélère sous polarisation anodique. Il contredit les modèles classiques de cinétique électrochimique, caractérisés par

l'équation de Butler-Volmer, selon laquelle la vitesse des processus cathodiques diminue exponentiellement avec l'augmentation du potentiel anodique [9]. En tenant compte du fait que le Mg a le potentiel électrochimique le plus négatif parmi tous les éléments d'ingénierie métalliques (Fe, Al et etc...), il peut être facilement polarisé anodiquement dans des applications réelles, ce qui rend ce phénomène important non seulement du point de vue fondamental mais aussi pour les applications pratiques. Un EH anormal peut également être nuisible pour les applications de batteries car il conduit à une réduction de l'efficacité d'utilisation (EU) de l'anode métallique et à une libération abondante de gaz pouvant entraîner la défaillance de la batterie [10-12].

La corrosion du Mg dans les électrolytes aqueux a été largement étudiée et de nombreux mécanismes ont été proposés pour le processus de corrosion du Mg et l'EDN (**Fig. 1**) [13], même si aucun mécanisme d'EDN n'est communément accepté par la communauté scientifique.

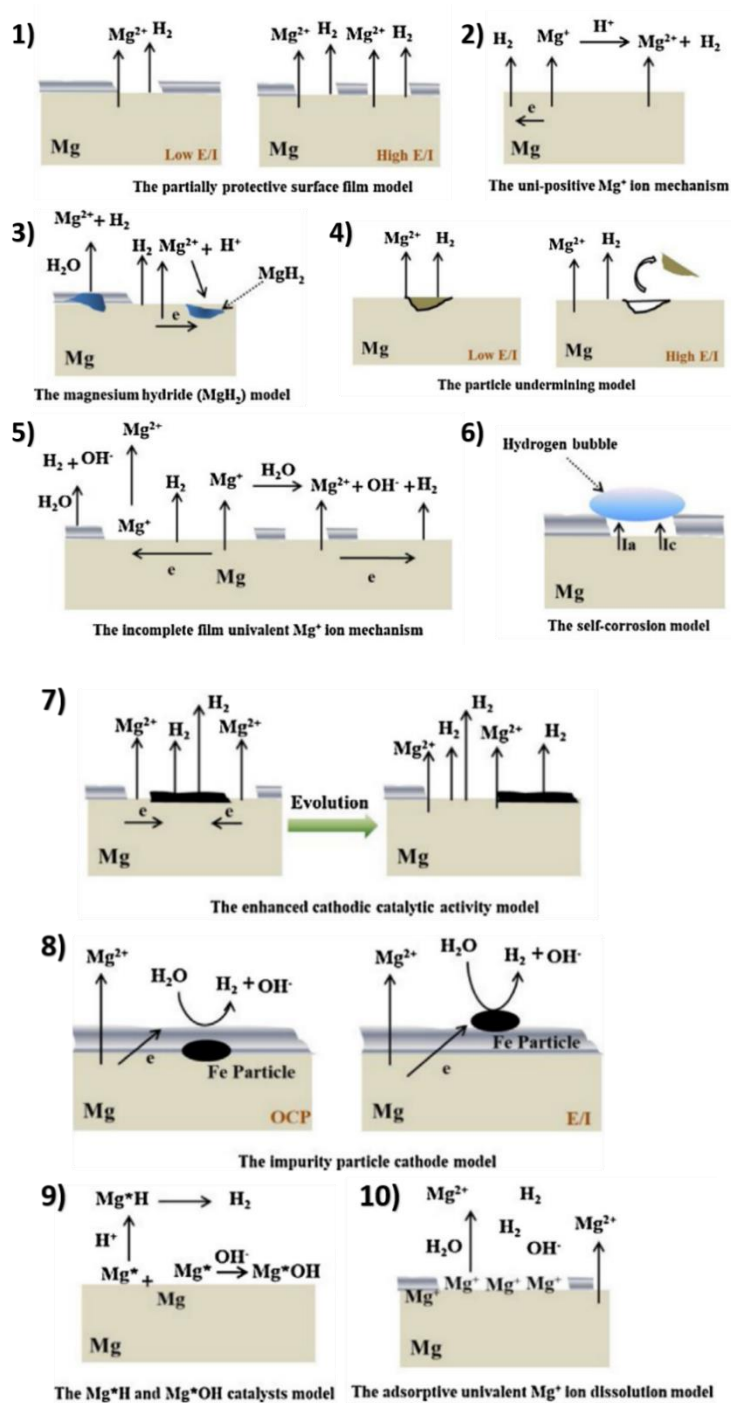


Fig. 1. Illustration schématique de divers modèles de dissolution de Mg ou d'EDN.

Adopté de [13].

En revanche, la possibilité d'une EDN n'a jamais été discutée pour les électrolytes non aqueux tels que les liquides ioniques, qui pourraient contenir de l'eau comme additif. Les liquides ioniques (LI) sont des composés ioniques dont la température de fusion est inférieure à 100 °C. Ils sont généralement constitués de cations organiques et d'anions organiques ou inorganiques et leur structure peut

contenir des fractions particulières comme des inhibiteurs de corrosion pour le Mg, ou des anions carboxylates. Les LIs constituent une classe relativement nouvelle d'électrolytes qui suscite un énorme intérêt pour les applications énergétiques en raison de leur haute conductivité, de leur bonne stabilité thermique, de leur large fenêtre de potentiel électrochimique, de leur faible volatilité [14-16].

L'utilisation pratique des LIs est toutefois limitée par leur stabilité restreinte en présence d'air et d'humidité, leur viscosité élevée et leurs propriétés de transport réduites. La formulation de LI hydrophiles et la dilution avec de l'eau peuvent aider à surmonter ces difficultés [17]. Cependant, l'ajout d'eau rétrécit la fenêtre de potentiel électrochimique (FPE) de l'électrolyte. Cet effet pourrait être potentiellement compensé et diminué par des interactions supplémentaires entre l'eau et les molécules de LI, par exemple la formation de liaisons hydrogène qui peut être possible entre l'eau et les groupes acétiques [18] et étheriques [19].

Malgré l'intérêt évident des mélanges eau - LIs, on sait très peu de choses sur le comportement des alliages de Mg dans ces électrolytes et sur le rôle des cations et anions des LIs dans les processus électrochimiques. Compte tenu de la réactivité du Mg dans les mélanges eau - LI, la question de l'existence de **l'EDN dans ces électrolytes est totalement inexplorée**. En tenant compte de ces circonstances, **le premier objectif de cette thèse est de découvrir de manière préliminaire la réactivité des alliages de Mg dans les mélanges eau-LI hydrophile, de vérifier l'absence ou la présence de l'EDN et de comparer le comportement de différents alliages de Mg dans différents LIs.**

Pour cela, un objectif intermédiaire était de concevoir de nouveaux LIs hydrophiles à température ambiante contenant des groupes étheriques et des anions acétate afin de comprendre les interactions entre l'eau et les fragments de LI, en particulier la capacité du cation à former des liaisons hydrogène intermoléculaires et son effet sur l'état moléculaire et la réactivité de l'eau.

Un autre objectif intermédiaire est d'explorer la chimie de l'interface solide - liquide entre le Mg et les électrolytes hybrides et la nature des films de surface existant dans de tels systèmes.

Une fois que la réactivité du Mg et la chimie de l'interface sont étudiées et que l'état moléculaire de l'eau dans l'électrolyte hybride est déterminé, le dernier objectif est de préciser le rôle du cation contenant des groupes fonctionnels spécifiques et de proposer des mécanismes provisoires de la réactivité du Mg et de l'activation ou de l'inhibition de l'EDN dans différents électrolytes.

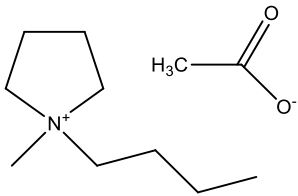
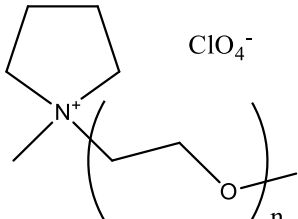
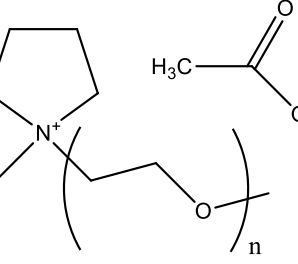
Les résultats de ce travail devraient contribuer à la compréhension fondamentale de la corrosion du Mg et du phénomène d'EDN dans les électrolytes H₂O-LIs, en particulier de l'effet du cation LIs, ainsi que de l'état moléculaire de l'eau dans ces électrolytes.

Approche méthodologique

Sur la base de la littérature, les liquides ioniques à base d'acétate ont été sélectionnés car ils ont révélé la meilleure capacité à former des liaisons hydrogène intermoléculaires avec l'eau et sont également censés agir comme des inhibiteurs de corrosion du Mg. Pour la conception du cation LI, une structure substituée par un polyéther a été proposée, car les atomes d'oxygène des groupes étheriques sont également censés former des liaisons hydrogène avec l'eau. De plus, il a été signalé que les liquides ioniques hydrophobes contenant du polyéthylène glycol (PEG) sec favorisaient le décapage du Mg. Afin de séparer les effets de l'anion acétique et du cation substitué par le PEG, des LI supplémentaires ont été conçus dans lesquels l'anion ou le cation étaient modifiés. Les LIs conçus sont présentés dans le tableau 1. Une voie de synthèse de ces électrolytes a été proposée et la synthèse a été réalisée. La composition des LIs a été vérifiée par résonance magnétique nucléaire (RMN) et spectroscopie de masse. La conductivité spécifique des mélanges H₂O-LIs a été mesurée par spectroscopie d'impédance électrochimique (SIE) et la mesure de la

fenêtre électrochimique a été réalisée dans une cellule électrochimique de petit volume (200 μ l) spécialement conçue.

Tableau 1. Noms systématiques, acronymes et formules développées des LIs conçues.

Liquide ionique; Leurs acronymes	Formule développée
Acétate de 1-butyl-1-méthylpyrrolidinium, [BMPyr]OAc; ILA	
Perchlorate de 1-méthoxy-polyéthylenglycol-1-méthylpyrrolidinium, [mPEG _n MPyr]ClO ₄ ; ILEP	
Acétate de 1-méthoxy-polyéthylenglycol-1-méthylpyrrolidinium, [mPEG _n MPyr]OAc ILE	

*n - signifie un nombre variable de groupes étheriques trouvés par MALDI-TOF, $4 \leq n \leq 16$ avec une valeur moyenne $\langle n \rangle = 7$.

La réactivité des alliages de Mg dans des mélanges eau - LI a été étudiée par des méthodes électrochimiques : polarisation potentiodynamique et polarisation potentiostatique cyclique. Une cellule électrochimique de fabrication artisanale a été

proposée pour les expériences électrochimiques, permettant de réduire le volume de l'électrolyte (700 μ l), de séparer les EH sur l'électrode de travail et sur la contre-électrode et d'étudier l'évolution de l'interface surface-solution par microscopie Time Lapse (TLM).

La spectroscopie Raman, la microscopie Raman confocale (MRC), la spectroscopie infrarouge à transformée de Fourier à réflectance totale atténuée (ATR-FTIR) et la spectrométrie de masse d'ions secondaires à temps de vol (ToF-SIMS) ont été utilisées pour étudier la composition chimique de la surface et de l'interface et détecter les produits de corrosion du Mg.

En outre, l'état moléculaire de l'eau et des fragments de LI dans les mélanges a été étudié par spectroscopie Raman, ATR-FTIR et simulation de dynamique moléculaire (DM). Pour vérifier l'effet des cations Mg^{2+} lessivés par la corrosion sur l'état moléculaire de l'électrolyte, des simulations DM des mélanges H_2O -LI avec et sans ajout d'ions Mg ont été réalisées.

Organisation du manuscrit et résumé des principaux résultats

Le manuscrit est composé de 4 parties principales.

Après cette introduction, **la partie 1 (Etat de l'art) propose une revue bibliographique de l'état de l'art permettant de comprendre le contexte du travail et de définir les questions scientifiques ouvertes auxquelles il sera répondu dans le manuscrit.**

La partie 2 (Développement méthodologique) explique le choix des matériaux et des méthodes et la stratégie expérimentale.

La partie 3 (Résultats) propose les réponses aux questions posées dans la partie (1) sur la base des résultats expérimentaux et théoriques. Cette partie est présentée sous la forme de 3 publications scientifiques et est complétée par plusieurs annexes à la fin du manuscrit.

Enfin, la quatrième partie formule les conclusions générales et les perspectives de l'ouvrage.

Les informations les plus importantes présentées dans chaque partie sont brièvement résumées ci-dessous :

Partie 1. Etat de l'art : Réactivité du Mg dans les électrolytes aqueux et non aqueux.

Cette section est organisée en 2 chapitres. **Le chapitre 1, "Réactivité du Mg dans les électrolytes aqueux"**, comprend un bref examen de certains principes de base décrivant la réactivité aqueuse des alliages de Mg. Le phénomène de l'effet de différence négative (EDN) est défini. En particulier, le rôle des films de surface et de la composition de l'électrolyte est souligné. **Le chapitre 2, "Mélanges eau-liquide ionique à température ambiante (RTIL) comme électrolytes pour le contrôle de la réactivité du Mg"**, présente les connaissances de base sur les liquides ioniques à température ambiante (RTIL ou LI), leur interaction avec les molécules d'eau et une revue détaillée de la littérature sur la réactivité du Mg (CP Mg et AZ61) dans les LI hydrophobes et hydrophiles et leurs mélanges avec l'eau.

Partie 2. Développement méthodologique.

Cette partie ne comprend que **le chapitre 3**, qui décrit brièvement la stratégie de conception de LI, les voies de synthèse, la conception des expériences électrochimiques et l'installation électrochimique, ainsi que le choix des techniques de caractérisation et donne une information théorique de base sur les techniques choisies de caractérisation en solution et de surface.

Partie 3. Résultats.

Cette partie est composée de trois chapitres présentant trois articles scientifiques publiés ou en cours d'évaluation. **Le chapitre 4, "Alliages de Mg dans l'eau - mélanges liquides ioniques hydrophiles : y a-t-il un effet de différence négative ?"** répond à la question de savoir si l'EDN est un effet universel en

présence d'eau ou s'il peut être supprimé dans les électrolytes hybrides. Les résultats électrochimiques et de microscopie à intervalle de temps sont comparés pour deux alliages de Mg disponibles dans le commerce (Mg pur et alliage AZ61 contenant de l'aluminium) dans deux LI acétate proposés dans ce travail contenant 10 % en poids d'eau. Un LI contient un cation avec une queue aliphatique ([BMPyr⁺]) et avec une queue étherique ([mPEG_nMPyr]OAc). Une EDN a été observée pour les deux alliages exposés dans l'électrolyte [BMPyr]OAc-H₂O. Cependant, dans l'électrolyte [mPEG_nMPyr]OAc-H₂O, la NDE a été supprimée sur le CP Mg tandis que le dégagement d'hydrogène a été complètement bloqué sur l'AZ61, ce qui est corrélé avec la formation d'un film gélatineux peu adhérent (**Fig. 2**) qui s'est formé et a cicatricé sous la polarisation anodique.

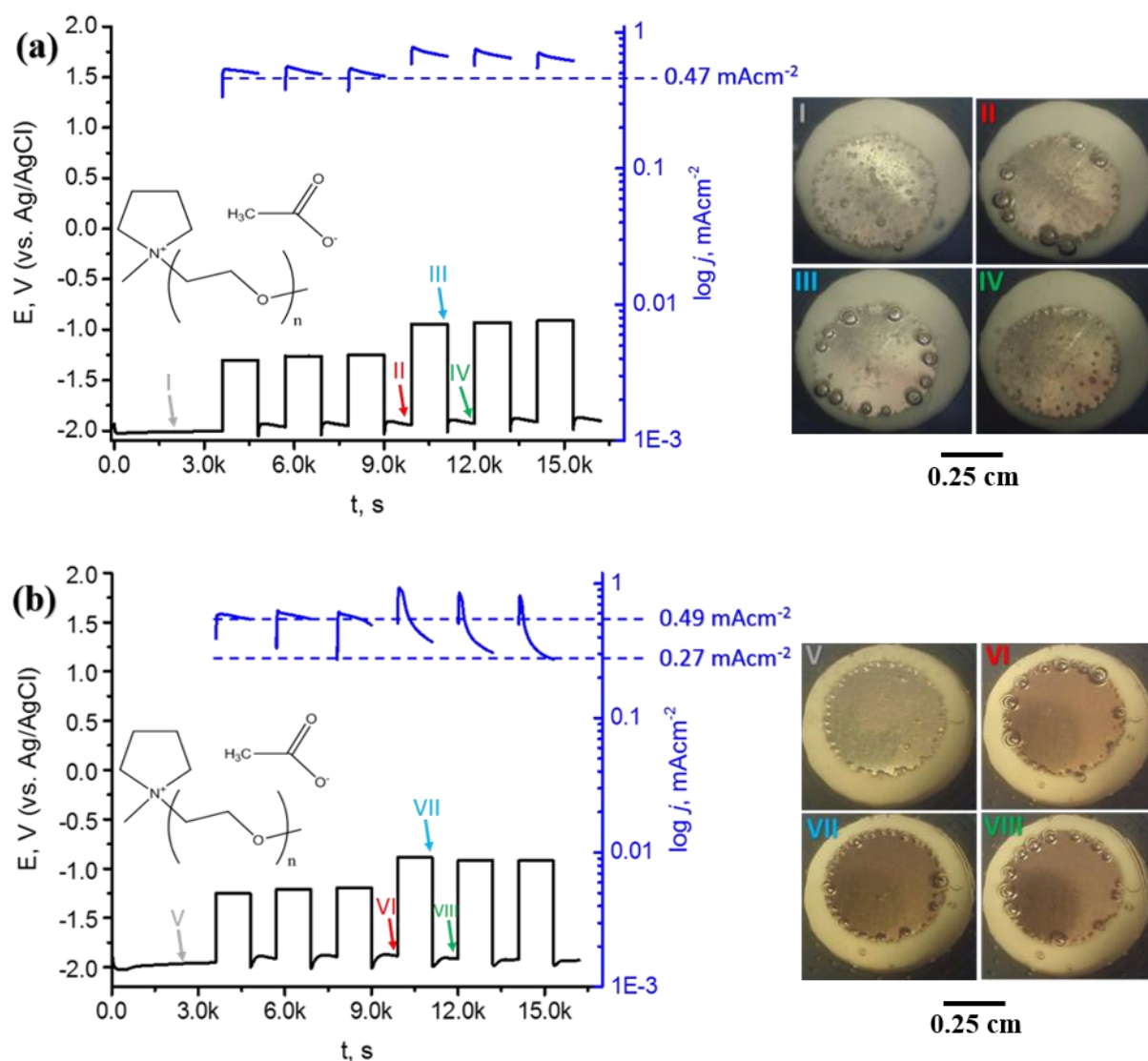


Fig. 2. Réponse électrochimique de (a) CP Mg et (b) AZ61 dans le mélange $[m\text{PEG}_n\text{MPyr}]\text{OAc-H}_2\text{O}$ et images TLM typiques de la surface prises pendant les expériences. Les moments auxquels les images sélectionnées ont été prises sont indiqués par des flèches (I-VIII) sur la courbe d'évolution du potentiel.

La microscopie Raman et la spectroscopie ATR-FTIR des surfaces humides après les expériences électrochimiques dans les deux électrolytes ont confirmé la présence d'acétate chimiquement lié à la surface après toutes les expériences, tandis qu'un film de $\text{Mg}(\text{OH})_2$ distribué de manière homogène s'est formé sur CP Mg mais aucun $\text{Mg}(\text{OH})_2$ n'a été détecté sur AZ61 indépendamment de l'électrolyte utilisé. Ceci indique que dans les mélanges eau-IL, la présence ou non de l'EDN ne peut être corrélée ni avec l'action des anions acétate (qui devaient limiter l'EDN à partir de

l'expérience de la corrosion aqueuse) ni avec la présence de produits de corrosion (qui devaient augmenter l'EDN à la suite de l'expérience de la corrosion aqueuse). L'article conclut que le rôle du cation pour la réactivité électrochimique de l'eau dans l'électrolyte hybride et pour la chimie du film de surface doit être mieux compris. Ces aspects sont traités dans les chapitres suivants.

Le chapitre 5, "Influence du cation contenant du PEG sur l'état moléculaire de l'eau dans les mélanges de liquides ioniques à base de H₂O-acétate", illustre en détails l'état moléculaire des ions des LI et de l'eau dans leurs mélanges. La synthèse et l'identification des liquides ioniques miscibles à l'eau à base d'acétate avec un cation MPyr hydrophobe à substitution aliphatique et une queue plus hydrophile à substitution polyétherique (mPEG_n-) dans le cation Mpyr⁺ ([BMPyr]OAc et [mPEG_nMPyr]OAc respectivement (voir le tableau 1 pour les structures graphiques) sont détaillées. Leurs propriétés électrochimiques telles que la fenêtre de potentiel électrochimique (FPE) (**Fig. 3**) et la conductivité ionique spécifique sont présentées. L'évolution de la conductivité et l'état moléculaire de l'électrolyte sont étudiés en fonction de la teneur en eau de l'électrolyte, qui varie dans un large domaine de concentration (de 2 à 99,8 % en masse d'eau).

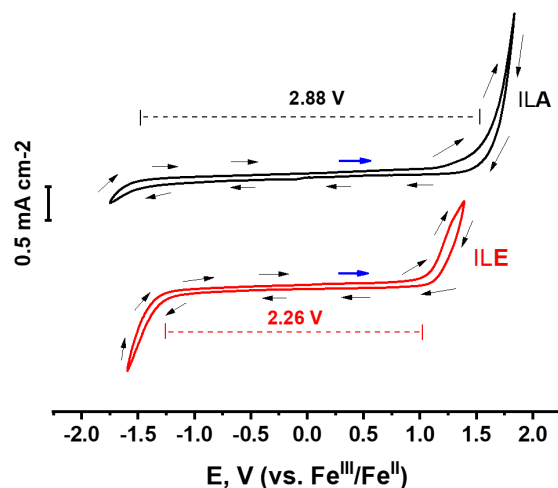


Fig. 3. Voltammogrammes cycliques enregistrés sur une électrode à disque de carbone vitreux de l'ILA et de l'ILE "tels que synthétisés", comme indiqué. Les flèches indiquent la direction de balayage du potentiel à partir du bleu. Vitesse de balayage 50 mVs^{-1} . La fenêtre de potentiel électrochimique est également représentée par des lignes en pointillés ; les limites sont déterminées à la coupure de densité de courant de $0,1 \text{ mA}\cdot\text{cm}^{-2}$.

Les interactions moléculaires entre l'eau et les ions IL dans l'électrolyte ont été suivies par des spectroscopies Raman et ATR-FTIR pour de multiples compositions de mélanges eau - LI. Sur la base des résultats de la spectroscopie de vibration, certaines idées sur l'environnement chimique des différents groupes fonctionnels et des molécules d'eau et sur l'organisation structurale de l'électrolyte sont proposées. Ces hypothèses sont corroborées par des simulations de dynamique moléculaire (DM) réalisées en collaboration avec l'Institut de Chimie pour les Sciences de la Vie et de la Santé, équipe TCM à Chimie ParisTech.

Les résultats révèlent que dans l'électrolyte [BMPyr]OAc- H_2O , les molécules d'eau forment des liaisons hydrogène avec les anions acétate ($\text{HOH}\cdots\text{OAc}$) (identifiées par des déplacements nets des positions des pics dans les spectres Raman et IR, voir l'exemple de la **Fig. 4 a**). La probabilité de formation de clusters d'eau est

très faible pour des rapports eau/IL allant jusqu'à $n(\text{H}_2\text{O}) / n(\text{ILA}) = 3$. Les molécules d'eau commencent à former des clusters d'eau à $n(\text{H}_2\text{O}) / n(\text{ILA}) \geq 3$.

En revanche, dans le $[\text{mPEG}_n\text{MPyr}]\text{OAc-H}_2\text{O}$, les molécules d'eau interagissent par liaisons hydrogène non seulement avec les anions acétate mais aussi avec les oxygènes de la chaîne étherique ($\text{HOH}\cdots\text{O}_{(\text{éthérique})}$) (**Fig. 4 b**). Une analyse minutieuse des spectres infrarouges dans la région des vibrations O-H, révèle que la croissance des amas d'eau ne commence qu'à $n(\text{H}_2\text{O}) / n(\text{ILE}) \geq 7$. La simulation DM a confirmé que si la dilution de l'ILA à substitution aliphatique entraîne une diminution continue de la probabilité des liaisons hydrogène entre l'eau et l'acétate et augmente donc fortement la probabilité de formation de clusters d'eau dans le LI à chaîne aliphatique, l'effet n'est pas le même pour l'ILE à substitution étherique. Pendant la dilution de l'ILE, les molécules d'eau continuent d'être liées par des liaisons H avec des groupes étheriques, ce qui limite considérablement la probabilité de formation d'amas d'eau.

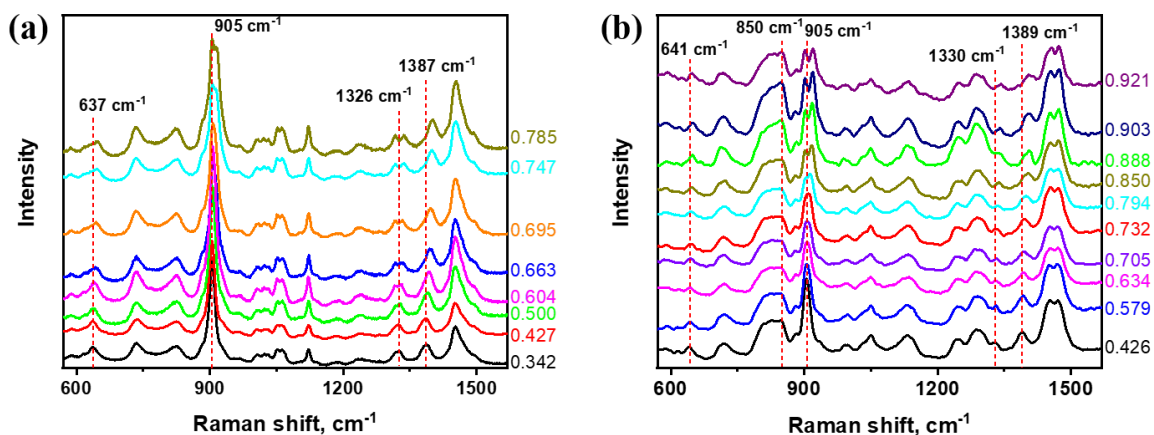


Fig. 4. Spectres Raman typiques de mélanges d'eau avec ILA (a) et ILE (b) avec différentes fractions molaires d'eau (comme indiqué). Sur (a), tous les décalages notés sont attribués aux vibrations des groupes acétate. Sur (b), 850 cm⁻¹ est attribué aux vibrations C-O-C, les autres - au groupe acétate. Pour des informations détaillées, voir le **chapitre 5**.

La modification de l'état moléculaire de l'eau avec la dilution de l'électrolyte peut être corrélée avec l'évolution de la conductivité ionique spécifique. La formation d'amas d'eau tend à augmenter significativement la conductivité ionique (**Fig. 5**). Une fois que la phase d'eau " libre " avec des liaisons hydrogène eau-eau est formée, la conductivité ionique augmente très rapidement dans les deux LIs. La transition entre l'augmentation de la conductivité avec l'ajout d'eau (comportement attendu pour des LIs légèrement diluées dans l'eau) et la diminution de la conductivité avec l'ajout d'eau (comportement typique des solutions aqueuses diluées) se produit à des rapports molaires eau/LI $n(\text{H}_2\text{O}) / n(\text{LI}) = 33$ pour les [BMPyr]OAc à substitution aliphatique et à $n(\text{H}_2\text{O}) / n(\text{LI}) = 145$ pour les [mPEG_nMPyr]OAc.

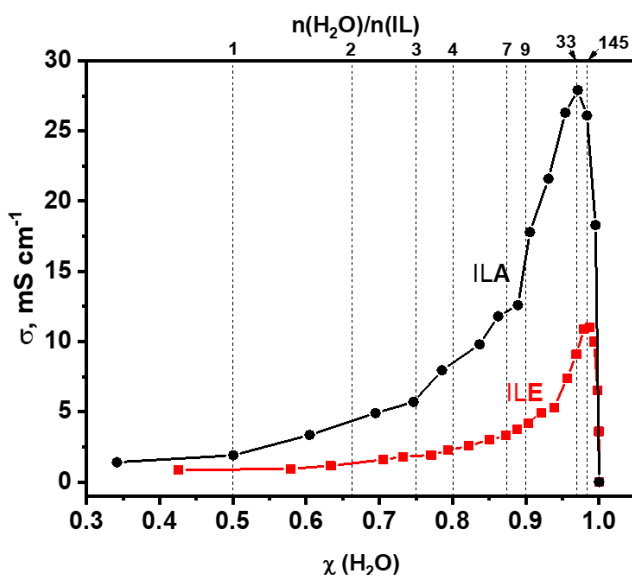


Fig. 5. Conductivité spécifique des mélanges eau-ILA et eau-ILE, σ , en fonction de la teneur molaire en eau $\chi(\text{H}_2\text{O})$. Les lignes verticales montrent les fractions pour certains rapports molaires sélectionnés entre les molécules d'eau et les molécules de LI $n(\text{H}_2\text{O}) / n(\text{LI})$ comme indiqué.

Dans le chapitre 6, " L'effet synergique du cation et de l'anion du liquide ionique (LI) inhibe l'effet de différence négative sur le Mg dans les mélanges eau - LI ", les origines de l'inhibition de l'EDN dans l'électrolyte [mPEG_nMPyr]OAc-H₂O et le rôle de l'anion acétate et du cation substitué par le

mPEG_n- et leur effet synergique sont démontrés. La nécessité des deux, l'anion et le cation, pour la suppression de l'EDN est démontrée par des expériences supplémentaires réalisées dans l'électrolyte spécialement conçu dans lequel le cation [mPEG_nMPyr⁺] est combiné non pas avec OAc⁻ mais avec ClO₄⁻. Si dans le mélange [mPEG_nMPyr]OAc-H₂O l'EDN était supprimée sur CP Mg, et l'EH complètement bloquée sur AZ61, dans le mélange [mPEG_nMPyr]ClO₄-H₂O une forte EH se produit et elle est augmentée sous la polarisation anodique (**Fig. 6**).

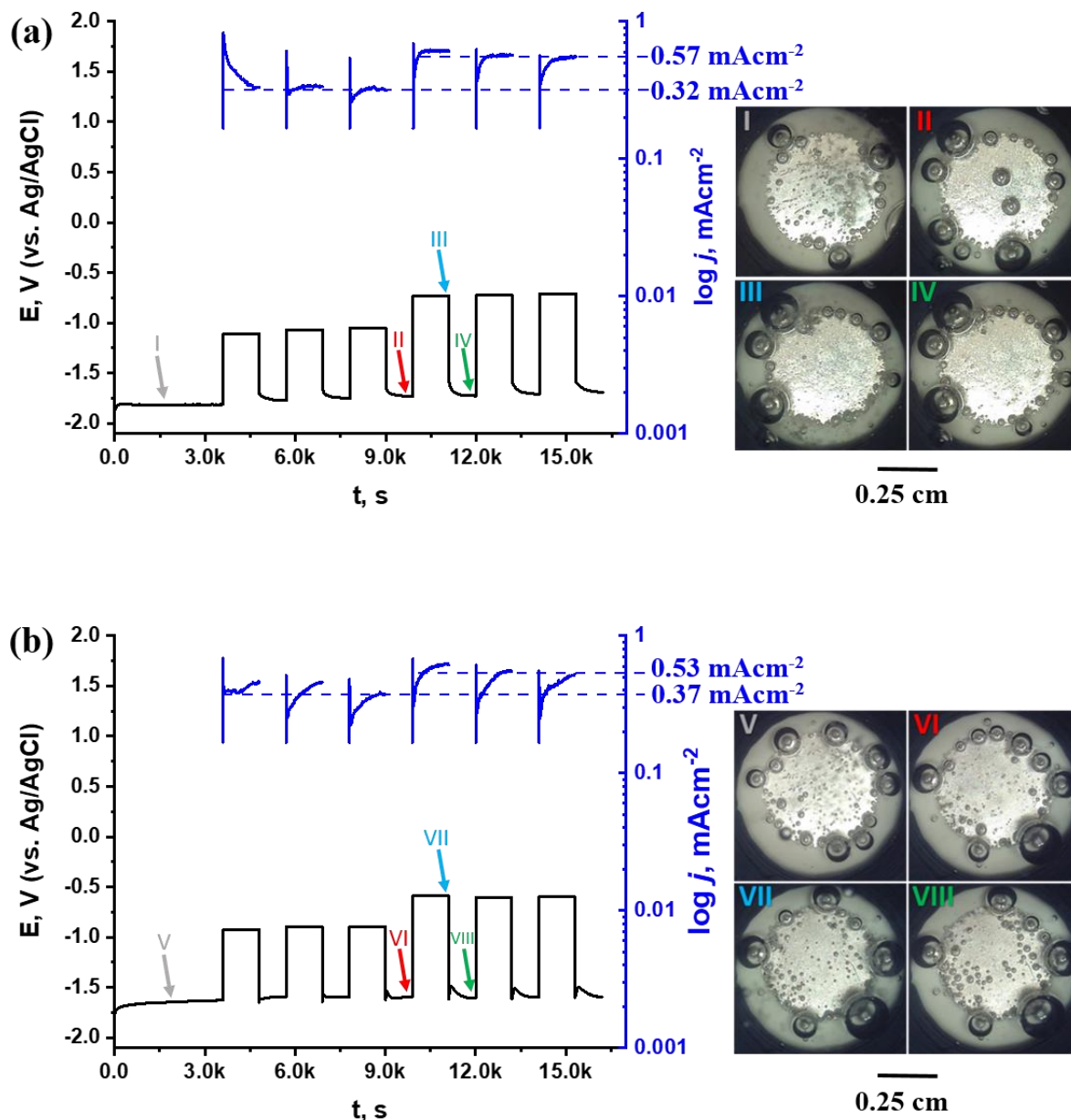


Fig. 6. Réponse électrochimique de (a) CP Mg et (b) AZ61 dans un mélange de $[m\text{PEG}_n\text{MPyr}]\text{ClO}_4\text{-H}_2\text{O}$ et images TLM typiques de la surface prises pendant les expériences. Le temps auquel les images sélectionnées ont été prises est indiqué par les flèches (I-VIII) sur la courbe d'évolution du potentiel.

L'examen des surfaces métalliques humides par spectroscopies vibrationnelles a révélé la même tendance à la formation de $\text{Mg}(\text{OH})_2$ que dans les LIs à base d'acétate (la présence sur CP Mg et l'absence sur AZ61) pour tous les électrolytes. Pour les échantillons ayant réagi dans $[m\text{PEG}_n\text{MPyr}]\text{ClO}_4\text{-H}_2\text{O}$ et

[mPEG_nMPyr]OAc-H₂O de légers décalages du Raman dans la région $\approx 790\text{-}830\text{ cm}^{-1}$, attribuée aux vibrations des groupes étheriques, étaient également présents. En même temps, l'évolution des spectres Raman autour de $\approx 1370\text{-}1381\text{ cm}^{-1}$ a suggéré une probable décomposition des groupes étheriques de l'électrolyte avec une catalyse des ions Mg²⁺ lessivés et des ions OH⁻ formés, ce qui a déjà été rapporté dans d'autres systèmes [20]. On doit donc conclure que l'anion OAc⁻ dans [mPEG_nMPyr]OAc-H₂O peut avoir un rôle supplémentaire, stabilisant le cation contre son oxydation électrochimique catalysée par Mg²⁺. En liant Mg²⁺ dans les complexes acétates, dont l'existence a été confirmée par spectroscopie vibrationnelle et ToF-SIMS.

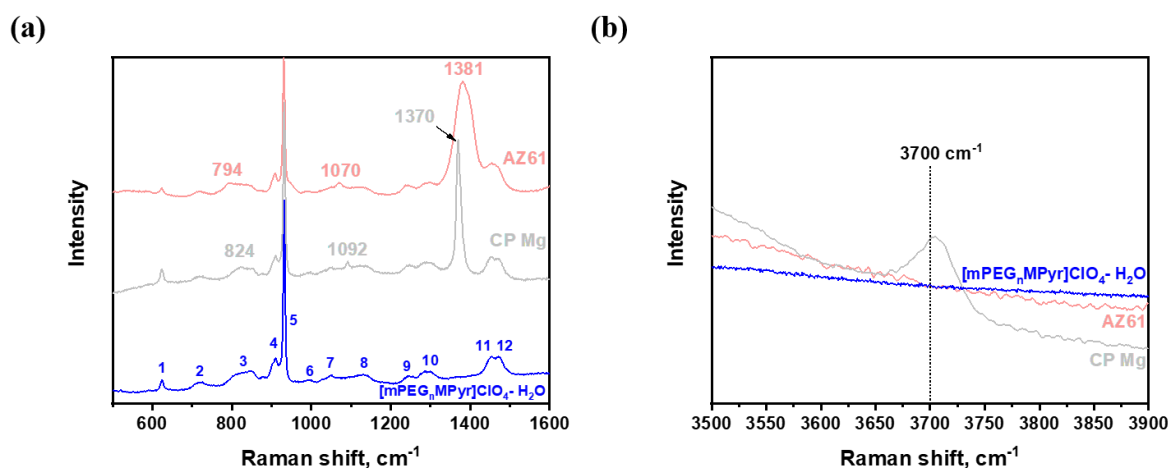


Fig. 7. Spectres Raman typiques enregistrés sur les surfaces de CP Mg et AZ61 (comme indiqué) après une expérience électrochimique dans [mPEG_nMPyr]ClO₄-H₂O dans les limites de 500-1600 cm⁻¹ (a), 3500-3900 cm⁻¹ (b). Le spectre de [mPEG_nMPyr]ClO₄-H₂O est présenté pour comparaison.

Les profils chimiques en profondeur obtenus par analyse ToF-SIMS ont permis de détailler la structure des films de surface et notamment d'une couche condensée prononcée à la surface de l'AZ61 après l'expérience électrochimique dans [mPEG_nMPyr]OAc-H₂O (**Fig. 8 b**) qui empêche probablement l'EDN. L'analyse détaillée par spectres de masse ToF-SIMS de ce film a révélé qu'il est principalement constitué de complexes à base de Al³⁺ et Mg²⁺ liés à des groupes étheriques et des

anions acétate. En revanche, seule une modification oxyde-hydroxyde et un film adsorbé, mais aucun film condensé, ont été observés sur CP Mg (**Fig. 8 a**) :

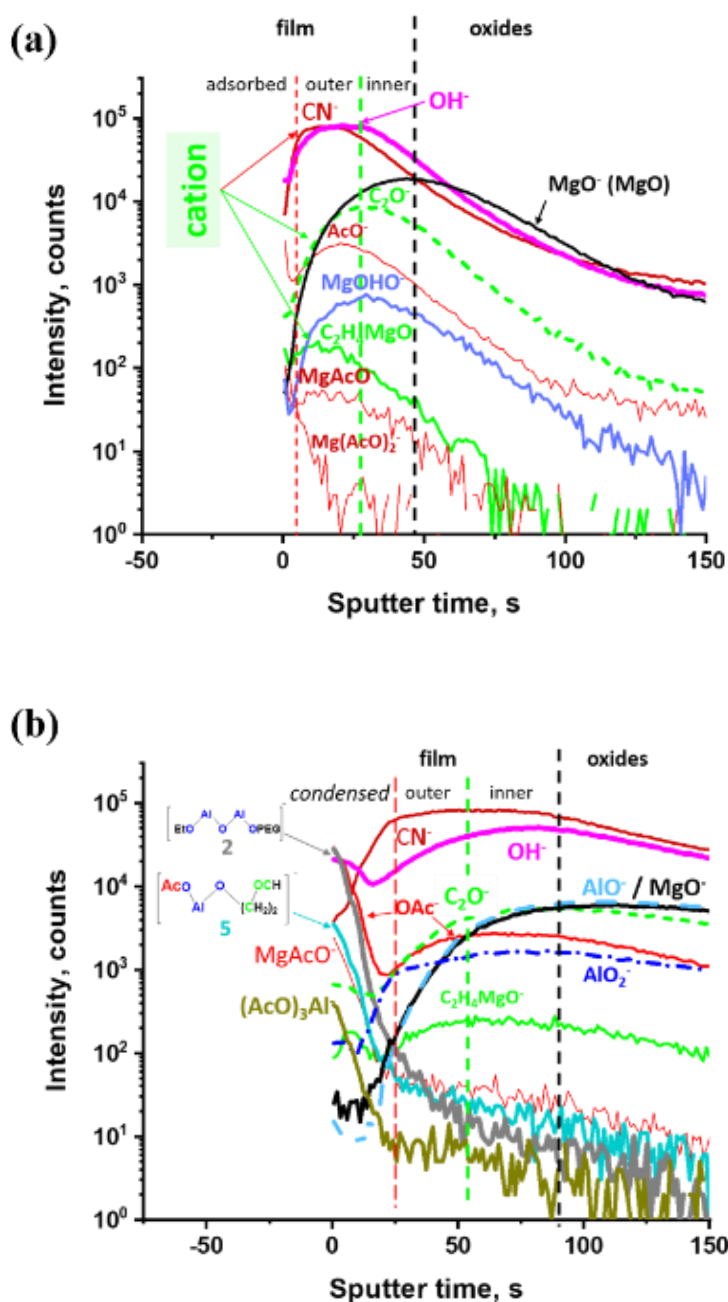


Fig. 8. Profil typique d'ions négatifs de profondeur ToF-SIMS obtenu après des expériences électrochimiques dans l'électrolyte $[\text{mPEG}_n\text{MPyr}]\text{OAc-H}_2\text{O}$ sur (a) CP Mg, (b) AZ61.

Une analyse détaillée des spectres IR dans la région vibratoire O-H ($3000\text{-}3700\text{ cm}^{-1}$) enregistrés sur les surfaces humides de CP Mg et AZ61 après des

expériences électrochimiques dans $[m\text{PEG}_n\text{MPyr}]\text{OAc-H}_2\text{O}$ a indiqué que les molécules d'eau sont toujours liées aux anions acétate et aux oxygènes des groupes étheriques. En même temps, dans $[\text{BMPyr}]\text{OAc-H}_2\text{O}$ et dans $[m\text{PEG}_n\text{MPyr}]\text{ClO}_4\text{-H}_2\text{O}$, les molécules d'eau semblent former des amas d'eau interconnectés (**Fig. 9**). La formation d'amas d'eau dans ces électrolytes pourrait expliquer la réactivité importante de l'eau et l'EH dans ces électrolytes, tandis que la liaison de l'eau dans $[m\text{PEG}_n\text{MPyr}]\text{OAc-H}_2\text{O}$ peut être considérée comme l'une des raisons de l'EH réduite.

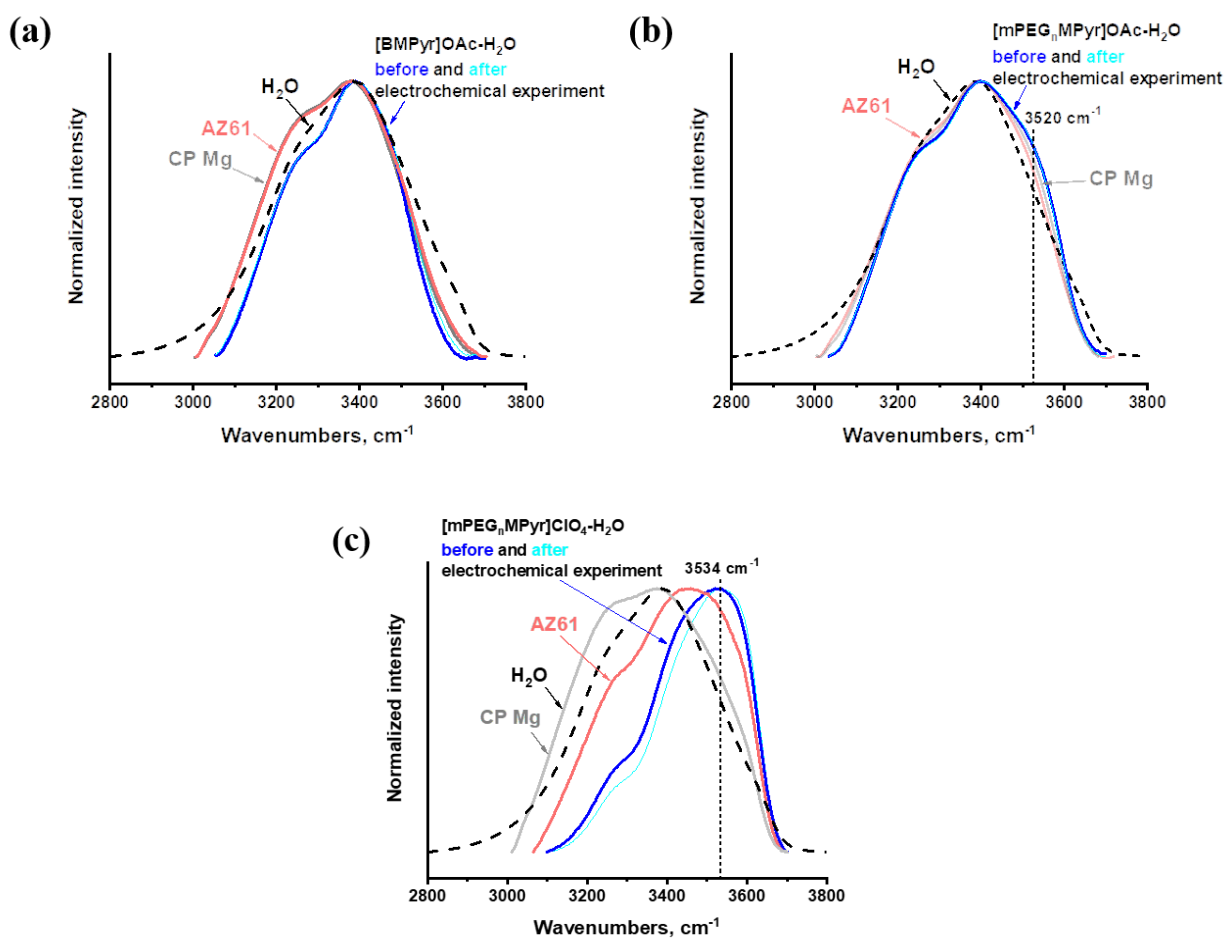


Fig. 9. Superposition des régions de vibration OH des spectres ATR-FTIR enregistrés sur les surfaces humides de CP Mg et AZ61 après l'expérience dans (a) - $[\text{BMPyr}]\text{OAc-H}_2\text{O}$; (b) - $[m\text{PEG}_n\text{MPyr}]\text{OAc-H}_2\text{O}$ électrolyte ; (c) - $[m\text{PEG}_n\text{MPyr}]\text{ClO}_4\text{-H}_2\text{O}$, comme indiqué. Les spectres de l'eau pure et de l'électrolyte avant et après l'expérience sont montrés pour comparaison.

Enfin, les simulations DM ont révélé que les ions Mg peuvent expulser avec succès les molécules de H₂O initialement liées à l'acétate pour rompre la liaison hydrogène (**Fig. 10 a**). Cependant, il semble que l'eau expulsée forme des liaisons hydrogène avec l'oxygène des groupes étheriques dans les mélanges [mPEG_nMPyr]OAc-H₂O, limitant ainsi la réactivité de l'eau et donc l'EH (**Fig. 10 b, c**).

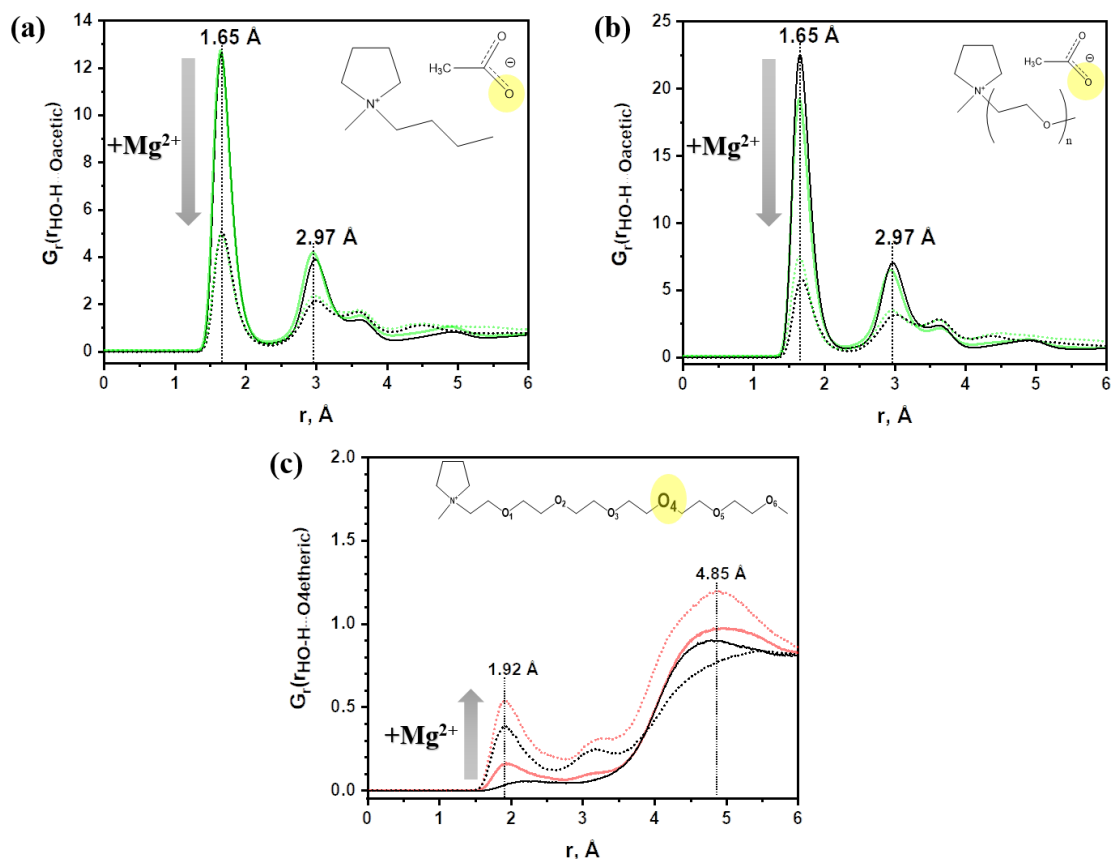


Fig. 10. Fonction de distribution radiale $G_r(r_{\text{HO-H}\dots\text{Oacetate}})$ (a, b) et $G_r(r_{\text{HO-H}\dots\text{Oetheric}})$ (c) des distances, r , entre l'oxygène de l'acétate ou l'oxygène de l'éther 4 (représenté dans les inserts) et l'hydrogène de l'eau le plus proche, calculées pour [BMPyr]OAc-H₂O (a) et [mPEG_nMPyr]OAc-H₂O (b, c) mélanges sans (lignes pleines) et avec (lignes pointillées) ions Mg²⁺ en solution. Des exemples de mélanges avec des rapports molaires entre l'eau et le LI $n(\text{H}_2\text{O}) / n(\text{IL}) = 1$ (noir) et $n(\text{H}_2\text{O}) / n(\text{IL}) = 2$ (rouge) sont présentés.

Ainsi, des mécanismes schématiques d'EDN sur CP Mg et AZ61 sont suggérés (**Fig. 11**). Deux contributions à l'inhibition de l'EDN sont proposées : (1) la liaison de l'eau dans l'électrolyte et (2) la formation du film de surface. L'effet synergique des anions acétate et du cation substitué étherique est discuté et proposé.

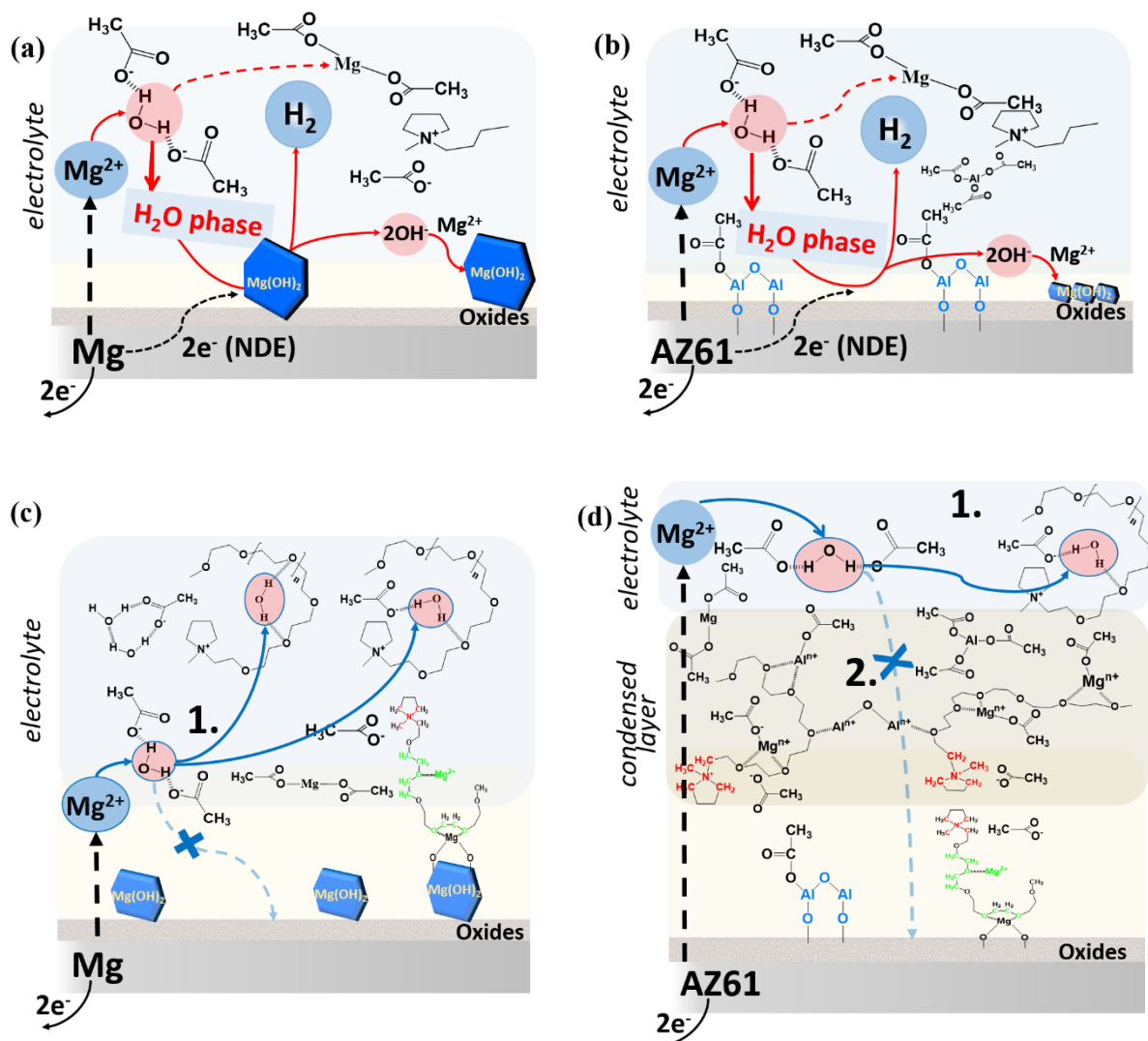


Fig. 11. Mécanismes schématiques de l'EDN dans [BMPyr]OAc-H₂O (**a, b**) et de l'inhibition de l'EDN dans [mPEG_nMPyr]OAc-H₂O sur CP Mg (**a, c**) et AZ61 (**b, d**).

Le chapitre 7, résultats et perspectives, résume les principales conclusions et constatations de ce travail. Les perspectives d'éventuels travaux de recherche ultérieurs et d'applications possibles sont proposées.

RÉSUMÉ

La réactivité des alliages de Mg est bien discutée dans la littérature et caractérisée par l'effet de différence négative (EDN). Cependant, la possibilité d'un EDN dans les mélanges eau - liquides ioniques hydrophiles (LI) n'a jamais été discutée et la réactivité du Mg dans ces mélanges reste inexplorée. Dans ce travail, trois liquides ioniques hydrophiles basés sur le cation N-méthyl-pyrrolidinium (MPyr⁺) avec des substitutions étheriques (mPEG_n⁻) et aliphatiques (butyl-) ont été conçus. Deux d'entre eux contenaient un anion acétate (OAc⁻) et un autre contenait ClO₄⁻. L'interaction des LIs avec l'eau ainsi que l'état moléculaire de l'eau dans les mélanges H₂O-LI ont été étudiés. La possibilité de formation de liaisons hydrogène intermoléculaires eau-acétate et eau-oxygène étherique a été démontrée. La réactivité du Mg pur et de l'AZ61 a été étudiée. L'EDN dans [BMPyr]OAc-H₂O quel que soit l'alliage a été observée. En revanche, dans [mPEG_nMPyr]OAc-H₂O, l'EDN a été supprimé sur le Mg pur et complètement bloqué sur l'AZ61. Des mécanismes d'effet synergique des anions acétate et du cation substitué polyétherique sont proposés.

MOTS CLÉS

Magnésium, liquides ioniques à base d'acétate, polyétherique, aliphatique, eau, EDN

ABSTRACT

The reactivity of Mg alloys is well discussed in the literature and characterized by Negative Difference Effect (NDE). However, possibility of NDE in the mixtures water – hydrophilic ionic liquids (ILs) has been never discussed and Mg reactivity in them remains unexplored. In this work, three hydrophilic ionic liquids based on N-methyl-pyrrolidinium (MPyr⁺) cation with etheric (mPEG_n⁻) and aliphatic (butyl-) substitutions were designed. Two of them contained acetate anion (OAc) and one contained ClO₄⁻. The interaction of ILs with water as well as molecular state of water in H₂O-IL mixtures were investigated. Possibility of formation intermolecular hydrogen bonds water-acetate and water-etheric oxygens has been demonstrated. Reactivity of pure Mg and AZ61 were studied. The NDE in [BMPyr]OAc-H₂O whatever the alloy was observed. On contrast, in [mPEG_nMPyr]OAc-H₂O, NDE was suppressed on pure Mg and completely blocked on AZ61. Mechanisms of synergistic effect of acetate anions and poly-etheric substituted cation are proposed.

KEYWORDS

Magnesium, acetate-based ionic liquids, polyetheric, aliphatic, water, NDE